Cracow University of Technology

Faculty of Civil Engineering

Tadeusz Kościuszko Cracow University of Technology

Faculty of Civil Engineering

Wind Engineering Laboratory (L-14)

Aleksander Pistol, MSc, Eng.

Influence of terrain roughness on boundary layer simulation in wind tunnel

Wpływ chropowatości terenu na symulację warstwy przyziemnej w tunelu aerodynamicznym

A dissertation submitted for the degree of doctor of philosophy

Supervisor: Andrzej Flaga, Prof., DSc, Eng.

Kraków, 2023

Table of Contents

Abstract

This dissertation mainly concerns experimental model tests in a wind tunnel. It is focused on the simulation of wind flow characteristics over different types of terrain roughness in a boundary layer wind tunnel. The motivation and importance of this work stem from the fact that wind tunnel tests are still the main research device for determining wind action on structures, which is particularly important in the case of tall buildings or large-span roofs. The work consists of 11 chapters.

The first two chapters, *Introduction* and *Theses and scientific originality of the work*, are dedicated to outlining the aims, motivation and problems to be undertaken in the thesis and highlighting its novelty. The main aim of this work is to find the most suitable arrangements of the turbulence-generating elements for simulating wind conditions associated with different terrain roughness categories in a wind tunnel. The secondary aim is the provision of more clear classification of terrain roughness.

The 3rd chapter, *Theoretical foundations and state of the art*, provides the essential information and formulas regarding wind flow characteristics, terrain roughness and wind tunnel simulation techniques. The described parameters, which will be subject to further analysis, are vertical mean wind speed and turbulence intensity profiles, longitudinal and vertical turbulence length scales, power density spectra, vertical co-coherence functions and frequency length scales. Terrain roughness categories and their implications on the wind flow characteristics are compared between different sources. This chapter also discusses the practical aspects of wind flow simulation and forming the air stream in wind tunnels.

In chapter 4, *Proposition of unification of terrain roughness classifications*, an authorial classification of the terrain roughness categories is proposed, which is based on various standards and analysis of the models of real-life areas. The aim of this classification is a more accurate description of the terrain roughness for the purposes of wind tunnel tests. The main novelty of this classification is the distinction between more categories related to suburban and urban terrain types. Moreover, the classification is based on two roughness parameters.

Chapter 5, *Wind tunnel simulations of different boundary layer types*, describes the experimental setup, measurement error assessment, formulation of the model scales used in the tests and a summary of the arrangements of different roughness elements used in the tests. The tests consisted of wind pressure measurements at 12 points arranged in a vertical setup. A total of 295 test cases were investigated in this work.

The results of these tests are processed according to the method presented in chapter 6, *Method applied for the results processing*. A comprehensive script in *MATLAB* was prepared that allows for the robust calculation of all the analysed wind flow characteristics from the obtained measurements. Furthermore, a Multi Attribute Decision Making method was applied to select the test cases that best match the wind flow characteristics of different terrain roughness categories according to the standards (PN-EN 1991-1-4, ISO 4354, ASCE/SEI-7).

The next two chapters are intended for the analysis of the tests results. Chapter 7, *Effects of roughness elements on different wind flow characteristics*, presents a study of the impact of different turbulence-generating elements – blocks, barriers, spires and a turbulising net – on

some of the key wind flow characteristics related to the vertical mean wind speed and turbulence intensity profiles, turbulence length scales and frequency length scales. The 8th chapter, *Results discussion and analysis for selected cases*, analyses in detail the five test cases that were chosen as representative for each of the terrain roughness categories according to the Eurocode. All the relevant plots are shown and discussed, the suitability of the simulations is evaluated and comparisons with various theoretical models are made.

The outcomes of the dissertation are summarised in the 9th chapter, *Conclusions and final remarks*. They are divided into four subsections, each one focused on a different aspect of the work. The first subsection lists the conclusions regarding the proposed terrain roughness classification. The second one sums up the findings about the simulation of different types of the atmospheric boundary layer in the wind tunnel. Brief guidelines for the proper simulation of various wind flow characteristics are formulated in the third subsection. The final subsection of this chapter outlines the plans for future research on the topics addressed in this work.

The last two subsections, *Literature* and *Attachments*, provide the bibliography for this dissertation and the list of enclosed attachments. These attachments are the complete *MATLAB* script used for the results processing, the spreadsheet with complete results of every test case and plots of all measuring signal and wind flow characteristics for the test cases chosen as most representative for each terrain category according to different standards.

Keywords: wind engineering, wind tunnel tests, boundary layer simulation, wind flow characteristics, terrain roughness.

Szczegółowe streszczenie w języku polskim (Extended abstract in Polish)

Praca ma przede wszystkim charakter eksperymentalny i dotyczy tematyki badań modelowych w tunelu aerodynamicznym. Głównym aspektem badawczym pracy jest symulacja struktury przepływu wiatru nad terenami o różnej chropowatości w tunelu aerodynamicznym z warstwą przyścienną. Tego typu tunele wykorzystywane są do badania zagadnień inżynierii wiatrowej związanej głównie z działaniem wiatru na obiekty budowlane, ludzi oraz do celów energetyki wiatrowej. Główną motywacją do podjęcia tej tematyki w pracy doktorskiej jest wciąż dominująca rola badań modelowych w celach wyznaczania działania wiatru na konstrukcje, kluczowa szczególnie w przypadku budynków wysokościowych lub przekryć o dużej rozpiętości. Praca liczy 11 rozdziałów. Poniżej znajduje się opis zawartości każdego z nich.

Rozdział pierwszy określa cele i motywacje powstania pracy. Głównym celem pracy jest znalezienie najbardziej odpowiednich ustawień elementów generujących turbulencję w tunelu aerodynamicznym (takich jak wysuwane klocki, iglice, bariery i siatka turbulizacyjna) do odwzorowania struktury przepływu powietrza charakterystycznej dla różnych kategorii chropowatości terenu. Drugim celem pracy jest zaproponowanie bardziej przejrzystej klasyfikacji chropowatości terenu.

W drugim rozdziale sformułowane są tezy pracy oraz jej naukowa oryginalność. Następujące tezy zostały postawione w niniejszej dysertacji:

1. Dodatkowe parametry służące do opisu chropowatości terenu mogą prowadzić do lepszej identyfikacji i klasyfikacji rzeczywistych lokalizacji do celów badań modelowych w tunelach aerodynamicznych.
2. Istnieje możliwość oceny wpływu różnych elementów turbulizujących, takich jak klocki, iglice i bariery, na różne charakterystyki przepływu. Takie podejście może poskutkować bardziej precyzyjną symulacją warstwy przyziemnej w tunelach aerodynamicznych.

Rozdział trzeci zawiera teoretyczne podstawy dotyczące struktury wiatru, przegląd i porównanie informacji na temat chropowatości terenu według różnych źródeł oraz zestawienie informacji na temat sposobów symulacji struktury przepływu w warstwie przyziemnej w tunelach aerodynamicznych. Najważniejszymi charakterystykami wiatru, na których skupia się praca, są: pionowe profile średniej prędkości wiatru i intensywności turbulencji, podłużne (wynikające z czasowej autokorelacji) i pionowe (wynikające z korelacji przestrzennej) skale długości turbulencji, gęstości widmowe mocy, koherencja zwyczajna i skale częstotliwości. Przeprowadzone porównania dotyczą najważniejszych charakterystyk przepływu i dotyczą różnych typów chropowatości terenu oraz obejmują normy PN-EN, ISO, ASCE/SEI i ESDU. Ostatnia część rozdziału szczegółowo opisuje formowanie przepływu i generację struktury wiatru w tunelach aerodynamicznych metodami pasywnymi oraz krótko charakteryzuje rzadziej stosowane metody aktywne.

Na podstawie literatury oraz obliczeń dotyczących modeli rzeczywistych lokalizacji, w rozdziale czwartym wyprowadzono autorską klasyfikację chropowatości terenu, która

wyróżnia łącznie 8 różnych kategorii terenu. Klasyfikacja ta skupia się głównie na terenach miejskich i podmiejskich, wprowadzając dodatkowe rozróżnienie oparte o charakter przeszkód. Poszczególne typy terenu zdefiniowane są na podstawie dwóch wartości: średniej wysokości chropowatości (parametru wymiarowego) oraz stosunku odchylenia standardowego wysokości chropowatości do średniej wysokości chropowatości (parametru bezwymiarowego). Takie określenie kategorii chropowatości skutkuje jednoznacznym i klarownym przyporządkowaniem dowolnego terenu do dokładnie jednej kategorii chropowatości. Pozwala przy tym na rozróżnienie pomiędzy terenami o gęstej, jednorodnej pod względem wysokości zabudowie i terenami o dużej rozbieżności wysokości zabudowy (np. centra dużych miast o szerokich ulicach i budynkach wysokościowych).

W rozdziale piątym przedstawiono opis eksperymentu. Kolejno opisane jest stanowisko pomiarowe – tunel aerodynamiczny Laboratorium Inżynierii Wiatrowej Politechniki Krakowskiej, aparatura – miniaturowe skanery ciśnień wraz z modułem pomiarowym, parametry pomiaru i przypadki badawcze. Dokonano tutaj także analizy potencjalnych błędów pomiarowych. Łącznie przebadano 295 różnych kombinacji klocków na wlocie do tunelu i na długości przestrzeni pomiarowej, iglic, barier i siatki turbulizacyjnej. Dokładne zestawienie wszystkich przypadków badawczych znajduje się w Załączniku nr 2 do niniejszej pracy, gdzie również zamieszczono szczegółowe wyniki dla każdego przypadku.

Rozdział szósty szczegółowo opisuje proces opracowania wyników badań. W rozdziale tym przedstawione i wyjaśnione są poszczególne części przygotowanego skryptu w programie *MATLAB*, który został wykorzystany do automatyzacji tego opracowania. Skrypt ten przeprowadza filtrację sygnału pomiarowego (wartości ciśnień), na ich podstawie wyznacza przebieg czasowy prędkości przepływu w każdym punkcie i oblicza wartość średnią i odchylenie standardowe. Następnie wyznaczane są podstawowe charakterystyki struktury przepływu w warstwie przyziemnej: pionowe profile średniej prędkości wiatru i intensywności turbulencji. Parametry tych profili wykorzystywane są do przyporządkowania danego przypadku badawczego do odpowiedniej kategorii chropowatości terenu według różnych norm. W kolejnych krokach obliczane są pozostałe charakterystyki przepływu: autokorelacja, skale długości turbulencji w kierunkach podłużnym i pionowym, gęstości widmowe mocy, koherencja zwyczajna i skale częstotliwości. Skrypt ponadto automatycznie tworzy i zapisuje wykresy dla każdej z tych charakterystyk i zapisuje wyniki w arkuszu kalkulacyjnym. Druga część tego rozdziału poświęcona jest doborze przypadków badawczych, w których zasymulowana struktura przepływu najbardziej odpowiada poszczególnym kategoriom chropowatości według różnych norm. Dla kategorii, do których przyporządkowano największą liczbę przypadków badawczych i gdzie istniały podstawy do selekcji na podstawie wielu argumentów, zastosowano wielokryterialną metodę wspomagania decyzji TOPSIS.

Rozdział siódmy zawiera wyczerpującą analizę wpływu różnych elementów generujących turbulencję w tunelu aerodynamicznym na poszczególne charakterystyki przepływu. Analiza ta dotyczy kolejno parametrów związanych z pionowymi profilami średniej prędkości wiatru i turbulencji, skali długości turbulencji i skali częstotliwości. Porównania dokonywane są najpierw dla różnych wysokości klocków przy tej samej konfiguracji iglic i barier, a następnie porównywany jest wpływ różnych wysokości iglic przy tych samych barierach oraz różnych typów barier przy tych samych iglicach. Analiza ta pozwala na znalezienie prawidłowości

rządzących wpływem tych elementów na strukturę wiatru, a w konsekwencji na sformułowanie wytycznych dotyczących symulacji różnych typów warstwy przyziemnej atmosfery w tunelu aerodynamicznym.

W ósmym rozdziale są natomiast zestawione wykresy dotyczące wszystkich analizowanych charakterystyk przepływu dla pięciu przypadków badawczych, które zostały wybrane jako najlepiej odwzorowujące poszczególne kategorie chropowatości terenu według PN-EN 1991-1-4. Dane te opatrzone są szczegółowym komentarzem, dokonano oceny dokładności symulacji dla każdej z kategorii i porównania z modelami teoretycznymi. Dla kategorii terenu odpowiadającym terenom otwartym, przedmieściom i miastom uzyskano bardzo dobrą precyzję symulacji, natomiast dla kategorii odpowiadającym terenom z dostępem do otwartego morza i terenom blisko jezior lub z pomijalnie niewielką roślinnością – wystarczająco dobrą precyzję.

Podsumowanie i wnioski końcowe z pracy zawarte są w rozdziale dziewiątym. Pierwsza część tego rozdziału skupia się na wnioskach dotyczących wprowadzonej klasyfikacji chropowatości terenu. Podsumowaniem tej części jest wykazanie, że pierwsza teza pracy jest prawdziwa. W drugiej części zestawione są konkluzje dotyczące symulacji struktury wiatru w tunelu aerodynamicznym. Ta część stanowi podstawę do udowodnienia drugiej tezy pracy. Następnie sformułowane zostały wytyczne dotyczące symulacji warstwy przyziemnej w tunelach aerodynamicznych, uwzględniające zaobserwowane możliwości sterowania niektórymi z jej charakterystyk poprzez odpowiedni dobór elementów turbulizujących. Ostatnia część tego rozdziału przedstawia planowane dalsze kierunki badań w tematyce poruszonej w niniejszej pracy. Kierunki te dotyczą pomiarów profili wiatru w skali rzeczywistej w celu walidacji zaproponowanej klasyfikacji chropowatości terenu, dodatkowych możliwości identyfikacji parametrów chropowatości terenów dla rzeczywistych lokalizacji, wykorzystania zaproponowanej metody symulacji do testowania i kalibracji innych tuneli aerodynamicznych oraz wyprowadzenia bardziej szczegółowych modeli działania wiatru na konstrukcje budowlane.

Dwa ostatnie rozdziały zawierają bibliografię, na której opierano się podczas przygotowywania niniejszej dysertacji oraz listę załączników. Załączniki do pracy to pełny skrypt do programu *MATLAB* wykorzystany do opracowania wyników, arkusz kalkulacyjny z dokładnym zestawieniem wszystkich przypadków badawczych i uzyskanych dla nich wyników oraz zbiór wykresów dla każdego przypadku, który został wybrany jako reprezentatywny dla jednej z kategorii chropowatości terenu według różnych norm.

Słowa kluczowe: inżynieria wiatrowa, badania w tunelu aerodynamicznym, symulacja warstwy przyziemnej, struktura przepływu powietrza, chropowatość terenu.

1. Introduction

Recreating the conditions expected in nature is a key part of any experiment, model tests performed in a wind tunnel notwithstanding. In the case of boundary layer wind tunnels where the investigations are conducted to determine the wind action on the more sophisticated types of structures, such as tall, slender buildings or large span roofs, this is usually done through certain methods of artificial generation of mean wind speed and turbulence intensity profiles that would correspond with conditions at a site. Understanding the importance of this preparational aspect before starting any tests is crucial, as its impact on the reliability of the results might be very significant. The main focus of this work is finding the most robust solutions to simulating the atmospheric boundary layer in wind tunnel tests, presented on an example of the wind tunnel of the Wind Engineering Laboratory of the Cracow University of Technology.

1.1. Aim and scope of the thesis

This work aims to find the most suitable arrangements of the flow modifying devices (such as blocks, spires, barriers and turbulising nets) for simulating wind conditions associated with different terrain roughness categories in a wind tunnel. The two most fundamental parameters taken into account are vertical profiles of mean wind speed and turbulence intensity. However, the comparison does not neglect more detailed characteristics, such as turbulence length scales (autocorrelation, which provides information on the dimensions of along-wind eddies and vertical correlation), power density spectra and frequency length scales, used for identifying the frequency domain of the gusts. Within this work, the data from wind tunnel measurements is compared against the information provided in the literature and building codes, effectively arranging for direct comparison and the possibility to determine the most suitable matches for different terrain categories. Moreover, the obtained data is used to formulate general guidelines for wind tunnel simulations of the atmospheric boundary layer that take into account the different effects of turbulence-generating elements in a wind tunnel on various wind flow characteristics, as evidenced through the performed investigations.

Furthermore, as some of these characteristics often vary quite significantly between the sources or are only provided in a descriptive form, a more exact approach for the terrain roughness classification is proposed. The main difference in this approach is the inclusion of another parameter, the standard deviation of the heights of roughness-generating elements, along with the more widely used roughness height. The estimation of these two parameters that would describe each roughness category as accurately as possible is based on a thorough analysis of several real-life terrain sectors for which sufficiently reliable data was available.

The scope of the experimental investigations conducted amounted to almost 300 measured cases of different arrangements of flow-modifying elements in the wind tunnel. The measurements were done using 12 Pitot tubes in a vertical setup under a set wind speed.

1.2. Motivation for undertaking the research

With the technological advancement in the field of structural design that can be observed for more than a century, ever more complex and challenging types of buildings are erected. Whether it is the extraordinary height of a tower – usually paired with its slenderness (Pistol et al., 2022), covering a massive surface with lightweight membranes (Rizzo et al., 2022) or

particularly original shape (Kłaput et al., 2022), such sophisticated constructions are not covered by the codes when it comes to environmental actions, thus they require individual, case-by-case treatment. And while alternative methods, such as computational fluid dynamics (CFD), have advanced significantly, wind tunnel tests are still the most reliable way of estimating wind effects on buildings.

The basic data from wind tunnel tests that are most often sought-after by constructors is pressure distribution on the building's external surfaces, which directly translates to wind actions (Ł. Flaga et al., 2022). However, there are also two different types of tests that are recently proving more pivotal for building designers: wind comfort analyses and wind-induced vibrations tests. The first are based on measurements of wind speed and location-specific meteorological data and their main purpose is to determine the impact of new developments on the wind microclimate in its surroundings and on people who perform different types of activities in its vicinity. The second, which require specific aeroelastic models (a model that recreates, with proper similarity criteria applied, the most significant dynamic characteristics of the building), are used for the assessment of the vibrational comfort of the occupants in the event of strong winds and the level of the dynamic component of wind action on the structure itself. These two additional types of applications of wind tunnels arguably require a higher degree of precision in the wind tunnel conditions than the pressure tests.

With the large number of projects consisting of these tests being commissioned each year to the Wind Engineering Laboratory, the need for a swift and reliable method of recreating wind conditions for the experiments has been identified. This has led to a more systematic approach in selecting the arrangement of turbulising elements best suitable for each case, which in itself is an iterative process. Moreover, developing an accurate and measurable terrain roughness categorisation would not only help define the category for each individual project more straightforwardly but also provide a sound and easy-to-understand explanation for architects and consulting engineers about the principles of wind tunnel investigations. These are the key factors that serve as a driving force behind this research, which prove its practical and universal application in the field of wind tunnel model studies.

2. Theses and scientific originality of the work

The following two theses are to be investigated in this work:

1) Additional parameters used to describe the terrain roughness can lead to better identification and classification of a real-life area for the purpose of wind tunnel tests.

2) It is possible to evaluate the effect of different roughness elements, such as elevated blocks, spires or barriers, on different wind flow characteristics. This approach can lead to more accurate boundary layer simulation in wind tunnel tests.

The scientific novelties of this work include:

- A proposition of extended terrain roughness classification, which distinguishes more terrain categories related to urban and suburban terrains. This proposition is based upon the analysis of real-life locations and different standards;
- A detailed analysis of the influence of different roughness elements in the wind tunnel on various wind flow characteristics. The analysis is based on extensive wind tunnel tests with different combinations of roughness elements. The results of this analysis are summarised in the form of concise guidelines and can be applied for a more effective and accurate simulation of a boundary layer in wind tunnels;
- A comprehensive script in *MATLAB* for the results processing, which can be implemented for robust and detailed analysis of wind flow parameters obtained in wind tunnel tests. This script can be easily adapted for different measurement setups.

3. Theoretical foundations and state of the art

Synoptic winds, which are the main focus of wind tunnel tests, can be satisfactorily described as stationary and non-uniform stochastic processes. At a single point, the wind velocity field can be characterised by several different parameters: mean wind speed $\bar{v}$, mean wind direction θ (most often limited to the direction in only a single, horizontal plane) and fluctuations (turbulence intensity) v'. However, when analysing a wind flow, additional characteristics are required, which can be summarised into several domains:

- Space domain: vertical mean wind speed profile $\bar{v}(z)$ and vertical turbulence intensity profile $I_v(z)$;
- Time domain: autocorrelations ρ_v, spatial correlations ρ_{vv} and turbulence length scales $L_x(z), L_y(z), L_z(z)$;
- Frequency domain: power spectral density $G_v(z, f)$, cross power spectral density (coherence) $G_{vivj}(z_1, z_2, f)$ and frequency scales f_x^*, f_y^*, f_z^*.

Furthermore, these characteristics are strongly influenced by the local boundary layer conditions resulting from the types, heights, geometries and density of the obstacles located on the ground, which are described under the general term *terrain roughness*. In most cases, it is described directly by several parameters, such as roughness height k_r or a graphic/verbal description (PN-EN 1991-1-4, 2011) which, even if not technically exact, gives a general concept of a terrain roughness type. Another method of describing different roughness terrain categories is indirect, through the flow parameters which are characteristic for a given terrain – most often regarding the vertical mean wind speed and turbulence intensity profiles.

Proper simulation of the flow characteristics is a key part of wind tunnel model tests, which usually cannot be performed by directly modelling the exact terrain in the windward section of the wind tunnel before the model. Certain techniques have been developed to either impact the flow with desired boundary conditions at the inlet of the wind tunnel or to modify the flow characteristics along its path before it reaches the model being investigated.

This chapter is dedicated to describing and exploring different aspects of these three problems, which are crucial to proceeding further with the experiments and results analysis in this work.

3.1. Wind flow characteristics in the atmospheric boundary layer

The wind is defined as a horizontal movement of air masses. In reality, it is never perfectly horizontal, however, the horizontal component of the wind velocity vector is always dominating over the vertical one. The wind system of coordinates is usually set so that the main wind direction is parallel to the *x* axis, with *y* axis being the lateral fluctuations and *z* axis – the vertical fluctuations. At any given point, this can be written as follows:

$$v_x(t) = \overline{v_x} + v_x'(t); \; v_y(t) = 0 + v_y'(t); \; v_z(t) = 0 + v_z'(t) \tag{3.1}$$

where: $\overline{v_x}$ – mean value of the horizontal component of the wind velocity in the mean wind direction; $v_x'(t)$ – fluctuations (turbulence) of the wind velocity in the mean wind direction;

$v'_y(t)$ – fluctuations (turbulence) in the lateral horizontal direction (perpendicular to the mean wind direction); $v'_z(t)$ – fluctuations (turbulence) in the vertical direction.

As the fluctuations in *y* and *z* directions are often negligible, this can be simplified to the following:

$$v(t) = \bar{v} + v'(t) \cong \overline{v_x} + v'_x(t) \tag{3.2}$$

The fluctuations from the mean for a given measured wind velocity time series can be calculated as the standard deviations of this time series σ_v. It is convenient to present them as a non-dimensional quality, *turbulence intensity I_v*, which is the ratio of the fluctuations to the mean wind speed value (similarly as before, the fluctuations in *y* and *z* are omitted as they are negligible):

$$I_v = \frac{\sigma_v}{\bar{v}} \tag{3.3}$$

Furthermore, same as the value of the wind velocity, its direction is also fluctuating around a mean value for a given measurement time. This direction or angle is usually considered only in the horizontal plane and can be defined at a given point as:

$$\theta(t) = \bar{\theta} + \theta'(t) \tag{3.4}$$

The wind angle θ is most often described as the direction azimuth with regard to the north direction (which is marked as wind direction 0°) or, in other words, as an angle between the projection of the wind velocity vector in the horizontal plane and the north direction, for example, 90° describes the winds inflowing from the east direction.

Another problem with measuring the wind speed is adopting a proper measurement time from which the mean value should be extracted, which would be representative of given wind conditions. In general, the shorter the averaging time, the higher the mean value of wind speed should be expected. Moreover, the ratio between the mean values of wind speed at different averaging times is influenced by the terrain roughness, measurement height above the ground level and type of atmospheric circulation (Durst, 1960; Mackey et al., 1970; Mackey & Pius, 1977; Nutt, 1963). For the purpose of standardization, the measurements of the base value of wind velocity are usually conducted in open flat terrain at a height of 10 m above the ground level. For such conditions, it has been empirically proven (Durst, 1960; Nutt, 1963) that the ratios of mean wind speed calculated for two different measurement times larger than 5 minutes are asymptotically converging to 1. This means that, in practice, the mean wind speeds for the averaging times of 5 minutes, 10 minutes or 1 hour are almost the same. Therefore, in meteorological measurements, averaging times of either 10 minutes or 1 hour are applied. For the purpose of wind action on buildings, averaging times of 10 minutes are more convenient and widespread (Żurański, 1978), hence this will be the reference used further within this work.

Besides the mean value, another useful characteristic that can be extracted directly from the measurement time series is the peak value, which provides information about gusts – brief increases in the wind speed that last for only a couple of seconds. The gusts may be significant for certain engineering applications, such as determining the local or global wind

action on a cladding/structure or pedestrian wind comfort/safety. This can be calculated with a *gust factor*, which can be defined as a ratio of maximal mean wind speed value over a very short measuring time (e.g. 3 s or 5 s) $v_{T_i}^{max}$ to the mean wind speed value in the total analysed measurement time v_T (A. Flaga, 2008):

$$G_v\left(\frac{T_i}{T}\right) = \frac{v_{T_i}^{max}}{v_T} = \frac{v_{T_i}^{max}}{\bar{v}} \tag{3.5}$$

The methodology for determining this factor is shown in Fig. 3.1. Tab. 3.1 lists the values of the gust factors for different averaging times in comparison to the mean value of 1 hour and 10 minutes, according to different authors.
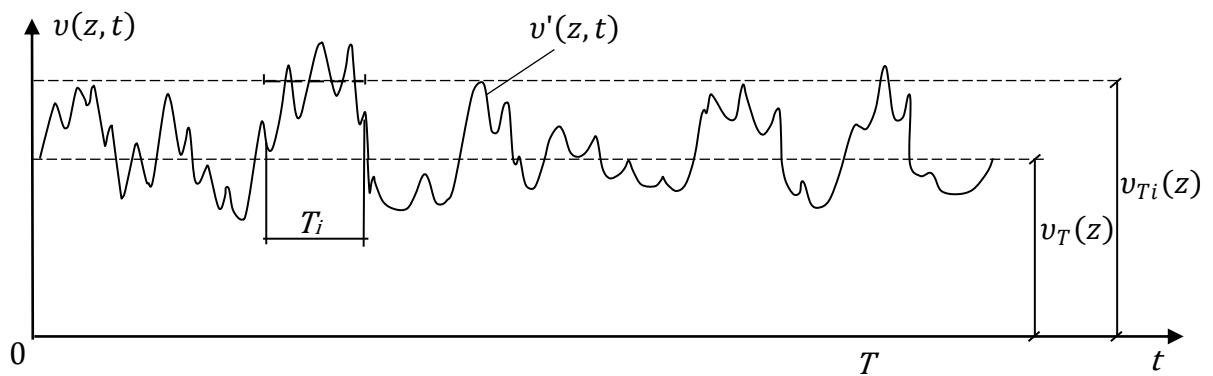
Fig. 3.1. Influence of the averaging time on the mean value of wind velocity for a given measurement time series (A. Flaga, 2008)

Tab. 3.1. Average values of gust factor $G_v\left(\frac{T_i}{T}\right)$ in reference to the averaging times of 1 hour and 10 minutes in open flat terrain

T_i [s]	3600	600	60	30	20	10	5	3	0.5
$G_v\left(\dfrac{T_i}{T = 3600\ s}\right)$ (Durst, 1960)	1.00	1.06	1.24	1.33	1.36	1.43	1.47	–	1.59
$G_v\left(\dfrac{T_i}{T = 600\ s}\right)$ (Sanz-Andres & Cuerva, 2006)	0.95	1.00	1.19	–	–	–	–	1.49	–

A different approach for taking the gusts into account, more common for the determination of pedestrian wind comfort, is using the *gust equivalent mean wind speed* v_{GEM}, which is defined as following (Lawson, 1980):

$$v_{GEM} = \max\left(\frac{v_{1h}}{1.103}, \frac{v_{P=93\%}}{1.434}, \frac{v_{P=99.99\%}}{1.875}\right) \tag{3.6}$$

where: v_{1h} – hourly mean wind speed value, $v_{P=93\%}$ – effective wind speed with an exceeding quantile of 93%, $v_{P=99.99\%}$ – effective wind speed with an exceeding quantile of 99.99%.

This value is defined so that on terrains with relatively low turbulence intensity levels (below 20%) at the pedestrian height (1.5-2.0 m), it would be close to the mean hourly wind speed, while on the terrains with higher turbulence intensity levels, it would be closer to the average or peak effective wind speed (to properly account for the impact of gusts on the pedestrian wind comfort).

As mentioned above, the flow characteristics at a given location vary with the height above the ground level. This can be described by vertical wind profiles, usually concerning either the mean wind speed or turbulence intensity. The mean wind speed value usually increases with height above the ground level, while the turbulence intensity decreases. Furthermore, this is highly influenced by the terrain roughness described in detail in the next subsection.

The vertical mean wind speed profile depends, besides the terrain roughness, on the following factors: averaging time, orography, type of atmospheric circulation and the way it is generated (A. Flaga, 2008). For higher averaging times (above 60 seconds), its plot starts to follow a pattern, which can usually be described by either a logarithmic (3.7) or a power-law (3.8) curve, which are defined in the most general form as:

$$\frac{\bar{v}(z_2)}{\bar{v}(z_1)} = \frac{\ln z_2 - \ln z_0}{\ln z_1 - \ln z_0} \tag{3.7}$$

$$\frac{\bar{v}(z_2)}{\bar{v}(z_1)} = \left(\frac{z_2}{z_1}\right)^{\alpha} \tag{3.8}$$

where: z_1, z_2 – height levels above the ground, z_0 – roughness length [m], α – exponent of the vertical power-law wind profile [-].

In practice – where the wind velocity measurement is taken at 10 m height – the formula for the power-law wind profile at a given height z can be written as:

$$\bar{v}(z) = \bar{v}(10 \text{ m})\left(\frac{z}{10}\right)^{\alpha} \text{ for } z \leq z_g$$
$$\bar{v}(z) = \bar{v}(10 \text{ m})\left(\frac{z_g}{10}\right)^{\alpha} \text{ for } z > z_g \tag{3.9}$$

where: z – height above the ground level in [m], z_g – gradient height, which is the height above the ground level where the surface friction has a negligible effect on the wind velocity.

Different sources prefer either of the two formulas given in Eq. (3.7) and Eq. (3.8) for the vertical wind speed profile description. In the case of wind tunnel tests, the advantage of using the power-law formula is that the parameter that defines it, exponent α, is non-dimensional (contrary to the roughness length z_0, which is given in [m]), therefore the transition between the model and real-life scales is direct and more intuitional. Another important parameter for the wind profile is z_{min}, which is the height below which it is assumed the wind speed is at a constant level, equal to its value at this height. More information about the vertical mean wind

speed profiles is given below in the subsection discussing the terrain roughness, which is intrinsically linked with the vertical wind speed and turbulence intensity profiles.

Similar to the mean wind speed, turbulence intensity also changes with height, and the pattern of this change can also be described with a logarithmic or power-law curve. However, as can be expected, this change with height is opposite to the change in mean wind speed, so with the increase of height, the turbulence intensity level decreases.

For synoptic winds, the values of turbulence intensity may reach up to around 30% at the near-ground level. Similar to the vertical wind speed profiles, more information regarding the change of wind turbulence with height depending on different types of terrain is provided in the next subsection.

Furthermore, the higher the measurement is done, the closer the approximation of the probability density distribution of the wind fluctuations to the normal distribution is (A. Flaga, 2008; Wittmann & Schneider, 1974). In such processes, the peak value coefficients at a given height z, $g_v(z)$ are in the range between (3÷4), hence for engineering practice, the gust coefficients defined in Eq. (3.5) are often approximated as:

$$G_v(z) \cong 3.5 I_v(z) \tag{3.10}$$

However, as the wind speed at a given point is a result of random atmospheric circulations (with different spatial and time scales) adding up together, its frequency and amplitude structure is rather complicated. A complete description of the wind structure in the time domain is possible with the correlation functions, and in the frequency domain – with the power density spectra (A. Flaga, 2008).

The correlation functions can be grouped into the following:

- Time autocorrelation functions, which determine the correlation between the values of a wind fluctuation at the same point, but during two different events, with a time lag of τ between them:

$$R_{vi}(x, y, z, \tau) = E[v'_i(x, y, z, t)v'_i(x, y, z, t + \tau)] \tag{3.11}$$

where: i – analysed wind fluctuation direction, τ – time step.

- Spatial correlation functions, which determine the correlation between the values of wind fluctuations during a single event (same time), but at two different points in space:

$$R_{vivj}(x_1, y_1, z_1, x_2, y_2, z_2) = E[v'_i(x_1, y_1, z_1, t)v'_j(x_2, y_2, z_2, t)] \tag{3.12}$$

where i, j – analysed wind fluctuation directions.

- Spatial-time correlation functions, which determine the correlation between the values of wind fluctuations at two different points and during two different time events:

$$R_{vivj}(x_1, y_1, z_1, x_2, y_2, z_2, \tau) = E\left[v'_i(x_1, y_1, z_1, t)v'_j(x_2, y_2, z_2, t + \tau)\right] \qquad (3.13)$$

Time autocorrelation functions are symmetrical against the *y* axis, with their maximum located at this axis. On the other hand, the spatial and spatial-time correlation functions are, in general, not symmetrical, due to the non-uniformity of the wind field in the space (A. Flaga, 2008).

In practice, usually, the correlation functions are normalised to 1.0 by dividing by either the variation or the product of the relevant standard deviations of the wind velocity components, which can be defined as follows:

$$\rho_{vi}(x, y, z, \tau) = \frac{R_{vi}(x, y, z, \tau)}{\sigma_{vi}^2(x, y, z)} \qquad (3.14)$$

$$\rho_{vivj}(x_1, y_1, z_1, x_2, y_2, z_2) = \frac{R_{vivj}(x_1, y_1, z_1, x_2, y_2, z_2)}{\sigma_{vi}(x_1, y_1, z_1)\sigma_{vj}(x_2, y_2, z_2)} \qquad (3.15)$$

$$\rho_{vivj}(x_1, y_1, z_1, x_2, y_2, z_2, \tau) = \frac{R_{vivj}(x_1, y_1, z_1, x_2, y_2, z_2, \tau)}{\sigma_{vi}(x_1, y_1, z_1)\sigma_{vj}(x_2, y_2, z_2)} \qquad (3.16)$$

where: ρ_{vi} – normalised autocorrelation function, ρ_{vivj} – normalised spatial correlation function.

In practice, autocorrelation functions are usually applied to obtain information about the longitudinal correlation (along the wind direction), which is otherwise difficult to directly measure through a spatial correlation. Furthermore, based on the field measurements (Duchêne-Marullaz, 1977), the following observations can be made about the autocorrelation function:

- It is dependent on the height above the ground level, and in most cases, the larger autocorrelation can be observed for the points at higher altitudes;
- Autocorrelation functions for the same location and height above the ground level, but different strong wind events, can differ significantly, which means that the wind fluctuations are not an ergodic process.

The spatial correlation is usually calculated for two points that are both located along the same line, either parallel or perpendicular to the wind direction. These correlations can be described as longitudinal, lateral and vertical. As mentioned above, direct measurement of the longitudinal correlation – which would require setting the measurement equipment at two different locations along the path of the wind flow, hence affecting it in the process – is rarely done, especially since similar information can be obtained from the autocorrelation. As for the lateral and vertical correlation, the following observations can be made based on the field measurements (Duchêne-Marullaz, 1977; Mackey & Pius, 1977; Shiotani & Iwatani, 1971):

- Both lateral and vertical normalised correlation functions are decreasing functions of the distance Δy or Δz between the two points where it is calculated;

- The lateral correlation between the two points increases with the height above the ground and usually decreases exponentially with the increase of the distance Δy between these two points;
- The vertical correlation is anisotropic – different values are obtained when moving upward from a set point at the bottom (usually close to an exponential curve) or moving downward from a set point at the top (usually close to a straight line).

The correlations of the wind fluctuations can be used to obtain the values of the turbulence length scales, which can be interpreted as measures of the spatial sizes of the gusts or vortices that compose the turbulence. These length scales can be defined as follows:

$$L_x(z) = \bar{v}(z) \int_0^\infty \rho_v(z, \tau) \, \mathrm{d}\tau \tag{3.17}$$

$$L_y(z) = \int_0^\infty \rho_{vv}(\Delta y, z) \, \mathrm{d}y \tag{3.18}$$

$$L_z(z) = \int_0^\infty \rho_{vv}(\Delta z, z) \, \mathrm{d}z \tag{3.19}$$

These three parameters are significantly different from each other at the same height; furthermore, they also largely depend on the height above the ground level. Exemplary values of the turbulence length scales, measured for both the main wind direction and the lateral fluctuation at different levels above the ground in suburban terrain, are shown in Tab. 3.2 (Duchêne-Marullaz, 1977) (the arrows mark the direction of the movement for the vertical turbulence length scales, either upward or downward).

Tab. 3.2. Turbulence length scales in suburban terrain (Duchêne-Marullaz, 1977)

Height above the ground level z [m]	Turbulence length scales [m]							
	L_x^{vx}	L_y^{vx}	$L_z^{vx} \uparrow$	$L_z^{vx} \downarrow$	L_x^{vy}	L_y^{vy}	$L_z^{vy} \uparrow$	$L_z^{vy} \downarrow$
10	75	25	40		35	30	15	
20	95	30			45	30		
30	125		45	25	55		20	10
40	145	45			65	45		
50	170				85			
60	190	60		35	85	55		20

Based on the values provided in Tab. 3.2, the following approximate relationships can be established regarding the relationships between the different turbulence length scales (Duchêne-Marullaz, 1977):

$$L_x^{vx} \cong 2L_x^{vy} \tag{3.20}$$

$$L_z \uparrow > L_z \downarrow \tag{3.21}$$

$$L_z \downarrow \cong \frac{1}{5} L_x \tag{3.22}$$

$$L_y \cong \frac{1}{3} L_x \tag{3.23}$$

However, the relationships between the turbulence length scales of different components of the wind velocity fluctuations given in (ESDU 85020, 2002) are different:

$$\frac{L_x^{vy}}{L_x^{vx}} = 0.5 \left(\frac{\sigma_{vy}}{\sigma_{vx}}\right)^3 ; \frac{L_x^{vy}}{L_x^{vx}} = 0.5 \left(\frac{\sigma_{vy}}{\sigma_{vx}}\right)^3 \tag{3.24}$$

Harris (1970) provided the value of the longitudinal turbulence length scale at the height of 100 m as $L_x(100 \text{ m}) = 230$ m, while (Shiotani & Iwatani, 1971) proposed different values of this characteristic depending on the fetch length from the wind flow direction, with $L_x(40 \text{ m}) = 154$ m for wind flowing above the ground and $L_x(40 \text{ m}) = 204$ m for wind flowing above the sea. As can be seen, while these values are, in general, comparable, there is a strong influence of not only the height, but also the terrain roughness on this parameter.

Mackey and Pius (1977) provided empirical formulas that can be used to estimate the values of different turbulence length scales depending on the height z above the ground, which in this case are based on the power-law curves:

$$L_x(z) = 210 \left(\frac{z}{10}\right)^{0.55} \tag{3.25}$$

$$L_y(z) = 55 \left(\frac{z}{10}\right)^{0.75} \tag{3.26}$$

$$L_z(z) = 60 \left(\frac{z}{10}\right)^{0.28} \tag{3.27}$$

It should be noted that the measurements that led to these findings were done during typhoons, which makes the values much larger than what was proposed by (Duchêne-Marullaz, 1977). However, a similar conclusion can be drawn when it comes to the mutual relations between the turbulence length scales in different directions, which can be interpreted as the vortices forming during the wind turbulence being of elliptical shapes, stretched along the main wind direction (Mackey & Pius, 1977).

Different formulas for the lateral and vertical turbulence length scales, which account only for higher altitudes above the ground level ($z > 55$ m), are given by (Sfintesco & Wyatt, 1977):

$$L_y(z) = 42 \left(\frac{z}{20}\right)^{0.25} ; L_z(z) = \sqrt{37z} \tag{3.28}$$

Furthermore, the values of turbulence length scales are also altered by wind speed. ESDU 86035 (2000) provides the values of turbulence length scales based on long-term field measurements for standard reference hourly mean wind speed (in open flat terrain) of 20 m/s, for different roughness types. It also includes scenarios where the roughness changes in the upwind direction from the site. The suggested correction multiplier to the provided values, which takes into account different reference wind speeds and changes in the Coriolis parameter at different latitudes, is given as:

$$k_L \approx \left(\frac{V_{10r}}{20} \frac{1 \cdot 10^{-4}}{f} \right)^{c_x}$$

(3.29)

where: V_{10r} – wind speed over uniform open country terrain measured at the height of 10 m [m/s], $f = 2\Omega \sin \varphi$ – Coriolis parameter, which is equal to about 10^{-4} in midlatitudes [rad/s], Ω – rotation rate of Earth [rad/s], φ – latitude, c_x – exponent dependent on the terrain roughness and height above the ground which can be estimated based on a nomogram in (ESDU 86035, 2000).

An earlier version of ESDU (ESDU 74031, 1974) based the turbulence length scales only on the height z above the ground and terrain roughness length z_0, without considering the dependence on reference wind speed. This results in generally lower values of turbulence length scales than in (ESDU 86035, 2000), however, it is more in line with other standards (Kozmar, 2011c). Furthermore, this approach is simpler and might be better as a reference in wind tunnel tests (Kozmar, 2011b).

Power density spectra are used for the analysis of the wind fluctuations structure in the frequency domain. Based on the frequency of the wind velocity fluctuations, these can be divided into larger-scale meteorological circulations (with periods between about 5 minutes to 1 year and above) and micrometeorological circulations (with periods between about 0.5 seconds to 5 minutes). From the perspective of wind engineering and, in particular, wind action on buildings, the latter are far more important, as they correspond to the gusts, which have a significant impact on e.g. wind-induced vibrations of structures or peak values of wind pressures. One-sided power spectral density at a given location $G_{vi}(x, y, z, f)$ can be calculated from the Fourier transform of the autocorrelation function and is defined as:

$$G_{vi}(x, y, z, f) = 4 \int_0^\infty R_{vi}(x, y, z, \tau) \cos(2\pi f \tau)\, \mathrm{d}\tau$$

(3.30)

where f – gust frequency [Hz].

From the inverse Fourier transform of this relationship, the following relationship can be calculated:

$$R_{vi}(x, y, z, \tau) = \int_0^\infty G_{vi}(x, y, z, f) \cos(2\pi f \tau)\, \mathrm{d}f$$

(3.31)

This leads to an important and useful relationship between the wind velocity standard deviation and power spectral density (A. Flaga, 2008):

$$R_{vi}(x, y, z, \tau) = \sigma_{vi}{}^2(x, y, z) = \int_0^\infty G_{vi}(x, y, z, f) \mathrm{d}f \tag{3.32}$$

$$\sigma_{vi}(x, y, z) = \sqrt{\int_0^\infty G_{vi}(x, y, z, f) \mathrm{d}f} \tag{3.33}$$

In this work, only the spectra in the main wind direction will be further discussed. Moreover, only the change with height will be analysed, therefore a simplified designation will be used from $G_{vi}(x, y, z, f)$ to $G_v(z, f)$, unless specified otherwise.

Similarly to the correlation functions, the power density spectra calculated for the time series from different measurements will largely vary. Furthermore, the deviation of the values from the mean is larger for lower heights, due to the influence of the boundary layer created by the terrain roughness (Kaimal et al., 1972; Simiu, 1974).

For practical reasons, particularly for clearer transition between the results in model and real-life scales, it is convenient to use a non-dimensional values of the power density spectrum and the gust frequency: $\check{G}_v(z, \check{f}) = \frac{fG_v(z,f)}{\sigma_v{}^2(z_{ref})}$ and $\check{f} = \frac{fz_{ref}}{\bar{v}(z_{ref})}$.

Different empirical formulas have been elaborated that would model the power density spectra. Among them, one of the most widely spread is by Davenport (1961), given in the dimensional form in Eq. (3.34) and normalised (non-dimensional) form in Eq. (3.35):

$$G_v(f) = K\bar{v}^2(10)\frac{1}{f}\frac{4m^2}{(1+m^2)^{4/3}}; m = \frac{fL}{\bar{v}(10)} \tag{3.34}$$

$$\frac{fG_v(f)}{\sigma_v{}^2} = \frac{2}{3}\frac{m^2}{(1+m^2)^{4/3}} \tag{3.35}$$

where: K – coefficient dependent on the terrain roughness, equal to 0.005 for open terrain, 0.015 for suburban or forest terrain and 0.05 for urban areas, $\bar{v}(10)$ – mean wind speed at the height of 10 m from sufficiently long averaging time (at least 10 minutes), f – gust frequency, L – length scale, equal to 1200 m.

As can be observed, the Davenport spectrum depends on the terrain roughness but is independent of the height above the ground level, hence it can be expected that it would only be comparable with the other spectra for a limited range of heights. The other popular spectrum, which is present in the standards (ESDU 82026, 2003), is the von Kármán spectrum. For the fluctuations of the wind velocity along the main wind direction, it is given by the following formula:

$$\frac{fG_v(f)}{\sigma_v{}^2} = \frac{4x_x}{(1 + 70.7x_x^2)^{5/6}} \; ; \; x_x = L_x^{vx}\frac{f}{\bar{v}(z)} \tag{3.36}$$

where: $L_x^{vx} = 300\left(\frac{z}{300}\right)^{1/k}$ – turbulence length scale, $\frac{1}{k} = 0.437 + 0.153\log z_0$ – coefficient dependent on the terrain roughness, z_0 – roughness length [m].

This spectrum also takes into account the power density spectra variation with height, as well as the terrain roughness. Another formula that can be often found in literature is the Kaimal spectrum (Kaimal et al., 1972) given by Eq. (3.37), which may be more convenient in practical implementation in a generalised form (Flaga et al., 2004), as presented in Eq. (3.38). This spectrum only depends on the height above the ground level and is independent of the terrain roughness.

$$\frac{fG_v(z,f)}{v_*^2} = \frac{105r}{(1 + 33r)^{5/3}} \; ; r = \frac{zf}{\bar{v}} \tag{3.37}$$

$$\frac{fG_{vi}(z,f)}{\sigma_{vi}{}^2} = \frac{0.164\frac{x}{a_i}}{1 + 0.164\left(\frac{x}{a_i}\right)^{4/3}} \; ; x = \frac{fz}{\bar{v}(z)} \; ; i = x, y, z \tag{3.38}$$

where: v_* – friction wind velocity, $a_x = 0.0144$; $a_y = 0.0265$; $a_z = 0.0962$ – coefficient dependent on the analysed wind fluctuations direction.

The plots of normalised power density spectra according to the formulas given in Eq. (3.35), Eq. (3.36) and Eq. (3.38), at the height of 50 m and in the urban area, are shown in Fig. 3.2. The plots are shown in different formatting on the vertical and horizontal axes for easier interpretation: linear-linear (Fig. 3.2a), linear-log (Fig. 3.2.b) and log-log (Fig. 3.2c). As can be seen, there is a very close match between all the 3 spectra in the decreasing part of the curve (which, in this case, corresponds to frequencies of about 0.05 Hz and higher) and shows discrepancies for lower frequencies, in particular between the Davenport spectrum against the two other spectra. Furthermore, it should be noted that for practical purposes (wind action on tall buildings), usually, frequencies between about 0.1 Hz to 1-2 Hz are of interest. This range is highlighted on the plots in Fig. 3.2 with black dashed vertical lines. As can be observed in these plots, the log-log presentation is most convenient for this characteristic, as it highlights the differences in the most apparent way. It is therefore widely considered a standard when presenting power spectral densities in wind engineering applications.
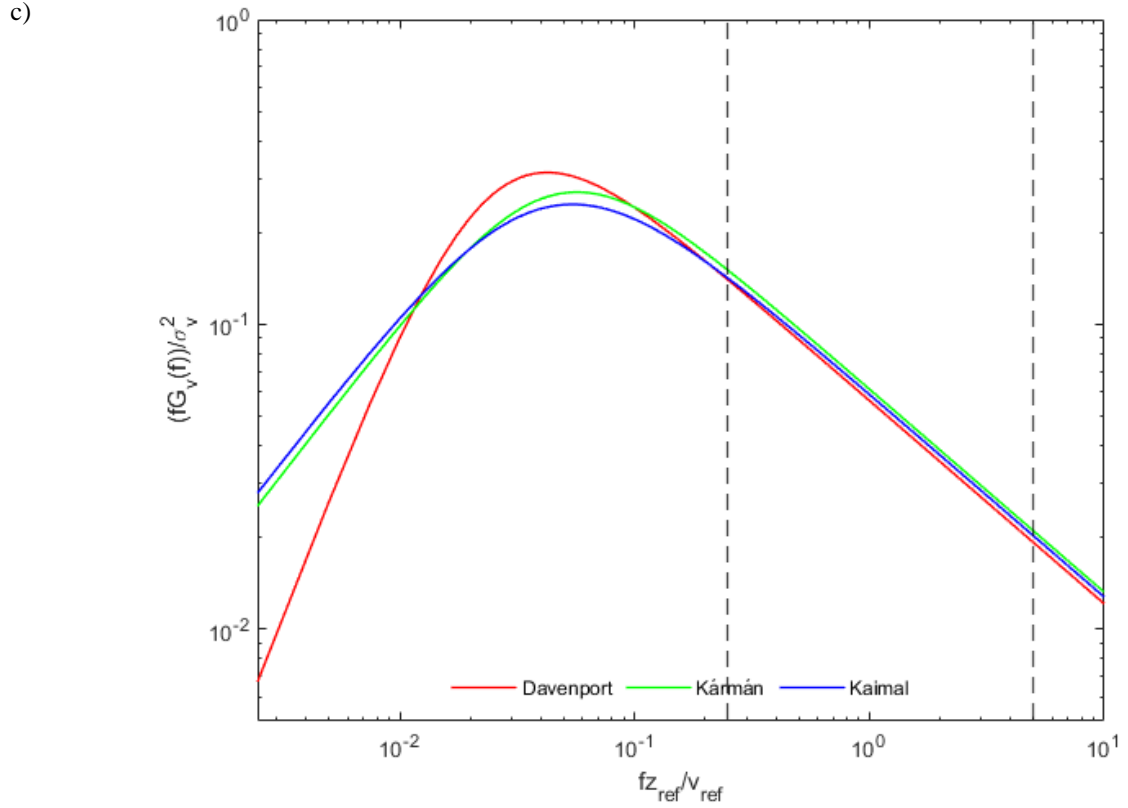
a)

b)

c)
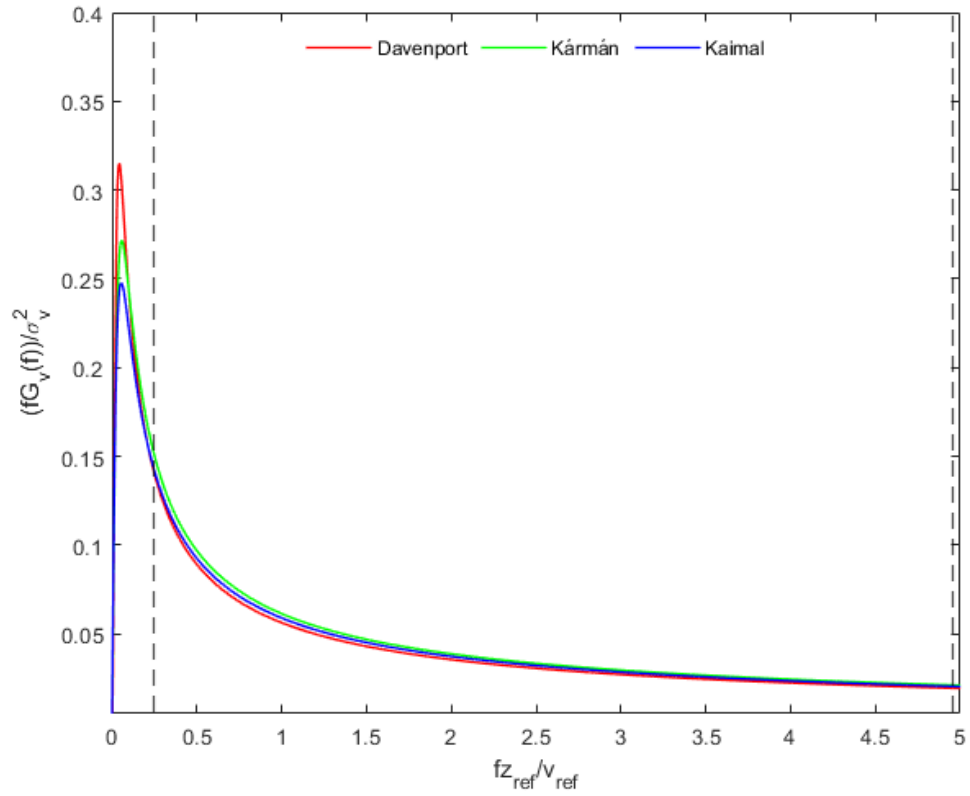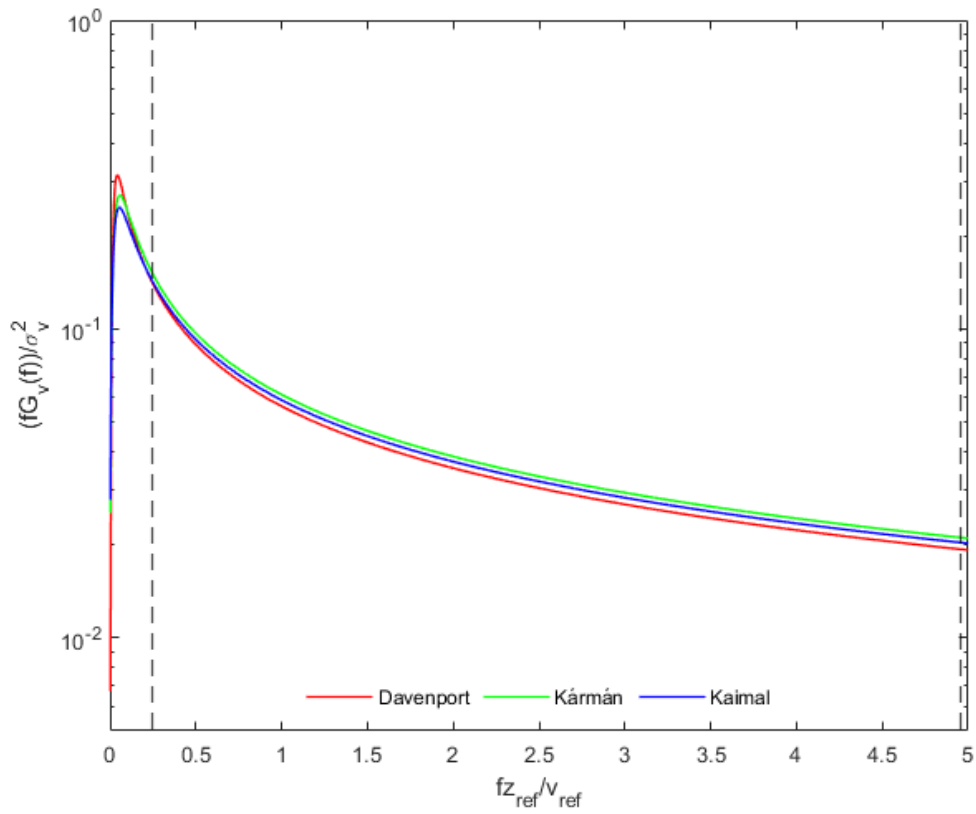
Fig. 3.2. Comparison of the power density spectra according to Davenport, von Kármán and Kaimal formulas at the height of 50 m and in the urban terrain: (a) linear-linear scale; (b) log-linear scale; (c) log-log scale

Similar to the spatial correlation functions described above, cross power spectral densities between any two points can be calculated. Two-sided cross power density spectra S_{vivj} can be calculated with the following formula:

$$S_{vivj}(x_1, y_1, z_1, x_2, y_2, z_2, f) = \int_{-\infty}^{\infty} R_{vi}(x_1, y_1, z_1, x_2, y_2, z_2, \tau)e^{-2\pi i f \tau}\mathrm{d}\tau \qquad (3.39)$$

where i – imaginary unit.

Typically, it is practical for both of these points to be at the same axis, either vertical or horizontal, perpendicular to the main wind direction. For the sake of brevity, further discussions will focus on the vertical cross-spectra, where $x_1 = x_2 = $ const and $y_1 = y_2 = $ const. Furthermore, the considerations will be limited to the main wind direction, so the indexes i and j of the wind direction will be omitted. In such case, one-sided power spectral density at a given location $G_{vv}(z_1, z_2, f)$ can be defined as:

$$G_{vv}(z_1, z_2, f) = \begin{cases} \int_{0}^{\infty} 2S_{vv}(z_1, z_2, f) \text{ for } f \in [0, \infty) \\ 0 \qquad\qquad\qquad \text{ for } f \in (-\infty, 0) \end{cases} \qquad (3.40)$$

As can be seen, the values of cross-spectrum are, in general, complex numbers, which are convenient to present as the modulus $|G_{vv}(z_1, z_2, f)|$ and argument (phase) $\varphi_{vv}(z_1, z_2, f)$:

$$G_{vv}(z_1, z_2, f) = |G_{vv}(z_1, z_2, f)|e^{i\varphi_{vv}(z_1, z_2, f)} \tag{3.41}$$

Modulus of the cross-spectrum can be normalised as a root-coherence function, with the real part named co-coherence $\gamma_{vv}(z_1, z_2, f)$ and imaginary part named quad-coherence $\rho_{vv}(z_1, z_2, f)$. The co-coherence for vertical separations can be defined as:

$$\gamma_{vv}(z_1, z_2, f) = \sqrt{\frac{|G_{vv}(z_1, z_2, f)|^2}{G_v(z_1, f)G_v(z_2, f)}} \tag{3.42}$$

The values of this function are in the range of $[0,1]$, where the value of 1 denotes the perfect correlation.

For practical reasons, it seems more convenient to use the vertical distance between the two considered points, Δz, as the argument for the coherence function. Furthermore, its value strongly depends on the height above the ground (Müller & Nieser, 1975; Sfintesco & Wyatt, 1977). One of the first and most commonly used models of the vertical coherence function is the Davenport model (Davenport, 1962):

$$\gamma_{vv}(z, \Delta z, f) = \exp\left[-C_z \frac{f|\Delta z|}{\bar{v}_m}\right] \tag{3.43}$$

where: C_z – exponential decay constant, $\Delta z = z_2 - z_1$ – vertical distance between the two points, $\bar{v}_m = \frac{\bar{v}(z_1) + \bar{v}(z_2)}{2}$ – mean wind velocity between the two points.

ISO 4354 (2009) refined this approach by formulating the following relationship of the exponential decay with the height above the ground:

$$C_z = 9\left(\frac{20}{z_m}\right)^{0.09} \tag{3.44}$$

where $z_m = \frac{z_1 + z_2}{2}$ – mean height between the two points.

Bowen, Flay and Panofsky (1983) also proposed the dependency of the exponential decay on the height above the ground level and, additionally, on the distance between the two considered measurement heights. This approach reflects the increasing size of the turbulent eddies with higher altitudes and the decreasing influence of the surface roughness (Bowen et al., 1983). The Bowen model is given by the formula:

$$\gamma_{vv}(z, \Delta z, f) = \exp\left[-\frac{c_1 f|\Delta z|}{\bar{v}_m}\right] \exp\left[-\frac{2c_2 f|\Delta z|^2}{(z_1 + z_2)\bar{v}_m}\right] \tag{3.45}$$

The Bowen model uses two decay parameters, c_1 and c_2, which are reported to be equal to 11 and 6, respectively, based on the field measurements (Bowen et al., 1983). Sufficiently far from the terrain surface, this model can be approximated by the Davenport model.

Cheynet (2018) introduced an additional decay parameter, c_3, which accounts for the limited size of the eddies so that the co-coherence would not always be equal to unity at zero frequency. This is known as the modified Bowen model (Cheynet, 2018):

$$\gamma_{vv}(z, \Delta z, f) = \exp\left\{-\left[\frac{|\Delta z|}{\bar{v}_m}\sqrt{(c_1 f)^2 + c_3{}^2}\right]\right\}\exp\left[-\frac{2c_2 f|\Delta z|^2}{(z_1 + z_2)\bar{v}_m}\right] \tag{3.46}$$

Similar analysis can be performed for the lateral direction y, where C_y coefficients are used. Different authors proposed empirical formulas for the coherence function and their propositions for the exponential decay coefficients, which are conveniently summarised in (Solari, 1987).

The phase of the cross-spectral power density is covered far more scantily in the research. Shiotani and Iwatani (1971) and Müller and Nieser (1975) suggest that the phase is approximately equal to 0 in the lateral horizontal axis y, while in the vertical axis z, it can be described by the linear function:

$$\varphi_{vv}(z_1, z_2, f) = -\varphi_0 \frac{2(z_1 - z_2)f}{\bar{v}(z_1) + \bar{v}(z_2)} \tag{3.47}$$

where $\varphi_0 \cong 11$.

Based on the coherence functions, frequency scales can be defined for the vertical and lateral directions, similar to the turbulence length scales defined earlier. The vertical frequency scale $f_z^*(z, \Delta z)$ [Hz] can be defined as follows:

$$f_z^*(z, \Delta z) = \int\limits_0^\infty \gamma_{vv}(z, \Delta z, f)\mathrm{d}f \tag{3.48}$$

This can be also approximated by one of the empirical formulas, e.g. Eq. (3.43), as:

$$f_z^*(z, \Delta z) = \frac{\bar{v}_m}{C_z(z, \Delta z)|\Delta z|} \tag{3.49}$$

The frequency scale can be interpreted as a supremum (least upper bound) of a frequency range f where a substitute random process given by Eq. (3.50)-Eq. (3.52) is completely stochastically dependent (A. Flaga, 2008).

$$\gamma_{vv}(z, \Delta z, f) = \begin{cases} 1 & \text{for } f \in [0, f^*) \\ 0 & \text{for } f > f^* \end{cases} \tag{3.50}$$

$$\int\limits_0^\infty \gamma_{vv}^*(z, \Delta z, f)\mathrm{d}f = \int\limits_0^\infty \gamma_{vv}(z, \Delta z, f)\mathrm{d}f \tag{3.51}$$

$$f_z^*(z, \Delta z) = f^* \tag{3.52}$$

With this interpretation of frequency scale, it can be stated that the gusts of the frequency f_z^* (or a period of $T_z^* = \frac{1}{f_z^*}$ [s]) are completely correlated over the (vertical) length of Δz or less, and only partially correlated for the larger values of Δz (with the correlation decreasing with the increase of Δz). Its practical applicability can be for modelling the wind actions on a building, in the models that use the peak wind pressure approach, to determine the time averaging period for a structural element of a given size.

3.2. Terrain roughness

The boundary layer thickness and velocity field of a flow over a flat solid surface are mostly influenced by three groups of factors:

- Type of fluid and kinematic characteristics of the velocity field in the boundary layer;
- Roughness of the contact surface over which the flow occurs;
- Changes in the roughness of the contact surface along the boundary layer.

Terrain roughness or, more broadly speaking, *surface roughness*, is a term used to describe the obstacles and irregularities which impact the airflow over a surface. This influence can be observed in both micro and macro scales, typically having the following effects on the flow:

- Having a crucial impact on the thickness of the boundary layer (Perret et al., 2019);
- Changing vertical profiles of wind speed and turbulence intensity (Davenport, 1960; Żurański, 1978);
- Affecting the flow separation point in streamlined bodies, thus allowing for an artificial transition between the ranges of Reynolds number (A. Flaga et al., 2020; Simiu & Scanlan, 1996).

The experimental part of this work will only focus on the first two aspects mentioned above, which are significant in the analysed phenomena. Furthermore, when it comes to the wind tunnel tests done for the purpose of civil engineering, mostly large-scale roughness (terrain roughness) is considered. However, for the sake of completeness, the roughness types of smaller scales are also briefly covered within this work.

In the case of flat outer surfaces of different materials, construction or structural elements etc., the surface irregularities are relatively small and may result from the natural roughness of a surface or additional (artificial) surface roughness.

Natural surface roughness depends on many characteristics, such as material facture, texture, production or treatment method, or the degree of corrosion/destruction. This kind of roughness is usually stochastically random, which means the size, form and length between the roughness elements are random and approximately uniformly distributed on the surface. Additional surface roughness results from extra solid elements, protrusions, grooves, etc. This kind of roughness can be e.g. stochastically or deterministically approximately uniformly located on the surface.

In the case of flat terrain, natural or additional irregularities of the surface can be characterised by a much larger scale. They can be classified into two main groups, both of which may be random, more or less deterministic or mixed, namely:

- Natural irregularities, which are the result of natural terrain cover with plants (trees, bushes, wild grasses etc.) and natural, small topography (small cliffs, hills, valleys etc.);
- Anthropogenic irregularities, which are the result of a variety of human activities, e.g. ecological and agricultural activities (plantations, trees or bushes planted by man), structural and civil or geotechnical engineering (buildings, houses, roads, bridges, earthworks etc.).

When it comes to small-scale roughness, it is generally assumed the irregularities have a random, chaotic and stochastically uniform distribution over the surface (Iwano & Einstein, 1993; Lanaro, 2000). This allows for relatively simple classification using a single parameter – either the surface roughness height (in most cases its mean value k_r, but sometimes also the maximum value) or *equivalent uniform sand grain roughness k_s*, which was introduced for approximate comparison between forces induced by the flow at real-life roughness conditions and reference conditions of uniform sand roughness, defined by roughness height parameter k_s (ESDU 84015, 2012). The equivalent uniform sand grain roughness values for a number of different materials are presented in Tab. 3.3.
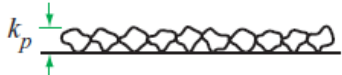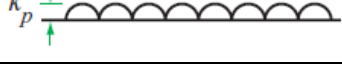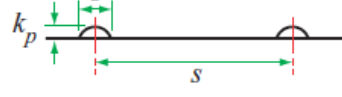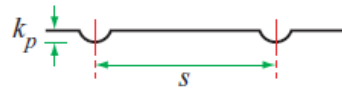
Tab. 3.3. Equivalent uniform sand grain roughness values in [m] for different materials (ESDU 84015, 2012; SimScale, 2022a)

Material	Equivalent uniform sand grain roughness [m]
Concrete, smooth wall	0.0045
Concrete, rough wall	0.013
Concrete, floor	0.04
Rubble	0.0175
Farmland	0.135
Farmland with crops	0.525
Grass with shrubs	0.265
Shrubbery	0.5
Grass and stone grid	0.0225
Gravel	0.075
Cast iron	0.000254
Commercial or welded steel	0.00004572
PVC	0.000001524
Glass	0.000001524
Wood	0.0005
Cast iron	0.00026
Concrete, smooth wall	0.0045
Concrete, rough wall	0.013

Material	Equivalent uniform sand grain roughness [m]
Concrete, floor	0.04
Rubble	0.0175
Farmland	0.135

Furthermore, ESDU 80025 (2019) provides the uniform sand grain roughness classification depending on the different types of surface finish, shown in Tab. 3.4. This is mostly useful for assigning the small-scale roughness, although it also covers another important factor for roughness determination, which is the shape of the elements. For wind tunnel simulations it may be practical e.g. for artificially changing the roughness of a surface to indirectly achieve an effect on the flow, e.g. a different Reynolds number regime. It should be noted that the shapes of the roughness listed there are perpendicular to the main flow direction.

Tab. 5.4 Equivalent roughness values for different types of surface finish according to (ESDU 80025, 2019)

Surface type	Scheme	Additional data		k_s/k_p
Uniform sand grains				1.0
Spheres				0.6
Domes				1.4
Circular arches		k_p/b	s/k_p	
		0.5	} 50-100	0.63
		0.067		0.05
Rounded grooves		s/k_p		
		20		0.15
		30		0.07
		40		0.04
Barriers		$\dfrac{s}{k_p} = 2.5$		2
Cones or ridges		δ	s/k_p	
		90°	} 50-100	1
		40°-75°		2
Machined surface (flow perpendicular to the pattern)				0.4

Another widely-used and convenient method of assigning the surface roughness value, more practical when considering the large-scale terrain, is the *aerodynamic roughness* or *roughness length* z_0. This can be defined as the maximal height above the ground level where the wind speed is equal to zero. This approach is used, for example, in the Eurocode (PN-EN 1991-1-4, 2011), particularly when determining the logarithmic wind profiles. Values of the aerodynamic roughness for some of the more common terrain types are summarised in Tab. 3.5. The ratio $\frac{x}{H}$ is the ratio of the average distance between the obstacles to the average obstacle height.

Tab. 3.5. Aerodynamic roughness values in [m] for different terrain types (PN-EN 1991-1-4, 2011; SimScale, 2022a)

Terrain type	Aerodynamic roughness value z_0 [m]
Open sea, fetch at least 5 km	0.0002
Sea or coastal area exposed to the open sea (terrain category 0 as per (PN-EN 1991-1-4, 2011))	0.003
Mud flats, snow: no vegetation, no obstacles	0.005
Lakes or flat and horizontal area with negligible vegetation and without obstacles (terrain category I)	0.01
Open flat terrain: grass, few isolated obstacles	0.03
Area with low vegetation such as grass and isolated obstacles (trees, buildings) with separations of at least 20 obstacle heights (terrain category II)	0.05
Low crops: occasional large obstacles, $\frac{x}{H} > 20$	0.10
High crops: scattered obstacles, $15 < \frac{x}{H} < 20$	0.25
Area with regular cover of vegetation or buildings or with isolated obstacles with separations of maximum 20 obstacle heights (such as villages, suburban terrain, permanent forest) (terrain category III)	0.3
Parkland, bushes: numerous obstacles, $\frac{x}{H} \approx 10$	0.5
Area in which at least 15% of the surface is covered with buildings and their average height exceeds 15 m (terrain category IV)	1.0

As can be seen from the values given in Tab. 3.3 and Tab. 3.4, aerodynamic roughness and equivalent sand grain roughness have vastly different scales. To approximately translate between these two values, the following equation can be applied (SimScale, 2022a):

$$k_s = z_0 \cdot 32.622 \qquad (3.53)$$

Lettau (1969) proposed a following relation between the sizes of obstacles and the value of roughness length:

$$z_0 = 0.5 H_{ob} \frac{S_{ob}}{A_{ob}} \qquad (3.54)$$

where: H_{ob} – average height of the roughness elements in the upwind terrain, S_{ob} – average frontal (windward) area of an obstacle in the vertical plane, A_{ob} – average area in plan occupied by a single obstacle, including the open area surrounding it.

For the purposes of wind engineering, different classifications of terrain roughness have been proposed, with the first widely accepted one being authored by (Davenport, 1960). This classification was based on the power-law wind profile (comp. Eq. (3.9)) and distinguished three different terrain categories: A – open flat terrain, B – forest or suburban terrain and C – urban areas. This classification, besides proposing the values of the α exponent, also suggests the gradient heights, z_g, which indicate the boundary layer thicknesses for each category. The characteristics of the Davenport scale are presented in Tab. 3.6.

Tab. 3.6. Davenport roughness classification (Davenport, 1960)

Terrain category	Description	Power-law wind profile exponent α [-]	Gradient height z_g [m]
A	Open flat terrain	0.16	270
B	Forests, suburbs	0.28	390
C	Urban areas	0.40	510

Later, in (Davenport, 1967), the values of the α exponent were corrected and slightly lowered for categories A and C, down to 0.14 and 0.36, respectively. This classification underwent further changes and expansions with the input of other authors (Wieringa, 1992).

Polish code for wind action on structures (PN-77/B-02011, 1977) recommended different values of these parameters and slight variations in the categories descriptions (namely suggesting a more precise distinction between categories B and C), which are shown in Tab. 3.7.

Tab. 3.7. Terrain roughness classification according to (PN-77/B-02011, 1977)

Terrain category	Description	Power-law wind profile exponent α [-]	Gradient height z_g [m]
A	Open terrain with few obstacles	0.14	300
B	Developed terrain with building heights below 10 m or forest areas	0.19	400
C	Urban areas with building heights above 10 m	0.24	500

ISO 4354 (2009) suggests both power-law and logarithmic curves for vertical mean wind speed descriptions, being somewhat more flexible than the other cited sources. Moreover, it also proposes the minimal and maximal heights where these laws for wind profiles are applicable, and another parameter, k_1 or k_2 which is used as an additional correction factor in the formulas that depends on terrain roughness. The values of these characteristics are given in Tab. 3.8 for power-law model and Tab. 3.9 for the logarithmic model, while the formulas for these models are defined as:

$$\bar{v}(z) = \bar{v}_A(10)k_1 \left(\frac{z}{10}\right)^\alpha \Bigg|_{H_{min}}^{H_{max}} \qquad (3.55)$$

$$\bar{v}(z) = \bar{v}_A(10)k_2 \ln\left(\frac{z}{z_0}\right) \Bigg|_{H_{min}}^{H_{max}} \qquad (3.56)$$

Tab. 3.8. Terrain roughness classification for power-law formula (3.55) according to (ISO 4354, 2009)

Terrain category	Exponent α [-]	Factor k_1 [-]	H_{min} [m]	H_{max} [m]
Coastal area exposed to the open sea, beaches	0.10	1.20	–	150
Open flat terrain	0.14	1.00	2	250
Forests, suburbs	0.21	0.80	6	300
Urban areas, city centres	0.32	0.50	15	350
Large city centres	(0.38)	(0.39)	(25)	(400)

Tab. 3.9. Terrain roughness classification for logarithmic formula (3.56) according to (ISO 4354, 2009)

Terrain category	z_0 [m]	Factor k_2 [-]	H_{min} [m]	H_{max} [m]
Coastal area exposed to the open sea, beaches	0.005	0.16	–	200
Open flat terrain	0.05	0.19	2	200
Forests, suburbs	0.30	0.23	5	200
Urban areas, city centres	1.0	0.27	15	200
Large city centres	(2.5)	(0.29)	(25)	(200)

The following observations can be made about the procedures given in (ISO 4354, 2009):

- There are two additional, extreme categories, compared to the first classifications with three categories: coastal areas exposed to the open sea as the *lowest* category and large city centres as the *highest* category;
- Open flat terrain is used as a reference category. This is a convenient and reasonable approach, as meteorological stations usually conduct their anemometric measurements at the height of 10 m above the ground level and in locations where the flow is relatively undisturbed, which would correspond with open flat terrain roughness categories;
- There are slight discrepancies between the minimal applicability heights given in (ISO 4354, 2009) for power-law and logarithmic wind profiles; also, the logarithmic wind profiles according to this code are only limited to the height of 200 m, the terrain roughness category notwithstanding;
- The values of the k_1 parameter decreases with terrain roughness categories for the power-law formula, while the value of the k_2 parameter increases with terrain roughness categories for the logarithmic formula.

The Eurocode (PN-EN 1991-1-4, 2011), which is currently the code in force in Poland and most of the Europe, proposes taking the roughness into account through a *roughness factor* $c_r(z)$. The vertical mean wind speed profile according to this code is given by the formula:

$$v_m(z) = c_r(z)c_o(z)v_b \tag{3.57}$$

where: $c_o(z)$ – orography factor, which is recommended to set at 1.0 in most cases of either approximately flat terrains or if the orography is accounted for in the basic wind velocity; this factor will be omitted in further analysis in this work, v_b – basic wind velocity, which is the 10 minutes mean wind speed at 10 m above ground level in open country terrain with low vegetation.

The roughness factor $c_r(z)$ is determined by the following equation, which reveals its link to the logarithmic wind profile:
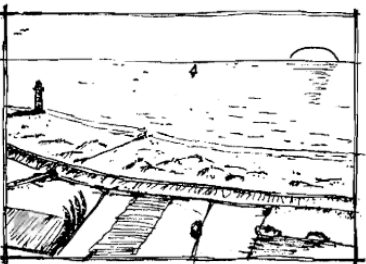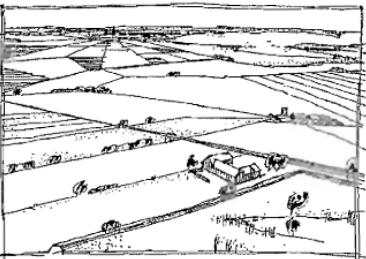
$$
\begin{aligned}
c_r(z) &= k_r \ln\left(\frac{z}{z_0}\right) && \text{for} \quad z_{min} \leq z \leq z_{max} \\
c_r(z) &= c_r(z_{min}) && \text{for} \quad z < z_{min}
\end{aligned}
\tag{3.58}
$$
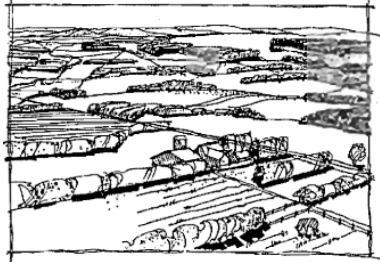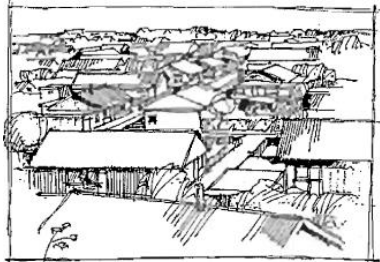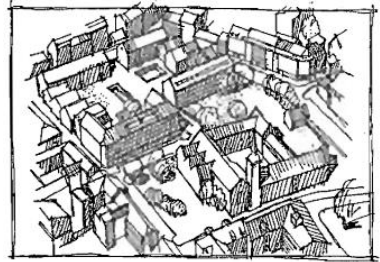
where: $k_r = 0.19\left(\frac{z_0}{z_{0,II}}\right)^{0.07}$ – terrain factor depending on the roughness length z_0, $z_{0,II}$ – roughness length in the 2nd terrain category (open country terrain with low vegetation).

The maximum height where this procedure is applicable is $z_{max} = 200$ m for all terrain categories. The values of the roughness parameters for different terrain categories according to (PN-EN 1991-1-4, 2011), along with exemplary illustrations of the terrain in each of these categories as per Annex A of this code, are summarised in Tab. 3.10.

Tab. 3.10. Terrain roughness classification for logarithmic formula according to (PN-EN 1991-1-4, 2011)

	Terrain category	z_0 [m]	Terrain factor k_r [-]	z_{min} [m]	Illustration
0	Sea, coastal area exposed to the open sea	0.003	0.156	1	
I	Lake or area with negligible vegetation and without obstacles	0.01	0.170	1	

	Terrain category	z_0 [m]	Terrain factor k_r [-]	z_{min} [m]	Illustration
II	Area with low vegetation such as grass and isolated obstacles (trees, buildings) with separations of at least 20 obstacle heights	0.05	0.190	2	
III	Area with regular cover of vegetation or buildings or with isolated obstacles with separations of maximum 20 obstacle heights (such as villages, suburban terrain, permanent forest)	0.30	0.215	5	
IV	Area in which at least 15% of the surface is covered with buildings and their average height exceeds 15 m	1.00	0.234	10	

As can be seen, this is very similar to the logarithmic procedure proposed in (ISO 4354, 2009). However, instead of the additional highest category for "centres of large cities", another category was proposed for lakes or areas with negligible vegetation and without obstacles. The values of roughness lengths z_0 and terrain factors k_r and k_2 are very similar between the corresponding categories in both of these documents.

Polish National Annex NB.3 to (PN-EN 1991-1-4, 2011) suggests a different procedure for the calculation of roughness factors $c_r(z)$, which is based in principle on the power-law wind profile. This approach is more similar to the Polish code that was replaced by the Eurocode (PN-77/B-02011, 1977), it is also worth noting that this is the recommended procedure, favoured over the logarithmic one in the Polish version of the Eurocode. The values of roughness factors for each of the terrain roughness categories according to this approach are presented in Tab. 3.11 (the height above ground level z should be input in metres).

Tab. 3.11. Terrain roughness classification for power-law formula according to (PN-EN 1991-1-4, 2011), Polish National Annex NB.3

	Terrain category	Roughness factor $c_r(z)$
0	Sea, coastal area exposed to the open sea	$1.27 \left(\dfrac{z}{10}\right)^{0.11}$
I	Lake or area with negligible vegetation and without obstacles	$1.18 \left(\dfrac{z}{10}\right)^{0.13}$

	Terrain category	Roughness factor $c_r(z)$
II	Area with low vegetation such as grass and isolated obstacles (trees, buildings) with separations of at least 20 obstacle heights	$\left(\dfrac{z}{10}\right)^{0.17}$
III	Area with regular cover of vegetation or buildings or with isolated obstacles with separations of maximum 20 obstacle heights (such as villages, suburban terrain, permanent forest)	$0.81\left(\dfrac{z}{10}\right)^{0.19}$
IV	Area in which at least 15% of the surface is covered with buildings and their average height exceeds 15 m	$0.62\left(\dfrac{z}{10}\right)^{0.24}$

A comparison can be made with the values given by (ISO 4354, 2009) for the power-law wind profiles (Tab. 3.7). The values of terrain factors are very similar for the corresponding categories, however, the value of the α exponent is notably lower for the urban category.

A contrary approach was suggested in the United Kingdom, where the National Annex (BS NA EN 1991-1-4, 2010) simplifies the roughness classification, grouping categories I and II as a single category under the name *Country terrain* and categories III and IV under the name *Town terrain*, which effectively reduces the number of the terrain categories to only three. However, the roughness factor $c_r(z)$ is defined precisely for the site location based on its upwind distances to the sea and – in the case of the town terrain category – to the edge of the urban areas, by the use of an additional parameter, roughness correction factor $c_{r,T}$. Instead of providing the exact formulas for these factors, their values can be read from nomograms.

American standard (ASCE/SEI 7, 2022; Simiu & Miyata, 2006) also recommend two different formulas: logarithmic and power-law. However, it limits the applicability of the logarithmic formula only to the lowest part of the atmospheric boundary layer, referred to as the *surface layer*. The depth of this layer, z_s, increases with wind speed and terrain roughness, but also depends on the geographic factors (directly on the angle of latitude). On the other hand, in the versions of the code released from 1995 onwards, the power-law profile exponents are given for 3-second gusts rather than for sustained wind, therefore – for comparison purposes – values from an older version will be presented herein (Simiu & Miyata, 2006). The values of the parameters for different terrain categories are in Tab. 3.12 for the logarithmic profile and Tab. 3.13 for the power-law profile. The formulas used for the calculation of the vertical wind profiles according to (ASCE/SEI 7, 2022) are following:

$$\bar{v}(z) = \bar{v}(z_{open})\left(\frac{z_0}{z_{0,open}}\right)^{0.07}\frac{\ln\left(\frac{z}{z_0}\right)}{\ln\left(\frac{z_{open}}{z_{0,open}}\right)} \tag{3.59}$$

$$\bar{v}(z) = \bar{v}(z_{open})\left(\frac{z_{g,open}}{z_{open}}\right)^{\frac{1}{\alpha_{open}}}\left(\frac{z}{z_g}\right)^{\frac{1}{\alpha}} \tag{3.60}$$

where: z_{open} – measurement height of the reference wind speed over open flat terrain, usually equal to 10 m, $z_{0,open}$ – roughness length at the open flat terrain [m], $z_{g,open}$ – gradient height over an open flat terrain [m], α_{open} – denominator of the exponent of the power-law wind profile over an open flat terrain [-].

Tab. 3.12. Terrain roughness classification for logarithmic formula (3.59) according to (ASCE/SEI 7, 2022)

	Terrain category	z_0 **[m]**	**Recommended value of** z_0 **[m]**
D	Water surfaces	0.005÷0.01	0.005
C	Open terrain	0.015÷0.15	0.02
B	Urban and suburban terrain, wooded areas	0.15÷0.7	0.3 (0.15*)

* The value of 0.15 was proposed as a more conservative approach that takes into account the presence of open spaces in urban areas, e.g. parking lots (Simiu & Miyata, 2006)

Tab. 3.13. Terrain roughness classification for power-law formula (3.60) according to (ASCE/SEI 7, 2022)

	Terrain category	**Exponent** $1/\alpha$ **[-]**	**Gradient height** z_g **[m]**
D	Water surfaces	1/10	213
C	Open terrain	1/7	274
B	Suburban terrain, towns	1/4.5	366
A	Centres of large cities	1/3	457

Fig. 3.3 and Fig. 3.4 show the comparison between the vertical wind profiles for 6 different terrain categories according to different sources mentioned above. For convenient and easy transition between full-scale and model values, vertical mean wind speed profiles are usually given in non-dimensional scales, obtained by dividing the height by reference height z_{ref} and dividing the wind speed by a certain set wind speed value that is comparable between the different profiles. The reference height usually corresponds with either the highest level where the wind profile is calculated or measured, or to the gradient height z_g. In this case, for the sake of inclusion of every mentioned formula, all of the plots are limited to the height of 200 m and the reference height is set at $z_{ref} = 200$ m. The reference wind speed is usually either the gradient wind speed v_g, which is the wind speed at the height z_g, or the basic wind velocity v_b, which is the wind speed value in open flat terrain and at 10 m height above the ground level (it depends only on the local wind conditions, altitude above the sea level, wind direction and, optionally, season of the year). In this case, the plots are made for non-dimensional parameters v/v_b and z/z_{ref}, as they seem more fit for the clarity of this comparison.
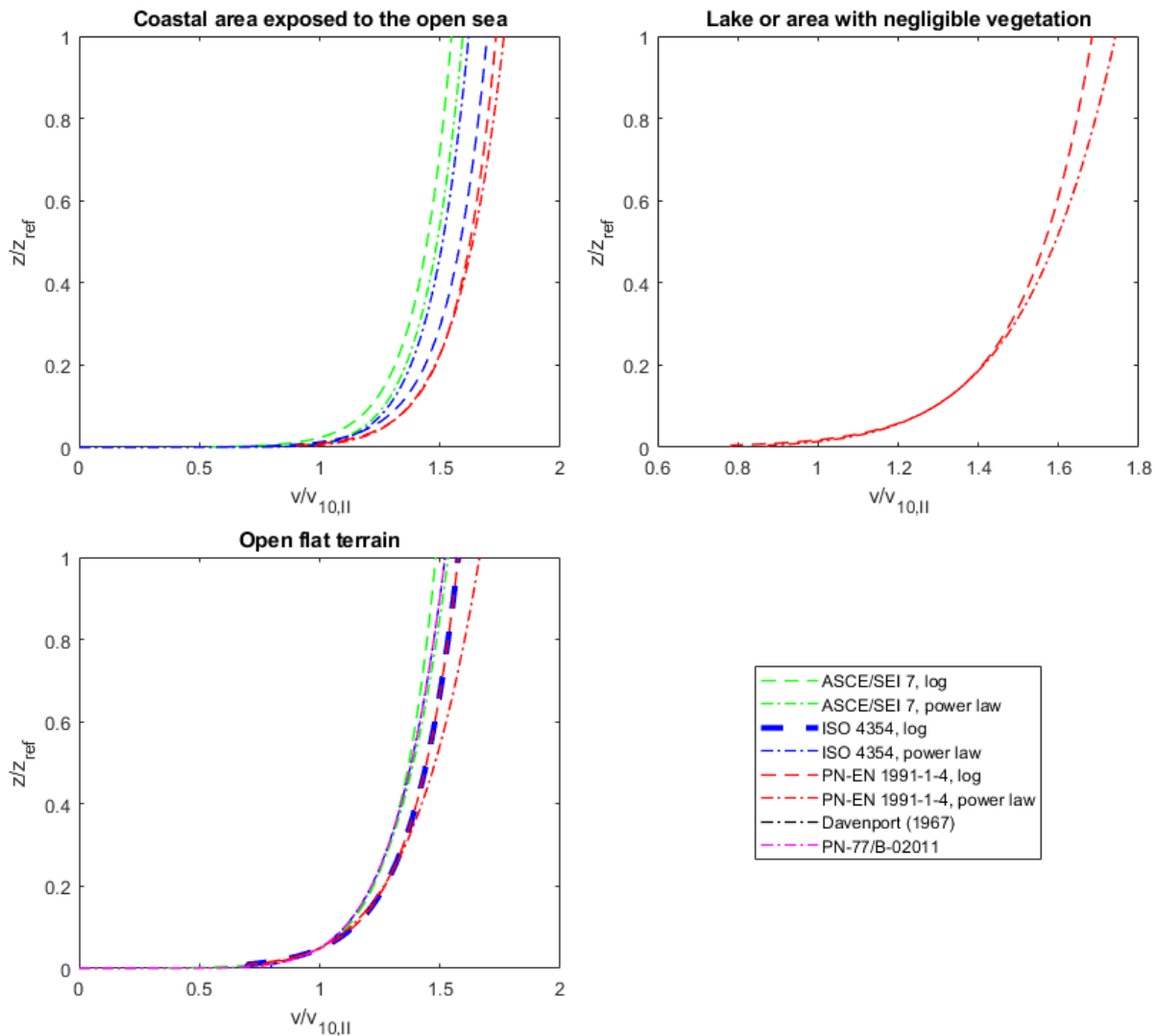
Fig. 3.3. Comparison of the vertical wind profile for terrain categories 0, I and II between different sources (ASCE/SEI 7, 2022; Davenport, 1960, 1967; ISO 4354, 2009; PN-77/B-02011, 1977; PN-EN 1991-1-4, 2011)

Based on these plots, the following observations can be made:

- Profiles according to (Davenport, 1967) diverge significantly from the other presented ones in the cases of suburban and urban terrains, especially at higher altitudes;
- The logarithmic and power-law wind profiles according to (PN-EN 1991-1-4, 2011) are matched very closely with each other, the closest of the three analysed codes that provide the two formulas. They only diverge noticeably at higher heights above the ground for the lower terrain categories (I and II in particular), which indicates that the description of the vertical wind profile for these categories can be reliably applied only to a limited height;
- The logarithmic and power-law wind profiles according to (ISO 4354, 2009) show the closest match for the suburbs/forest terrain category, however, the discrepancies between them are, in general, larger than between the two types of wind profiles given in (PN-EN 1991-1-4, 2011) or (ASCE/SEI 7, 2022);
- For the open flat terrain category, there is almost an exact match between the power-law wind profiles given by (PN-77/B-02011, 1977) and (ISO 4354, 2009), as well as

between the logarithmic wind profiles given by (ISO 4354, 2009) and (PN-EN 1991-1-4, 2011);

- The power-law wind profiles for the terrain category corresponding to large city centres given by (ISO 4354, 2009) and (ASCE/SEI 7, 2022) are close to each other, with the logarithmic profile from (ISO 4354, 2009) being significantly translated to the right;

- Furthermore, the wind profiles provided by (ISO 4354, 2009) and (PN-EN 1991-1-4, 2011) are, in general, matching closely. This is noticeable in particular for the terrain roughness categories III and IV (according to (PN-EN 1991-1-4, 2011)) – especially in the latter case, where the power-law wind profile according to (ISO 4354, 2009) is closer to the wind profiles given by (PN-EN 1991-1-4, 2011) than to the logarithmic wind profile given by (ISO 4354, 2009);
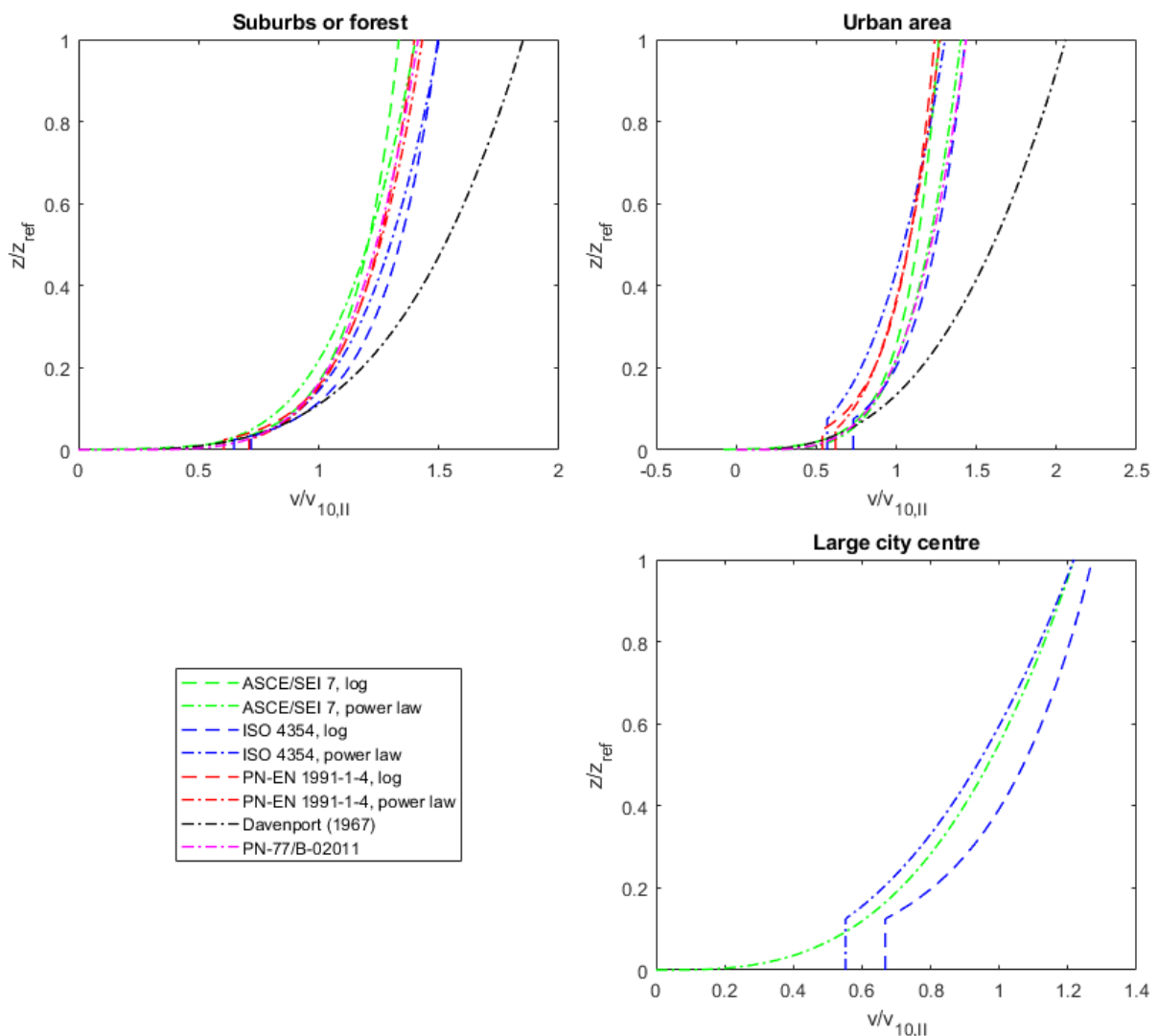

Fig. 3.4. Comparison of the vertical wind profile for terrains categories III, IV and an additional category for large city centres between different sources (ASCE/SEI 7, 2022; Davenport, 1960, 1967; ISO 4354, 2009; PN-77/B-02011, 1977; PN-EN 1991-1-4, 2011)

- Limiting the applicability of the wind profile description to a certain lowest height above the ground level, which depends on the terrain roughness category, seems like a valid suggestion, as due to high turbulence and a large number of obstacles below this

height, providing an exact and reliable description of mean wind speed in this region is impossible. Therefore, applying the same value of mean wind speed as at the minimal height of applicability z_{min} or H_{min} is a proper solution that is on the conservative side from the perspective of the structural safety;

- In the wind tunnel tests aimed at determining the wind action on structures, the higher terrain categories that correspond with suburbs or urban areas are of interest in most cases, as such terrains most commonly serve as locations for structures particularly vulnerable to wind actions. Due to the large potential differences between the actual wind conditions in smaller or average and larger cities, the additional terrain category for the centres of large cities seems like a reasonable addition.

Based on the previous observations, it seems reasonable that a 6th, additional terrain roughness category – corresponding to the large city centres – could be added also in the descriptions provided by (PN-EN 1991-1-4, 2011), and that it would be reasonable to perform this extrapolation by adapting the values suggested by (ISO 4354, 2009).

It should be noted that the change in the terrain roughness does not *immediately* cause the change in the wind profile over this particular terrain (A. Flaga, 2008). Most sources suggest analysing the upwind/upstream terrain over a sufficiently long distance called *fetch length*. ISO 4354 (2009) suggests a smooth transition between the two different profiles proceeded by adopting the profile of the lower category over the border perimeter between the terrains of two different roughness for a distance of 500 m (Fig. 3.5).
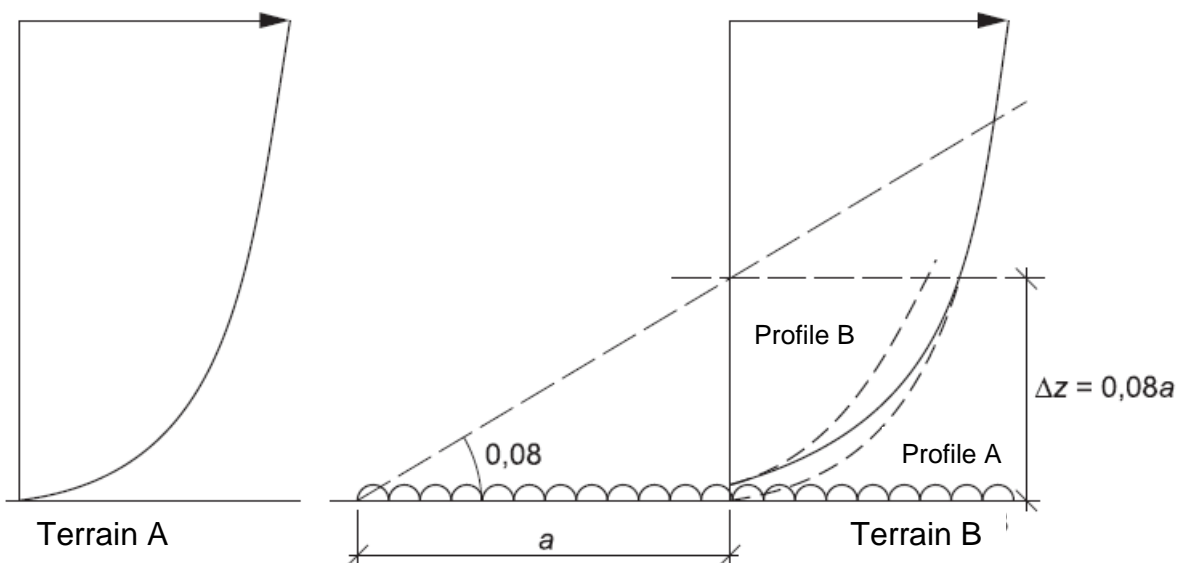

Fig. 3.5. Determination of the wind profile between two terrains with different roughness according to (A. Flaga, 2008; ISO 4354, 2009)

PN-EN 1991-1-4 (2011) recommends analysing an angular sector of 30° from the upstream direction and considering the roughness (if uniform, with less than 10% deviation) of this area, as shown in Fig. 3.6. If two or more different roughness types are present in this sector, then are with the lowest roughness length should be applied as the most conservative choice (yielding the highest wind speed). The Annex A.2 in this code is detailing two procedures of specifying the terrain roughness category based on the roughness of the fetch length – simplified one (adopting the smoother categories if the subject structure is located less than

2 km from the terrain with category 0 or less than 1 km from the (smoother) terrain of category I, II or III) and a more refined one, which takes into account the structure's height, angular sector and the distance from the border between the two categories. The Annex provides the exact values for the transitions between different categories, depending on these parameters.
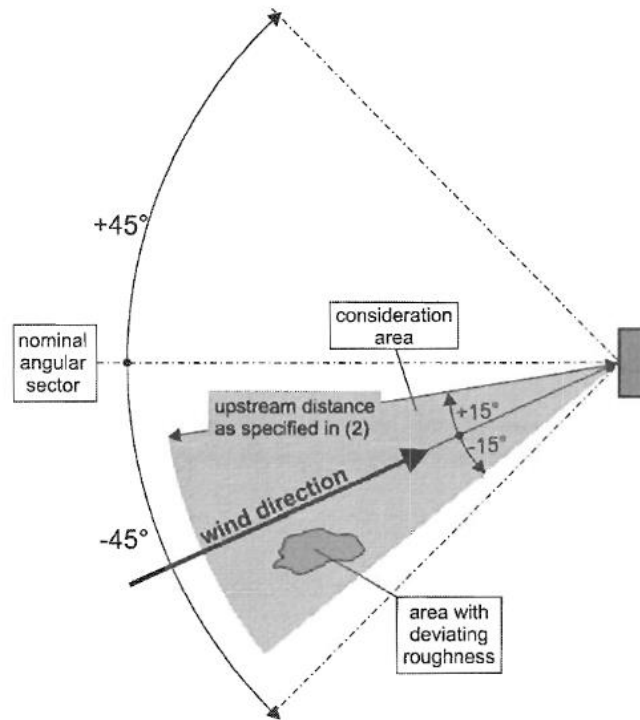

Fig. 3.6. Assessment of terrain roughness according to (PN-EN 1991-1-4, 2011)

ASCE/SEI 7 (2022) specifies, in addition to the roughness categories, *exposure categories*. Exposure B applies for terrains where the roughness category B (suburban terrains, towns) prevails in the upwind direction for a distance of at least 800 m or 20 times the building height (whichever is greater), for buildings of up to 10 m, this value might be reduced to 460 m. Exposure D requires at least 1500 m or 20 times the building height (whichever is greater) of roughness D (water surfaces) and extends for 200 m or 20 times the building height inland from the shoreline. Exposure C (open terrain exposure) applies where neither of the two other exposure categories applies. Furthermore, for a site located in the transition zone between the two exposure categories – similarly to the Eurocode – the exposure category resulting in higher wind speeds should be used, unless an intermediate roughness for this zone can be determined (Simiu & Miyata, 2006).

Turbulence intensity is also strongly influenced by the terrain roughness – however, contrary to the wind velocity, higher turbulences occur in the terrains with higher roughness categories. Davenport (1967) suggested a simplification of using a constant standard deviation of the wind speed, based on the approximate value of this parameter at the reference height of 10 m:

$$\sigma_v(z) \cong \bar{\sigma}_v = 2.45\sqrt{K}\bar{v}(10) \tag{3.61}$$

where K – roughness parameter depending on the terrain category, equal to 0.005 for open flat terrain, 0.015 for suburbs/forest areas and 0.05 for urban areas.

Applying this formula results in the following equation for the turbulence intensity vertical profile:

$$I_v(z) \cong \bar{\sigma}_v = 2.45\sqrt{K}\left(\frac{z}{10}\right)^{-\alpha} \tag{3.62}$$

ISO 4354 (2009) suggests a logarithmic formula for the turbulence intensity vertical profile:

$$I_v(z) \cong \frac{\bar{\sigma}_v(z)}{\bar{v}(z)} = \frac{1}{\ln\left(\frac{z}{z_0}\right)} \tag{3.63}$$

This results in the value of the standard deviation depending only on the roughness terrain category, by applying the formula for logarithmic wind profile according to this code given in Eq. (3.56):

$$\bar{\sigma}_v = \bar{v}_A(10)k_2 \tag{3.64}$$

PN-EN 1991-1-4 (2011) recommends a very similar approach to calculating the turbulence intensity, however, it also takes into account the orography factor c_o (in the cases of uneven terrain) and the turbulence factor k_l (for which it recommends the value of 1.0 in general, leaving it up to the national annexes applicable in each country. In the Polish version of the code, this factor is not elaborated on in any of the national annexes). In practice, this renders the formula for turbulence intensity identical to the one given in Eq. (3.63):

$$I_v(z) = \frac{\sigma_v(z)}{v_m(z)} = \frac{k_l}{c_o(z)\ln\left(\frac{z}{z_0}\right)} \tag{3.65}$$

A more general power-law function for the turbulence intensity profile can also be written as (A. Flaga, 2008):

$$I_v(z) = \frac{\sigma_v(z)}{\bar{v}(z)} \cong \frac{\sigma_v(z_{ref})}{\bar{v}(z_{ref})\left(\frac{z}{z_{ref}}\right)^{\alpha}} = \frac{\sigma_v(z_{ref})}{\bar{v}(z_{ref})}\left(\frac{z}{z_{ref}}\right)^{-\alpha} \tag{3.66}$$

While these formulas are the most commonly used approaches for assigning the vertical turbulence intensity profiles, they are simplifications of nature, which assume that the value of wind fluctuations σ_v is the same along the whole considered height, so that the vertical change in turbulence intensity is completely related to the vertical change in wind speed – which is not necessarily true. Sfintesco and Wyatt (1977) suggested an approach that would take this into account, with the range of applicability of 20 m or more above the ground:

$$I_v(z) \cong \frac{\bar{\sigma}_v}{\bar{v}(z)}\left(\frac{z}{20}\right)^{-0.03} \tag{3.67}$$

Davenport (1984) observed the relationship between the α exponent of the power-law vertical profile and the turbulence intensity at 30 m, where its value is very similar to this exponent. This characteristic suggests that $I_v(30)$ (further abbreviated as $I_{v,30}$ within this work) might

be another significant, non-dimensional parameter of the wind flow description. This relationship is shown in Fig. 3.7 and Eq. (3.68).

$$I_v(30) = \left(\ln \frac{30}{z_0}\right)^{-1} \cong \alpha \qquad (3.68)$$
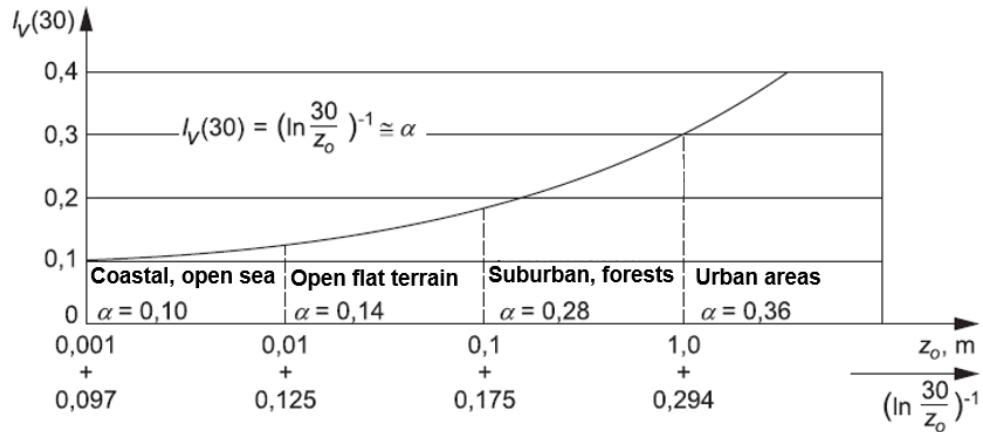

Fig. 3.7. Relationship of the turbulence intensity and vertical wind profile according to (Davenport, 1984; A. Flaga, 2008)

Values of turbulence intensity at different heights and for values of the roughness length z_0) are given in (ESDU 85020, 2002). This is given with a reference wind speed of 20 m/s measured at 10 m height at open flat terrain. For other wind speeds, a correction factor has to be applied. The values of turbulence intensity for different z_0 values corresponding to the terrain categories in (PN-EN 1991-1-4, 2011) are shown in Fig. 3.8.
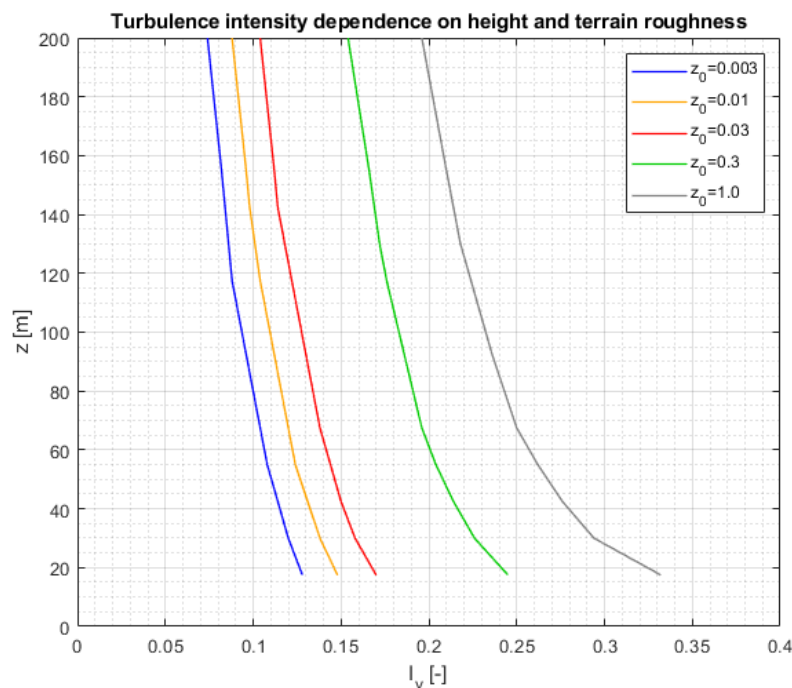

Fig. 3.8. Turbulence intensity dependence on height and terrain roughness for a mean wind speed of 20 m/s at 10 m height in open flat terrain according to (ESDU 85020, 2002)

Since the values of the α exponent and the roughness length z_0 for the vertical mean wind speed profile and turbulence intensity profiles are not necessarily the same in all cases in

reality, due to the simplification pointed out above, they will be denoted with different symbols further in this work. This also seems in line with the findings of measurements in the real-life scale (Hui et al., 2009; Tamura et al., 2007). The exponent for the power-law turbulence intensity profile will be marked as β (which by default assumes negative values to reduce the minus sign in the equation) and the roughness length for the logarithmic turbulence intensity profile will be marked as z_0^T.

Another group of wind flow characteristics that heavily depend on the terrain roughness are turbulence length scales. ESDU 86035 (2000) covers a variety of different terrain types and provides the values of longitudinal turbulence length scales along the main component of the wind direction, L_x^{vx}, depending on the height z above the ground (for the heights between 10 and 300 m). These values are given depending on the roughness lengths z_0. According to this standard, the roughness lengths correspond to city centres/forests ($z_0 = 0.7$), small towns and suburbs ($z_0 = 0.3$), outskirts of small towns and villages ($z_0 = 0.1$), open flat terrain, typical farmland ($z_0 = 0.03$) and flat areas with no obstructions, runways of airports and sea during extreme storms ($z_0 = 0.003$). This data is presented in Tab. 3.14 and Fig. 3.9. It should be noted that the large discrepancies with Tab. 3.2 are a result of different scaling with reference wind speed.

Tab. 3.14. Longitudinal turbulence length scales L_x^{vx} depending on the terrain roughness length z_0 and height above the ground (ESDU 86035, 2000) for a mean wind speed of 20 m/s at 10 m height in open flat terrain

Height above the ground z [m]	Roughness length z_0 [m]				
	0.003	0.03	0.1	0.3	0.7
10	156	108	84	64	50
15	202	158	129	103	84
20	231	199	171	142	119
30	260	260	241	213	187
40	274	300	294	275	251
50	283	328	336	327	309
60	291	350	370	373	362
70	299	368	398	412	410
80	308	384	423	447	454
90	315	399	445	479	494
100	323	413	465	508	531
120	335	438	501	559	598
140	345	461	534	605	658

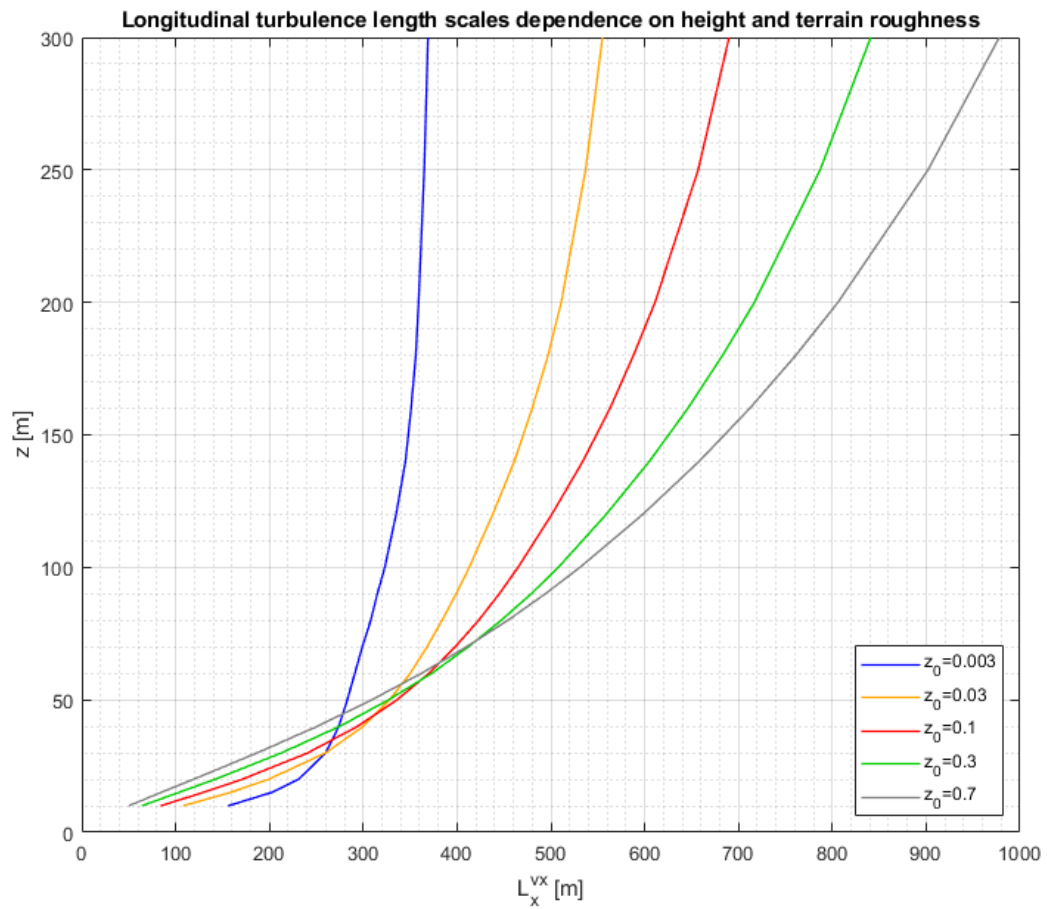| Height above the ground z [m]	Roughness length z_0 [m]				
	0.003	**0.03**	**0.1**	**0.3**	**0.7**
160	351	480	563	646	712
180	356	497	588	683	761
200	359	511	611	717	806
250	365	537	657	787	902
300	369	555	690	841	978

Fig. 3.9. Change of longitudinal turbulence length scale L_x^{vx} along the height for different types of terrains (ESDU 86035, 2000)

As can be observed, the turbulence length scales for the terrain categories with lower roughness lengths are higher at the lower heights above the ground than for the terrains with higher roughness lengths. However, the increase with height is much slower in the cases of lower terrain roughness, which means that at the larger altitudes (closer to the edge of boundary layer thickness), the turbulence length scales are much higher at the terrains with larger roughness length values. Overall, it seems that the curves describing the turbulence

lengths scales are asymptotically converging to a value they reach around the gradient height z_g for the respective terrain roughness category.

PN-EN 1991-1-4 (2011) provides a formula for calculating the turbulence length scales depending on the terrain category. This formula is given as part of the calculations required for a structural factor $c_s c_d$ and should be considered as more of an approximation, as it assumes a fixed value of turbulence length scale of 300 m at 200 m reference height (which is also the maximum height where the formula is applicable). This formula is defined as:

$$L_x^{vx}(z) = L_t \left(\frac{z}{z_t}\right)^{\alpha^*} \qquad \text{for} \quad z \geq z_{min}$$

$$L_x^{vx}(z) = L_x^{vx}(z_{min}) \qquad \text{for} \quad z < z_{min}$$

(3.69)

where: L_t – reference turbulence length scale equal to 300 m, z_t – reference height of 200 m, $\alpha^* = 0.67 + 0.05 \ln(z_0)$.
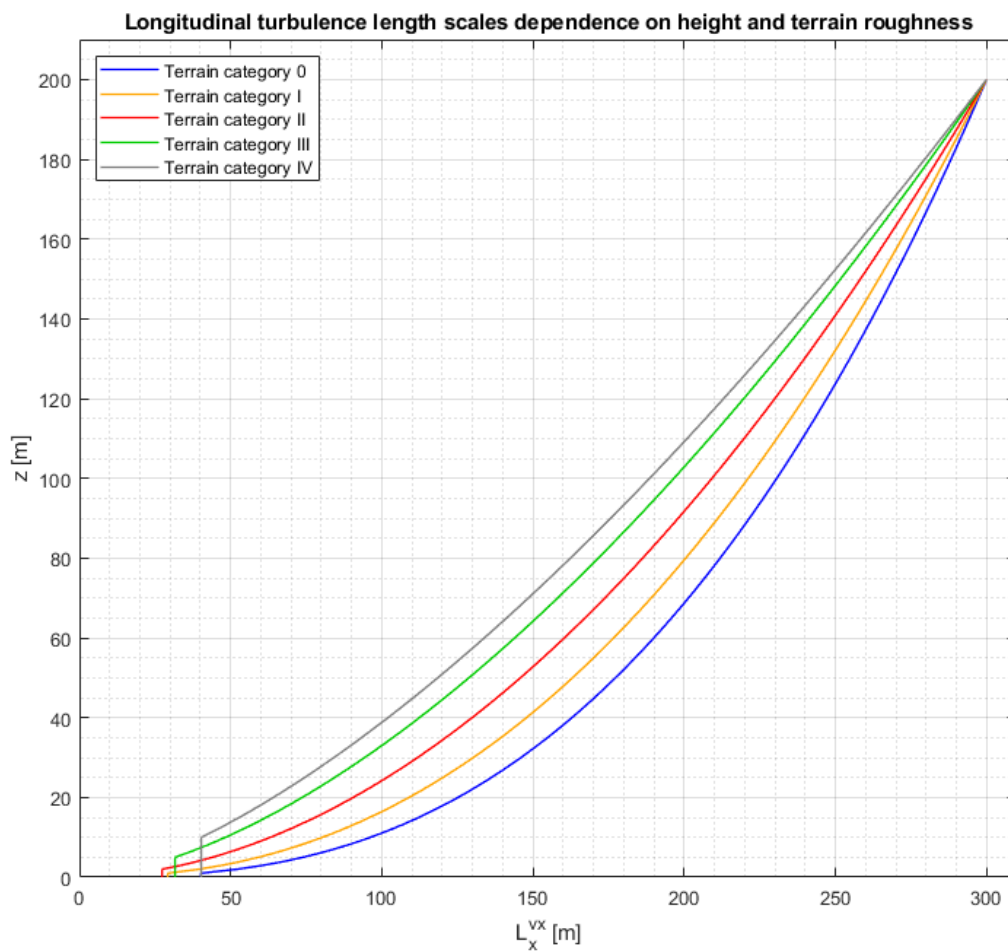

Fig. 3.10. Change of longitudinal turbulence length scale L_x^{vx} along the height for different terrain categories (PN-EN 1991-1-4, 2011)

The plots of turbulence length scales according to (PN-EN 1991-1-4, 2011) are shown in Fig. 3.10. As can be seen, the convergence of all the plots at the height of 200 m of these

scales results in trends of the plots for different terrain categories being vastly different from the ones shown in Fig. 3.9, especially above the height of about 50-60 m.

Summing up the state-of-the-art knowledge about the terrain roughness and current trends in its codification, the following observations can be made:

- The terrain roughness categories given in the codes (ASCE/SEI 7, 2022; ISO 4354, 2009; PN-77/B-02011, 1977; PN-EN 1991-1-4, 2011) and other sources are rather descriptive and general;
- The wind flow description according to these categories is mostly limited to the vertical mean wind speed profile and a simplified description of the turbulence intensity – which seems reasonable for standard engineering practice, but may not be sufficient for proper wind tunnel simulation, which in most cases relates to more refined structures where the wind is one of the main loads considered for the design;
- The descriptions of these categories do not cover different aspects influencing the roughness, such as the distribution and shape of the obstacles or their height variations;
- While it would be impossible to take all of these parameters into account at once, it is suggested to use at least one more parameter besides the roughness height k_r, for example, the standard deviation of the obstacles' heights σ_r for the roughness description.

3.3. Methods of simulating the wind flow in wind tunnels

Most wind tunnels are made for the purposes of aerospace engineering, which means that they need to generate the specific parameters of the high-speed flow typically acting on e.g. wings of a plane in the higher layers of the atmosphere (e.g. in the stratosphere). These flows are characterised by high speeds, which often result in air density variations from air compressibility, possible at speeds above 0.3 Mach number (0.3 of the speed of sound) and very low turbulence level (about 0.2%) typical for the higher atmospheric layers where the flow is almost laminar (Abramson & Rogers, 1983; SimScale, 2022b). However, this work will only focus on the other type of wind tunnels, which are commonly used for the purposes of civil engineering, wind energy or environmental engineering. Such wind tunnels are characterised by much lower wind speeds (usually no higher than about 50 m/s) and larger turbulence levels (up to about 30%), typical for the boundary layer flows in the lower parts of the troposphere. Due to reducing the flow speed, these types of wind tunnels may have larger cross-sections, which also helps in the proper simulation of turbulence (Cermak, 2003).

For most problems related to civil engineering, the models inside the wind tunnel are scaled down. However, scaling the geometry also requires proportional scaling down of the other parameters, which is why the similarity criteria and similarity scales, based on the dimensional analysis and Buckingham π theorem (Buckingham, 1915) are widely used in wind engineering (Simiu & Scanlan, 1986).

One of the most commonly used similarity criteria is the Reynolds number, which governs the flow separation, in particular for bluff bodies. This number is the ratio of inertial forces to viscous forces and is defined as:

$$\text{Re} = \frac{\rho v D}{\mu} = \frac{v D}{\nu} \qquad (3.70)$$

where: ρ – fluid density (about 1.25 kg/m^3 for air), v – flow velocity [m/s], D – characteristic dimension [m], μ – dynamic viscosity of the fluid ($1.81 \cdot 10^{-5}$ kg/ms for air at 15° C), ν – kinematic viscosity of the fluid ($1.48 \cdot 10^{-5}$ m^2/s for air at 15° C).

As the parameters of air (density and dynamic or kinematic viscosity) do not scale and are the same in the case of model tests as in real-life but the characteristic dimension of the model is scaled by the geometric scale, it is clear that this criterion is impossible to fulfil in wind tunnel model tests. However, it is usually sufficient to have the Reynolds number in the same range as in a real-life scale, in particular (Scruton & Rogers, 1971):

- Subcritical $\text{Re} < (1.0 - 1.4)10^5$
- Critical $(1.0 - 1.4)10^5 < \text{Re} < (3.5 - 5.0)10^5$
- Supercritical $(3.5 - 5.0)10^5 < \text{Re} < (3.5 - 5.0)10^6$

In general, the flow is more laminar at low Reynolds numbers, where viscous forces dominate over the inertial forces, and more turbulent for higher Reynolds numbers that are dominated by inertial forces. Moreover, it should be noted that this similarity criterion is particularly important for objects without edges or protrusions, where the separation region is uncertain and may change.

Another important similarity criterion in wind tunnel tests, in particular the ones concerning structural dynamics, is the kinematic Strouhal number, which is a non-dimensional parameter related to the gust frequency of the wind. It is defined as:

$$\text{St} = \frac{f D}{v} \qquad (3.71)$$

where f – gust frequency.

This parameter is especially important in the tests of structures which may be vulnerable to wind-induced vibrations, such as slender structures (tall buildings, chimneys or towers) or lightweight membrane roofs, in cases where the gust frequency might be close to the natural frequency of the structure.

While not all of these criteria are always required to be fulfilled for a given experimental case, it is important to assess their importance at the stage of experiment planning to obtain reliable results and adopt proper similarity scales.

For simulating the wind flow in boundary layer wind tunnels, it is desired to have as uniform as possible airstream inflowing into the wind tunnel, both in terms of even speed distribution over the whole cross-section and low fluctuations (A. Flaga, 2008). This can be achieved through the use of the so-called *beehive frames*, which are sheets of tiny metal plates with a depth of a few centimetres, evenly spaced in two perpendicular directions to form relatively small rectangular holes, placed at the inlet of the wind tunnel, after the guide vanes or flow-generating fan. An example of beehive frames installed at the inlet of a wind tunnel is shown

in Fig. 3.11. Another type of elements that help to maintain a uniform flow at the inlet are windscreens of streamlined airfoil profiles, also placed at the inlet. It is only relevant to start forming the proper, desired wind flow characteristics along the fetch length after obtaining this uniform flow at the inlet.
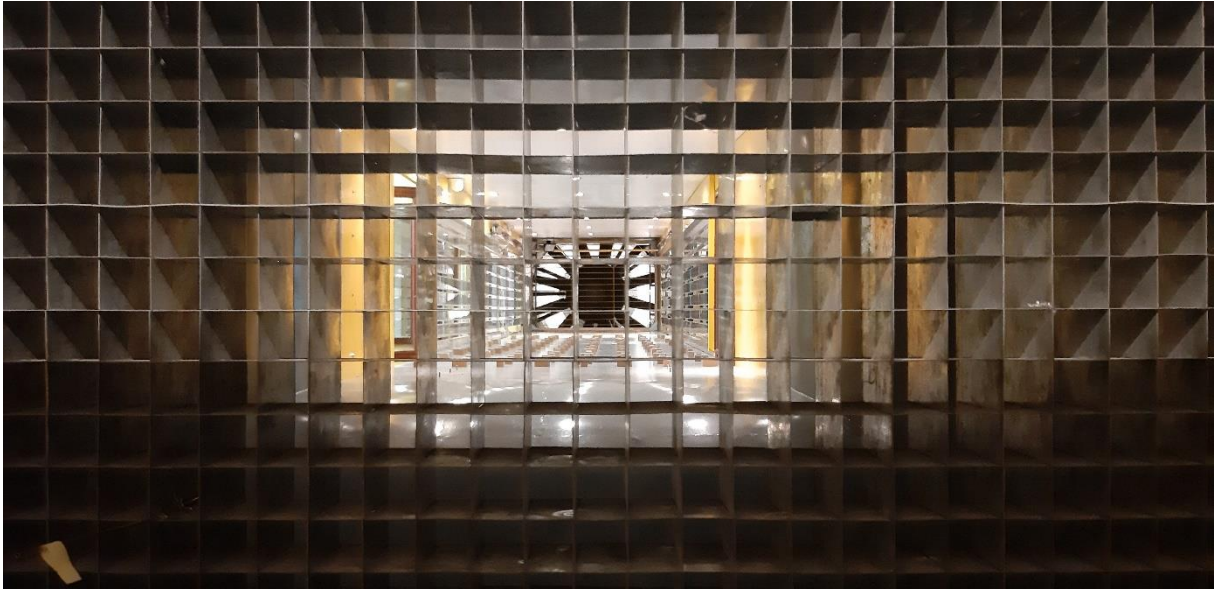

Fig. 3.11. Beehive frame at the inlet of the wind tunnel of the Wind Engineering Laboratory of Cracow University of Technology

Furthermore, it is important to minimise the influence of the fans that generate the inflow in the wind tunnel, which are often located on the suction side of the tunnel, behind the model. The fans may create large and artificial vorticity that would not correspond with the types of atmospheric circulations present in nature. Therefore, additional airfoil profiles can be used to mitigate this effect by breaking down these vortices. An example of this is shown in Fig. 3.12.
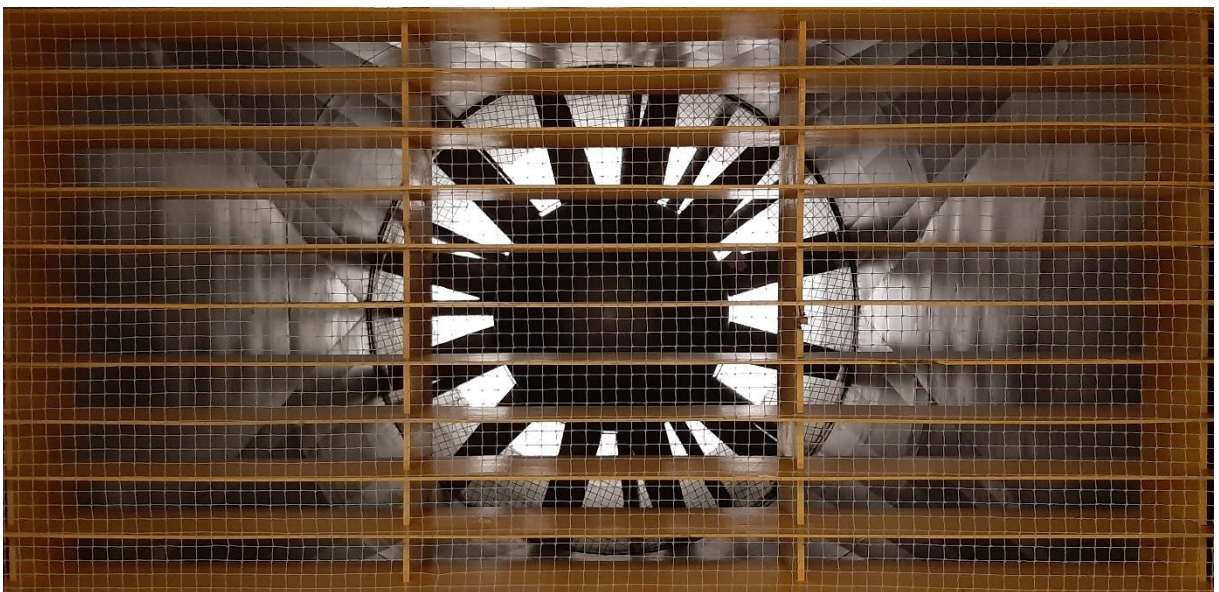
Fig. 3.12. Airfoil profiles located between the model and the fan on the suction side of the wind tunnel of the Wind Engineering Laboratory of Cracow University of Technology

In close-circuit wind tunnels, the air circulates in the wind tunnels around a loop, which requires proper re-shaping of the flow at the corners. This is usually achieved by *guide vanes*, which are arch-shaped airfoil profiles, usually manufactured from smooth metal sheets, that redirect the flow and minimise the turbulisation and losses at the corners. Proper design of the guide vanes can largely improve the performance of the wind tunnel (Calautit et al., 2014). This might be optimised even further by enabling the calibration of the guide vanes depending on the flow parameters (Kłaput, 2020). Two examples of guide vanes are shown in Fig. 3.13.

a)   b)
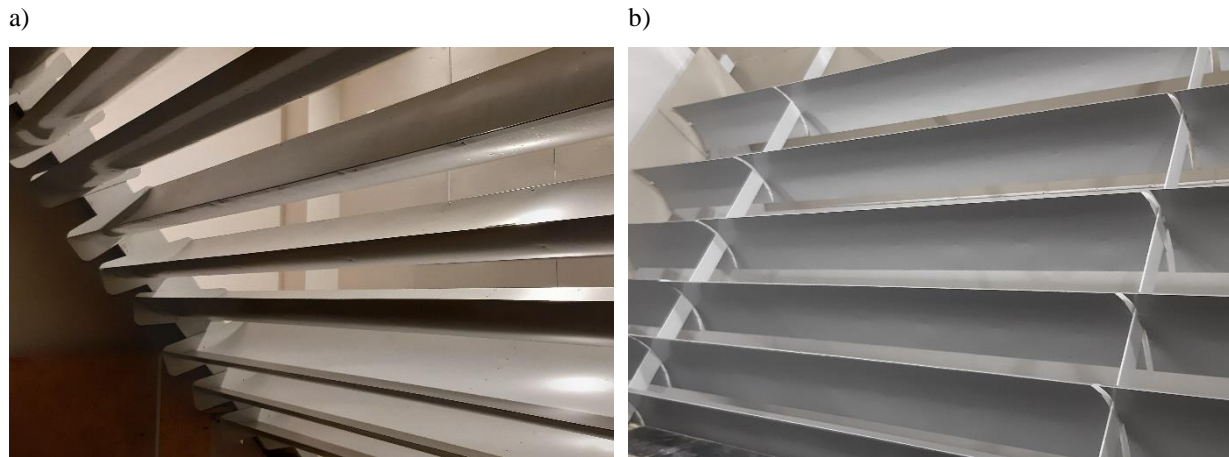
Fig. 3.13. Guide vanes at the wind tunnel of the Wind Engineering Laboratory of Cracow University of Technology (a) and Laboratory of Environmental Aerodynamics of Cracow University of Technology (b)

Another important parameter during wind tunnel tests is the blockage ratio, which is the ratio of the area of the model in the wind tunnel projected on a vertical plane perpendicular to the main wind flow direction to the cross-section of the wind tunnel. The impact of this effect on the wind flow is also dependent on the model shape, with cylindrical models being more prone to larger distortions.

Fig. 3.14. Slotted sidewalls at the wind tunnel of the Wind Engineering Laboratory of Cracow University of Technology

Takeda and Kato (1992) found large distortions even for the blockage ratio of 5%, however other sources (Choi & Kwon, 1998) suggest higher values of around 10%. Moreover, methods of mitigating this effect up to some level have been developed, for example by using slotted walls or ceilings with certain slot parameters (Kłaput, 2020). Glanville and Kwok (1997) applied a slotted ceiling and obtained correct pressure distributions on a half-cylinder model with up to 25% of blockage ratio. An example of the slotted walls is shown in Fig. 3.14.

After achieving a satisfactorily uniform wind flow at the inlet, it can be formed to obtain the desired flow structure. The generation of vertical wind and turbulence profiles can be achieved through two different methods – passive or active, with the former being far more common in wind tunnels worldwide (A. Flaga, 2008). The passive methods rely on static elements of different shapes – such as blocks, spires, barriers or grids/nets with different hole sizes – which introduce controlled vorticity in the flow, thus increasing its turbulence. Depending on the type of the elements, different vortices in different planes and of different length scales can be created within the flow. Kozmar (2011) discussed in detail the possibility of simulating different wind flow characteristics with the use of passive turbulence methods.

Turbulising grids are one of the earliest techniques for simulating turbulence inside wind tunnels (Karman & Howarth, 1938). They can be mounted at the inlets of wind tunnels. They may consist of different-shaped elements with either uniform or varying (e.g. with height) sizes of the openings. They can either produce a nearly uniform turbulence level distributed over the whole cross-section of the flow, or basic mean wind speed and turbulence profiles with properly calibrated openings variations. However, their large disadvantage compared to other types of elements of passive turbulence generation is the high blockage ratio introduced to the flow, which may significantly reduce the speed of the flow. On the other hand, their advantage is the relatively shorter distance required to obtain a homogenous and isotropic flow than for techniques that require roughness modelling along the fetch length (Vita et al., 2018). An example of a turbulising net is shown in Fig. 3.15.

Fig. 3.15. Turbulising net at the Wind Engineering Laboratory of Cracow University of Technology

Spires (also known as *vortex generators*), which are usually mounted at the inlet of the wind tunnel, generate large-scale vortices in the horizontal plane, similar to what would be expected of an aerodynamic wake of tall buildings. Furthermore, due to their size narrowing with the height, they reduce the wind speed near the floor level (due to higher blockage) while allowing more of the flow to pass at the higher levels, influencing the vertical mean wind speed profile (Armitt & Counihan, 1968).
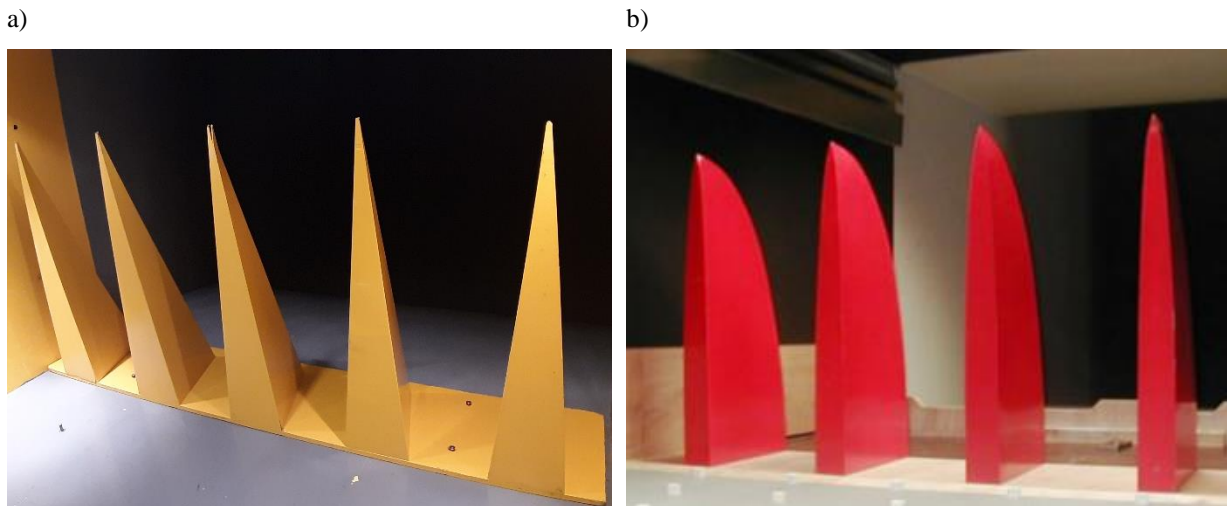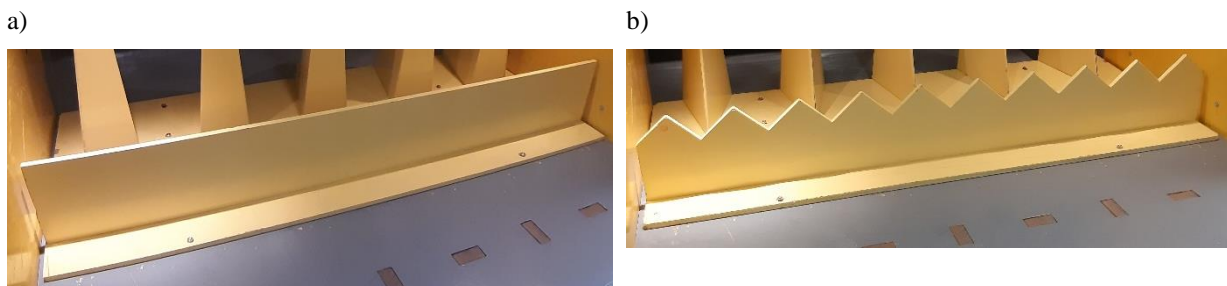
a)   b)

Fig. 3.16. Different types of spires: (a) pyramidal spires at the Wind Engineering Laboratory of Cracow University of Technology and (b) Counihan spires at the boundary layer wind tunnel at the Technische Universität München (Kozmar, 2011b)

Different shapes of spires are used, from T-shaped cross sections and pyramidal ones (A. Flaga, 2008) to elliptical *Counihan* vortex generators (Kozmar & Laschka, 2019; Kuznetsov et al., 2017), which are recently gaining popularity. Both of these types are shown in Fig. 3.16.

Barriers, also located at the inlets of wind tunnels, are applied to reduce the wind speed at the near-ground level and to create mid- to large-scale vertices in the vertical planes parallel to the flow direction. They might have different shapes, from full rectangular without any protrusions (Fig. 3.17a), through triangular prongs (Fig. 3.17b) to *castellated*, with prongs shaped as horizontally stretched trapezoids (Fig. 3.17c), which affects their exact impact on the flow by varying the vorticity distribution along the width of the wind tunnel. They can be mounted either on the windward or the leeward side of the spires.

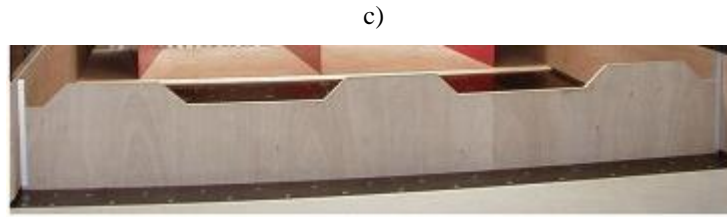a)   b)

c)

Fig. 3.17. Different types of barriers: (a) rectangular barrier at the Wind Engineering Laboratory of Cracow University of Technology; (b) triangular prongs barrier at the Wind Engineering Laboratory of Cracow University of Technology and (c) castellated barrier at the boundary layer wind tunnel at the Technische Universität München (Kozmar & Laschka, 2019)

The elevated blocks are elements that are distributed along the fetch length to simulate the terrain roughness caused by the presence of buildings or other obstacles in the way of the wind flow. They are one of the most commonly used elements in various wind tunnels, often with the possibility of automated elevation at different heights and variations across several autonomous segments on the path of the flow for more precise adjustments. Two examples of the blocks with different configurations and densities over the fetch length from different wind tunnels are shown in Fig. 3.18. Instead of elevated blocks fixed to the wind tunnel floor, some wind tunnels use different elements that are not permanently connected to the wind tunnel floor (e.g. bricks). This allows for larger flexibility in selecting the configuration of the elements and also achieving a smooth floor surface if there are no elements present (Fossati et al., 2006). However, the main disadvantage of this technique is the tedious, manual process of preparing the experimental setup, which usually requires an iterative process to set up properly. Kozmar (2008) used LEGO bricks to study the influence of different spatial configurations of the roughness elements on wind flow in a wind tunnel. Kim et al. (2022) developed an even more refined technique of simulating heterogeneous terrain roughness, similar to that in the real world with the *Terraformer*, a computer-controlled 62 × 18 roughness grid of independent blocks. The height of each element can be set between 0 and 160 mm and their orientation can be varied between 0° and 360°. This can be automated by directly inputting the roughness data measured in the field.

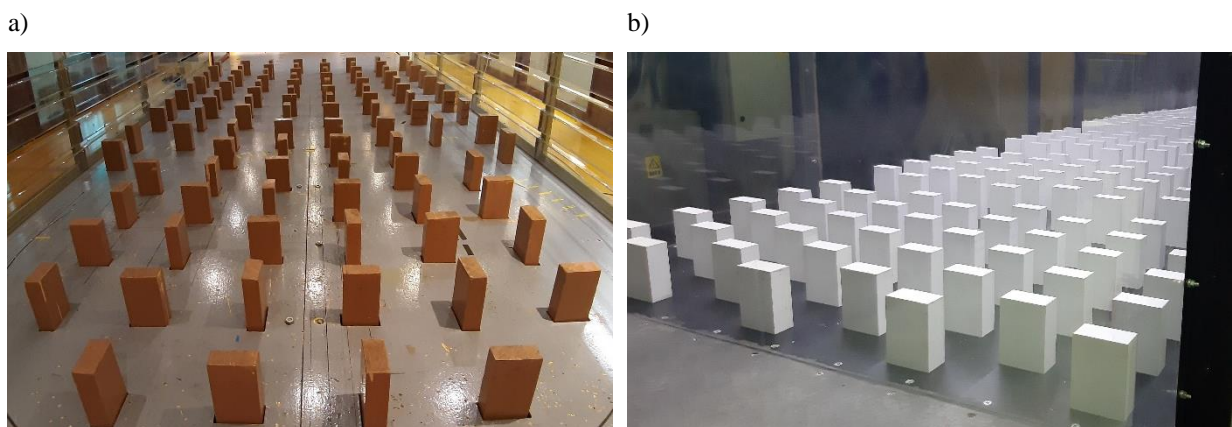a)   b)

Fig. 3.18. Elevated blocks at the Wind Engineering Laboratory of Cracow University of Technology (a) and at the wind tunnel of Technical University of Civil Engineering in Bucharest (b)

As for the active methods, they rely on introducing additional airstreams to the main flow inside a wind tunnel. Bienkiewicz et al. (1983) showed that this modelling technique may

result in much larger (by one order of magnitude) turbulence length scales, which might be useful in wind tunnels of smaller sizes. These additional airstreams should be perpendicular to the main flow direction (e.g. vertical) to disturb it and create turbulence. This can be achieved with, for example, pressurised tubes injecting the stream into the wind tunnel (Aufderheide et al., 2014) or by smaller axial fans producing a cross-flow (Franco et al., 2022). This method can be seen in Fig. 3.19. Besides being implemented for artificial turbulence generation, this method might be also applied to simulate complex flow interactions, such as pollutant dispersion from chimneys or volcanic eruptions. A different approach for an active method of turbulence simulation is having moving parts inside the wind tunnel. However, these methods are rather rarely used compared to passive means of turbulence generation and will not be covered further in this work.
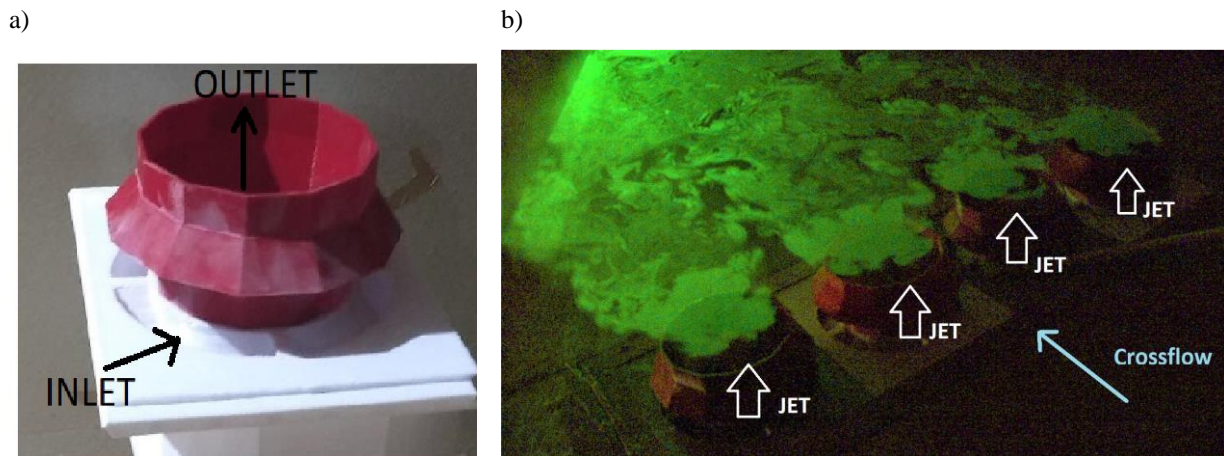
a)   b)

Fig. 3.19. Axial fans for introducing additional airstream perpendicular to the main inflow in a wind tunnel: (a) image of a single axial fan; (b) flow visualisation of the mixing between the different airstreams in crossflow (Franco et al., 2022)

More details about different elements used for passive turbulence generation can be found in chapter 5 of this work, which discusses the experimental setup (in particular in Tab. 5.2).

4. Proposition of unification of terrain roughness classifications

Due to the notable discrepancies in the parameters provided for the terrain roughness categories in different codes and the generally inexact description of these categories which may lead to non-conclusive assignment, an authorial classification of categories of terrain roughness is proposed. This classification is mostly introduced for the purpose of wind tunnel tests, where a more precise simulation of the wind conditions at a site is usually highly sought-after in order to achieve results closer to reality, rather than having to rely on a large margin of uncertainties.

The basis of this classification are various roughness parameters (A. Flaga, 2022). Therefore, it is a more direct approach to the terrain roughness assignment than basing on the wind flow structure over the terrain. The wind flow structure, on the other hand, is related to and may be derived (after field measurements validation) from these roughness characteristics.

4.1. Terrain roughness assignment on wind tunnel models of real-life locations

As a first step in the process of roughness classification, a number of real-life locations were examined. Each of these locations came from actual tests performed in the wind tunnel of the Wind Engineering Laboratory of the Cracow University of Technology, which gives them more relevancy when it comes to practical application planned for the classification. These models represent urbanised areas in Poland and the United Kingdom. The models are shown in Fig. 4.1-Fig. 4.5.
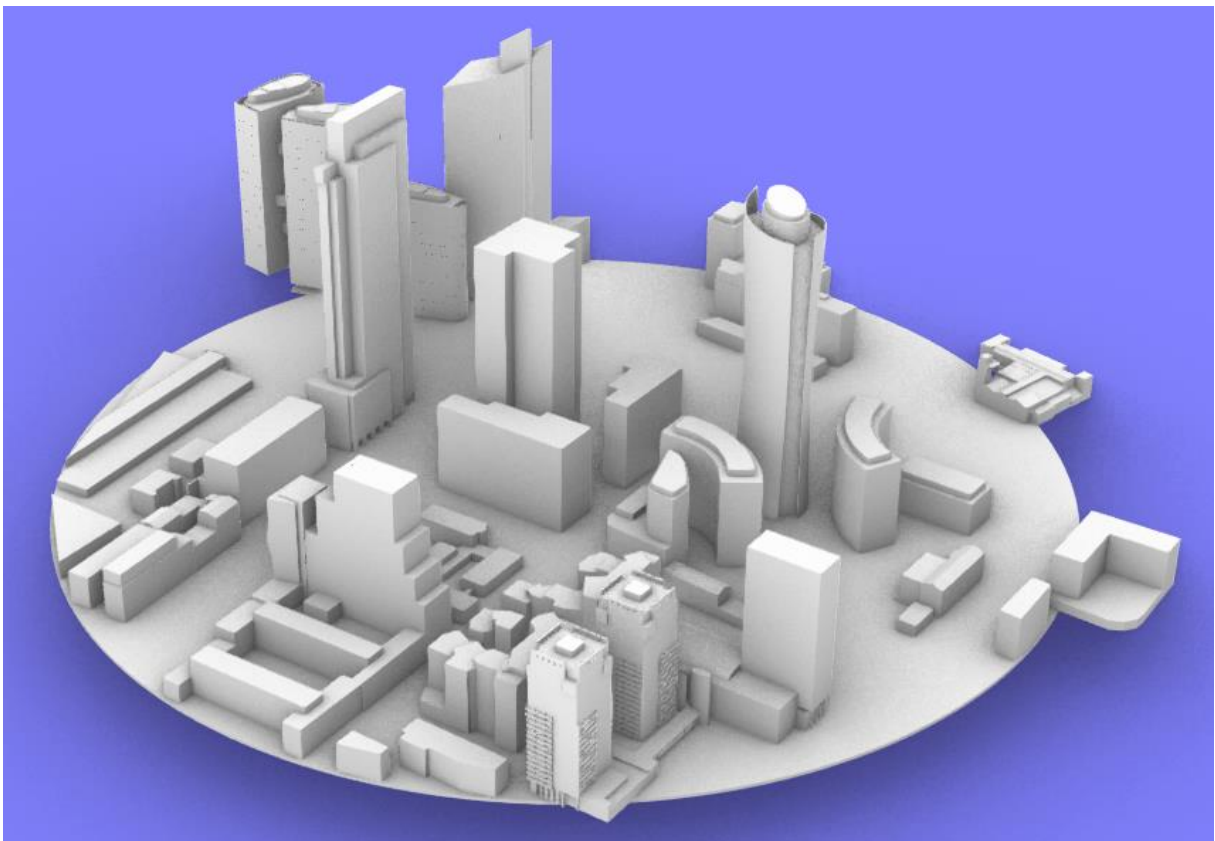

Fig. 4.1. Model #1 used for terrain roughness assignment (location: Warsaw, Poland)
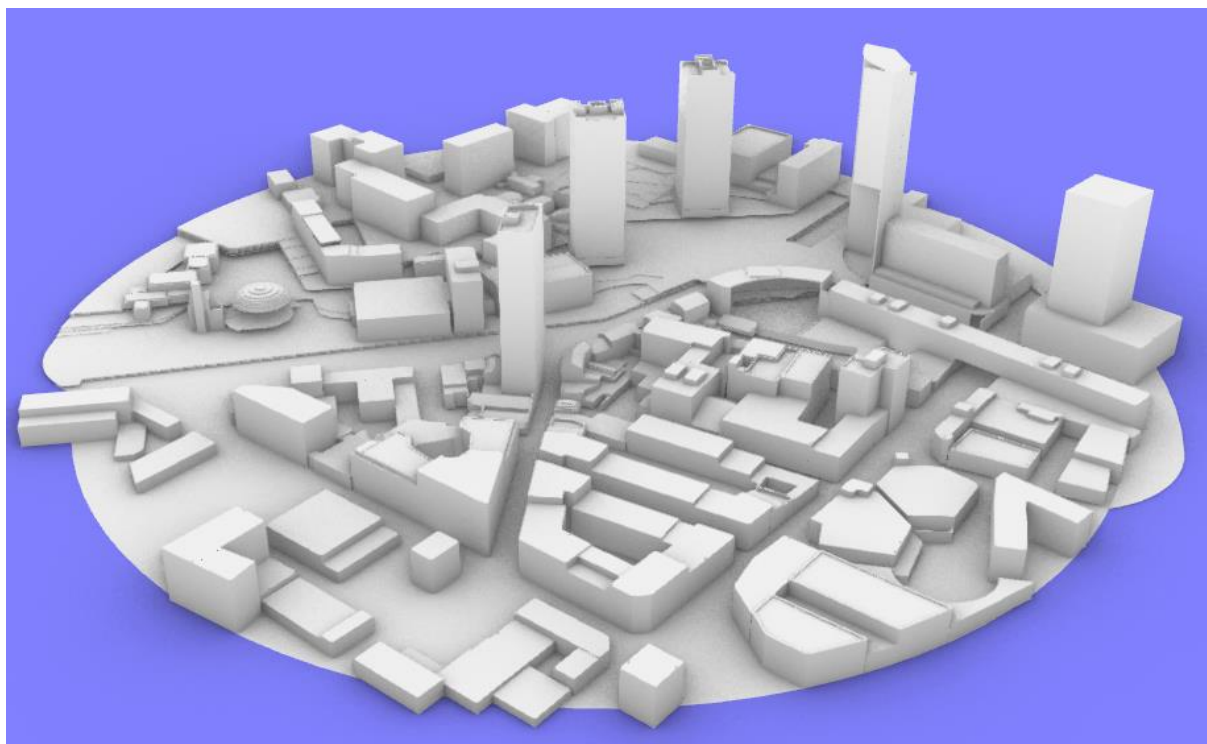
Fig. 4.2. Model #2 used for terrain roughness assignment (location: Birmingham, United Kingdom)
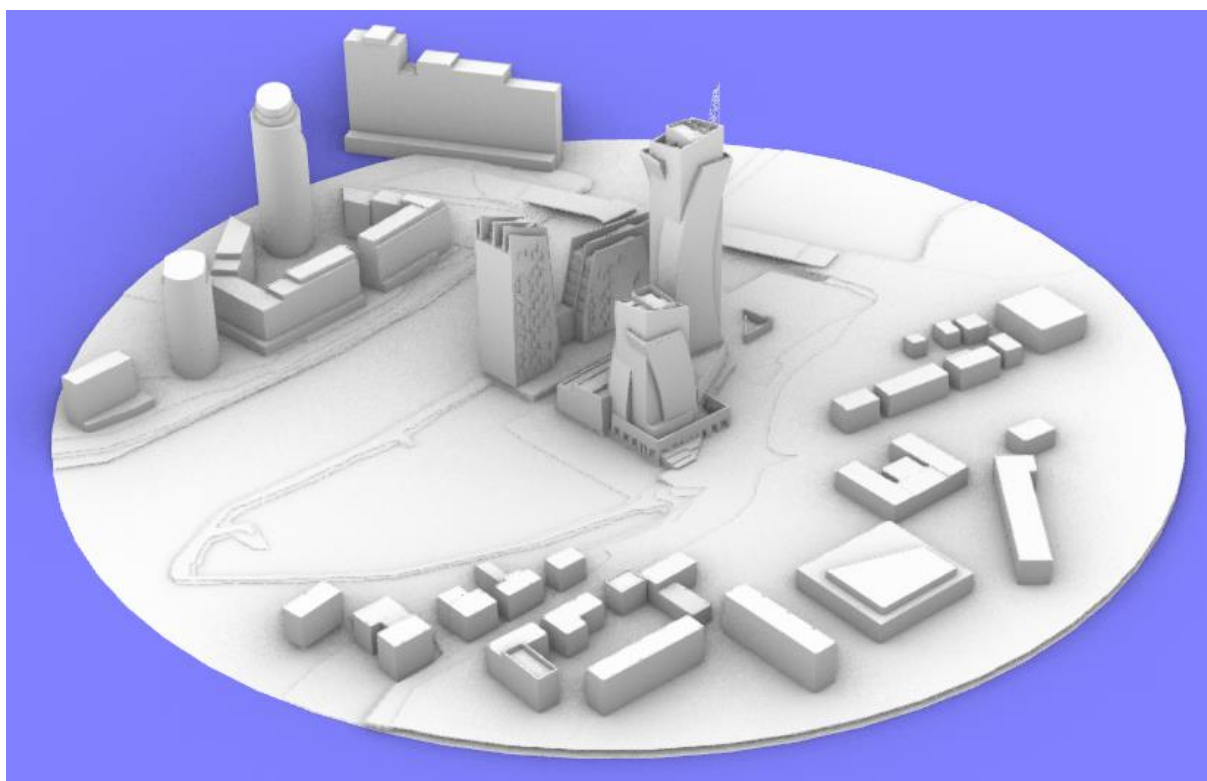

Fig. 4.3. Model #3 used for terrain roughness assignment (location: Rzeszów, Poland)

Fig. 4.4. Model #4 used for terrain roughness assignment (location: Sheffield, United Kingdom)
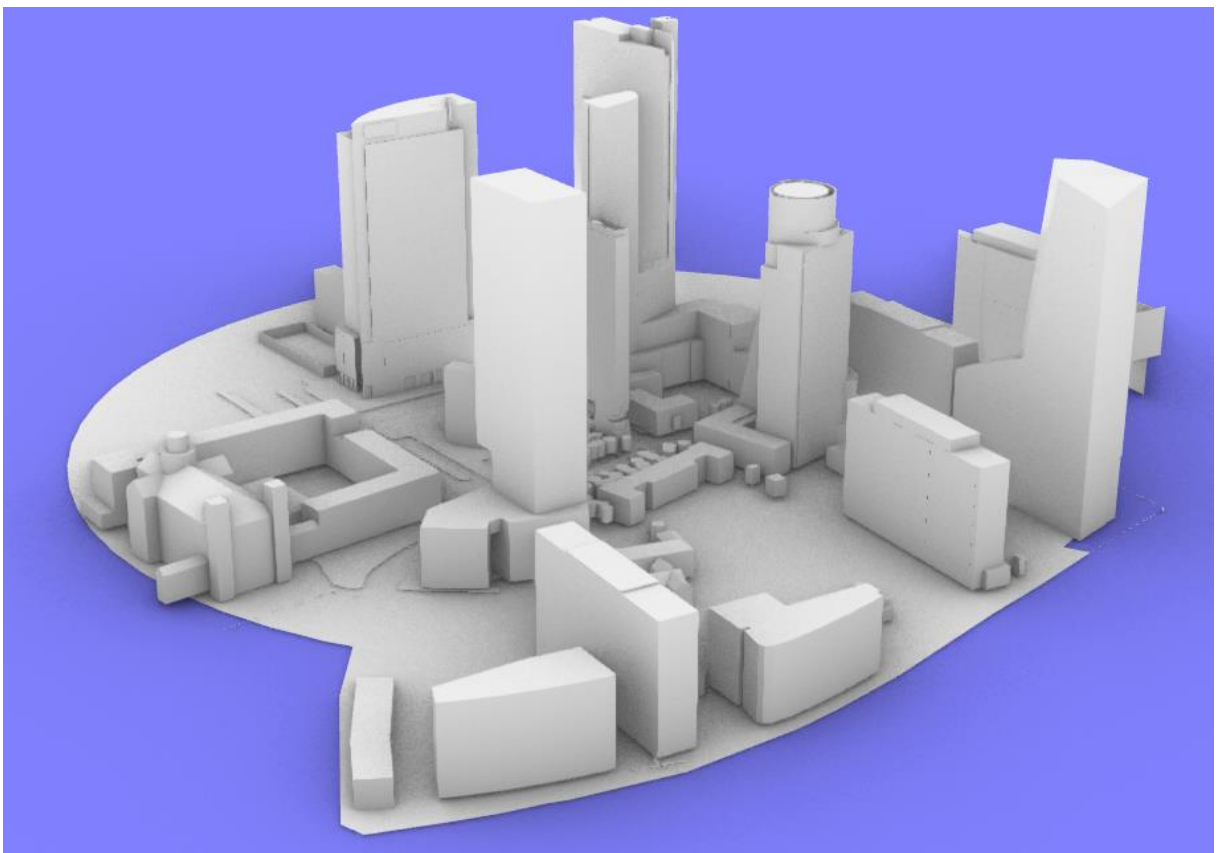

Fig. 4.5. Model #5 used for terrain roughness assignment (location: Warsaw, Poland)

3D modelling program *Rhino* 7 was used for the preparation of the models, calculations of different values used for roughness assignments and rendering of the pictures shown in this chapter. The scale of the models was either 1:250 or 1:300, which also determined the extent of the model perimeter to fit on a 2 m diameter rotational table in the wind tunnel.

The following principles were applied for the selection of the models and the roughness parameters for these calculations:

- The terrain roughness characteristics that should be considered are average roughness height k_r, the boundary layer height δ (or the gradient height z_g), the standard deviation of the roughness σ_r and the ratio of the built-up area $\check{A}_r$. The exact definitions and methods of calculating these parameters are elaborated below. It should be noted that for a given type of terrain, these parameters might not be mutually-independent;
- The models should be located in urban or suburban terrain due to the following reasons: (1) it is the most common location for buildings which require the wind tunnel tests and (2) it is the most convenient and accurate to calculate the roughness parameters based on deterministic irregularities, such as buildings or other engineering structures;
- The elevations of the terrain are not considered in the roughness calculations, as they are not directly involved in the suburban or urban terrain roughness (usually being one or two orders of values lower than the roughness resulting from the building heights) and are covered in most of the standards by another parameter, e.g. orography factor $c_o(z)$ in (PN-EN 1991-1-4, 2011).

Model scales applied during the wind tunnel tests were either 1:300 (model #1) or 1:250 (models #2-#5), which resulted from a compromise between recreating large enough surroundings around the investigated buildings and fitting the model into the working space of the wind tunnel without too high a blockage effect. This resulted in the total areas which were recreated on the rotational table that are taken into account during the calculations.

The first roughness parameter to consider is the mean roughness height k_r, which can be calculated as follows:

$$k_r = \sum_{i=1}^{n} \Omega_i \frac{1}{A_{total}} \tag{4.1}$$

where: Ω_i – volume of the i-th element (e.g. building) located on the model [m^3], A_{total} – total area of the model [m^2], n – total number of protruding elements/objects (e.g. buildings) on the model [-].

Another roughness parameter of the model is the standard deviation of the height of the protruding elements σ_r, which can be defined as:

$$\sigma_r = \sqrt{\frac{1}{A_{total}} \sum_{i=1}^{n} \left(\frac{\Omega_i}{A_i} - k_r \right)^2 A_i} \qquad (4.2)$$

where: A_i – area of the *i*-th element (e.g. building) located on the model [m^2].

It should be noted that the roughness distribution over an area, in particular as diverse as a city, will not be uniform over the whole area of the model, therefore the two roughness parameters introduced in Eq. (4.1) and (4.2) are not exactly the same in any given area of the model. However, it is assumed that when considering the scale of wind flows, it is sufficient for these roughness parameters to be similar over any given e.g. circular area of about 200-250 m radius within the surroundings of the model and along the fetch length, for these parameters to be considered representative for a terrain class.

Another important parameter, not directly related to the roughness, but nevertheless providing important information on the type of terrain, is the ratio of built-up area $\check{A}_r$, which is the ratio of the total area of all buildings, engineering objects, trees, etc. that are protruding over the considered area to the total area. This can be calculated as:

$$\check{A}_r = \sum_{i=1}^{n} A_i \frac{1}{A_{total}} \qquad (4.3)$$

The final parameter to consider is the boundary layer thickness δ (which is equal to the gradient height z_g, but will be further denoted as δ for consistency). The following should be considered when estimating this parameter:

- For a number of terrain roughness types, there are known values of boundary layer thickness δ measured experimentally (comp. Tab. 3.8, Tab. 3.13);
- This parameter cannot be directly calculated, but only estimated based on analysing the roughness of a given area;
- In wind tunnel tests, it is not always necessary (or possible) to simulate the wind profile along the whole height of the boundary layer, usually it is sufficient to properly simulate it 20-30 m above the tallest structure (e.g. building) included in the model.

Therefore, it seems that the most valid approach, in this case, would be to base the value of this parameter on the other codes and suggest a range for each category rather than giving a direct value of the boundary layer height.

The main roughness parameters calculated for the models are summarised in Tab. 4.1. An additional, non-dimensional parameter was derived for the purpose of the model analysis, which is the ratio of the standard deviation to the mean roughness height σ_r / k_r.

Tab. 4.1. Roughness characteristics of the exemplary models (all values given in relation to the real-life scale)

Model	Model scale	Total area A_{total} [m²]	Mean roughness height k_r [m]	Standard deviation σ_r [m]	Ratio of the built-up area $\breve{A}_r$ [-]	Ratio σ_r / k_r [-]
#1	1:300	279 923	14.61	34.56	0.28	2.37
#2	1:250	236 504	6.25	12.52	0.36	2.00
#3	1:250	187 293	3.80	13.27	0.13	3.49
#4	1:250	190 140	7.33	11.03	0.43	1.50
#5	1:250	193 318	12.37	33.99	0.22	2.75

Based on the calculations in the table, the following conclusions can be drawn to be used further in this classification:

- The mean roughness height k_r [m] will be assumed as the main dimensional parameter for the description of each category in the proposed classification. This is the most intuitive parameter for early estimation of the roughness category;
- Instead of the value of the roughness standard deviation, the parameter proposed earlier in the table – the ratio of the standard deviation to the mean roughness height – seems to provide important information that distinguishes the analysed models from each other, therefore it can be adopted as another, 2nd, non-dimensional parameter used for the classification:

$$\breve{\sigma}_r = \frac{\sigma_r}{k_r} \tag{4.4}$$

- The value of boundary layer height δ will be based on the values provided by (ASCE/SEI 7, 2022; ISO 4354, 2009) for power-law profiles and indicate the maximum height where the vertical wind profile description can be valid. Furthermore, another non-dimensional parameter is introduced for informative purposes, which is the ratio of the mean roughness height k_r to the boundary layer height δ:

$$\breve{k}_r = \frac{k_r}{\delta} \tag{4.5}$$

- While practical for this analysis, it can be noticed that the ratio of the built-up area seems to be heavily related to the $\breve{\sigma}_r$, with the relation being inversely proportional. Therefore, it seems reasonable to reduce the parameter $\breve{A}_r$ in the further analysis as directly mutually dependent on the other parameters.

Therefore, the proposed roughness classification will be based on two parameters: mean roughness height k_r [m] and non-dimensional standard deviation of the roughness height $\breve{\sigma}_r$

[-], with the boundary layer height δ (and the non-dimensional ratio $\check{k}_r$) provided as an additional, informative parameter.

4.2. Authorial roughness classification

The following factors were taken into account when deciding on the principles of the proposed classification:

- For the purposes of civil engineering, most objects that require wind tunnel tests are located in areas with higher roughness categories (suburban or urban). Therefore, it seems most rational to expand the classification mostly within these categories;
- Although the shapes and configuration of the elements can have a significant impact on the flow, due to the generalization they are impossible to account for in this classification. Therefore, it is assumed that the roughness type are discontinuous, random or deterministic, irregular protrusions;
- This classification concerns even terrains, with little to no changes in the orography over the considered area. It is a practical simplification which is satisfactory in most cases of simulating urban areas in wind tunnel tests, where sufficiently small terrain elevations are often neglected – however, the more complex terrains require the recreation of ground-level elevations for the wind tunnel tests (comp. Fig. 4.4);
- Terrains with *developed* roughness over a sufficiently large area from the upwind direction are considered in this classification. In the cases of roughness changes, the method proposed in (ISO 4354, 2009) (comp. Fig. 3.5) seems as the most accurate and reliable one. Furthermore, the wind sector, based on the angle of wind attack, should correspond to each of the tested wind directions in the wind tunnel (e.g. in the case of testing 24 wind directions, angular sectors of 15° should be considered);
- For wind tunnel tests and CFD simulations, it is recommended to recreate building details of up to 0.5 m, particularly if located in areas where they can affect the flow (RWDI, 2019). Therefore, the surface roughness of smaller scales (e.g. of materials and elements) is not considered in the classification.

Based on the detailed roughness calculations conducted on the models in subsection 4.1, a classification with a total of 8 different terrain categories is proposed. The lower terrain categories: 0, I and II according to (PN-EN 1991-1-4, 2011) remain practically unchanged in comparison with the standards, while the terrain categories related to forest/suburbs are divided into 2 different categories, and categories related to urban areas are divided into 3 different categories. Most of the values of the considered parameters are given as ranges rather than exact values. Following that approach, the proposed authorial classification that is based on two roughness parameters is presented in Tab. 4.2.

Tab. 4.2 Authorial classification of terrain roughness categories based on two roughness parameters

Roughness category	Description	k_r [m]	$\breve{\sigma}_r$ [-]	δ [m]	$\breve{k}_r$ [-]
0	Open sea, coastal area open to the sea	~0	~0	100-150	~0
I	Lake or area with negligible vegetation, lack of trees or crops and no obstacles	0÷0.5	~0	150-200	0÷0.003
II	Open flat terrain with low vegetation such as grass and rare isolated obstacles	0.5÷1.5	0÷0.1	200-250	0.002÷0.008
III	Forest or suburban area with generally uniform buildings heights	1.5÷5	0.1÷2.2	250-300	0.005÷0.02
IV	Suburban or industrial area with large height differences (isolated tall buildings, chimneys, towers)	1.5÷5	2.2÷5	300÷350	0.004÷0.017
V	Urban area with generally uniform buildings heights and relatively dense development	5÷15	0.1÷2.2	350÷400	0.013÷0.043
VI	Urban area with large height difference (tall buildings), city centre with broad streets	5÷15	2.2÷5	400÷450	0.011÷0.038
VII	Urban area densely covered in buildings, with very tall structures	>15	1÷5	450÷550	~0.03

It should be noted that, although much higher buildings exist, there is no reason to continue with further categories above VII, as they would require proportionally long fetch lengths with similar roughness that would not apply to any actual location in real-life. The proposed terrain category VII covers all the potentially taller/more densely developed city centres.

With the proposed roughness terrain classification (Tab. 4.2), models #1 and #5 (located in Warsaw) are placed in the roughness category VI, models #2 and #4 (located in the United Kingdom) are placed in the roughness category V, and model #3 (located in Rzeszów, on the outskirts of the town) is placed in the roughness category IV. The exact values for each of the proposed roughness parameters could be more precisely calibrated based on the roughness analysis of more areas, however, in the current state, they seem to capture different types of cities and suburban areas, which might have a significant impact on the wind flow

characteristics. Furthermore, they provide precise criteria, by which any given area could be unequivocally classified into exactly one terrain roughness category.

4.3. Potential impact of the proposed roughness categories on wind flow

The further discussion in this chapter will focus on categories III-VII, which are the original aspect of the proposed terrain roughness classification. Based on the information from the literature, analysis of the recommendations of different codes and the author's experience in wind tunnel testing, the following aspects of the wind flow will distinguish these categories from each other:

- Vertical mean wind speed profiles – it is to be expected that three different types of wind profiles would be distinguishable between these categories – one for suburban terrain categories III and IV, one for urban terrain categories V and VI and the last one for the VII terrain category that covers large cities. The differences between the wind profiles for categories III and IV and for categories V and VI are expected to be smaller and mostly resulting from the different endpoint of each profile (different gradient height z_g) rather than from different steepness of the curve;
- Vertical turbulence intensity profiles – the largest differences between categories III and IV, and categories V and VI, are expected in this field. This is due to having different types of turbulence-generating elements or, if applying the parametric description, different values of the roughness height standard deviation (in comparison with the mean roughness height). Therefore, it would be reasonable to introduce different parameters for power-law and logarithmic turbulence intensity profiles that would reflect these changes, even if the α exponent and the roughness length z_0 for the vertical mean wind speed profiles are similar;
- Turbulence length scales and vorticity – similar to the turbulence intensity, different types of vortex shedding (dominating vortices in the vertical plane for categories III and V compared to potential large vortices in the horizontal plane for categories IV and VI) are expected. This would result in different height distributions of the correlations, in particular, it can be expected that the longitudinal correlation would be higher for categories III and V, and their increase with height would be steeper than in categories IV and VI. In category VII, it can be expected that the strong aerodynamic interference would heavily distort the curve that describes the vertical change in the turbulence length scales.

For the purpose of wind tunnel simulation at the Wind Engineering Laboratory of the Cracow University of Technology, a calculation similar to the one conducted for the models (Tab. 4.1) was performed for the elevated blocks, which are the main turbulence-generating elements at the inlet and over the fetch length in the working section of the wind tunnel. The results are shown in Tab. 4.3.

Tab. 4.3. Roughness characteristics of the elevated blocks at the wind tunnel of the Wind Engineering Laboratory of the Cracow University of Technology

Type and height of blocks	Total area A_{total} [cm²]	Mean roughness height k_r [cm]	Standard deviation σ_r [cm]	Ratio of the built-up area $\breve{A}_r$ [-]	$\breve{\sigma}_r$ [-]
Inlet, 5 cm	36720	0.22	1.01	0.044	4.53
Fetch, 5 cm	121920	0.19	0.95	0.039	4.88
Inlet, 10 cm	36720	0.44	2.02	0.044	4.53
Fetch, 10 cm	121920	0.39	1.89	0.039	4.88
Inlet, 15 cm	36720	0.67	3.02	0.044	4.53
Fetch, 15 cm	121920	0.58	2.84	0.039	4.88
Inlet, 20 cm	36720	0.89	4.03	0.044	4.53
Fetch, 20 cm	121920	0.78	3.79	0.039	4.88

Translated for the adopted model scale of 1:250, the mean roughness heights k_r would be between 0.49 m and 2.22 m, while the standard deviations σ_r between 2.37 m and 10.08 m. Therefore, the values of the roughness parameters do not correspond at all to the values calculated for real-life locations. The ratios of built-up area (which in this case are the working section areas covered with blocks) are about one order of magnitude smaller than the ones for the real-life locations in suburban and urban terrains. The mean roughness heights k_r are also much smaller (about one order of magnitude in the case of mean roughness heights). On the other hand, the values of the ratio of the standard deviation of the roughness height to the mean roughness height are significant at about 4.5-5.

Based on the above, it can be stated that for the wind flow simulation in the wind tunnel at the Wind Engineering Laboratory of the Cracow University of Technology, it is impossible to simply assume similar roughness parameters to the real-life model on the blocks. Therefore, for a proper simulation, additional turbulence-generating elements – such as spires, barriers or turbulising net described in subsection 3.3 – are required to artificially achieve wind flow characteristics similar to what can be expected in the real-life scale rather than relying on direct recreation of the surface roughness. Different combinations of spires, barriers, turbulising net and blocks' elevations at the inlet and along the fetch length, together with their effects on various wind flow characteristics, are investigated further within this work.

5. Wind tunnel simulations of different boundary layer types

This chapter describes in detail the wind tunnel tests conducted to empirically find the best configurations of turbulising elements that generate wind flow conditions corresponding to the nature for different terrain roughness categories. Furthermore, the scope of the tests will allow for an in-depth analysis of the effect of each turbulising element on a variety of wind flow characteristics.

5.1. Experimental setup

5.1.1. The wind tunnel

The experiments were conducted in the wind tunnel of the Wind Engineering Laboratory of the Cracow University of Technology. It is a wind tunnel of a mixed circuit, either closed, when the throttles are closed and the air flowing out of the tunnel through the outlet is directed to the return channel above the working section and then to the beginning of the tunnel or open, when the airflow enters from outside the building through an air scoop and is exhausted after exiting the outlet by an air launcher. In the case of these experiments, the closed circuit was utilised, as is with most of the regular wind tunnel tests. The top and side views of the wind tunnel are shown in Fig. 5.1.
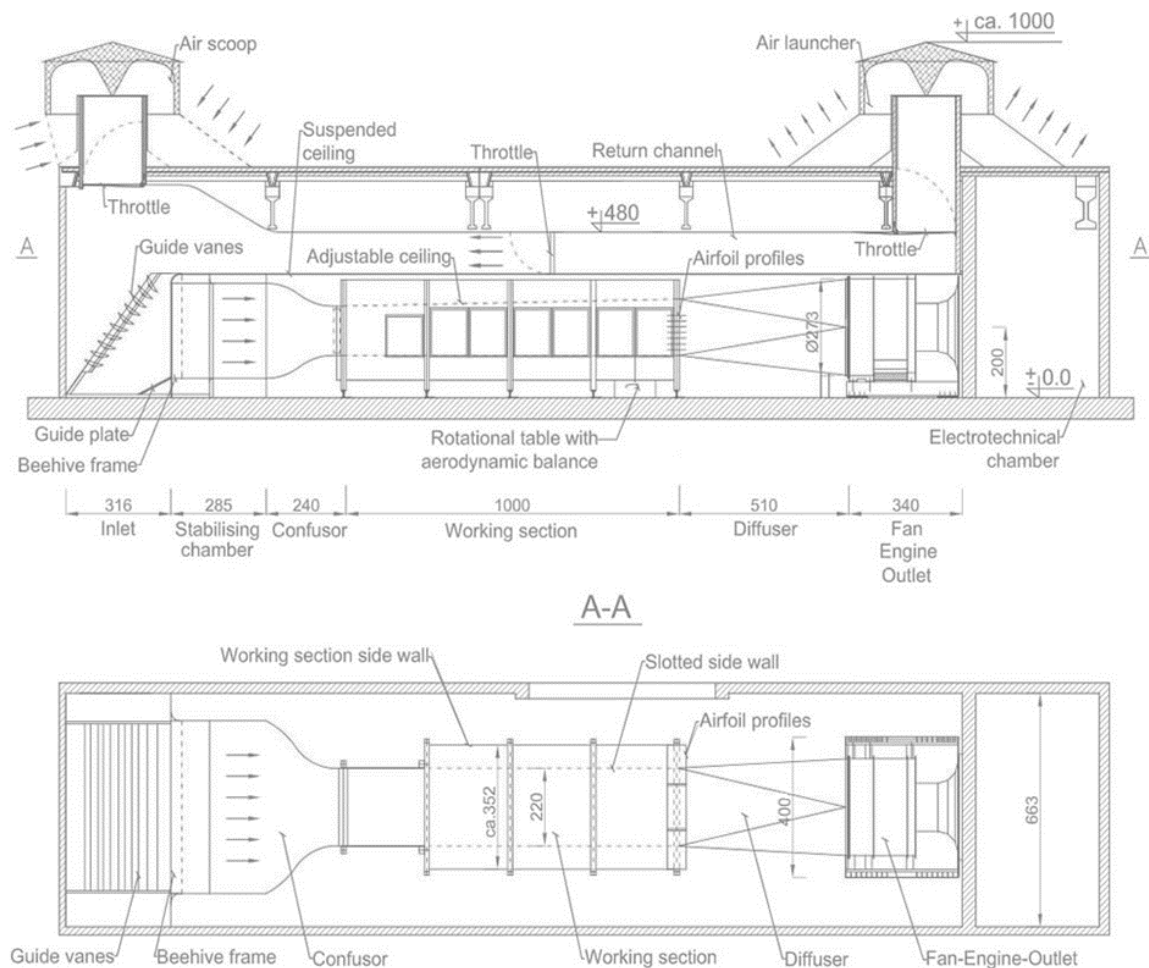
Fig. 5.1. Top and side views of the wind tunnel (all dimensions in [cm])

The basic dimensions of the working section are:

- Width: 2.20 m between the slotted walls (3.40 m between the full sidewalls, including the compensational chambers at the sides);
- Height: between 1.40 m at the beginning and 1.60 m at the end of the working section, adjustable along the length of the working section between these values throughout several segments continuously connected by joints;
- Length: 10 m (working section), divided into 4 characteristic segments of 2.5 m each.

The fan which generates the airflow inside the wind tunnel is located at the end of the suction side of the facility. It has an outer diameter of 2.72 m, single-stage efficiency of 0.8-0.9 and the top speed of the end of the blade can reach 100 m/s. The fan is powered by the engine of an alternate current with a power of 200 kW and supply voltage of 220 V, controlled by the inverter. The nominal revolution of the fan is 750 rpm and the maximum wind speed attainable inside the working section is 40 m/s.
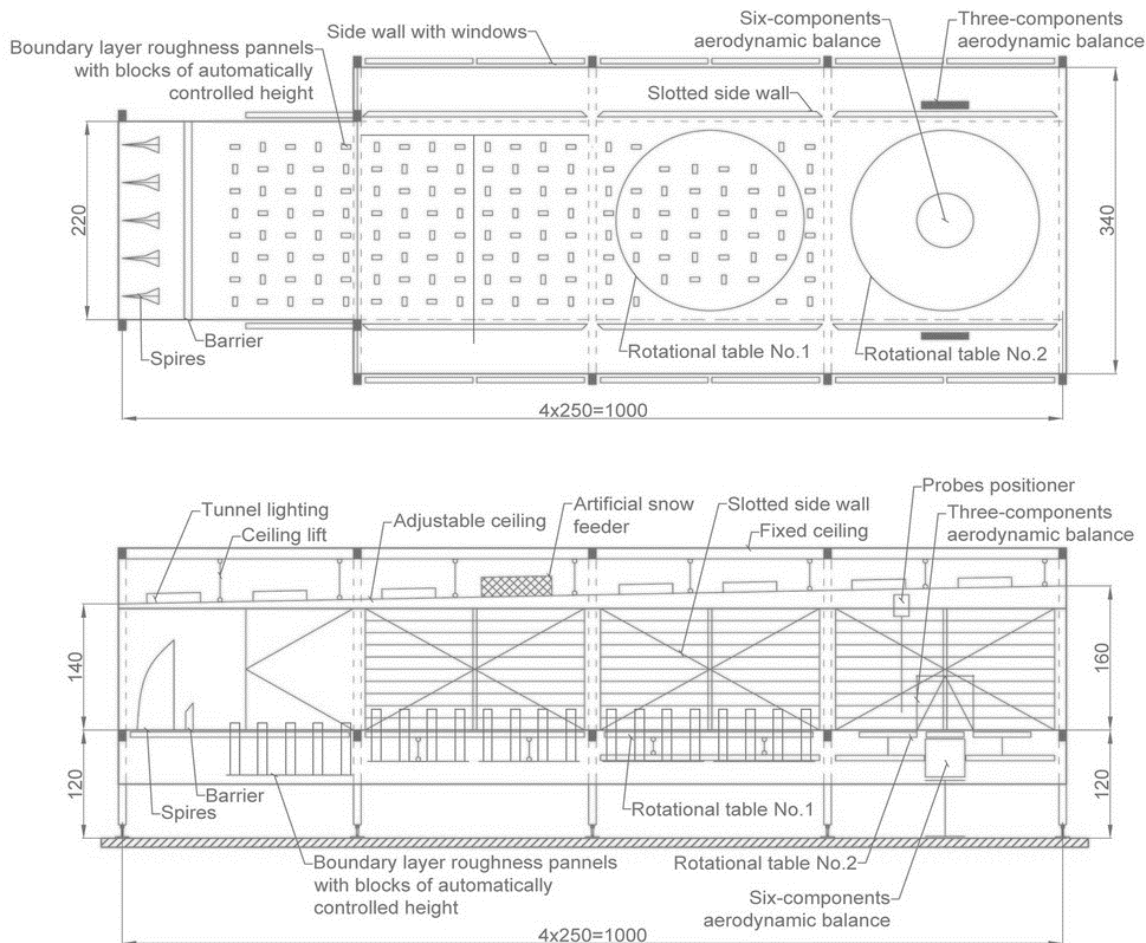
Fig. 5.2. Top and side views of the wind tunnel working section (all dimensions in [cm])

Before reaching the working section, the airflow passes through guide vanes that redirect the inflow from the return channel, the beehive frame that helps make the flow uniform, the stabilisation chamber and the confusor, an element with a narrowing rectangular cross-section which increases the wind speed while reducing the pressure. The main purpose of these

elements is to provide a uniform inflow at the inlet of the tunnel, where it will be reshaped through the addition of turbulising elements.

The working section ends with a cascade of horizontal airfoil profiles that reduce the influence of vortices generated by the fan on the airflow around the rotational table located at the last segment of the working section. This table is mainly used for the tests regarding wind action on buildings, wind turbines or other objects tested in the wind tunnel. The top and side views of the working section are shown in Fig. 5.2.

5.1.2. Measuring system

Wind flow parameters, such as vertical wind profile, can be obtained either by directly measuring the flow velocity (e.g. with hot-wire anemometers) or through pressure measurements, which in turn can be relatively easily translated into flow velocity values. While both of these approaches have their advantages and disadvantages, which are strongly influenced by parameters such as the range of measured wind speeds or turbulence intensity levels, the measurement of wind pressures was selected as the best option for these experiments.

Fig. 5.3. *DTC Initium* data acquisition system with miniature pressure scanners *DTC ESP*-64*HD*

This was done with a multichannel differential miniature pressure scanner *DTC ESP*-64*HD* (TE Connectivity, 2021) connected to the *DTC Initium* data acquisition system (TE Connectivity, 2017) (Fig. 5.3). It allows for direct measurement of the total pressure at a given point, then automatically subtracts the global value of static pressure to obtain the value of dynamic pressure. The scanner is connected through silicon tubes of 1 mm in diameter to a *Dwyer* model 167-12-CF Pitot-static tube, which also provides the static pressure input to the scanner, and 11 additional Pitot tubes 0.8 mm in diameter installed at different elevations. Analogue voltage signals from the scanners are subsequently collected with the *DTC Initium Utility Software* system. The most important specifications of the scanner and the data acquisition system are given in Tab. 5.1. The scheme of the measurement configuration is shown in Fig. 5.4.

Tab. 5.1. Declared specifications of *DTC Initium* data acquisition system and *DTC ESP-64HD* pressure scanners (TE Connectivity, 2017, 2021)

DTC Initium		
Parameter	**Value**	**Unit**
Static accuracy (after re-zero)	±0.1	[%Full Scale]
Total thermal error	±0.004	[%FS/°C]
Measurement resolution	0.003	[%FS]
Supply voltage	18 to 36	[VDC]
Supply current	0.8 to 1.6	[A]
Operating temperature	0 to 70	[°C]
DTC ESP-64HD		
Parameter	**Value**	**Unit**
Number of pressure inputs	64	[–]
Pressure range (full scale)	±20	[inH$_2$O]
Proof pressure	400	[%FS]
Static accuracy (after re-zero)	±0.06	[%FS]
Total thermal stability	±0.004	[%FS]
Operating temperature	-25 to 80	[°C]
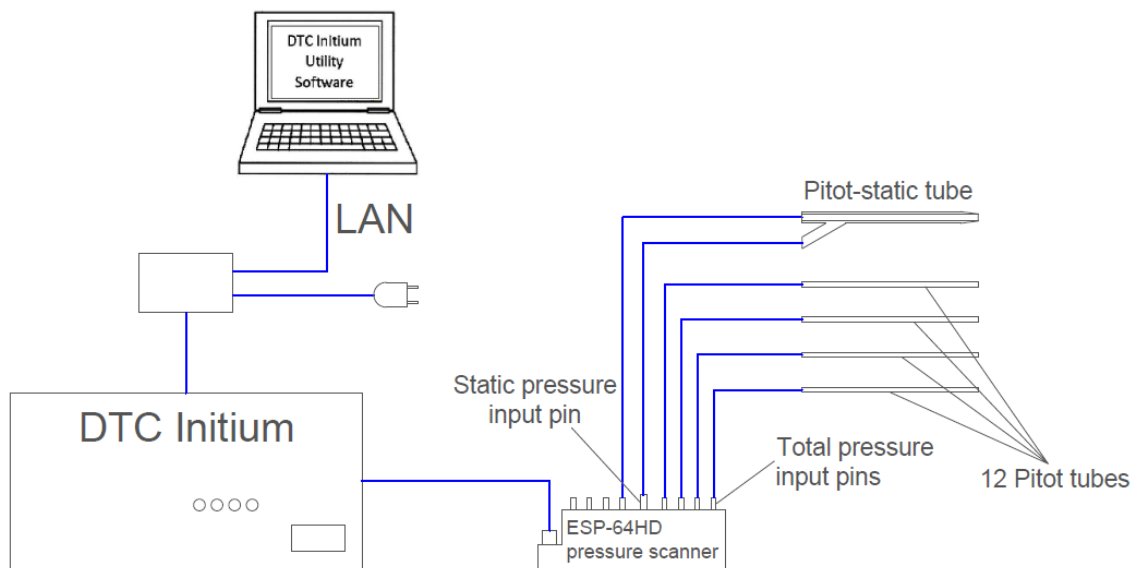
Fig. 5.4. The scheme of measurement line for the pressure scanner system

5.1.3. Measurement setup and conditions

Every measurement conducted in the wind tunnel results in 15 000 samples for each point (60 seconds measurement with a sampling frequency of 250 Hz). During the tests, the reference wind speed inside the wind tunnel was maintained at a level corresponding to about 12-12.5 m/s at a height of 60 cm above the floor in an empty working section. The ceiling height was between 142 cm at the inlet and 152 cm at the end of the working section, with a steady curve of inclination along the length.

The measurements were taken at elevations between 7 and 62 cm above the floor, with an increment of 5 cm. The Pitot-static tube, used for the reference velocity, was mounted at the highest level. The stand used for measurements was located in the central longitudinal cross-section of the wind tunnel, at the 2nd rotational table according to the findings of (Kłaput, 2020). This configuration is presented in Fig. 5.5.
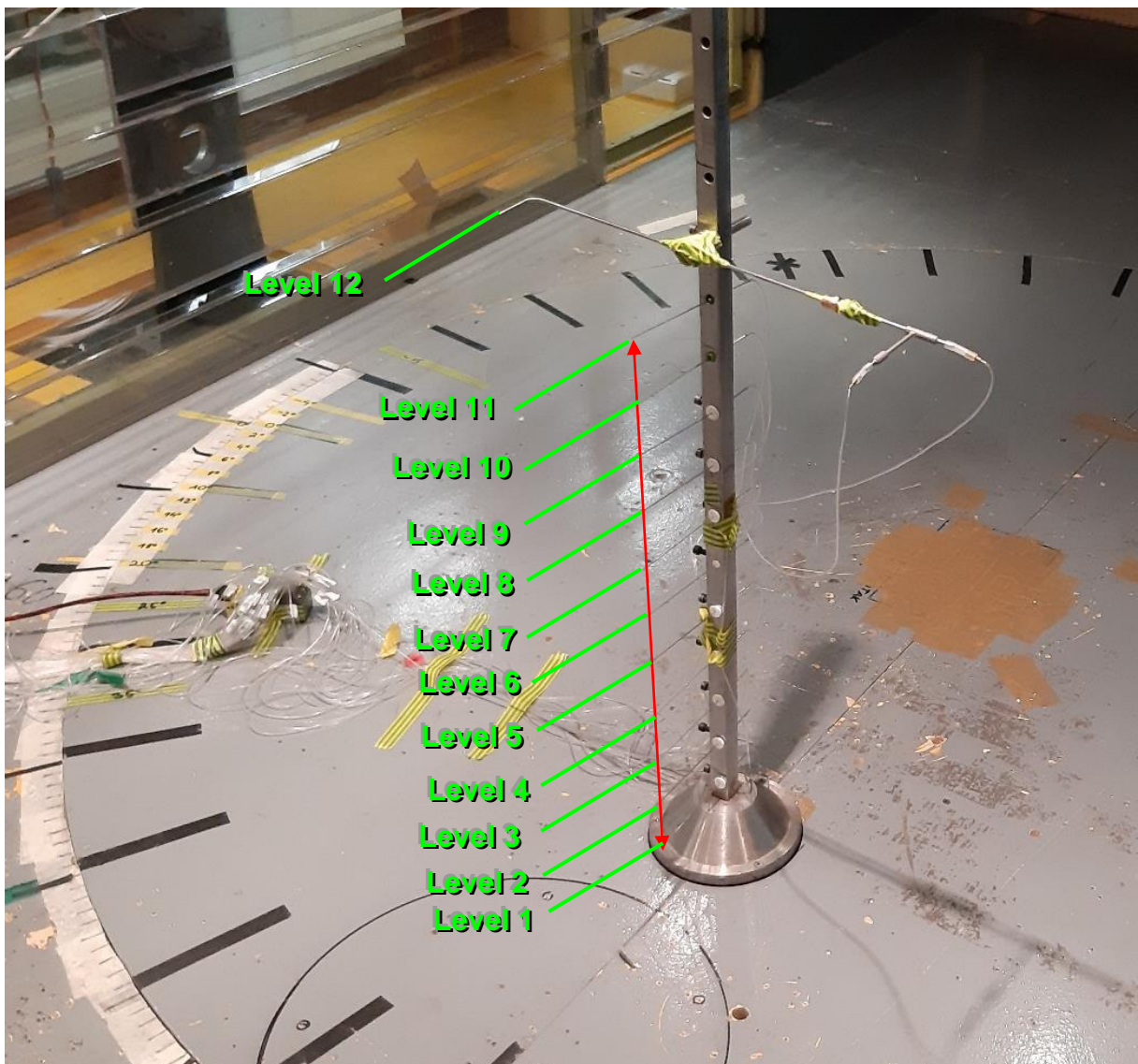
Fig. 5.5. Measurement setup (Pitot-static tube and 11 Pitot tubes on a stand) as implemented during the wind tunnel tests

5.1.4. Measurement accuracy assessment

The following sources of inaccuracies in the pressure measurements can be identified:

- Errors related to the static accuracy of the measuring system;
- Thermal errors of the measuring system;
- Errors resulting from the length of the silicone tubes and their connections.

The static accuracy of the system is the largest value taken from both its components (as these errors do not sum), which in this case is 0.1% Full Scale error of the *DTC Initium* system. This parameter includes the combined errors due to non-linearity (maximum deviation of the output curve from a specified straight line on the plot of the relationship between the input/sensed parameter and the output), hysteresis (the maximum difference in output at any pressure value within the specified range, when the value is approached increasing and decreasing pressure) and non-repeatability (the ability of a transducer to reproduce output readings when the same pressure value is applied to it consecutively, under the same conditions and from the same direction) (Lish, 2016). This value is provided in relation to the "Full Scale", which is the total range of pressure. In the case of the pressure sensor used in the tests, this range is equal to 20 inches water column, thus the declared static accuracy is about 5 Pa. This is a relatively high value compared to the dynamic wind pressures registered in a wind tunnel, however, it should be noted that this is the total band error, which refers to the *worst case error* that is very rarely met in actual measurements. To evaluate the error values that can be expected in the actual measurements, an accuracy demonstration test was run, which enabled the assessment of the mean value and standard deviation of the error. The results are presented in Fig. 5.6.

CRS	RSSPP	P_avg	Avg Error	PerCent-FS	bad-chnls
111	101	-0.05392	-0.05392	-0.00108	
111	102	-0.12263	-0.12263	-0.00245	
111	103	-0.15353	-0.15353	-0.00307	
111	104	-0.09699	-0.09699	-0.00194	
111	105	-0.21666	-0.21666	-0.00433	
111	106	-0.25545	-0.25545	-0.00511	
111	107	-0.00427	-0.00427	-0.00009	
111	108	-0.14992	-0.14992	-0.00300	
111	109	-0.12066	-0.12066	-0.00241	
111	110	-0.00033	-0.00033	-0.00001	
111	111	-0.13775	-0.13775	-0.00276	
111	112	-0.18181	-0.18181	-0.00364	

Mean Error - px and % FS	Accuracy Spec.	Pass Count	Fail Count
- 0.11466 (eu) or - 0.00229 %FS	.1	128	0

Statistical Data

```
std dev of error =  0.10155
99 percent confidence level =  0.30464

Std Dev as a percent of full scale =  0.00203
```

Fig. 5.6. Accuracy demonstration for the miniature pressure scanners *DTC ESP*-64*HD* used in the tests

The statistics shown refer to all of the 128 pressure channels over the two miniature scanners tested. In the case of these tests, only the 12 channels from one scanner were used, for which the data is explicitly given in Fig. 5.6. Considering only these channels, the obtained mean static accuracy is 0.124 Pa (or 0.002% Full Scale), the maximal error is 0.255 Pa (0.005% Full Scale) and the standard deviation of the error is 0.074 Pa (0.001% Full Scale). These values can be considered highly precise for the conducted wind tunnel tests.

The thermal errors of the system are significantly reduced by the Digital Temperature Compensation (DTC) feature. This method measures the temperature of each pressure sensor and transmits this information to the data acquisition system, where it is compensated in real time against the calibration data. This reduces thermal errors by a factor of 20 in comparison with conventional pressure scanners and results in negligible thermal errors over the range of actual operating temperature in the wind tunnel.

The last group of measurement errors is related to the silicone tubes that connect the sensors with Pitot tubes. While it can be stated that the Pitot tubes are sufficiently long, so that the proximity of the stand on which they are mounted does not affect the measurement, the length and cross-section diameter of the tubes as well as their connections may result in measurement errors. In general, it is advisable to use tubes shorter than 40 cm for the best accuracy. Kłaput et al. (2021) made a thorough evaluation of measurement error with different tube diameters (1 mm and 3 mm), lengths (ranges of 20-50 cm and 120-150 cm) and connectors. The results showed that the influence of the connectors is negligible and tubes of 1 mm diameter result in much better accuracy than tubes of 3 mm diameter. While the longer length of the tubes did have a deteriorating impact on the measurement error, it was mostly observed in suction areas, whereas the effect on the windward part was very small. Considering that in the case of the tests conducted in this work, only positive values of pressure are measured, the effect of the length of the tubes can also be considered negligible.

5.2. Similarity scales adopted in the wind tunnel tests

For the results of this work to be comparable with the literature and feasible for practical application in the future, the model scales have to be determined to fulfil certain constraints. While wider-known similarity criteria such as the Reynolds number defined in Eq. (3.70) might have a crucial impact on certain wind tunnel tests (e.g. wind flow around circular/cylindrical objects with no clear points of boundary layer separation or aeroelastic tests of the building's vibrations), they are not necessarily important in this research and therefore do not have to be fulfilled. However, it is important to set the similarity scales regarding the model geometry, wind velocity, time and frequency to properly model the desired wind flow characteristics.

Firstly, the geometrical scale is required to adhere to the following conditions:

1) The model has to be large enough to allow for the recreation of details of about 30-50 cm in a real-life scale and the installation of pressure taps with sufficiently dense distribution on the external surfaces of the model.
2) The blockage ratio should be relatively low in order not to distort the flow and affect the measurements. A value of 10% blockage ratio is generally adopted as acceptable

in the wind tunnel of the Wind Engineering Laboratory of Cracow University of Technology (A. Flaga, 2008; Kłaput, 2020).

3) The model has to recreate an area of at least a δ radius around the point of interest, where δ is the boundary layer thickness. According to the analysis of different terrain roughness (ISO 4354, 2009; PN-EN 1991-1-4, 2011), this is about 200-300 m.

The works conducted thus far in the wind tunnel of the Wind Engineering Laboratory of Cracow University of Technology have proven the scales of 1:250 and 1:300 to be the most suitable in the cases regarding wind action on buildings, hence the geometrical scale is adopted as:

$$k_L = 1:250 = 0.004 \tag{5.1}$$

Subsequently, the velocity scale and the time scale (and also the frequency scale, which is the inversion of the time scale) are dependent on each other based on the adopted geometrical scale. Furthermore, they should fulfil the following requirements:

1) The time of the measurement should correspond in a real-life scale to at least 10 minutes, which is the usual averaging time on meteorological stations (Żurański, 1978). Moreover, the data for mean wind speed is taken from several measurement 'blocks', each of 10 minutes, therefore the longer real-life counterpart of the measurement time is generally more desired for statistical purposes (Teunissen, 1980).
2) The sampling frequency should be high enough (in relation to the frequency scale) so that the Nyquist frequency is higher than the maximum frequency of gusts relevant to the tests. According to (A. Flaga, 2008), in the case of wind action on buildings, this is about 1 Hz.
3) Most of the wind tunnel tests are conducted with a focus on strong winds, which are winds with speeds of about 10-12 m/s or higher. Therefore, the wind speed, after scaling to real life, should be in this range. As this is done to recreate a mean wind speed in nature, the value should be no higher than about 40 m/s. Within this range, the applied criteria for wind flow description (such as vertical profiles) are valid.
4) The actual wind speed used during the wind tunnel tests should be in the most accurate range of the measuring devices and, naturally, no higher than the top speed obtainable in the wind tunnel itself.

The governing equation between the three main model scales used in this work is:

$$k_v = \frac{k_L}{k_t} \tag{5.2}$$

where: k_v – velocity scale and k_t – time scale.

To fulfil the conditions listed above, the velocity scale was adopted as:

$$k_v = 1:2 = 0.5 \tag{5.3}$$

This resulted in the wind speed used in the wind tunnel tests corresponding to 24-25 m/s in a real-life scale (at the reference height), which matches the range of characteristic wind speeds

according to (PN-EN 1991-1-4, 2011) that would usually act on tall buildings in Poland. Furthermore, the following relationships are implied:

$$k_t = \frac{k_L}{k_v} = 1:125 = 0.008; \; k_f = \frac{1}{k_t} = 125 \qquad (5.4)$$

where k_f – frequency scale.
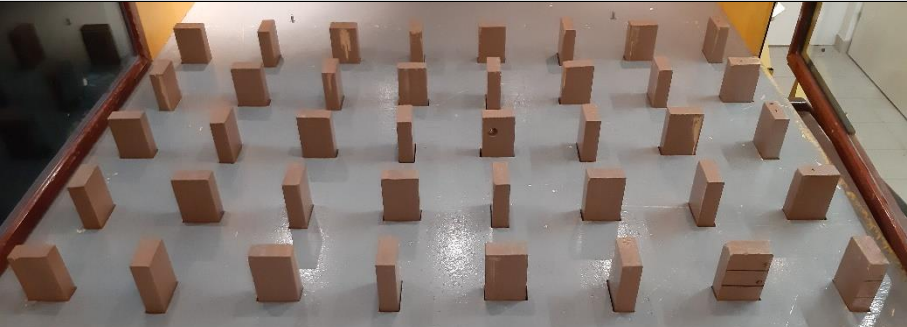
This results in the measurement time corresponding to 7 500 seconds in a real-life scale, which is equal to 125 minutes. This provides about 12 blocks of measurement data (10 minutes each). The sampling frequency corresponds to 2 Hz, hence the Nyquist frequency is equal to 1 Hz, which is the threshold value for wind action on structures. Consequently, all the aforementioned conditions are fulfilled.
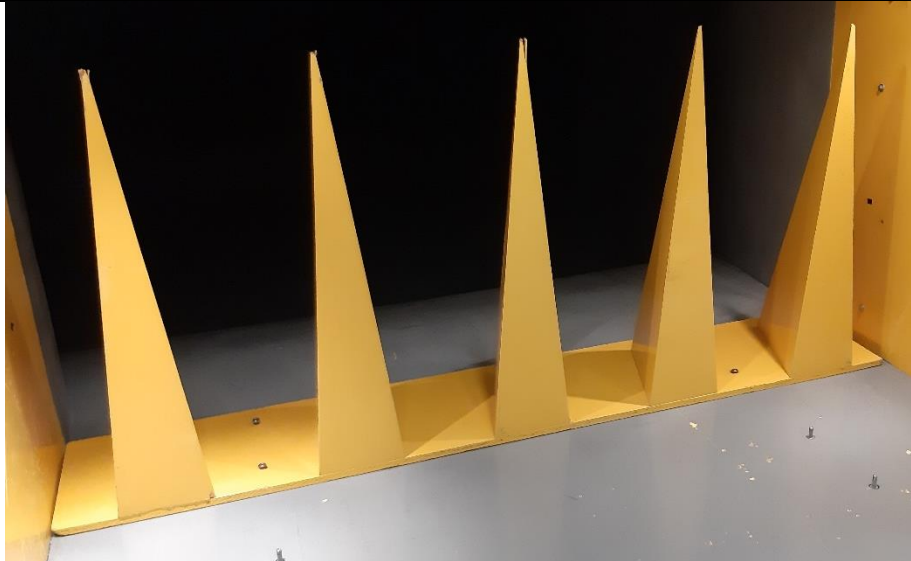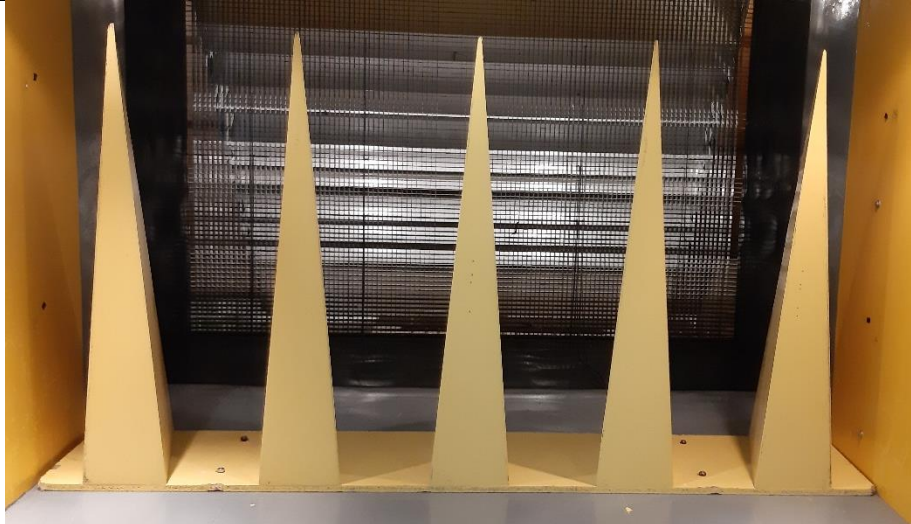
5.3. Summary of the test cases

A total of 295 cases have been tested, each utilising different types and dimensions of turbulising elements. The cases are summarised in detail in the attached *Excel* spreadsheet **Results.xlsx**. In this spreadsheet, *turbulising net* refers to the metal grating mounted at the inlet, *spires* refer to a set of 5 pyramidal elements of a certain height, mounted to a single baseplate and fixed at the inlet, *barrier* refers to a lower longitudinal element either in the shape of a rectangle or triangular prongs that is mounted in front of the spires and *blocks* refer to the 3 segments of elevating cuboidal elements, either at the inlet (1st segment) or at the working section (2nd and 3rd segments). The images of all different types of elements that were used in the tests are presented in Tab. 5.2.

Cases 1-1 to 1-25 were conducted without any spires or barriers. Cases 2-1 to 2-75 were conducted with the spires of 80 cm height, including cases 2-1 to 2-25 without any barrier, cases 2-26 to 2-50 with triangular prongs barrier and cases 2-51 to 2-75 with a rectangular barrier. Cases 2-76 to 2-150 were conducted with the spires of 100 cm height, including cases 2-76 to 2-100 with a rectangular barrier, cases 2-101 to 2-125 without any barrier and cases 2-126 to 2-150 with triangular prongs barrier. Cases 3-1 to 3-75 were conducted with the spires of 120 cm height, including cases 3-1 to 3-25 with triangular prongs barrier, cases 3-26 to 3-50 without any barrier and cases 3-51 to 3-75 with a rectangular barrier. Cases 3-96 to 3-120 were conducted with the turbulising net and neither spires nor barriers. The blocks at each of the sections (the inlet or the fetch length) were raised at either 0, 5, 10, 15 or 25 cm, which in total gives 25 combinations for each setup of spires, barriers and turbulising net used. Additionally, cases 3-76 to 3-95 were conducted with the spires of 120 cm in a backwards arrangement, either without any barrier (cases 3-76 to 3-85) or with the triangular prongs barrier (cases 3-86 to 3-95). These cases utilised fewer combinations of blocks at the inlet and at the fetch length, in which the blocks at the fetch length were always at the same or higher elevation level as the blocks at the inlet.

Tab. 5.2. Turbulising elements used in the tests

Name of the element	Picture
Blocks at the inlet	
Blocks at the fetch length	
Barrier, rectangular	
Barrier, triangular prongs	

Name of the element	Picture
Spires, 80 cm	
Spires, 100 cm	
Spires, 120 cm	

Name of the element	Picture
Turbulising net (bars/patches)	

5.4.   Data obtained from the tests

PSI Utility, a dedicated software for the pressure scanners' data acquisition, was used to save the data. A total of 295 files in CSV (*comma separated values*) format have been acquired, named CASE-X-Y.CSV, where X and Y are the case numbers. The files also include auxiliary data, such as the time of the measurement, the temperature at each scanner and additional scanner data. The probes used for measurements were connected to ports 1-12, from bottom to top. The pressure time series for each of the points is in the columns AC-AN, between rows 4-15 003.

6. Method applied for the results processing

This chapter of the work presents the method applied for obtaining the wind flow characteristics from the measurements and discusses their processing in detail. Furthermore, it also presents the method used for selecting the test cases that are the most suitable for simulating different terrain categories.

6.1. MATLAB subroutine for data processing

A subroutine for data processing was written using *MATLAB* 2022b to allow for automated calculation, saving the results into an *Excel* spreadsheet and generating figures into PDF files that would be easy to analyse and incorporate in the work. The subroutine was prepared in such a way that besides being tailored for the specific experimental setup of these tests, it can be also easily adapted in the future for general wind tunnel tests, with different sampling frequencies, numbers of measurement points or times of measurements. The complete subroutine is attached to the thesis within the file *Windflow.m*, the detailed description of the used functions can be found below.

6.1.1. Loading the data

The first subsection of the file – *Input data* – requires the user to fill in the basic data about the tests, such as the number of measurement points, their heights and positions on the pressure scanner, the location of the reference velocity point, measurement time and sampling frequency, and model length and velocity scales. Furthermore, in this subsection, the case number is defined. The whole subroutine was scripted as an outer function that would be called from another file to allow for automated processing of the results of all of the test cases in a single run. This is the only subsection that should be manipulated in any way by the user. The second subsection – *Basic parameters* – contains some basic wind flow equations and constants that are referred to throughout the rest of the programme's run. The code for these 2 subsections is included in Fig. 6.1.

```
%% INPUT DATA
day=xxx; %day of tests
cn=yyy; %tested case

n=12; %number of measurement points
plot_colours=zeros(n,3); %plot colours
for i=1:n
    plot_colours(i,:)=[(i/n)^2,i/n,1/i];
end
fs=250; %[Hz] - sampling frequency
Tm=60; %[s] - measurement time
scanners=[1 2 3 4 5 6 7 8 9 10 11 12]; %connected pressure scanners
k_L=1/250; %geometrical scale
Mheights=[0.07 0.12 0.17 0.22 0.27 0.32 0.37 0.42 0.47 0.52 0.57 0.62];↙
%measurement heights in the model scale
n_ref=n; %reference height/velocity, the highest probe by default
k_v=1/2; %velocity scale

%% BASIC PARAMETERS
ro=1.225; %[kg/m^3] - air density
m=fs*Tm; %number of samples
ts=1/fs; %time step
```

```
Pheights=Mheights/k_L; %wind profile heights in real-life scale
Zref=Pheights(n_ref); %reference height in real-life scale
time_=(ts:ts:Tm); %vector of time steps
NpWelch=2^nextpow2(m)/8; %number of points for discrete Fourier transform in the✓
%Welch spectral analysis
k_t=k_L/k_v; %time scale
k_f=1/k_t; %frequency scale
```

Fig. 6.1. *MATLAB* code for the subsections *Input data* and *Basic parameters*

The pressure data is loaded in the next subsection through the command *xlsread* to directly import the data from the CSV file created during the measurement. The data is then analysed for any negative pressure values that could be the result of the scanners being shielded by some of the roughness-generating elements (elevated blocks). A warning is issued if any negative values are found and in such a case, these values are replaced with zeros to mitigate their impact on the results. This part of the subroutine ends with plotting the graphs of each of the raw wind pressure signals. The code for this subsection is shown in Fig. 6.2.

```
%% LOADING AND VALIDATION OF THE DATA
disp(['Calculations for CASE-' num2str(day) '-' num2str(cn)])
data_raw=xlsread(['CASE-' num2str(day) '-' num2str(cn) '.CSV']);
pressures_th=zeros(m,n);
for i=1:m
    for j=1:n
        pressures_th(i,j)=data_raw(3+i,27+scanners(j));
    end
end

pressures_check=0;
for i=1:m
    for j=1:n
        if pressures_th(i,j)<0
            pressures_check=pressures_check+1;
        else
            pressures_check;
        end
    end
end
if pressures_check>0 && pressures_check<2
    disp('There is a single negative pressure value in the measurement.')
elseif pressures_check>=2 && pressures_check<5
    disp(['There are ' num2str(pressures_check) ' negative pressure values in the✓
measurement.'])
elseif pressures_check>=5
    disp(['WARNING: there are ' num2str(pressures_check) ' negative pressure✓
values in the measurement.'])
else
    disp('The measurement is correct - no negative pressure values.')
end
```

Fig. 6.2. MATLAB code for the subsection *Loading and validation of the data*

6.1.2. Data filtering

Before proceeding with the more specific operations on the data, it is filtered through a lowpass Chebyshev Type I filter with a passband frequency set at 120 Hz and stopband frequency set at 125 Hz (which is the Nyquist frequency for the base signal sampled at 250 Hz). A total of 4 different additional filters were tested (other IIR filters: Butterworth and *MATLAB* default lowpass filter and FIR filters: two variants of equiripple filter), before the decision was made on the Chebyshev Type I filter, based on the results they yielded and the literature (MATLAB Help Center, 2022c). The code for the filter is shown in Fig. 6.3 and the filter design in Fig. 6.4.

```
%% DATA FILTERING
Fpass=0.48*fs;    %Passband Frequency [Hz]
Fstop=0.5*fs;    %Stopband Frequency [Hz]
Apass=0.1;           %Passband Ripple [dB]
Astop=80;          %Stopband Attenuation [dB]
match='passband'; %Band to match exactly
Chebyshev1_filter=fdesign.lowpass(Fpass,Fstop,Apass,Astop,fs);
Signal_Filter=design(Chebyshev1_filter,'cheby1','MatchExactly',match); %Chebyshev↙
%I filter
pressures_filt=filter(Signal_Filter,pressures_th); %filtering of pressure time↙
%series
```

Fig. 6.3. *MATLAB* code for the subsection *Data filtering*
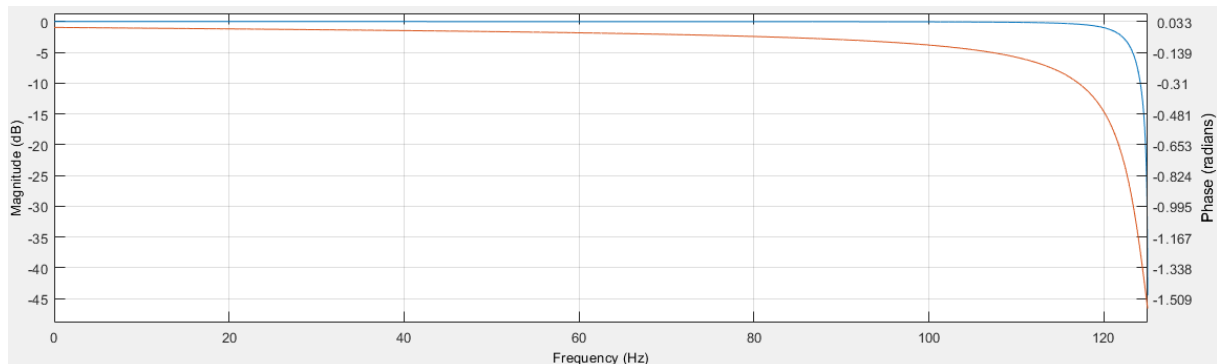
Fig. 6.4. Design of the used Chebyshev Type I lowpass filter: magnitude response (blue line) and phase response (orange line)

6.1.3. Wind speed and turbulence intensity calculation

The next 5 subsections of the subroutine are dedicated to calculating the wind speed and its characteristics, such as turbulence intensity and vertical profiles. They also automatically categorise the roughness category based on the comparison with values from codes and literature and assign additional parameters to plot the proper graphs.

The first of these subsections, *Calculation of wind velocity values, mean wind speeds and turbulence intensities*, calculates the momentary values of wind speed at each measurement point from the pressures, based on the following equation:

$$p(t) = 0.5\rho v(t)^2 \tag{6.1}$$

where: $p(t)$ – momentary value of wind pressure, ρ – air density in regular conditions, adopted as 1.225 [kg/m^3] in standard conditions (atmospheric pressure of 101.325 kPa and temperature of 15° C) as per (ISO 2533, 1975), $v(t)$ – momentary value of wind velocity. Taking into account the fact that all the potential negative pressure values are nullified within the signal, the momentary wind velocity can be calculated as:

$$v(t) = \sqrt{\frac{2p(t)}{\rho}} \tag{6.2}$$

From the velocity time series calculated this way for each of the measurement points, mean values, standard deviations and variations are extracted at each location. The turbulence intensity of the wind flow is then calculated as (comp. Eq. (3.3)):

$$I_{v,i} = \frac{\sigma_{vi}}{\overline{v_i}} \tag{6.3}$$

where: $I_{v,i}$ – turbulence intensity at the i-th point, σ_i – wind velocity standard deviation at the i-th point, $\overline{v_i}$ – mean wind speed at the i-th point. This subsection ends with the plots of all the velocity time series calculated from the base pressure signals. The code for this subsection is supplied in Fig. 6.5.

```
%% CALCULATION OF WIND VELOCITY VALUES, MEAN WIND SPEEDS AND TURBULENCE
%INTENSITIES
velocity_th=zeros(m,n);
for i=1:m
    for j=1:n
        if pressures_filt(i,j)<0
            velocity_th(i,j)=0;
        else
            velocity_th(i,j)=(2*abs(pressures_filt(i,j))/ro)^(0.5);
        end
    end
end

v_mean=zeros(n,1); %mean wind speed at each level
for i=1:n
    v_mean(i)=mean(velocity_th(:,i));
end

v_std=zeros(n,1); %standard deviation at each level
for i=1:n
    v_std(i)=std(velocity_th(:,i));
end

v_var=zeros(n,1); %variation at each level
for i=1:n
    v_var(i)=var(velocity_th(:,i));
end

Iv=zeros(n,1); %turbulence intensity at each level
for i=1:n
    Iv(i)=v_std(i)/v_mean(i);
```

```
end

Vref=v_mean(n_ref); %reference wind speed
Iv_ref=Iv(n_ref); %reference turbulence intensity
```

Fig. 6.5. *MATLAB* code for the subsection *Calculation of wind velocity values, mean wind speeds and turbulence intensities*

The next subsection, *Mean wind speed and turbulence intensity profiles*, calculates the data for power-law and logarithmic curves for the mean wind speed and turbulence intensity, based on the data from the measurements. The code is generated from the *MATLAB Curve Fitter* tool (MATLAB Help Center, 2022b) and adjusted for automation within the subroutine. These profiles are calculated for the values normalised to 1.0 so as to appear in a non-dimensional form, by adopting the reference at the highest measurement point and dividing the height and velocity values at each point by the reference height z_{ref} and the reference wind velocity v_{ref}, respectively. The mean wind speed and turbulence intensity profiles are calculated through the following formulas (comp. Eq. (3.8), (3.7), (3.66) and (3.63)):

$$v(\check{z}) = a_w \check{z}^\alpha \tag{6.4}$$

$$v(\check{z}) = \frac{v_{ref,log}}{v_{ref}} \frac{\ln\left(\frac{\check{z}}{\check{z}_0}\right)}{\ln\left(\frac{1}{\check{z}_0}\right)} \tag{6.5}$$

$$I_v(\check{z}) = a_{Iv} \check{z}^\beta \tag{6.6}$$

$$I_v(\check{z}) = \frac{a_{Iv,log}}{\ln\left(\frac{\check{z}}{\check{z}_0^T}\right)} \tag{6.7}$$

where: $v(\check{z})$ – vertical mean wind speed profile function, $I_v(\check{z})$ – vertical turbulence intensity profile function, $\check{z}$ – non-dimensional height related to z_{ref} ($\check{z} = z/z_{ref}$), α – exponent for power-law mean wind speed profile, β – exponent for power-law turbulence intensity profile (the value of β is always negative), $\check{z}_0$ – non-dimensional roughness length ($\check{z}_0 = z_0/z_{ref}$ where z_0 is roughness length in [m]), $\check{z}_0^T$ – non-dimensional roughness length for turbulence intensity profile ($\check{z}_0^T = z_0^T/z_{ref}$ where z_0^T is roughness length for turbulence intensity logarithmic profile in [m]), a_w – correction factor for power-law mean wind speed profile, a_{Iv} – correction factor for power-law turbulence intensity profile, v_{ref} – reference wind velocity at z_{ref}, $v_{ref,log}$ – corrected reference wind velocity for logarithmic mean wind speed profile, $a_{Iv,log}$ – correction factor for logarithmic turbulence intensity profile.

The correction factors are required to achieve the proper fit, as without them all the curves for vertical mean wind speed profiles would be anchored at the point (1.0, 1.0) on the normalised plot. This part of the subroutine also provides information on the level of fitting based on the Nonlinear Least Square Method, namely R-square, Adjusted R-square (MATLAB Help Center, 2022a) and Root Mean Square Error (RMSE). The code for the automatic curve

fitting for the different vertical mean wind speed and turbulence intensity profiles is given in Fig. 6.6.

```matlab
%% MEAN WIND SPEED AND TURBULENCE INTENSITY PROFILES
Z_=(Pheights/Zref)'; %dimensionless height values normalised to 1.0
z_30=30/Zref; %30 m height in the dimensionless scale
V_=v_mean/Vref; %dimensionless wind velocity values normalised to 1.0

[xData,yData]=prepareCurveData(Z_,V_); %power law curve fitting
ft=fittype('power1');
opts=fitoptions('Method','NonlinearLeastSquares');
opts.Display='Off';
opts.Lower=[-Inf -Inf];
opts.StartPoint=[1 0.23];
opts.Upper=[Inf Inf];
[fitresult,gof]=fit(xData,yData,ft,opts);
alfa=fitresult.b; %[-] - alfa exponent
a_w=fitresult.a; %correctional factor - power law function multiplier
GoF_power_law=[gof.rsquare,gof.adjrsquare,gof.rmse]; %level of fitting -✓
%Nonlinear least square method: R^2, Adjusted R^2, RMSE
z_discrete=(0:0.01:1); %data on Y
v_power_law=zeros(length(z_discrete),1); %data on X
for i=1:length(z_discrete)
    v_power_law(i)=a_w*z_discrete(i)^alfa;
end

[xData,yData]=prepareCurveData(Z_,Iv); %turbulence intensity power law curve✓
%fitting
ft=fittype('power1');
opts=fitoptions('Method','NonlinearLeastSquares');
opts.Display='Off';
opts.Lower=[-Inf -Inf];
opts.StartPoint=[Iv_ref -0.3];
opts.Upper=[Inf Inf];
[fitresult,gof]=fit(xData,yData,ft,opts);
beta=fitresult.b; %[-] beta exponent
a_Iv=fitresult.a; %correctional factor - power law function multiplier
GoF_power_law_Iv=[gof.rsquare,gof.adjrsquare,gof.rmse]; %level of fitting -✓
%Nonlinear least square method: R^2, Adjusted R^2, RMSE
Iv_power_law=zeros(length(z_discrete),1); %data on X
for i=1:length(z_discrete)
    Iv_power_law(i)=a_Iv*z_discrete(i)^beta;
end

[xData,yData]=prepareCurveData(Pheights',v_mean); %logarithmic curve fitting
ft=fittype('vref*log(x/a)/log(zref/a)','independent','x','dependent','y');
opts=fitoptions('Method','NonlinearLeastSquares');
opts.Display='Off';
opts.Lower=[0 -Inf Zref];
opts.StartPoint=[1 Vref Zref];
opts.Upper=[Inf Inf Zref];
[fitresult,gof]=fit(xData,yData,ft,opts);
z0=fitresult.a; %[m] - z0 in real-life scale, as real-life scale data is input✓
%here
Vref_log=fitresult.vref; %[m/s] - correction to mean wind speed
Zref_log=fitresult.zref; %[m] - reference height
GoF_log=[gof.rsquare,gof.adjrsquare,gof.rmse]; %level of fitting - Nonlinear✓
%least square method: R^2, Adjusted R^2, RMSE
```

```
v_log=zeros(length(z_discrete),1); %data on X
z0_=z0/Zref_log; %z0 from full-scale normalised to 1.0
for i=1:length(z_discrete)
    v_log(i)=Vref_log/Vref*log(z_discrete(i)/z0_)/log(1/z0_);
end

[xData,yData]=prepareCurveData(Pheights',Iv); %turbulence intensity logarithmic↙
%curve fitting
ft=fittype('a/log(x/b)','independent','x','dependent','y');
opts=fitoptions('Method','NonlinearLeastSquares');
opts.Display='Off';
opts.Lower=[0 0];
opts.StartPoint=[1 1];
opts.Upper=[Inf Inf];
[fitresult,gof]=fit(xData,yData,ft,opts);
z0T=fitresult.b; %[m] - z0T in real-life scale, as real-life scale data is input↙
%here
a_Iv2=fitresult.a; %[m/s] - correctional factor
GoF_log_Iv=[gof.rsquare,gof.adjrsquare,gof.rmse]; %level of fitting - Nonlinear↙
%least square method: R^2, Adjusted R^2, RMSE
Iv_log=zeros(length(z_discrete),1); %data on X
z0T_=z0T/Zref_log; %z0T from full-scale normalised to 1.0
for i=1:length(z_discrete)
    Iv_log(i)=a_Iv2/log(z_discrete(i)/z0T_);
end

z30_dif=abs(z_discrete-z_30);
min_z30=min(z30_dif);
z_30_index=find(z30_dif(:)==min_z30);
Iv30=Iv_power_law(z_30_index);
```

Fig. 6.6. *MATLAB* code for the subsection *Mean wind speed and turbulence intensity profiles*

This data is then compared to the values for different terrain roughness categories from codes (ASCE/SEI 7, 2022; ISO 4354, 2009; PN-EN 1991-1-4, 2011), as discussed in subsection 3.2. The assignment to one of the categories is directly based on the value of either the α exponent or the roughness length z_0, whichever of these parameters produces the smaller relative error with the value from the standard (the assignment according to (ASCE/SEI 7, 2022) is based only on the α exponent, as only the power-law profile according to this code is taken into account). After the assignment, the relative errors are calculated for the remaining compared values, which are β exponent, z_0^T roughness parameter for turbulence intensity and turbulence intensity at 30 [m] height. Besides assigning a terrain category, the value of z_{min} (or H_{min}) is assigned, which is the lowest height at which the mean wind speed profile can be reasonably determined. The code for this subsection is shown in Fig. 6.7.

```
%% ROUGHNESS CATEGORY ASSIGNMENT
%Data from codes and literature
alfa_PNEN=[0.11 0.13 0.17 0.19 0.24]; %Tab. 3.11 in the thesis (PN-EN 1991-1-4↙
%NB.3)
z0_PNEN=[0.003 0.01 0.05 0.3 1]; %Tab. 3.10 in the thesis (PN-EN 1991-1-4)

cr_factor_PNEN=[1.27 1.18 1 0.81 0.62]; %Tab. 3.11 in the thesis (PN-EN 1991-1-4↙
%NB.3)
kr_PNEN=[0.156 0.17 0.19 0.215 0.234]; %Tab. 3.10 in the thesis (PN-EN 1991-1-4)
```

```matlab
zmin_PNEN=[1 1 2 5 10]; %Tab. 3.10 in the thesis (PN-EN 1991-1-4)


Iv30_ref=[0.097 0.11 0.125 0.175 0.294]; %Fig. 3.7 in the thesis (Davenport↵
%(1984), Flaga A. (2008))
beta_ref=[-0.11 -0.13 -0.17 -0.19 -0.24]; %Tab. 3.11 in the thesis (PN-EN↵
%1991-1-4 NB.3), assuming beta ~= -alfa


alfa_ISO=[0.1 0.14 0.21 0.32 0.38]; %Tab. 3.8 in the thesis (ISO 4354)
z0_ISO=[0.005 0.05 0.3 1 2.5]; %Tab. 3.9 in the thesis (ISO 4354)
k1_ISO=[1.2 1 0.8 0.5 0.39]; %Tab. 3.8 in the thesis (ISO 4354)
k2_ISO=[0.16 0.19 0.23 0.27 0.29]; %Tab. 3.9 in the thesis (ISO 4354)
HminISO=[0 2 6 15 25]; %Tab. 3.8 in the thesis (ISO 4354)


alfa_ASCE=[1/10 1/7 1/4.5 1/3]; %Tab. 3.13 in the thesis (ASCE/SEI 7)
zg_ASCE=[213 274 366 457]; %Tab. 3.13 in the thesis (ASCE/SEI 7)


Delta=zeros(8,1); %relative errors of various wind speed profile and turbulence↵
%intensity profile parameters


% Terrain category selection according to PN-EN 1991-1-4:


alfa_dif=abs(alfa_PNEN-alfa);
min_alfa_dif=min(alfa_dif);
index_alfa=find(alfa_dif(:)==min_alfa_dif);
Delta(1)=min_alfa_dif/alfa_PNEN(index_alfa);


z0_dif=abs(z0_PNEN-z0);
min_z0_dif=min(z0_dif);
index_z0=find(z0_dif(:)==min_z0_dif);
Delta(2)=min_z0_dif/z0_PNEN(index_z0);


TC_PNEN={'0';'I';'II';'III';'IV'};


if index_z0==index_alfa
    index_category=index_alfa;
    disp(['Simulated boundary layer was assigned to '
char(TC_PNEN(index_category)) ' category according to PN-EN 1991-1-4 based on↵
both alfa and z0. Relative error of the alpha parameter is ' num2str(Delta(1),3)↵
' and of z0 is ' num2str(Delta(2),3) '.'])
else
    if Delta(1)<Delta(2)
        index_category=index_alfa;
        disp(['Simulated boundary layer was assigned to '
char(TC_PNEN(index_category)) ' category according to PN-EN 1991-1-4 based on↵
alfa. Relative error of the alpha parameter is ' num2str(Delta(1),3) ' and of z0↵
is ' num2str(Delta(2),3) '.'])
    else
        index_category=index_z0;
        disp(['Simulated boundary layer was assigned to '
char(TC_PNEN(index_category)) ' category according to PN-EN 1991-1-4 based on↵
z0. Relative error of the alpha parameter is ' num2str(Delta(1),3) ' and of z0↵
is ' num2str(Delta(2),3) '.'])
    end
end


Terrain_category_PNEN=index_category-1;
```

```matlab
zmin=zmin_PNEN(index_category);
zmin_=zmin/Zref;
zmin_dif=abs(z_discrete-zmin_);
min_zmin=min(zmin_dif);
zmin_index=find(zmin_dif(:)==min_zmin);


Delta(3)=abs((beta_ref(index_category)-beta)/beta_ref(index_category));
Delta(4)=abs((z0_PNEN(index_category)-z0T)/z0_PNEN(index_category));
Delta(5)=abs((Iv30_ref(index_category)-Iv30)/Iv30_ref(index_category));

% Terrain category selection according to ISO 4354:
alfa_ISO_dif=abs(alfa_ISO-alfa);
min_alfa_ISO_dif=min(alfa_ISO_dif);
index_alfa_ISO=find(alfa_ISO_dif(:)==min_alfa_ISO_dif);
Delta(6)=min_alfa_ISO_dif/alfa_ISO(index_alfa_ISO);


z0_ISO_dif=abs(z0_ISO-z0);
min_z0_ISO_dif=min(z0_ISO_dif);
index_z0_ISO=find(z0_ISO_dif(:)==min_z0_ISO_dif);
Delta(7)=min_z0_ISO_dif/z0_ISO(index_z0_ISO);


if index_z0_ISO==index_alfa_ISO
    index_ISO=index_alfa_ISO;
    Terrain_category_ISO=index_ISO;
    disp(['Simulated boundary layer was assigned to '
num2str(Terrain_category_ISO) ' category according to ISO 4354 based on both alfa↵
and z0. Relative error of the alpha parameter is ' num2str(Delta(6),3) ' and of↵
z0 is ' num2str(Delta(7),3) '.'])
else
    if Delta(6)<Delta(7)
        index_ISO=index_alfa_ISO;
        Terrain_category_ISO=index_ISO;
        disp(['Simulated boundary layer was assigned to '
num2str(Terrain_category_ISO) ' category according to ISO 4354 based on alfa.↵
Relative error of the alpha parameter is ' num2str(Delta(6),3) ' and of z0 is '↵
num2str(Delta(7),3) '.'])
    else
        index_ISO=index_z0_ISO;
        Terrain_category_ISO=index_ISO;
        disp(['Simulated boundary layer was assigned to '
num2str(Terrain_category_ISO) ' category according to ISO 4354 based on z0.↵
Relative error of the alpha parameter is ' num2str(Delta(6),3) ' and of z0 is '↵
num2str(Delta(7),3) '.'])
    end
end


Hmin=HminISO(index_ISO);
Hmin_=Hmin/Zref;
Hmin_dif=abs(z_discrete-Hmin_);
min_Hmin=min(Hmin_dif);
Hmin_index=find(Hmin_dif(:)==min_Hmin);


Delta(8)=abs((-alfa_ISO(index_ISO)-beta)/(-alfa_ISO(index_ISO)));
Delta(9)=abs((alfa_ISO(index_ISO)-Iv30)/alfa_ISO(index_ISO));


% Terrain category selection according to ASCE/SEI 7 (power law wind profile):
alfa_ASCE_dif=abs(alfa_ASCE-alfa);
min_alfa_ASCE_dif=min(alfa_ASCE_dif);
```

```
index_ASCE=find(alfa_ASCE_dif(:)==min_alfa_ASCE_dif);
Delta(10)=min_alfa_ASCE_dif/alfa_ASCE(index_ASCE);
TC_ASCE=['D';'C';'B';'A'];
Terrain_category_ASCE=5-index_ASCE;
disp(['Simulated boundary layer was assigned to ' TC_ASCE(index_ASCE) ' category↙
according to ASCE/SEI 7 power-law profile. Relative error of the alpha parameter↙
is ' num2str(Delta(10),3) '.'])


Delta(11)=abs((-alfa_ASCE(index_ASCE)-beta)/(-alfa_ASCE(index_ASCE)));
Delta(12)=abs((alfa_ASCE(index_ASCE)-Iv30)/alfa_ASCE(index_ASCE));
```

Fig. 6.7. *MATLAB* code for the subsection *Roughness category assignment*

The issue of this minimal height z_{min} is addressed within the next subsection, *Wind velocity and turbulence intensity profiles after the correction*, which takes this value into account to determine the proper functions of vertical mean wind speed and turbulence intensity profiles. Also, the standard power-law wind profiles according to different codes are calculated in this subsection for comparison. The comparison is based on a Root Mean Square Error (RMSE) between the two curves, the best fit for measurements and the model curve from the standards. Such comparison is made for power-law and logarithmic mean wind speed profiles according to (PN-EN 1991-1-4, 2011), power-law and logarithmic mean wind speed profiles according to (ISO 4354, 2009) and power-law mean wind speed profile according to (ASCE/SEI 7, 2022).

Similarly, the turbulence intensity values are compared to the values from (ESDU 85020, 2002; PN-EN 1991-1-4, 2011). The reference values from the Eurocode are based on Eq. (3.65) and the standard deviation of mean wind speed σ_v is calculated as:

$$\sigma_v = k_r v_b k_l \tag{6.8}$$

where: k_r – terrain factor (see Tab. 3.10), v_b – basic wind velocity [m/s], k_l – turbulence factor (with a recommended value of 1.0).

It should be noted that the values of turbulence intensity according to (PN-EN 1991-1-4, 2011) are also dependent on mean wind speed at each height, which is taken from the wind profiles calculated for each test case. Therefore, in the cases where the mean wind speed profiles have large discrepancies from the standard, the reference values of turbulence intensity calculated from this method are also incorrect. The values according to (ESDU 85020, 2002) were read from the nomograms, which is why they are explicitly input into the script. The values are adopted for different terrain roughness categories based on the roughness length z_0, precisely for $z_0 = 0.003$ (terrain category 0), $z_0 = 0.01$ (terrain category I), $z_0 = 0.03$ (terrain category II), $z_0 = 0.3$ (terrain category III) and $z_0 = 1.0$ (terrain category IV). Once again, the comparison for turbulence intensity is based on RMSE values. Furthermore, for both presented approaches, boundaries are drawn in the plot for turbulence intensity to indicate the recommended range of values. ESDU 85020 (2002) suggests a ±10% uncertainty for turbulence intensity in the cases with no roughness changes and ±20% uncertainty for the cases with non-uniform roughness. It was decided to adopt the ±20% uncertainty for wind tunnel tests after Kozmar (2011c). The code for this section is provided in Fig. 6.8.

The fifth subsection, *Plots for wind velocity and turbulence intensity profiles*, is solely dedicated to plotting the results in the form of vertical wind profiles and vertical turbulence intensity profiles.

```matlab
%% WIND SPEED AND TURBULENCE INTENSITY PROFILES AFTER THE CORRECTION
z_full=z_discrete*Zref;
v_power_law2=zeros(length(z_discrete),1); %data on X with regard to z_min
for i=1:zmin_index
    v_power_law2(i)=a_w*z_discrete(zmin_index)^alfa;
end
for i=zmin_index:length(z_discrete)
    v_power_law2(i)=a_w*z_discrete(i)^alfa;
end

v_log2=zeros(length(z_discrete),1); %data on X with regard to z_min
for i=1:zmin_index
    v_log2(i)=Vref_log/Vref*log(z_discrete(zmin_index)/z0_)/log(1/z0_);
end
for i=zmin_index:length(z_discrete)
    v_log2(i)=Vref_log/Vref*log(z_discrete(i)/z0_)/log(1/z0_);
end

Iv_power_law2=zeros(length(z_discrete),1); %data on X with regard to z_min
for i=1:zmin_index
    Iv_power_law2(i)=a_Iv*z_discrete(zmin_index)^beta;
end
for i=zmin_index:length(z_discrete)
    Iv_power_law2(i)=a_Iv*z_discrete(i)^beta;
end

Iv_log2=zeros(length(z_discrete),1); %data on X with regard to z_min
for i=1:zmin_index
    Iv_log2(i)=a_Iv2/log(z_discrete(zmin_index)/z0T_);
end
for i=zmin_index:length(z_discrete)
    Iv_log2(i)=a_Iv2/log(z_discrete(i)/z0T_);
end
for i=1:length(z_discrete) %correction necessary due to logarithmic curve↙
%characteristic
    if Iv_log2(i)>=Iv_power_law2(zmin_index)
        for j=1:i
            Iv_log2(j)=Iv_power_law2(zmin_index);
        end
    end
end

%Model profiles according to PN-EN 1991-1-4

Vref_PNEN1=cr_factor_PNEN(index_category)*(Zref/10)^alfa_PNEN(index_category);
Vref_PNEN2=kr_PNEN(index_category)*log(Zref/z0_PNEN(index_category));

v_PNEN_power=zeros(length(z_discrete),1);
v_PNEN_log=zeros(length(z_discrete),1);
for i=1:zmin_index

v_PNEN_power(i)=cr_factor_PNEN(index_category)*(z_full(zmin_index)/10)^alfa_PNEN(↙
index_category)/Vref_PNEN1;
```

```matlab
v_PNEN_log(i)=kr_PNEN(index_category)*log(z_full(zmin_index)/z0_PNEN(index_catego↙
ry))/Vref_PNEN2;
end
for i=zmin_index:length(z_discrete)

v_PNEN_power(i)=cr_factor_PNEN(index_category)*(z_full(i)/10)^alfa_PNEN(index_cat↙
egory)/Vref_PNEN1;

v_PNEN_log(i)=kr_PNEN(index_category)*log(z_full(i)/z0_PNEN(index_category))/Vref↙
_PNEN2;
end

%Model profiles according to ISO 4354

Vref_ISO1=k1_ISO(index_ISO)*(Zref/10)^alfa_ISO(index_ISO);
Vref_ISO2=k2_ISO(index_ISO)*log(Zref/z0_ISO(index_ISO));

v_ISO_power=zeros(length(z_discrete),1);
v_ISO_log=zeros(length(z_discrete),1);
for i=1:Hmin_index

v_ISO_power(i)=k1_ISO(index_ISO)*(z_full(Hmin_index)/10)^alfa_ISO(index_ISO)/Vref↙
_ISO1;

v_ISO_log(i)=k2_ISO(index_ISO)*log(z_full(Hmin_index)/z0_ISO(index_ISO))/Vref_ISO↙
2;
end
for i=Hmin_index:length(z_discrete)
    v_ISO_power(i)=k1_ISO(index_ISO)*(z_full(i)/10)^alfa_ISO(index_ISO)/Vref_ISO1;
    v_ISO_log(i)=k2_ISO(index_ISO)*log(z_full(i)/z0_ISO(index_ISO))/Vref_ISO2;
end

%Model power-law profile according to ASCE/SEI 7
Vref_ASCE=(zg_ASCE(2)/10)^alfa_ASCE(2)*(Zref/zg_ASCE(index_ASCE))^alfa_ASCE(index↙
_ASCE);
v_ASCE=zeros(length(z_discrete),1);
for i=1:length(z_discrete)

v_ASCE(i)=(zg_ASCE(2)/10)^alfa_ASCE(2)*(z_full(i)/zg_ASCE(index_ASCE))^alfa_ASCE(↙
index_ASCE)/Vref_ASCE;
end

z_10=10/Zref;
z10_dif=abs(z_discrete-z_10);
min_z10=min(z10_dif);
z_10_index=find(z10_dif(:)==min_z10);
v10=v_power_law(z_10_index)*Vref/k_v;
v_b=(a_w*v10/cr_factor_PNEN(index_category)); %basic wind velocity
sigma_v=kr_PNEN(index_category)*v_b;
Iv_PNEN=zeros(length(z_discrete),1); %turbulence intensity according to PN-EN↙
%1991-1-4, Eq. (3.66) in the thesis
for i=1:length(z_discrete)
    Iv_PNEN(i)=sigma_v/(Vref_log*v_PNEN_log(i)/k_v);
end

Iv_ESDU=[12.8 14.8 17 24.5 33.2
    12 13.8 15.8 22.6 29.4
    11.4 13.1 15 21.4 27.6
    10.8 12.4 14.4 20.4 26.2
```

```
   10.4 12 13.8 19.6 25
   10 11.6 13.4 19.1 24.3
   9.6 11.2 13 18.6 23.6
   9.2 10.8 12.6 18.1 23
   8.8 10.4 12.2 17.6 22.4
   8.6 10.1 11.8 17.2 21.8
   8.4 9.8 11.4 16.9 21.4
   8.2 9.6 11.2 16.6 21]; % [%] - Turbulence intensities at the heights↙
%corresponding to measurement levels for different terrain categories according↙
%to Fig. 1 in ESDU 85020

%RMSE values between fit and model wind speed profiles according to different↙
%codes
RMSE_full=zeros(5,1);
ISO_min=max(Hmin_index,zmin_index);

RMSE_full(1,:)=sqrt(sum((v_power_law2(zmin_index:length(z_discrete))-↙
v_PNEN_power(zmin_index:length(z_discrete))).^2)/length(z_discrete));

RMSE_full(2,:)=sqrt(sum((v_log2(zmin_index:length(z_discrete))-↙
v_PNEN_power(zmin_index:length(z_discrete))).^2)/length(z_discrete));

RMSE_full(3,:)=sqrt(sum((v_power_law2(ISO_min:length(z_discrete))-↙
v_ISO_power(ISO_min:length(z_discrete))).^2)/length(z_discrete));

RMSE_full(4,:)=sqrt(sum((v_log2(ISO_min:length(z_discrete))-↙
v_ISO_power(ISO_min:length(z_discrete))).^2)/length(z_discrete));

RMSE_full(5,:)=sqrt(sum((v_power_law(:)-v_ASCE(:)).^2)/length(z_discrete));

%RMSE values between fit and model turbulence intensity profiles according to↙
%PN-EN 1991-1-4 and ESDU 85020
RMSE_PNEN_log=sqrt(sum((Iv_power_law2(zmin_index:length(z_discrete))-↙
Iv_PNEN(zmin_index:length(z_discrete))).^2)/length(z_discrete));

RMSE_PNEN_power_law=sqrt(sum((Iv_log2(zmin_index:length(z_discrete))-↙
Iv_PNEN(zmin_index:length(z_discrete))).^2)/length(z_discrete));

RMSE_ESDU=sqrt(sum((Iv(:)-(Iv_ESDU(:,index_category)/100)).^2)/n);
```

Fig. 6.8. *MATLAB* code for the subsection *Wind velocity and turbulence intensity profiles after the correction*

6.1.4. Autocorrelation and longitudinal turbulence length scales

Estimators $\bar{R}_{vi}$ for the time correlation (autocorrelation) functions for a given measurement point are defined as follows (A. Flaga, 2008):

$$\bar{R}_{vi}(\tau) = \overline{v_i(t)v_i(t+\tau)} = \frac{1}{T}\int_0^T v_i(t)v_i(t+\tau)\mathrm{d}t; 0 \le \tau \le T \qquad (6.9)$$

where: v_i – wind speed fluctuation at each time step [m/s], T – total time of the process, τ – time step. In numerical calculations, the integration is done through discrete values and τ is equal to the smallest time step in the time series, which in this case is 0.004 [s].

Usually, this is also normalised to 1.0 through dividing by the variation of the wind velocity, as shown earlier in the work in Eq. (3.14):

$$\rho_{vi} = \frac{R_{vi}(\tau)}{\sigma_{vi}{}^2} \qquad (6.10)$$

where ρ_{vi} – normalised autocorrelation function.

These calculations are only done for the main component of the wind velocity (along the X axis), hence $i = x$. This allows for the calculation of the partial time scales for each time step, which is done in the subsection *Calculation of turbulence length scale (autocorrelation) for each point*. The time scale at each measuring point is the integral of the autocorrelation function over time step τ, or numerically – a sum of these partial time scales, until the point at which they cross the X axis on the graph, which means that they assume negative values. In order to mitigate potential fluctuations of negligible character, in the subroutine this point of crossing the X axis is determined as the point where the three consecutive values of the partial time scales are below 0. Finally, the length scale is calculated as the product of the time scale and mean wind speed at each point, which is done for both model and prototype scales. The subsection ends with plotting the graphs of the normalised autocorrelation function at each point and the vertical distribution of the longitudinal turbulence length scales.

The longitudinal length scale values are plotted in a chart and compared with the values from (ESDU 74031, 1974). This standard was selected as a reference based on the findings of (Kozmar, 2011b, 2011c). The values from the standard are explicitly taken from the nomogram at 4 heights of 50 m, 100 m, 150 m and 200 m and plotted as a range with ±30% uncertainty bounds. This comparison was only made for the three basic categories (open flat terrain, suburban terrain and urban terrain), which are typically simulated in the wind tunnel. The *MATLAB* code for the subroutine is provided in Fig. 6.9.

```matlab
%% CALCULATION OF TURBULENCE LENGTH SCALE (AUTOCORRELATION) FOR EACH POINT
Rvi=zeros(length(velocity_th),length(velocity_th),n); %[m^2/s^2] -↙
%autocorrelation function estimators for every time step and every point
for i=1:size(Rvi,1)
    for j=1:size(Rvi,2)
        for k=1:n
            if i+j<=size(Rvi,1)
                Rvi(i,j,k)=(velocity_th(i,k)-v_mean(k))*(velocity_th(i+j,k)-↙
v_mean(k));
            else
                Rvi(i,j,k)=0;
            end
        end
    end
end

Rvx=zeros(length(velocity_th),n); %[m^2/s^2] - mean autocorrelation function
for j=1:size(Rvx,1)
    for k=1:n
        Rvx(j,k)=mean(Rvi(:,j,k));
    end
end
```

```matlab
ro_vx=zeros(length(Rvx),n); %[-] - normalised autocorrelation function (divided↙
%by variation)
for j=1:size(ro_vx,1)
    for k=1:n
        ro_vx(j,k)=Rvx(j,k)/v_var(k);
    end
end

T_scale_i=zeros(length(Rvx),n); %[s] - partial time scales for each step
for k=1:n
    T_scale_i(1,k)=(ro_vx(1,k)+1)/2*ts;
end
for j=2:size(T_scale_i,1)
    for k=1:n
        T_scale_i(j,k)=(ro_vx(j,k)+ro_vx(j-1,k))/2*ts;
    end
end

index_time=zeros(n,1); %vector for the point of crossing the X axis, where the↙
%condition is 3 subsequent negative values in the series
for k=1:n
    for j=1:(size(T_scale_i,1)-2)
        if ((T_scale_i(j,k)<0) && (T_scale_i(j+1,k)<0) && (T_scale_i(j+2,k)<0))
            index_time(k,1)=j;
            break
        end
    end
end

Tx=zeros(n,1); %[s] - time scale up to the point of crossing the X axis
for k=1:n
    Tx(k,1)=sum(T_scale_i(1:index_time(k),k));
end

Lx_ESDU=[110 103 93
142     133     120
165     154     139
183     171     154]; %ESDU 7431, for open terrain, suburban terrain and urban↙
%terrain
z_ESDU=[50 100 150 200]/Zref;

L_model=Tx.*v_mean; %[m] - model turbulence length scale
L_proto=L_model/k_L; %[m] - real-life turbulence length scale
```

Fig. 6.9. *MATLAB* code for the subsection *Calculation of turbulence length scale (autocorrelation) for each point*

6.1.5. Spatial correlation and vertical turbulence length scales

Due to the nature of these tests and the implemented setup in the wind tunnel, the only spatial correlation that was possible and reasonable to extract from the data is the vertical correlation. As mentioned before, this function is anisotropic and yields different values when moving upward or downward from a set point, therefore, two different values of the vertical length scale will be given by the equations, setting either the lowest or the highest point in the measurement as a reference.

Estimators $\bar{R}_{vivj}$ for the vertical spatial correlation functions between the two measurement points are defined as follows (A. Flaga, 2008):

$$\bar{R}_{vivj}(z_1, z_2) = \overline{v_i(z_1, t)v_j(z_2, t)} = \frac{1}{T} \int_0^T v_i(z_1, t)v_j(z_2, t)\mathrm{d}t \tag{6.11}$$

where: T – total time of the process, z_1, z_2 – considered heights.

As with the autocorrelation, this can also be normalised to 1.0 by dividing by the product of the standard deviations of the wind velocity at both considered points (comp. Eq. (3.15)):

$$\rho_{vivj} = \frac{R_{vivj}(z_1, z_2)}{\sigma_{vi}(z_1)\sigma_{vj}(z_2)} \tag{6.12}$$

where ρ_{vivj} – normalised spatial correlation function.

These calculations are only done for the main component of the wind velocity (along the X axis), hence $i, j = x$. The *MATLAB* code for this part of the subroutine can be found in Fig. 6.10.

```matlab
%% CALCULATION OF SPATIAL VERTICAL LENGTH SCALE - UPWARD AND DOWNWARD
Rvzz_u=zeros(m,n); %[m^2/s^2] - vertical correlation function estimator, upward
Rvzz_d=zeros(m,n); %[m^2/s^2] - vertical correlation function estimator, downward
for i=1:m
    for j=1:n
        Rvzz_u(i,j)=(velocity_th(i,1)-v_mean(1))*(velocity_th(i,j)-v_mean(j));
        Rvzz_d(i,j)=(velocity_th(i,n)-v_mean(n))*(velocity_th(i,j)-v_mean(j));
    end
end

Rvzz_up=zeros(n,1); %[m^2/s^2] - mean vertical correlation function estimator,✓
%upward
Rvzz_down=zeros(n,1); %[m^2/s^2] - mean vertical correlation function estimator,✓
%downward
for j=1:n
    Rvzz_up(j,1)=mean(Rvzz_u(:,j));
    Rvzz_down(j,1)=mean(Rvzz_d(:,j));
end

Delta_z_up=zeros(n,1);
Delta_z_down=zeros(n,1);
for j=1:n
    Delta_z_up(j,1)=Pheights(j)-Pheights(1);
    Delta_z_down(j,1)=Pheights(n)-Pheights(j);
end

ro_vzz_up=zeros(n,1); %[-] - normalised correlation function, upward
ro_vzz_down=zeros(n,1); %[-] - normalised correlation function, downward
for j=1:n
    ro_vzz_up(j,1)=Rvzz_up(j)/(v_std(1)*v_std(j));
    ro_vzz_down(j,1)=Rvzz_down(j)/(v_std(n)*v_std(j));
end
```

```
Lz_up_step=zeros(n-1,1);
Lz_down_step=zeros(n-1,1);
for j=2:n
    Lz_up_step(j-1,1)=((ro_vzz_up(j)+ro_vzz_up(j-1))/2)*(Delta_z_up(j)-↙
Delta_z_up(j-1));
    Lz_down_step(j-1,1)=((ro_vzz_down(j)+ro_vzz_down(j-1))/2)*(Delta_z_down(j-1)-↙
Delta_z_down(j));
end

Lz_up=sum(Lz_up_step); %[m] - upward vertical correlation scale, real-life scale
Lz_down=sum(Lz_down_step); %[m] - downward vertical correlation scale, real-life↙
%scale
```

Fig. 6.10. *MATLAB* code for the subsection *Calculation of spatial vertical length scale – upward and downward*

6.1.6. Power density spectra

The subsequent part of the code in the *MATLAB* subroutine is dedicated to the calculation of power density spectra at each measurement point and comparing them with the standard spectra from the literature, established by Davenport (Davenport, 1961), von Kármán (ESDU 82026, 2003) and Kaimal (Kaimal et al., 1972, Flaga et al., 2004). The power density spectra are calculated with 2 different methods: directly from the Fourier spectrum, according to the method proposed by Moravej (2019), or using a *MATLAB* default function, by the Welch method (MATLAB Help Center, 2022d). For clearer comparison between the spectra and not having them affected by the model scales, they are provided in a non-dimensional form. The code that generates the plots for the three different spectra from the literature at each measurement point and calculates the power density spectra of the measurement signals is shown in Fig. 6.11. The spectra are then plotted in both linear-linear and log-log scales.

```
%% POWER SPECTRAL DENSITIES FOR EACH POINT
z_10=10/Zref;
z10_dif=abs(z_discrete-z_10);
min_z10=min(z10_dif);
z10_index=find(z10_dif(:)==min_z10);

f_PSD=0:0.001:fs-0.001; %[Hz] - frequency range
fn=length(f_PSD);
L_Davenport=1200; %[m] - length scale
v_Davenport=v_power_law(z10_index)*Vref/k_v; %[m/s] - wind speed at 10 m height
m_Davenport=zeros(fn,1);

for i=1:fn
    m_Davenport(i)=(f_PSD(i)*L_Davenport)/v_Davenport;
end
Davenport=zeros(fn,1);
for i=1:fn
    Davenport(i)=2/3*(m_Davenport(i)^2)/((1+m_Davenport(i)^2)^(4/3)); %formula↙
%for Davenport spectrum in non-Dimensional form
end

k_Karman=1/(0.437+0.153*log(z0));
LxVx_Karman=zeros(n,1);
for i=1:n
```

```matlab
        LxVx_Karman(i)=300*(Pheights(i)/350)^(1/k_Karman);
end
xx_Karman=zeros(fn,n);
for i=1:fn
    for j=1:n
        xx_Karman(i,j)=LxVx_Karman(j)*f_PSD(i)/(v_mean(j)/k_v);
    end
end
Karman=zeros(fn,n);
for i=1:fn
    for j=1:n
        Karman(i,j)=(4*xx_Karman(i,j))/((1+70.7*xx_Karman(i,j)^2)^(5/6));
%formula for von Karman spectrum in non-Dimensional form
    end
end

ax_Kaimal=0.0144;
x_Kaimal=zeros(fn,n);
for i=1:fn
    for j=1:n
        x_Kaimal(i,j)=f_PSD(i)*Pheights(j)/(v_mean(j)/k_v);
    end
end
Kaimal=zeros(fn,n);
for i=1:fn
    for j=1:n

Kaimal(i,j)=(0.164*x_Kaimal(i,j)/ax_Kaimal)/(1+0.164*(x_Kaimal(i,j)/ax_Kaimal)^
(5/3));
    end
end
fzref_vref_P=f_PSD*Zref/(Vref/k_v);

velocity_norm=zeros(m,n);
for i=1:m
    for j=1:n
        velocity_norm(i,j)=(velocity_th(i,j)-v_mean(j));
    end
end

n_PSD=NpWelch/2+1; %number of frequency samples - frequency resolution for PSD
%calculation
spectrumPwelch=zeros(n_PSD,n); %power spectral density calculated directly
%through Welch method
frequencyPwelch=zeros(n_PSD,1);
for j=1:n
    [spectrumPwelch(:,j),frequencyPwelch]=pwelch(velocity_norm(:,j),[],[],NpWelch
,fs);
end

FourierPSD=zeros(m,n);
for j=1:n
    FourierPSD(:,j)=fft(velocity_norm(:,j))/m;
end

Fourier_step=fs/m;
Freq_Range=0+Fourier_step:Fourier_step:0.5*fs;
Svi=zeros(m/2,n);
```

```matlab
for j=1:n
    Svi(:,j)=[2*abs(FourierPSD(2:m/2,j)).^2; abs(FourierPSD(m/2+1,j)).^2];
end


Gvi=zeros(m/2,n);
for j=1:n
    Gvi(:,j)=Svi(:,j)/Fourier_step; %one-sided power density spectrum
end


fzref_vref_M=zeros(n_PSD,1);
for i=1:n_PSD
    fzref_vref_M(i)=frequencyPwelch(i)*Zref*k_L/Vref; %normalised frequency↙
%f*zref/vref
end
PSD_th=zeros(n_PSD,n); %normalised one-sided power density spectrum↙
%f*G(f)/sigma_v^2 - Welch method
for i=1:n_PSD
    for j=1:n
        PSD_th(i,j)=(spectrumPwelch(i,j)*frequencyPwelch(i))/v_var(n);
    end
end


fzref_vref_M_FFT=zeros(m/2,1);
for i=1:m/2
    fzref_vref_M_FFT(i)=Freq_Range(i)*Zref*k_L/Vref;
end


PSD_FFT=zeros(m/2,n); %normalised one-sided power density spectrum↙
%f*G(f)/sigma_v^2 - FFT method
for i=1:m/2
    for j=1:n
        PSD_FFT(i,j)=(Gvi(i,j)*Freq_Range(i))/v_var(n);
    end
end
```

Fig. 6.11. *MATLAB* code for the subsection *Power spectral densities for each point*

After calculating the power density spectra, a validation check of Parseval's identity (Siktar, 2019) is performed. In this case, this is addressed by comparing the value of the wind speed variation at each point to the sum of squares of the Fourier coefficients of a function (or, in geometrical terms, the area under the plot of the power density spectrum). This is done for both the Welch method and for the direct calculation from the Fourier transform. The mean squared errors for both of these are then calculated and displayed. The code for this part of the subroutine is included in Fig. 6.12.

```matlab
%% PARSEVAL IDENTITY CHECK FOR CALCULATED PSD
Parseval=zeros(3,n);
for j=1:n
    Parseval(1,j)=v_var(j);
    Parseval(2,j)=trapz(frequencyPwelch,spectrumPwelch(:,j));
    Parseval(3,j)=sum(Svi(:,j));
end
PSD_SE=zeros(2,n);
for j=1:n
    PSD_SE(1,j)=(Parseval(1,j)-Parseval(2,j))^2;
```

```
    PSD_SE(2,j)=(Parseval(1,j)-Parseval(3,j))^2;
end
PSD_MSE=zeros(2,3); %mean, max and min squared error between the results of↙
%Parseval's identity for all points and both methods
for i=1:2
    PSD_MSE(i,1)=mean(PSD_SE(i,:));
    PSD_MSE(i,2)=max(PSD_SE(i,:));
    PSD_MSE(i,3)=min(PSD_SE(i,:));
end
disp(['Mean squared error for Parceval identity is ' num2str(PSD_MSE(1,1),2) '↙
for Welch method and ' num2str(PSD_MSE(2,1),2) ' for Fourier calculation.'])
```

Fig. 6.12. *MATLAB* code for the subsection *Parceval identity check for calculated PSD*

The final part of the subroutine is dedicated to calculating the vertical coherence between each pair of measurement points and, subsequently, the frequency length scales over the vertical axis. In the subsection *Vertical coherence*, the coherence is calculated between each pair of the 12 measurement points, which results in a total of 66 different coherence functions from these combinations. The order of these points is determined in the first part of the code in this subsection. Next, the cross-spectra between each pair of points are calculated, as given in Eq. (3.40) and Eq. (3.41), as well as simplified power density spectra at each point for the calculation of the root-coherence as in Eq. (3.42). Then the co-coherence is obtained as the real part of the cross-spectra and quad-coherence – as the imaginary part of the cross-spectra. Only the co-coherence functions are of interest to the scope of this work. These functions are subsequently approximated with the Davenport model, the Bowen model and the modified Bowen model. The exponential decay constants for each of these models are calculated for each of the co-coherence functions. The code for this section is provided in Fig. 6.13.

```
%% VERTICAL COHERENCE
v_fluctuations=detrend(velocity_th)/k_v; %detrending the velocity time series,↙
%leaving only the fluctuations components
window_CPSD=round(m/30); %window for the cross-spectrum calculation
noverlap_CPSD=round(m/60); %number of overlapped samples for the cross-spectrum↙
%calculation
NFFT_CPSD=round(m/30); %number of DFT points for the cross-spectrum calculation

num_cpsd=nchoosek(1:1:n,2); %pairs of points
coh_num=nchoosek(n,2);
delta_z_coh=zeros(coh_num,1); %distance between the points
vm=zeros(coh_num,1); %mean wind speed for each pair of points
zm=zeros(coh_num,1); %mean height for each pair of points
for i=1:coh_num
    delta_z_coh(i)=Pheights(num_cpsd(i,2))-Pheights(num_cpsd(i,1));
    vm(i)=(v_mean(num_cpsd(i,1))+v_mean(num_cpsd(i,2)))/2/k_v;
    zm(i)=(Pheights(num_cpsd(i,1))+Pheights(num_cpsd(i,2)))/2;
end
coh_sets=cat(2,num_cpsd,delta_z_coh,vm,zm); %all of the combinations of pairs of↙
%the points in the vertical axis and the relative distances between each pair

f_coh=(0:fs/2/noverlap_CPSD:fs/2)/k_f;
f_dzvm=zeros(noverlap_CPSD+1,coh_num); %normalised frequency f*delta z/vm
for i=1:noverlap_CPSD+1
    for j=1:coh_num
        f_dzvm(i,j)=f_coh(i)*delta_z_coh(j)/vm(j);
```

```matlab
        end
end

cross_spectrum=zeros(noverlap_CPSD+1,coh_num); %vertical cross-spectrum between↙
%each pair of measurement points (at different heights)
for i=1:coh_num

cross_spectrum(:,i)=cpsd(v_fluctuations(:,(coh_sets(i,1))),v_fluctuations(:,(coh_↙
sets(i,2))),window_CPSD,noverlap_CPSD,NFFT_CPSD,fs);
end

pds_z=zeros(noverlap_CPSD+1,n); %power density spectra for each point

for i=1:n

pds_z(:,i)=cpsd(v_fluctuations(:,i),v_fluctuations(:,i),window_CPSD,noverlap_CPSD↙
,NFFT_CPSD,fs);
end

cocoherence=zeros(noverlap_CPSD+1,coh_num); %co-coherence
quadcoherence=zeros(noverlap_CPSD+1,coh_num); %quad-coherence
for i=1:noverlap_CPSD+1
    for j=1:coh_num

cocoherence(i,j)=real(cross_spectrum(i,j)/sqrt(pds_z(i,coh_sets(j,1))*pds_z(i,coh↙
_sets(j,2))));

quadcoherence(i,j)=imag(cross_spectrum(i,j)/sqrt(pds_z(i,coh_sets(j,1))*pds_z(i,c↙
oh_sets(j,2))));
    end
end

Cz=zeros(coh_num,1); %exponential decay for Davenport model
for i=1:coh_num
    [xData,yData]=prepareCurveData(f_coh,cocoherence(:,i));
    ft=fittype('exp(-Cz*x*deltaz/v_m)','independent','x','dependent','y');
    opts=fitoptions('Method','NonlinearLeastSquares');
    opts.Display='Off';
    opts.Lower=[0 delta_z_coh(i) vm(i)];
    opts.Robust='LAR';
    opts.StartPoint=[5 delta_z_coh(i) vm(i)];
    opts.Upper=[100 delta_z_coh(i) vm(i)];
    [fitresult,gof]=fit(xData,yData,ft,opts);
    Cz(i)=fitresult.Cz;
end

Davenport_coherence=zeros(noverlap_CPSD+1,coh_num); %Davenport model for co-↙
%coherence
for i=1:noverlap_CPSD+1
    for j=1:coh_num
        Davenport_coherence(i,j)=exp(-Cz(j)*f_coh(i)*delta_z_coh(j)/vm(j));
    end
end

c1=zeros(coh_num,1); %exponential decay c1 for Bowen model
c2=zeros(coh_num,1); %exponential decay c2 for Bowen model
for i=1:coh_num
    [xData,yData]=prepareCurveData(f_coh,cocoherence(:,i));
```

```matlab
    ft=fittype('exp(-c1*x*deltaz/v_m)*exp(-
(2*c2*x*deltaz^2)/((z1+z2)*v_m))','independent','x','dependent','y');
    opts=fitoptions('Method','NonlinearLeastSquares');
    opts.Display='Off';
    opts.Lower=[0 0 delta_z_coh(i) vm(i) Pheights(coh_sets(i,1))↵
Pheights(coh_sets(i,2))];
    opts.Robust='LAR';
    opts.StartPoint=[10 5 delta_z_coh(i) vm(i) Pheights(coh_sets(i,1))↵
Pheights(coh_sets(i,2))];
    opts.Upper=[100 100 delta_z_coh(i) vm(i) Pheights(coh_sets(i,1))↵
Pheights(coh_sets(i,2))];
    [fitresult,gof]=fit(xData,yData,ft,opts);
    c1(i)=fitresult.c1;
    c2(i)=fitresult.c2;
end

Bowen=zeros(noverlap_CPSD+1,coh_num); %Bowen model for co-coherence
for i=1:noverlap_CPSD+1
    for j=1:coh_num
        Bowen(i,j)=exp(-c1(j)*f_coh(i)*delta_z_coh(j)/vm(j))*exp(-(2*c2(j)*f_coh(↵
i)*delta_z_coh(j)^2)/((Pheights(coh_sets(j,1))+Pheights(coh_sets(j,2)))*vm(j)));
    end
end

c1m=zeros(coh_num,1); %exponential decay c1 for modified Bowen model
c2m=zeros(coh_num,1); %exponential decay c2 for modified Bowen model
c3m=zeros(coh_num,1); %exponential decay c3 for modified Bowen model
for i=1:coh_num
    [xData,yData]=prepareCurveData(f_coh,cocoherence(:,i));
    ft = fittype( 'exp(-(deltaz/v_m*sqrt((c1m*x)^2+c3m^2)))*exp(-↵
(2*c2m*x*deltaz^2)/((z1+z2)*v_m))', 'independent', 'x', 'dependent', 'y' );
    opts = fitoptions( 'Method', 'NonlinearLeastSquares' );
    opts.Display = 'Off';
    opts.Lower = [0 0 0 delta_z_coh(i) vm(i) Pheights(coh_sets(i,1))↵
Pheights(coh_sets(i,2))];
    opts.Robust='LAR';
    opts.StartPoint = [10 5 5 delta_z_coh(i) vm(i) Pheights(coh_sets(i,1))↵
Pheights(coh_sets(i,2))];
    opts.Upper = [100 100 100 delta_z_coh(i) vm(i) Pheights(coh_sets(i,1))↵
Pheights(coh_sets(i,2))];
    [fitresult,gof]=fit(xData,yData,ft,opts);
    c1m(i)=fitresult.c1m;
    c2m(i)=fitresult.c2m;
    c3m(i)=fitresult.c3m;
end

Bowen_mod=zeros(noverlap_CPSD+1,coh_num); %Bowen model for co-coherence
for i=1:noverlap_CPSD+1
    for j=1:coh_num
        Bowen_mod(i,j)=exp(-delta_z_coh(j)/vm(j)*sqrt((c1m(j)*f_coh(i))^2+c3m(j)↵
^2))*exp(-
(2*c2m(j)*f_coh(i)*delta_z_coh(j)^2)/((Pheights(coh_sets(j,1))+Pheights(coh_sets(↵
j,2)))*vm(j)));
    end
end
```

Fig. 6.13. *MATLAB* code for the subsection *Vertical coherence*

After calculating the co-coherence functions between each pair of points, the frequency length scales are calculated in the next subsection, *Frequency scales*. This is done based on the actual calculated values of the co-coherence functions and the approximation by the Davenport model. The function plots two graphs of the frequency length scales in relation to the distance between the two points Δ_z, always taking either the lowest or the highest measurement point as a reference. Both of these graphs include the relations of frequency length scales for the actual values of the co-coherence functions and for the Davenport approximation. The code for this subsection is shown in Fig. 6.14.

```matlab
%% FREQUENCY SCALES
fz_int=zeros(coh_num,1); %frequency scales directly from integration of the co-↙
%coherence function
fz_approx=zeros(coh_num,1); %frequency scales from approximation using the Cz↙
%exponential decay from the Davenport model
Tz_int=zeros(coh_num,1); %approximation period based on fz_int
Tz_approx=zeros(coh_num,1); %approximation period based on fz_approx

for i=1:coh_num
    fz_int(i)=trapz(f_coh,cocoherence(:,i));
    fz_approx(i)=vm(i)/Cz(i)/delta_z_coh(i);
    Tz_int(i)=1/fz_int(i);
    Tz_approx(i)=1/fz_approx(i);
end

fscale_z1_nums=find(coh_sets(:,1)==1);
fscale_z2_nums=find(coh_sets(:,2)==12);
fscale_z1=zeros(n-1,2);
fscale_z2=zeros(n-1,2);
for i=1:n-1
    fscale_z1(i,1)=fz_int(fscale_z1_nums(i));
    fscale_z1(i,2)=fz_approx(fscale_z1_nums(i));
    fscale_z2(i,1)=fz_int(fscale_z2_nums(i));
    fscale_z2(i,2)=fz_approx(fscale_z2_nums(i));
end
```

Fig. 6.14. *MATLAB* code for the subsection *Frequency scales*

The subroutine presented in this chapter also plots the figures of all the relevant data, as described, and saves the data to an excel sheet and the figures to a PDF document.

6.2. Selection of the test cases that best match the different terrain roughness categories

After the calculations described in subsection 6.1, a selection of the test cases that best match the different terrain roughness categories according to different standards was performed. As mentioned above, the categories were automatically assigned to each test case based on the vertical mean wind speed profile parameters. Tab. 6.1 summarises the statistics of how many test cases (and a percentage of the total) were assigned to each terrain roughness category according to different standards.

Tab. 6.1. Statistics of the test cases terrain roughness category assignment according to (ASCE/SEI 7, 2022; ISO 4354, 2009; PN-EN 1991-1-4, 2011)

PN-EN 1991-1-4		
Terrain roughness category	**Number of assigned test cases**	**Percentage of total test cases**
0	4	1.4%
I	4	1.4%
II	22	7.5%
III	23	7.8%
IV	242	82.0%
ISO 4354		
Terrain roughness category	**Number of assigned test cases**	**Percentage of total test cases**
1	4	1.4%
2	23	7.8%
3	46	15.6%
4	70	23.7%
5	152	51.5%
ASCE/SEI 7		
Terrain roughness category	**Number of assigned test cases**	**Percentage of total test cases**
D	4	1.4%
C	30	10.2%
B	62	21.0%
A	199	67.5%

Most of the test cases were assigned to terrain roughness category IV according to (PN-EN 1991-1-4, 2011), which corresponds to urban areas. This is not necessarily a disadvantage, as this is also the category that is most often simulated in the wind tunnel tests, because it corresponds to urban environments/city centres where the tallest buildings that require wind tunnel tests are usually located. Moreover, it should be noted that this assignment also includes the cases with much higher values of α exponent and/or roughness length z_0, which might be far from the proper approximation of the wind profiles. A similar trend can be noticed for the other standards as well.

Due to the large number of parameters upon which the selection should be based and a large number of cases for categories II, III and IV according to (PN-EN 1991-1-4, 2011) and for categories 2, 3, 4 and 5 according to (ISO 4354, 2009), a Multiple Attribute Decision Making (MADM) method was applied for this task. For the other categories or classifications, there were too few matching test cases or too few parameters to require such a method, therefore they were selected manually. The Technique for Order Preference by Similarity to Ideal Solution (TOPSIS) (Chakraborty, 2022) was chosen for this application. This method uses the following steps to find the optimal solution:

1) Calculating the normalised performance ratings. In this step, vector normalisation is used to obtain normalised performance ratings according to the following equation:

$$y_{ij} = \frac{x_{ij}}{\sqrt{\sum_{i=1}^{m} x_{ij}^2}}; i = 1,2,\dots,m \; j = 1,2,\dots,n \tag{6.13}$$

where: y_{ij} – normalised rating of i-th alternative over the j-th attribute, x_{ij} – performance rating of i-th alternative over the j-th attribute.

This makes the comparison across different parameters easier due to conversion to non-dimensional values.

2) Integrating weights with ratings. In this step, the normalised ratings are multiplied by the weights assigned for each attribute. The weights should be between 0 and 1, and the total sum of weights for all the attributes should be 1.

$$v_{ij} = w_j \cdot y_{ij} \tag{6.14}$$

where: v_{ij} – weighted-normalised rating of i-th alternative over the j-th attribute, w_j – weight of the j-th attribute.

3) Finding positive (ideal best) and negative (ideal worst) ideal solutions. The ideal best solution V_j^+ of the j-th attribute is either the maximum (for benefit attributes which are to be maximised in the optimal solution) or the minimum (for cost attributes which are to be minimised in the optimal solution) of the weighted-normalised rating values over the alternatives v_{ij}. On the other hand, the ideal worst solution V_j^- of the j-th attribute is either the minimum (for benefit attributes which are to be maximised in the optimal solution) or the maximum (for cost attributes which are to be minimised in the optimal solution) of the weighted-normalised rating values over the alternatives v_{ij}.

4) Obtaining the separation measures of each alternative rating from the positive and negative ideal solutions. This is done based on the Euclidean distance theory:

$$S_i^+ = \sqrt{\sum_{j=1}^{n} \left(v_{ij} - V_j^+\right)^2} \tag{6.15}$$

$$S_i^- = \sqrt{\sum_{j=1}^{n} \left(v_{ij} - V_j^-\right)^2} \tag{6.16}$$

where: S_i^+ – Euclidean distance of i-th alternative from ideal best solution, S_i^- – Euclidean distance of i-th alternative from ideal worst solution.

5) Calculating the overall preference score. This is based on the Euclidean distances from both the positive and negative ideal solutions. The alternatives are then ranked based on the higher preference score values (which can range between 0 and 1):

$$P_i = \frac{S_i^-}{S_i^- + S_i^+} \tag{6.17}$$

where P_i – preference score for the i-th alternative.

The following 6 parameters were accounted for as the attributes for the TOPSIS method: relative error of the α exponent of the power-law wind profile Δ_α, relative error of the β exponent Δ_β of the power-law turbulence intensity profile, relative error of the roughness length z_0 for the logarithmic wind profile Δ_{z_0}, RMSE between the power-law mean wind speed profile fit to the measured data and model power-law wind profile according to the code, RMSE between the logarithmic mean wind speed profile fit to the measured data and model logarithmic wind profile according to the code and RMSE between the measured values of turbulence intensity at each of the measurement heights and the reference turbulence intensity values from (ESDU 85020, 2002) on the corresponding heights (in the case of the application of this method for terrain categories according to (ISO 4354, 2009), instead of the last mentioned parameter, a relative error of the turbulence intensity value at the height of 30 m above the ground level $\Delta_{I_{v,30}}$ was used as a more appropriate one). The values of all these parameters were minimalised for the ideal solution. Different weights were selected for each of the parameters for the analyses done for different terrain categories and according to different standards. This was based on the overall distribution of these parameters for a given category, in a way that the method would accurately select the most optimal case. The values of weights assigned to each of the parameters for different analyses are shown in Tab. 6.2.

Tab. 6.2. Parameters and their weights taken into account for the TOPSIS method applied for different terrain categories and according to different standards

Parameter / Category	Δ_α	Δ_{z_0}	Δ_β	RMSE, power-law profile	RMSE, logarithmic profile	RMSE, turbulence intensity
II (PN-EN 1991-1-4)	0.2	0.1	0	0.15	0.15	0.4
III (PN-EN 1991-1-4)	0.05	0.05	0.1	0.25	0.25	0.3
IV (PN-EN 1991-1-4)	0.15	0.15	0.1	015	0.15	0.3
Parameter / Category	Δ_α	Δ_{z_0}	Δ_β	RMSE, power-law profile	RMSE, logarithmic profile	$\Delta_{Iv,30}$
2 (ISO 4354)	0.2	0.2	0	0.2	0.2	0.2
3 (ISO 4354)	0.2	0.2	0.05	0.2	0.2	0.15
4 (ISO 4354)	0.2	0.2	0.1	0.2	0.2	0.1
5 (ISO 4354)	0.1	0.1	0.05	0.3	0.3	0.15

The cases that best match each terrain category according to different standards are summarised in Tab. 6.3. For the cases where the TOPSIS method was used for the selection, preference scores for the chosen cases are also provided. The test cases selected as best matching the terrain categories according to (PN-EN 1991-1-4, 2011) are analysed in detail in chapter 8.

Tab. 6.3. Cases selected as best matching different terrain categories according to (ASCE/SEI 7, 2022; ISO 4354, 2009; PN-EN 1991-1-4, 2011)

Terrain roughness category	Selected case	Preference score
0 (PN-EN 1991-1-4)	3-98	–
I (PN-EN 1991-1-4)	3-99	–
II (PN-EN 1991-1-4)	2-128	0.831
III (PN-EN 1991-1-4)	3-10	0.706
IV (PN-EN 1991-1-4)	2-82	0.988
1 (ISO 4354)	3-98	–
2 (ISO 4354)	3-99	0.896
3 (ISO 4354)	3-10	0.874
4 (ISO 4354)	3-14	0.911
5 (ISO 4354)	3-69	0.912
D (ASCE/SEI 7)	3-98	–
C (ASCE/SEI 7)	2-126	–
B (ASCE/SEI 7)	2-135	–
A (ASCE/SEI 7)	3-15	–

7. Effects of roughness elements on different wind flow characteristics

A set of comparisons between the results of the test cases is made within this chapter. These comparisons depend on the turbulence-generating elements which were changed between the test cases. The purpose of this is an evaluation of the effect of each of these elements on various wind flow characteristics. Three different groups of parameters are analysed: parameters of the vertical mean wind speed and turbulence intensity profiles (exponents α and β, roughness length z_0 and turbulence intensity value at 30 m $I_{v,30}$), longitudinal and vertical length scales (L_x, $L_z \uparrow$ and $L_z \downarrow$) and frequency length scales f_z^*.

7.1. Effects of roughness elements on vertical mean wind speed and turbulence intensity profiles

In the first part of this analysis, the most important parameters of mean wind speed and turbulence intensity profiles are compared: power-law exponents of the vertical wind speed profile α, power-law exponent of the vertical turbulence intensity profile β (taken with a minus sign, for convenience of the presentation), roughness length z_0 for the logarithmic mean wind speed profile and turbulence intensity value at the height of 30 m.

Fig. 7.1-Fig. 7.12 show the comparison of these 4 parameters depending on the elevation of blocks at the inlet and at the fetch length for each of the 12 combinations of barriers, spires and turbulising net. All of the arrangements that were tested in cases 3-76 to 3-95, which include 120 cm spires mounted backwards, are shown in the same chart (Fig. 7.12).
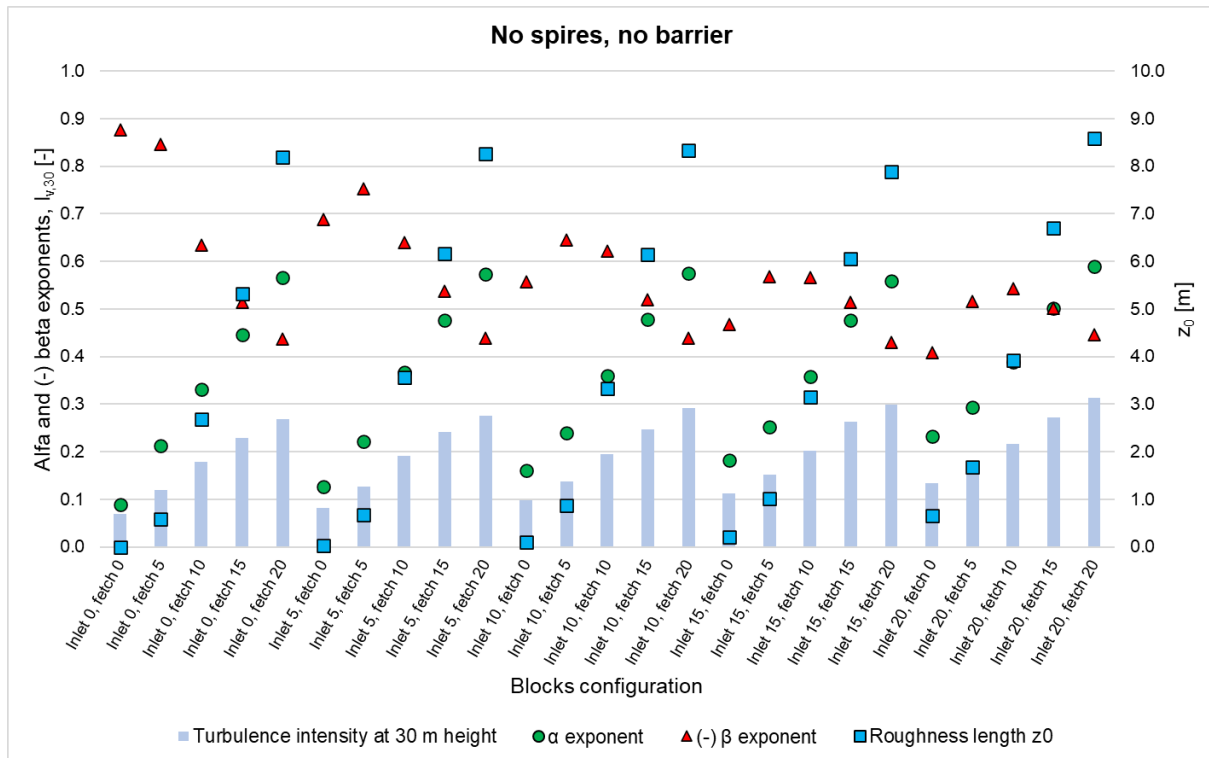
Fig. 7.1. Comparison of vertical wind profile and turbulence intensity parameters for different blocks elevations for the arrangements without spires or barrier (cases 1-1 to 1-25)
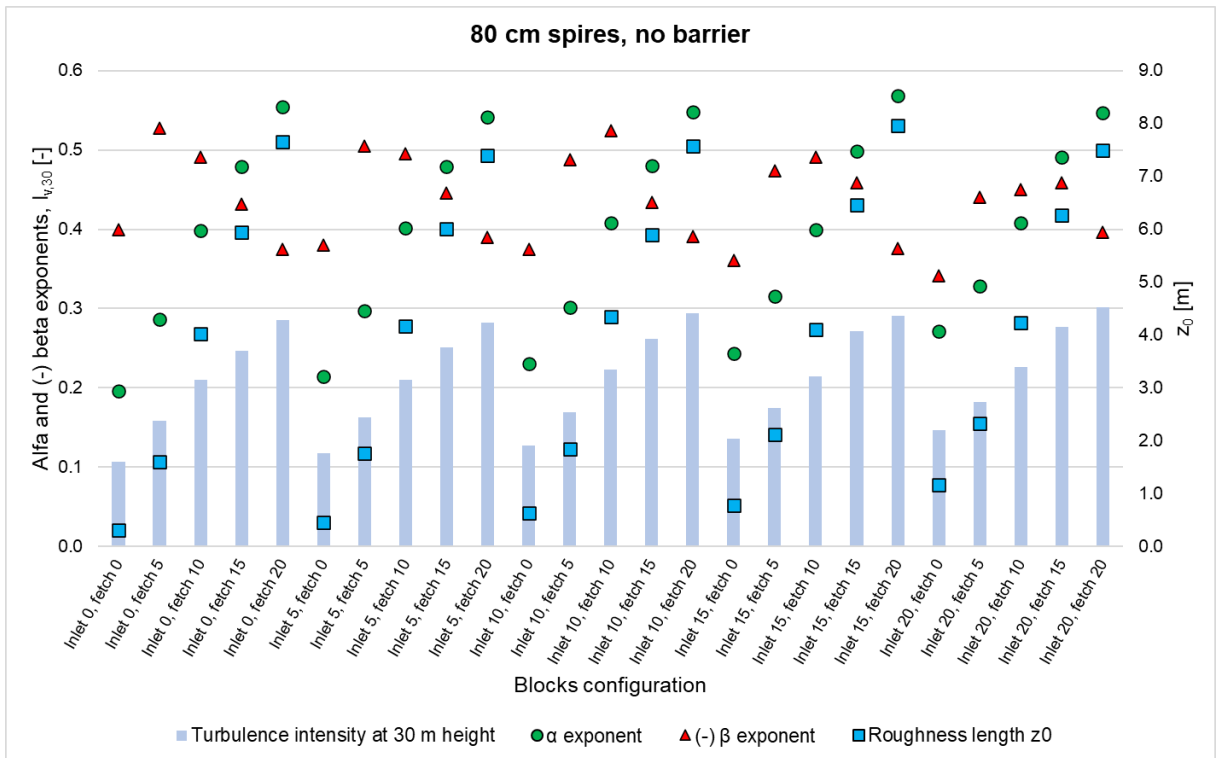
Fig. 7.2. Comparison of vertical wind profile and turbulence intensity parameters for different blocks elevations for the arrangements with 80 cm tall spires and no barrier (cases 2-1 to 2-25)
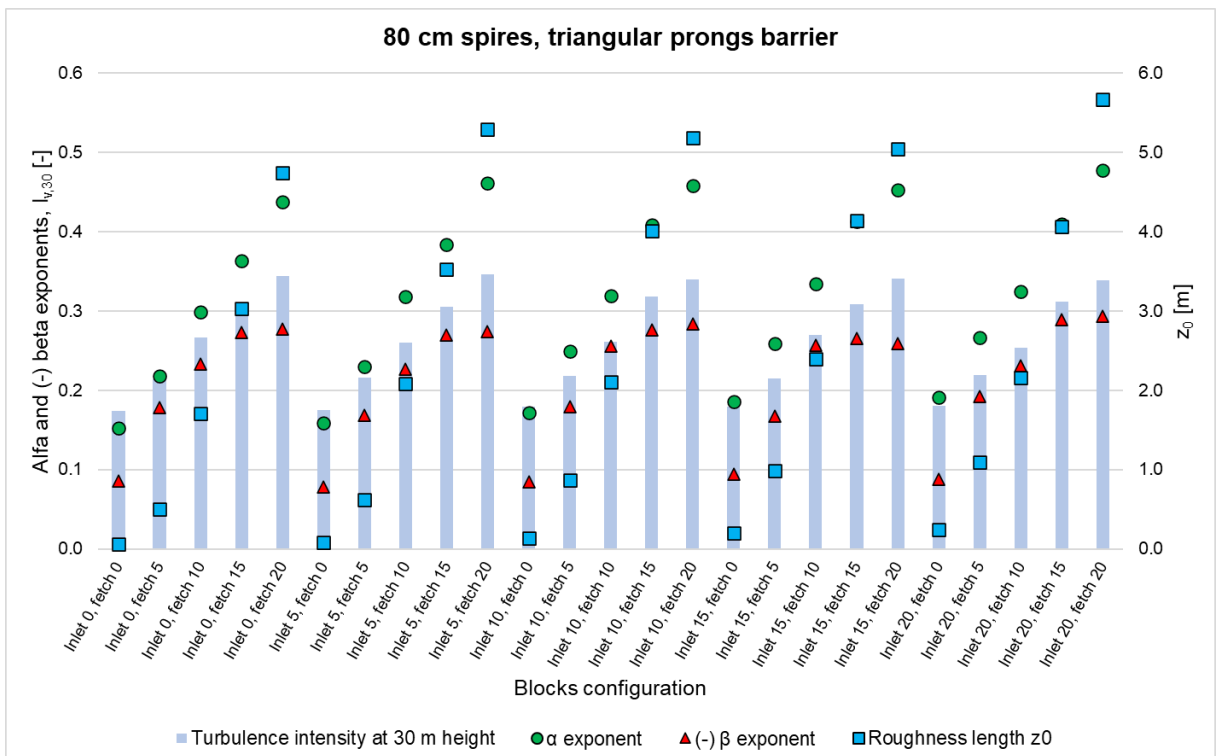
Fig. 7.3. Comparison of vertical wind profile and turbulence intensity parameters for different blocks elevations for the arrangements with 80 cm tall spires and triangular prongs barrier (cases 2-26 to 2-50)
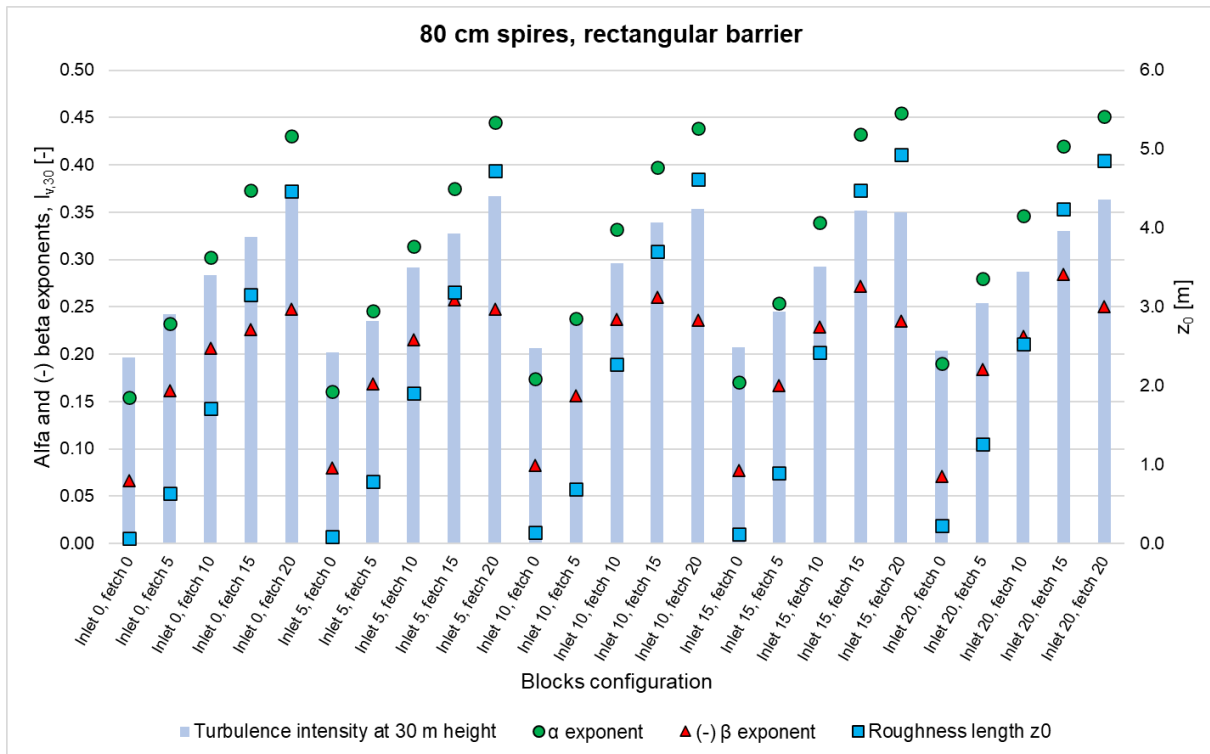
Fig. 7.4. Comparison of vertical wind profile and turbulence intensity parameters for different blocks elevations for the arrangements with 80 cm tall spires and rectangular barrier (cases 2-51 to 2-75)
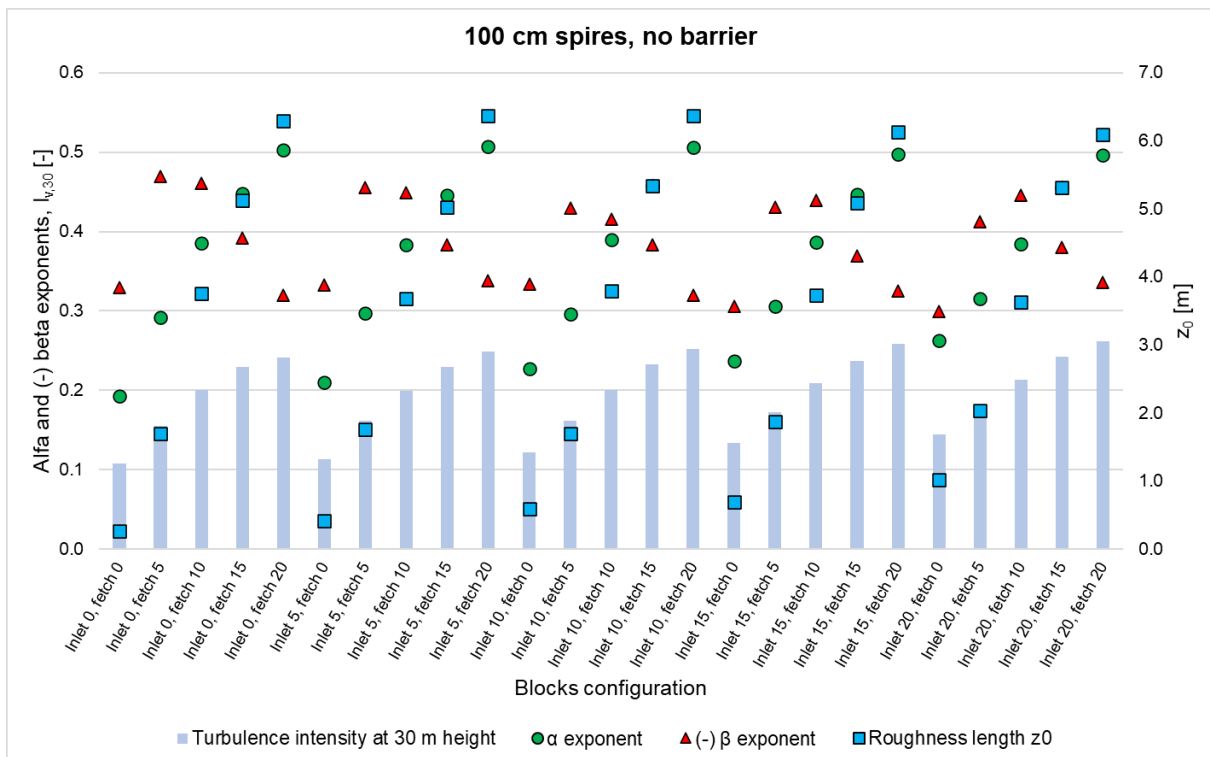
Fig. 7.5. Comparison of vertical wind profile and turbulence intensity parameters for different blocks elevations for the arrangements with 100 cm tall spires and no barrier (cases 2-101 to 2-125)
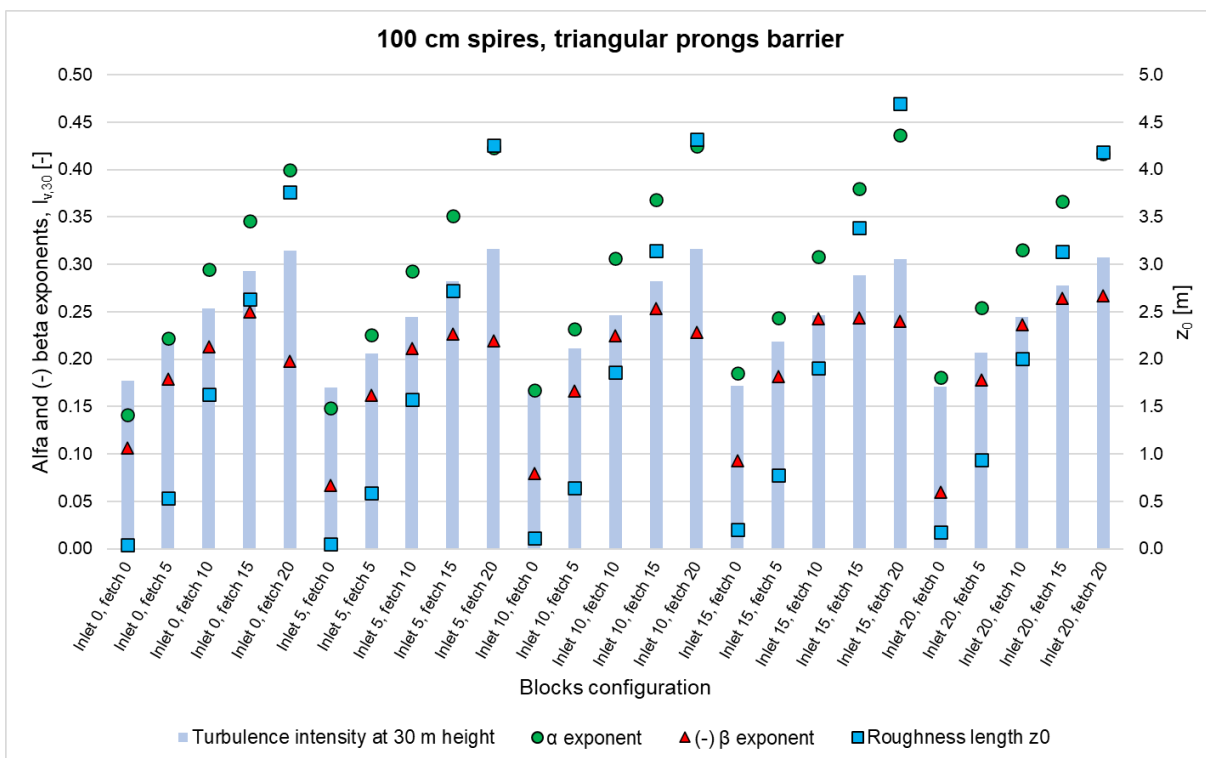
Fig. 7.6. Comparison of vertical wind profile and turbulence intensity parameters for different blocks elevations for the arrangements with 100 cm tall spires and triangular prongs barrier (cases 2-126 to 2-150)
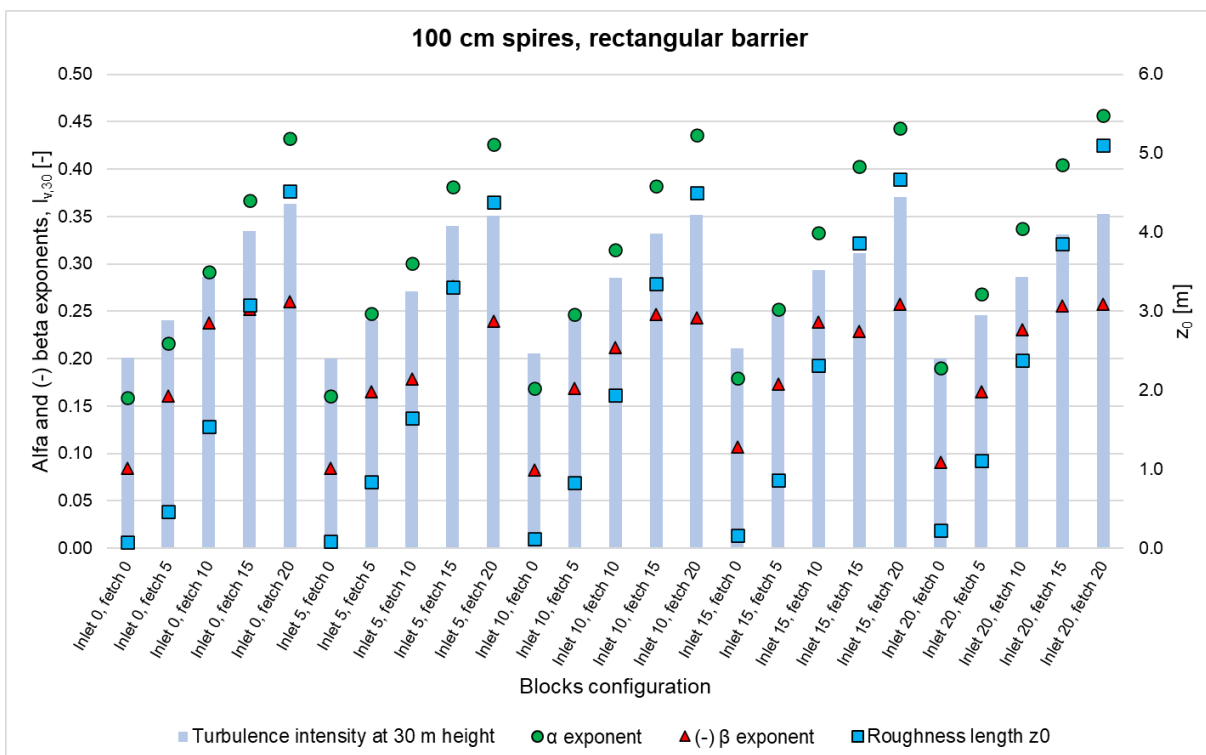
Fig. 7.7. Comparison of vertical wind profile and turbulence intensity parameters for different blocks elevations for the arrangements with 100 cm tall spires and rectangular barrier (cases 2-76 to 2-100)
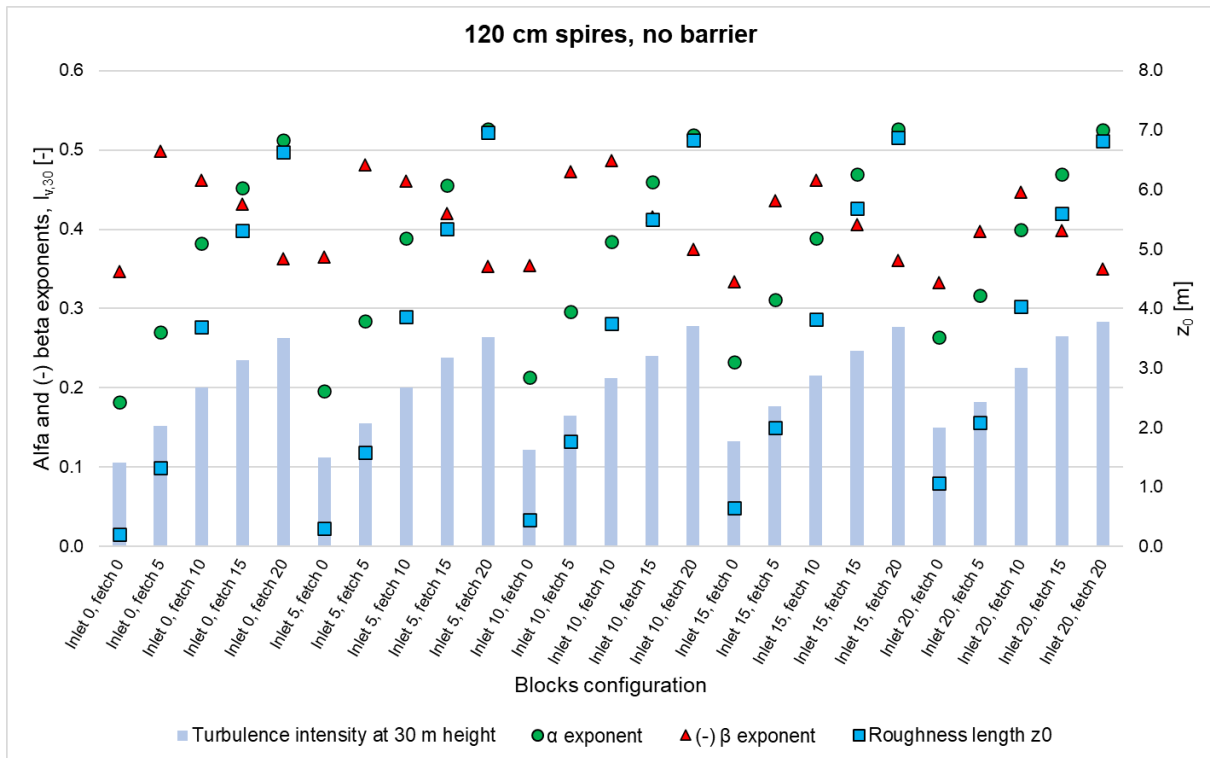
Fig. 7.8. Comparison of vertical wind profile and turbulence intensity parameters for different blocks elevations for the arrangements with 120 cm tall spires and no barrier (cases 3-26 to 3-50)
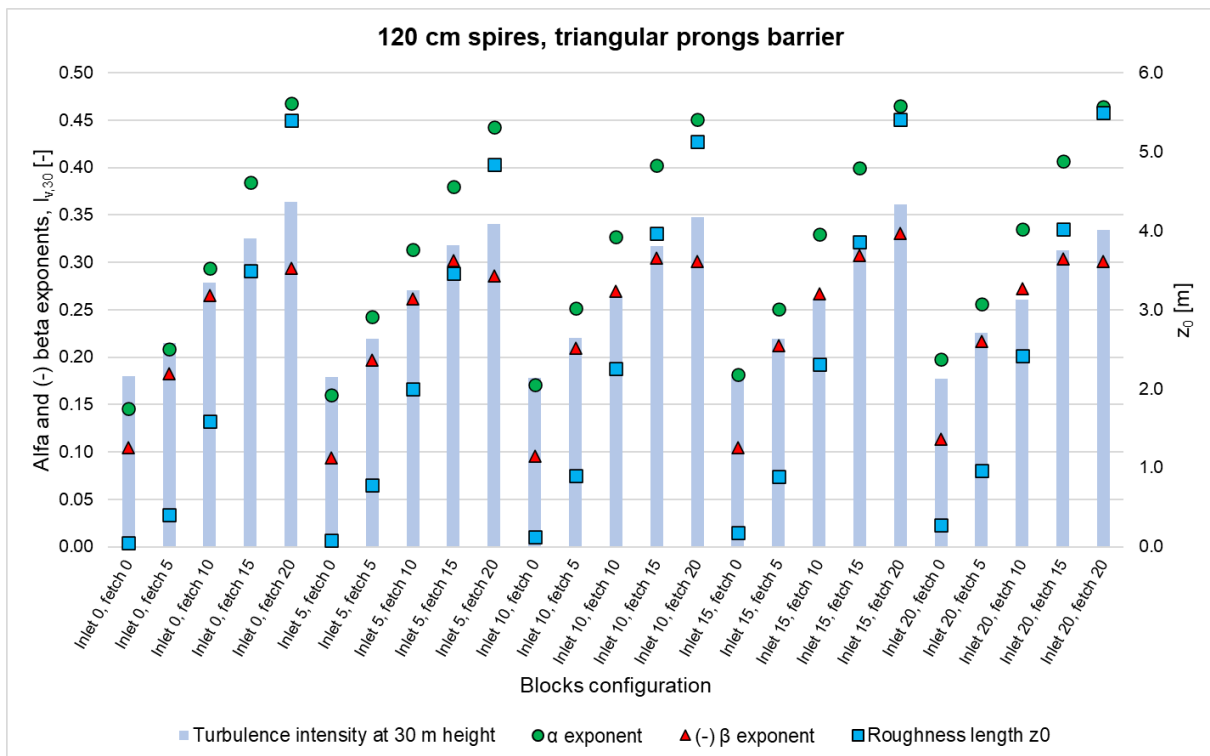
Fig. 7.9. Comparison of vertical wind profile and turbulence intensity parameters for different blocks elevations for the arrangements with 120 cm tall spires and triangular prongs barrier (cases 3-1 to 3-25)
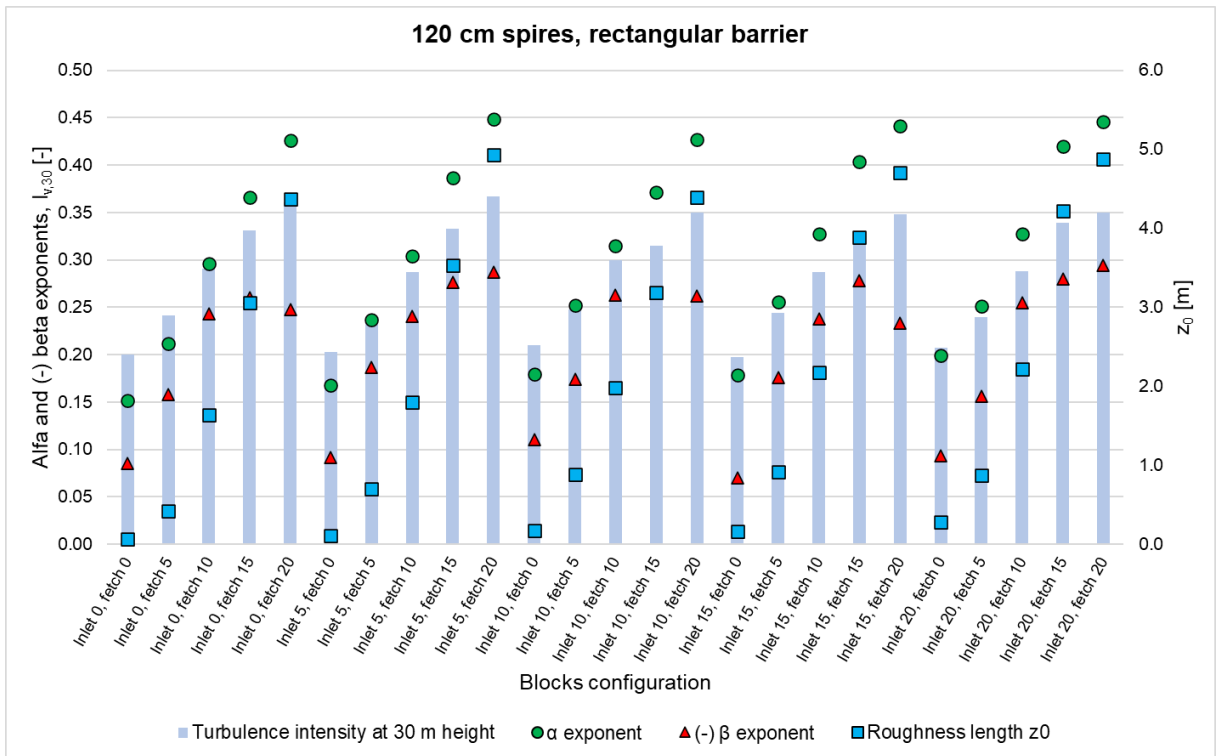
Fig. 7.10. Comparison of vertical wind profile and turbulence intensity parameters for different blocks elevations for the arrangements with 120 cm tall spires and rectangular barrier (cases 3-51 to 3-75)
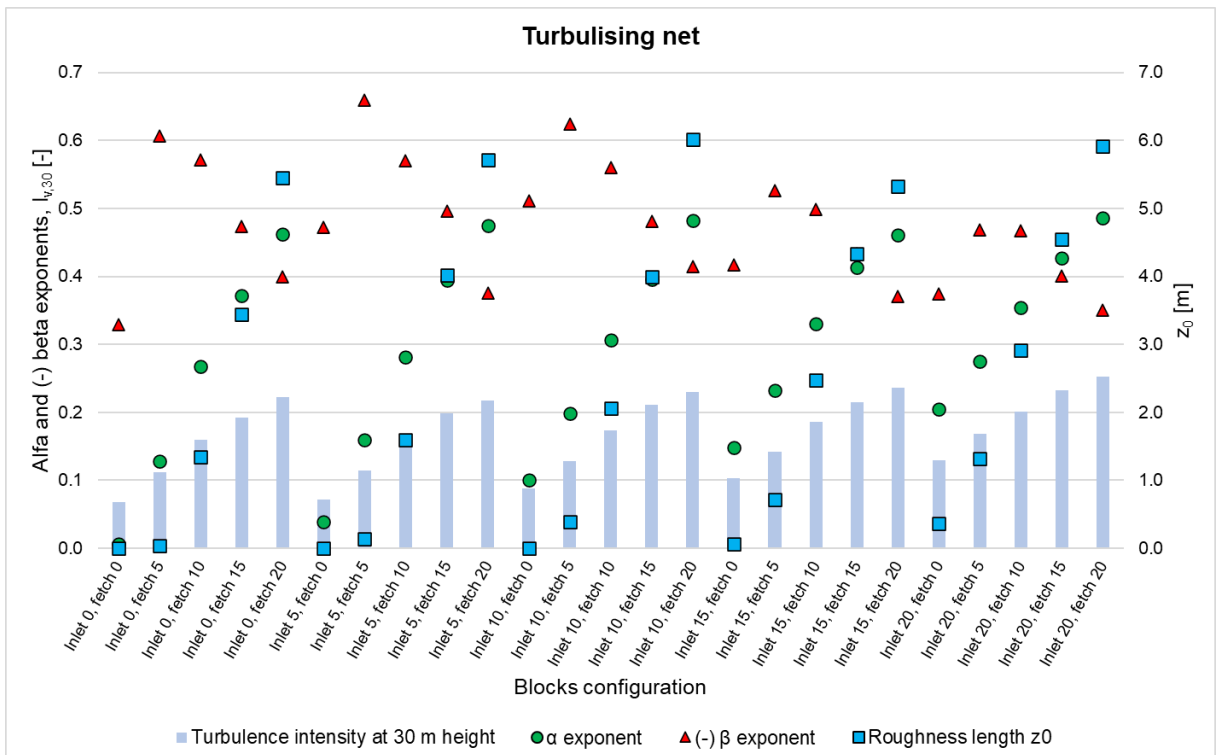
Fig. 7.11. Comparison of vertical wind profile and turbulence intensity parameters for different blocks elevations for the arrangements with turbulence net (bars and patches) (cases 3-96 to 3-120)
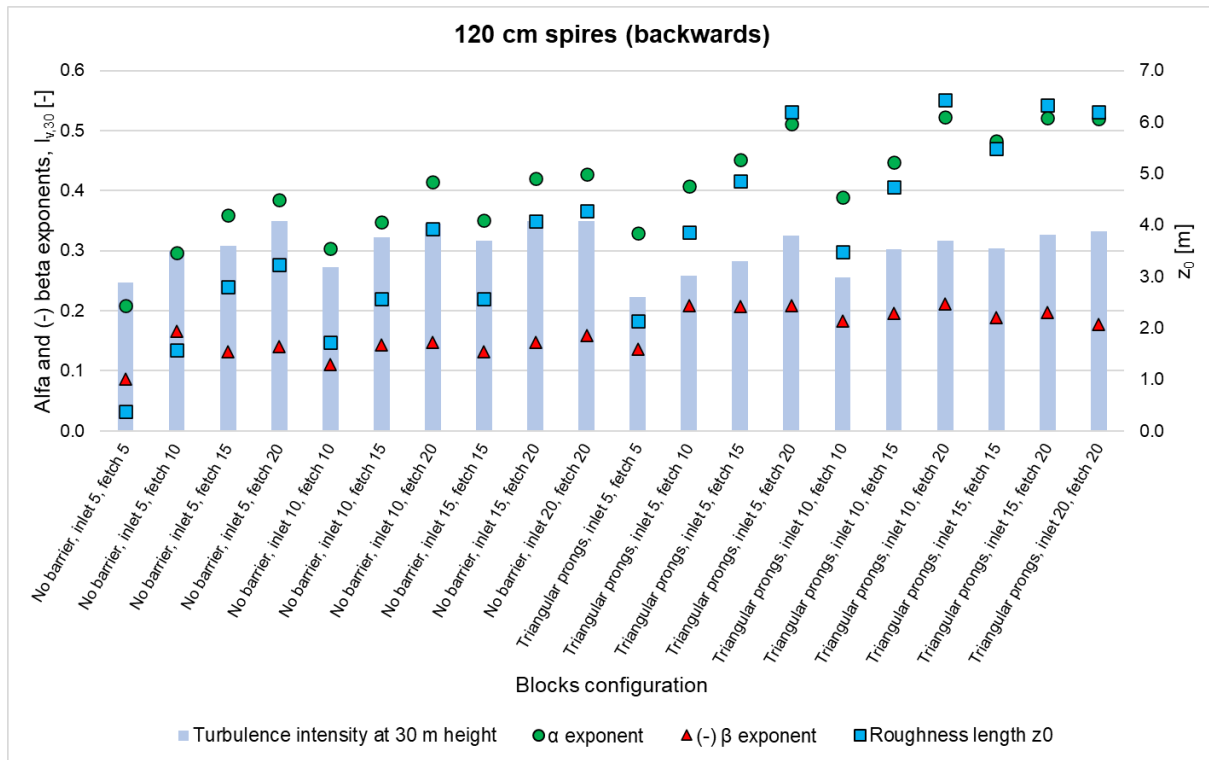
Fig. 7.12. Comparison of vertical wind profile and turbulence intensity parameters for different blocks elevations and barrier types for the arrangements with 120 cm spires mounted backwards (cases 3-76 to 3-95)

The first thing that can be noticed in these charts, is that there is very little impact on the four analysed parameters from the height of the blocks at the inlet (first segment) of the wind tunnel in most of the arrangements. In fact, the blocks' height at the inlet seems to have a significant impact on the results only in the cases without any spires or barrier, either with or without the turbulising net (Fig. 7.1 and Fig. 7.11). Furthermore, there is some influence from the blocks at the inlet in the cases where the spires are present, but there are no barriers (Fig. 7.2, Fig. 7.5 and Fig. 7.8). This is observable in particular on the values of the roughness length z_0, which is largely influenced by the height of the blocks at the inlet in the cases without barriers and with the low elevation of the blocks (0 or 5 cm) on the fetch length. For the other cases, this influence is almost negligible compared to the impact of the blocks at the fetch length.

On the other hand, clear patterns can be observed for each of the analysed parameters which are repeated when considering the heights of the blocks at the fetch length in the same spires/barrier arrangements. The α exponent, which defines the shape of the power-law vertical mean wind speed profile, increases in a linear trend with increasing heights of the blocks at the fetch length.

Similarly, there is an increase of the turbulence intensity level at the height corresponding to 30 m in real-life scale with the taller elevation of the blocks at the fetch length. In the cases without any barrier, the trend of this increase is steeper for the lower blocks elevations, while in the cases with a rectangular barrier, it is almost linear. As for the cases with the triangular prongs barrier, the trend seems to be in the middle between the two other arrangements of the barrier. As mentioned before, according to (Davenport, 1984), the value of turbulence intensity at this level is approximately equal to the α exponent. This is best met for the cases

with either rectangular or triangular prongs barriers, blocks at the fetch length at 5 cm and blocks at the inlet at 0, 5 or 10 cm. For the cases with blocks at the fetch length at 0 cm, the α exponent is usually smaller than $I_{v,30}$, while for the cases with blocks at the fetch length higher than 5 cm, it is greater than $I_{v,30}$.

The roughness length z_0 also shows an increasing trend, however, the pattern is non-linear and more similar to an exponential curve, with only a slight increase between 0 to 5 cm blocks at the fetch length, larger between 5 to 10 cm and the largest between 10 to 15 cm and 15 to 20 cm. This trend is less visible in the cases without the barriers, where the increasing trend is closer to linear. It should also be noted that according to various codes, this value is usually no larger than 1.0 m (2.5 m for the additional terrain roughness category concerning the large city centres as per (ISO 4354, 2009)). The roughness length in the wind tunnel tests is in this range for the blocks' elevation at the fetch length of 0 cm and 5 cm (10 cm if considering the values of about 2, but only in the cases with either type of barrier).

Finally, the β exponent, which determines the shape of the vertical turbulence intensity power-law profile, has vastly different trends for different barrier arrangements. These exponents seem to be maximal for the cases where the blocks at the fetch length are at 5 or 10 cm, with a steep increase between 0 to 5 cm and a calmer decrease for 15 and 20 cm. For the cases with triangular prongs barrier, there is also a very steep increase between 0 and 5 cm, but the increase continues and peaks at 15 or 20 cm blocks elevation. For the cases with a rectangular barrier, a steep increase can be usually observed for the change of elevation from 0 to 5 cm and 5 to 10 cm, while the value of this exponent is kept at an almost constant level for the elevations of 10, 15 and 20 cm.

For the two configurations without any spires or barriers (Fig. 7.1 and Fig. 7.11), similar trends can be observed for the α exponent, roughness length z_0 and turbulence intensity at 30 m height, i.e. increasing in a linear way with the increase of blocks elevations at the fetch length. However, an increase in the values of these parameters can also be observed with the increase in the elevation of the inlet blocks. As for the β exponent, there is no clear trend to be observed for these cases, however, it can be noticed that in most cases, this exponent has the highest values when the blocks at the fetch length are at 5 cm elevation. The value of this exponent obtained for the case with a completely empty tunnel (case 1-25), where the blocks are at 0 cm elevation at both the inlet and the fetch length, seems less reliable, as the turbulence has very low values and barely varies along the height of the wind tunnel, meaning its vertical profile might not be best described by the power-law curve.

The configurations with 120 cm spires mounted backwards at the inlet of the wind tunnel show similar patterns of influence on the α exponent and turbulence intensity value at the height of 30 m as the corresponding cases with the spires mounted regularly, however, the increase of these values seems to be significantly less steep. In the case of the β exponent, it is kept at a very similar level for all of the blocks combinations, at about -0.19 without any barrier and -0.14 with the triangular prongs barrier, which is much lower than for the corresponding cases with the spires mounted regularly. The values of the α exponent are, on average, on a very similar level as for the corresponding cases with the spires mounted regularly for the cases without any barrier and at about 10% lower value on average for the cases with the triangular prongs barrier. The turbulence intensity at 30 m height, on the other

hand, is on a very similar level on average as for the corresponding cases with the spires mounted regularly for the cases with triangular prongs barrier (3% difference on average), while it differs largely for the cases without any barrier (with the spires mounted backwards, the values are 23% higher on average). As for the β exponent, for the setups that include the barrier, its values are much lower (about 52% lower on average) than for the corresponding cases with the spires mounted regularly. Finally, the trend of the roughness length values changes to more linear, with significantly higher values of the roughness length for most cases. These significant changes in the β exponent and roughness length values seem to be the most significant difference when it comes to the method of mounting the spires at the inlet and as can be seen, the spires mounted backwards tend to result in combinations of the vertical wind speed and turbulence intensity profiles that do not match the standard terrain categories. Furthermore, these arrangements introduce a larger blockage ratio to the flow (thus significantly reducing the wind speed in the wind tunnel), which, in general, may have a negative effect on the results.

For a clearer analysis and presentation of the influence of the different types and heights of the spires and barriers on the vertical wind profile parameters, another set of charts presents the influence of different spires heights with the same barrier arrangements (Fig. 7.13-Fig. 7.15) and the influence of different barrier types for the same height of the spires (Fig. 7.16-Fig. 7.18). For the sake of brevity and according to the conclusions drawn from Fig. 7.2-Fig. 7.10 presented above, regarding the small influence of the blocks at the inlet of the wind tunnel, the charts presented below are made only for a single elevation of the inlet blocks at 5 cm, as representative of all the similar arrangements (differing by the height of the blocks at the inlet) with an approximation sufficient for this analysis.
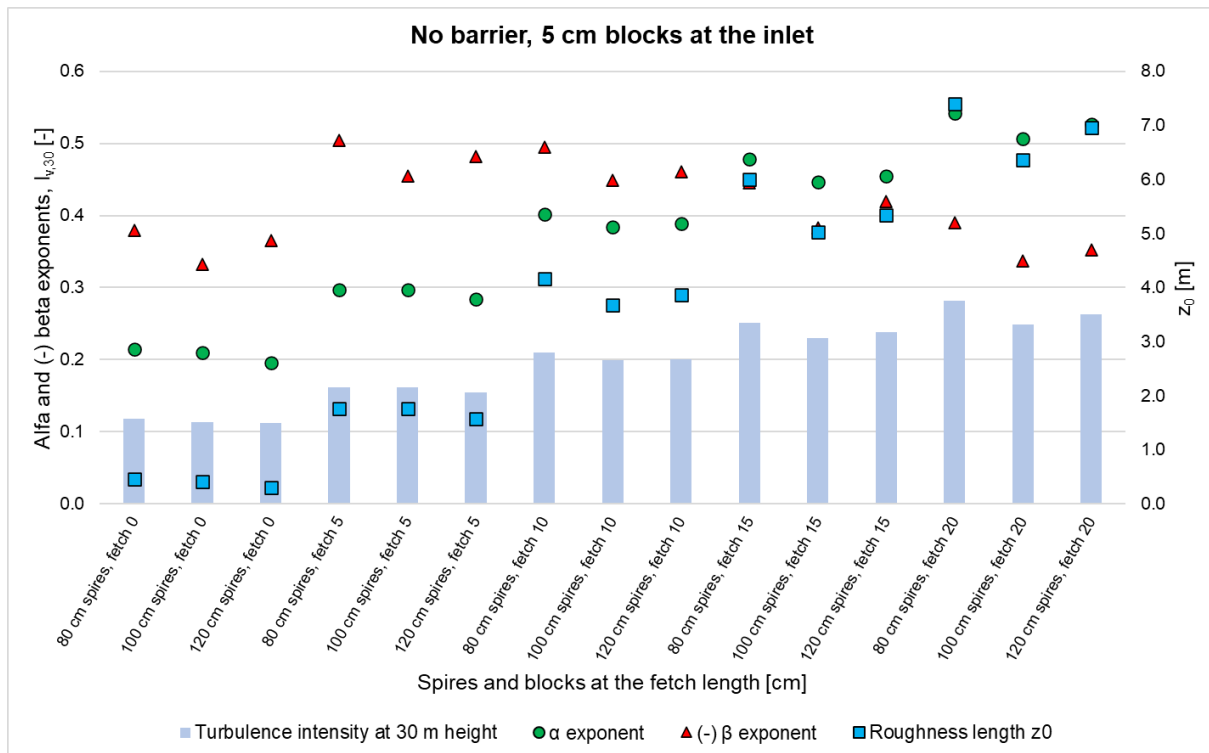
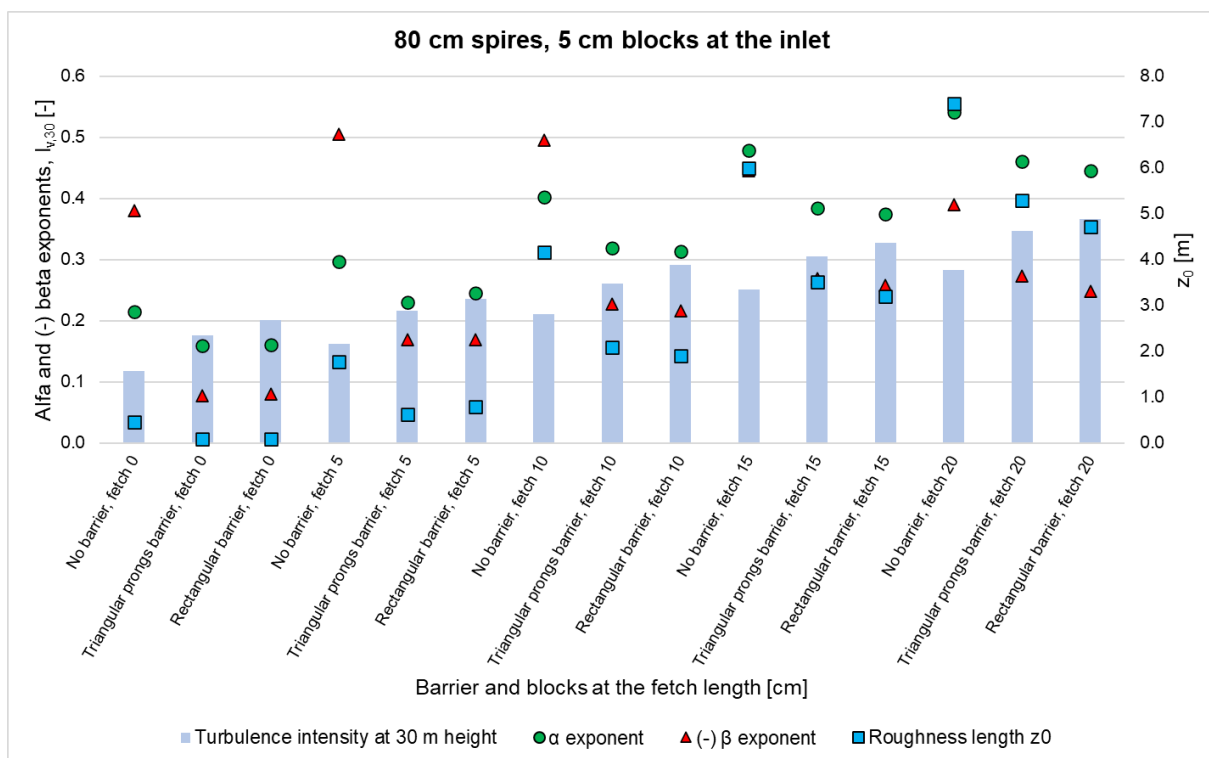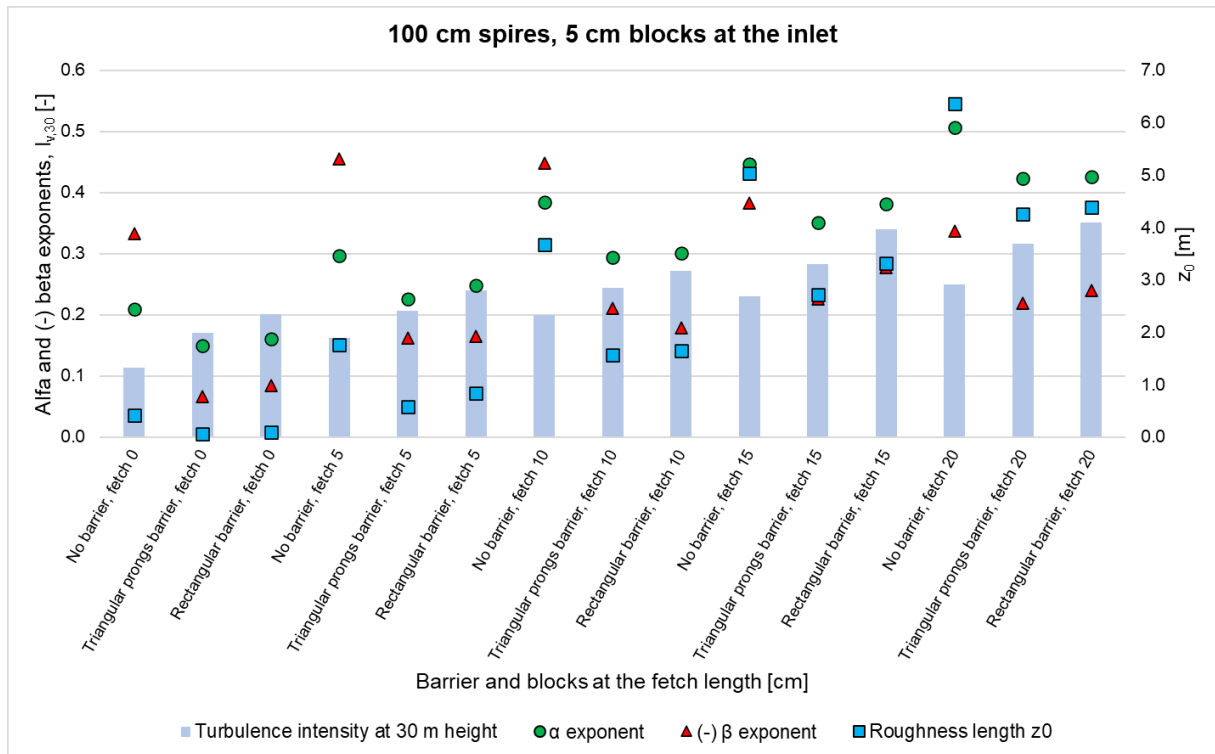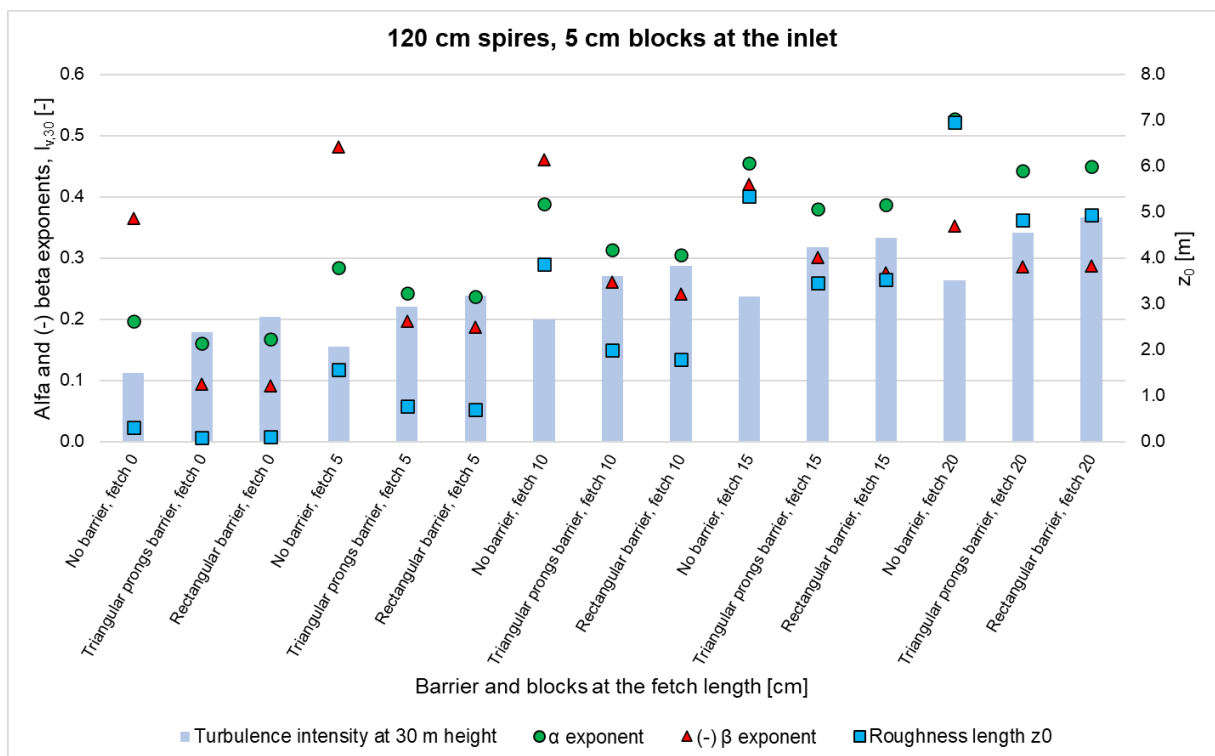

Fig. 7.13. Comparison of vertical wind profile and turbulence intensity parameters for different blocks elevations at the fetch length and spires heights for the arrangements with no barrier (cases 2-2, 2-9, 2-12, 2-19, 2-22, 2-102, 2-109, 2-112, 2-119, 2-122, 3-27, 3-34, 3-37, 3-44 and 3-47)
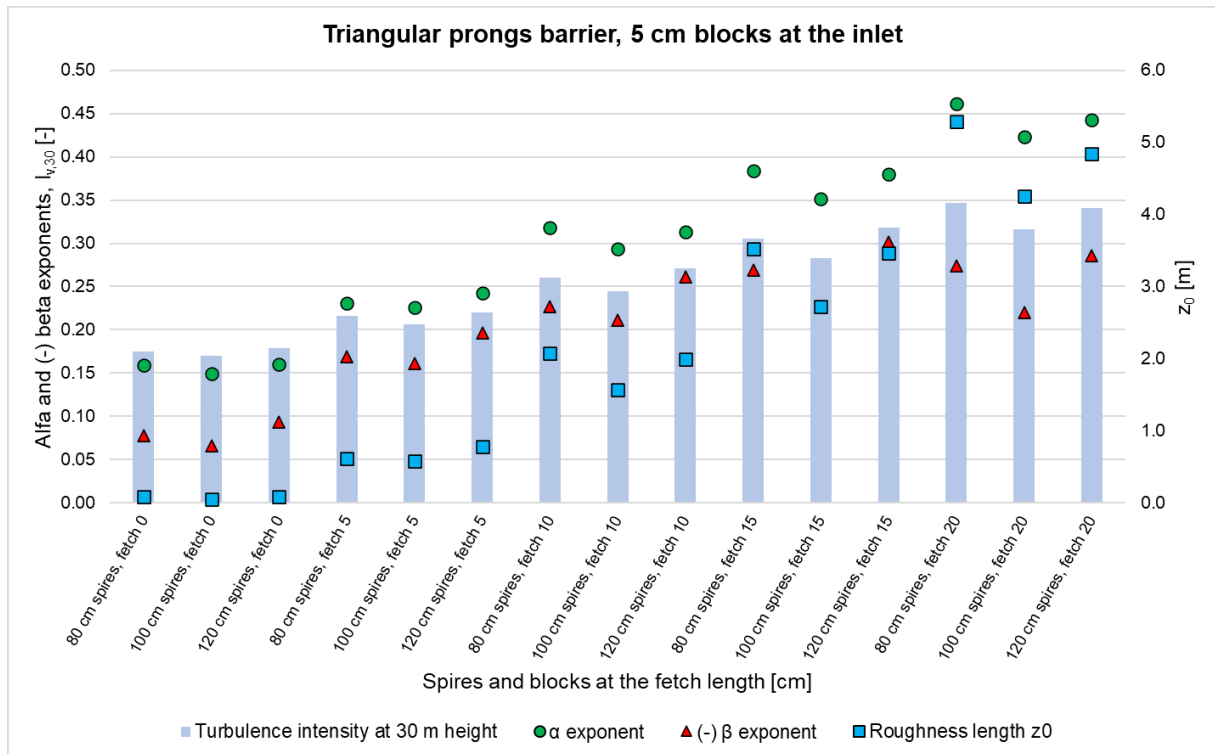
Fig. 7.14. Comparison of vertical wind profile and turbulence intensity parameters for different blocks elevations at the fetch length and spires heights for the arrangements with triangular prongs barrier (cases 2-27, 2-34, 2-37, 2-44, 2-47, 2-127, 2-134, 2-137, 2-144, 2-147, 3-2, 3-9, 3-12, 3-19 and 3-22)
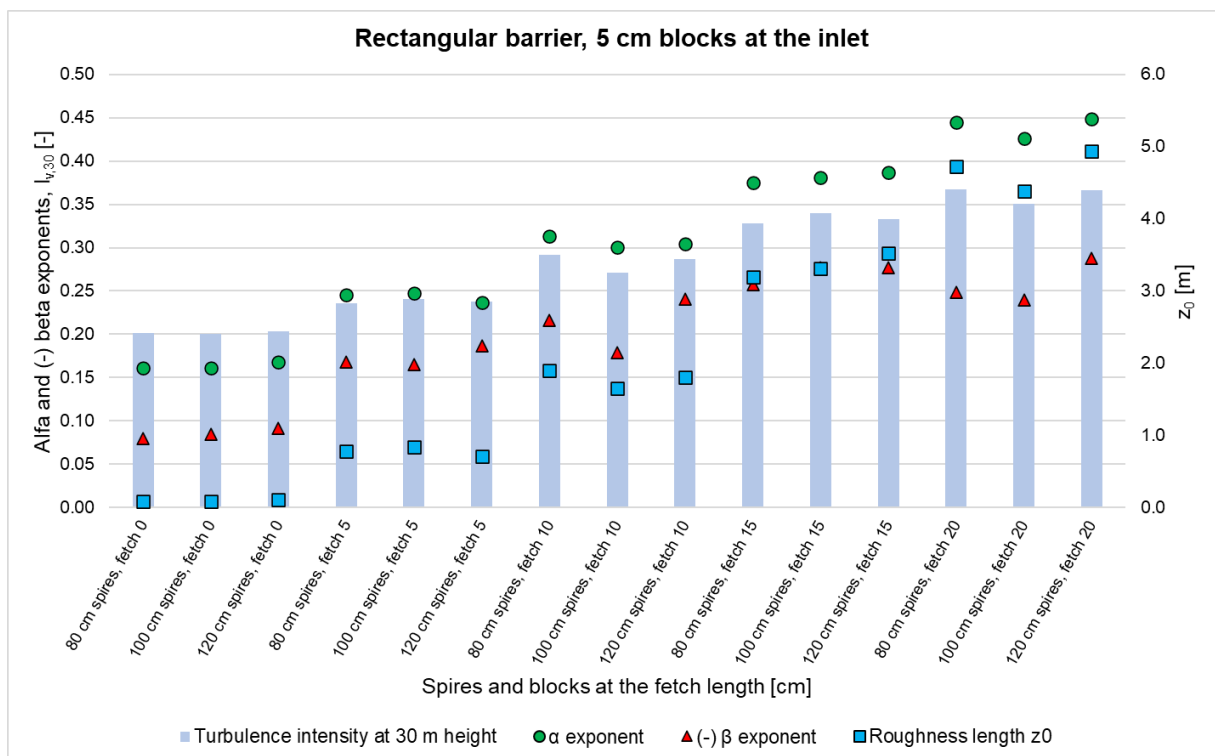
Fig. 7.15. Comparison of vertical wind profile and turbulence intensity parameters for different blocks elevations at the fetch length and spires heights for the arrangements with rectangular barrier (cases 2-52, 2-59, 2-62, 2-69, 2-72, 2-77, 2-84, 2-87, 2-94, 2-97, 3-52, 3-59, 3-62, 3-69 and 3-72)

Conclusions about the influence of the spires' height on the vertical wind profiles can be drawn from Fig. 7.13-Fig. 7.15 presented above. In the cases without the barrier, this influence manifests itself mostly through the values of the β exponent, which is largest in the cases with 80 cm spires and smallest in the cases with 100 cm spires. Such a pattern suggests that this influence is non-linear, which can be partially a result of different blockage ratios at the inlet of the wind tunnel resulting from the different heights of spires or larger influence of the blocks at the fetch length in the cases with shorter (80 cm and 100 cm) spires compared to the 120 cm spires.

A very similar trend can be observed for the roughness length z_0, α exponent and – to a lesser extent – $I_{v,30}$, for the cases with a higher elevation of blocks at the fetch length (10, 15 or 20 cm), with the smallest values occurring for the 100 cm spires. This is most visible in the cases with the triangular prongs barrier. This further supports the conclusion that the influence of the blocks' elevation at the fetch length might be higher in the cases with 80 cm and 100 cm spires.

For the cases with blocks at the fetch length of 0 or 5 cm elevation, the roughness length z_0, α exponent and $I_{v,30}$ values are relatively stable with regard to the height of the spires.

With the rectangular barrier, the differences depending on the height of the spires are least visible, furthermore, there is no clear pattern influenced by the height of the spires on any of the considered parameters. The largest differences between these cases can be observed for the values of the β exponent.

Fig. 7.16. Comparison of vertical wind profile and turbulence intensity parameters for different blocks elevations at the fetch length and barrier types for the arrangements with 80 cm spires (cases 2-2, 2-9, 2-12, 2-19, 2-22, 2-27, 2-34, 2-37, 2-44, 2-47, 2-52, 2-59, 2-62, 2-69 and 2-72)

Fig. 7.17. Comparison of vertical wind profile and turbulence intensity parameters for different blocks elevations at the fetch length and barrier types for the arrangements with 100 cm spires (cases 2-77, 2-84, 2-87, 2-94, 2-97, 2-102, 2-109, 2-112, 2-119, 2-122, 2-127, 2-134, 2-137, 2-144 and 2-147)

Fig. 7.18. Comparison of vertical wind profile and turbulence intensity parameters for different blocks elevations at the fetch length and barrier types for the arrangements with 120 cm spires (cases 3-2, 3-9, 3-12, 3-19, 3-22, 3-27, 3-34, 3-37, 3-44, 3-47, 3-52, 3-59, 3-62, 3-69 and 3-72)

The three charts presented above in Fig. 7.16-Fig. 7.18 allow for a comparison of different types of barriers used with the same height of the spires. The most obvious observation for all the heights of the spires is that both the α and β exponents and the roughness length z_0 are highest in cases without any barrier (when comparing the same elevations of the blocks at the fetch length). These differences are relatively largest for the cases with lower elevations of the blocks at the fetch length (0 and 5 cm) and for the values of β exponent.

Furthermore, there is a clear pattern of the influence of the type of barriers on the turbulence intensity level at 30 m, which can be observed for all the cases with different blocks' elevations at the fetch length or spires height. The value of this parameter is always the lowest in cases without any barriers and highest in cases with a rectangular barrier. This is a significant finding, as it shows how the turbulence intensity level at the lower (closer to the ground) layers of the inflow can be manipulated relatively easily without substantially influencing the other parameters of the vertical wind velocity and turbulence intensity profiles.

Finally, a comparison between the values of the α and β exponents was made (taking into account the absolute values of β exponents). According to the approximate formula for the vertical wind turbulence intensity profile given in Eq. (3.66), β can be assumed as equal to negative α. The comparison showed that only in 51 cases (17%), β was in the range of $\alpha \pm 20\%$. In 68 cases (23%), β was larger than 120% of α and in the vast majority of the test cases (176 or 60%), β was smaller than 80% of α. This shows that, while reasonably practical for casual engineering applications, the approximate equation for turbulence intensity profile might be too much of a simplification for the scientific purposes and model tests in the wind tunnels.

The roughness length z_0^T for logarithmic turbulence intensity profile was not considered for these comparisons, as its values are in a much larger range than these of z_0, therefore it was decided to omit this parameter for the sake of clarity of the comparison plots.

7.2. Effects of roughness elements on turbulence length scales

A similar analysis to the one described above was done for the parameters related to the turbulence length scales. The longitudinal turbulence length scale L_x, which was obtained from the autocorrelation of the wind velocity time series, was calculated at each of the 12 measuring heights. For the sake of clarity of the plots, only the results from 4 of these heights are presented: at 17.5 m (1st probe at the lowest level), 55 m (4th probe), 105 m (8th probe) and 155 m (12th probe at the highest level). The plots also show vertical turbulence length scales moving in upward and downward directions, which are calculated based on vertical spatial correlations. The values of the turbulence length scales are given in a dimensional form, after the transition from the model scale to the real-life scale.

The layout of the analysis presented herein is very similar to the one in subsection 7.1, i.e. at first, a detailed analysis of the influence of the heights of the blocks at the inlet and at the fetch length is shown for each of the 12 setups of barriers, spires and turbulising net (Fig. 7.19-Fig. 7.30). Then once again, an analysis is made for a set value of blocks' elevation at the inlet (at 5 cm) regarding the influence of different heights of spires or different types of barrier.
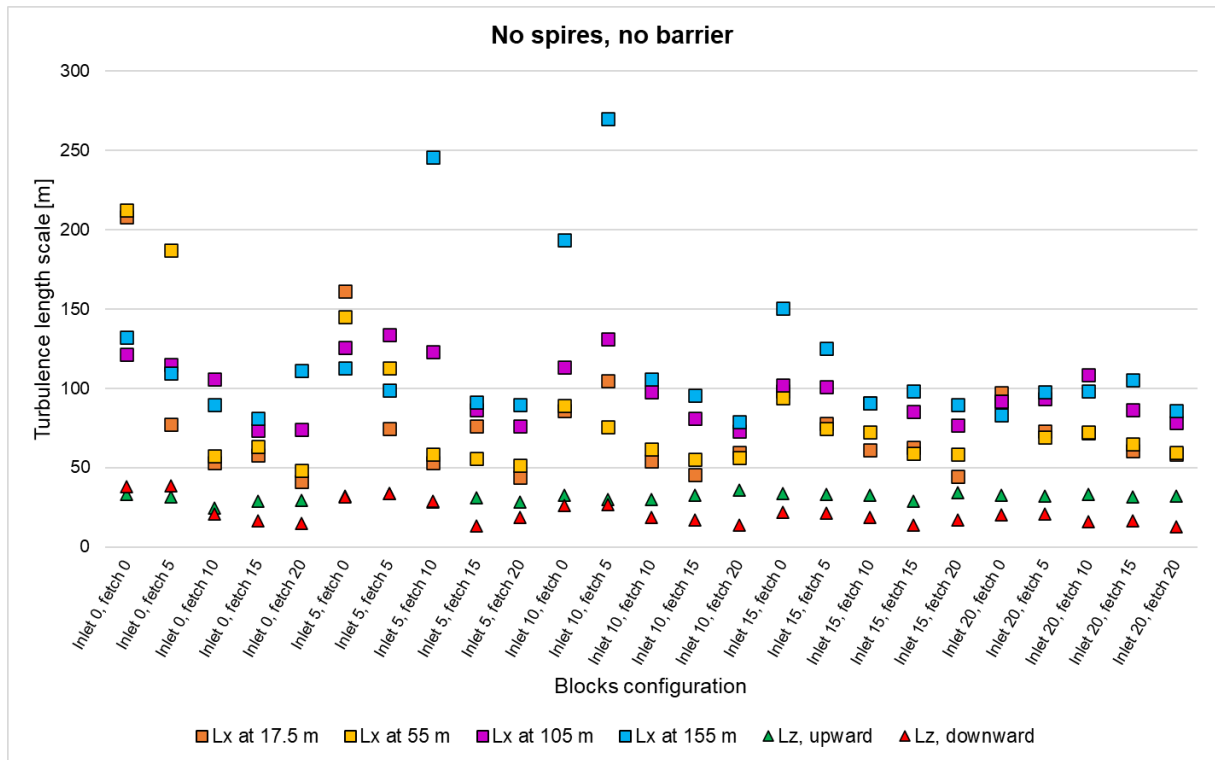
Fig. 7.19. Comparison of turbulence length scales values for different blocks elevations for the arrangements without spires or barrier (cases 1-1 to 1-25)
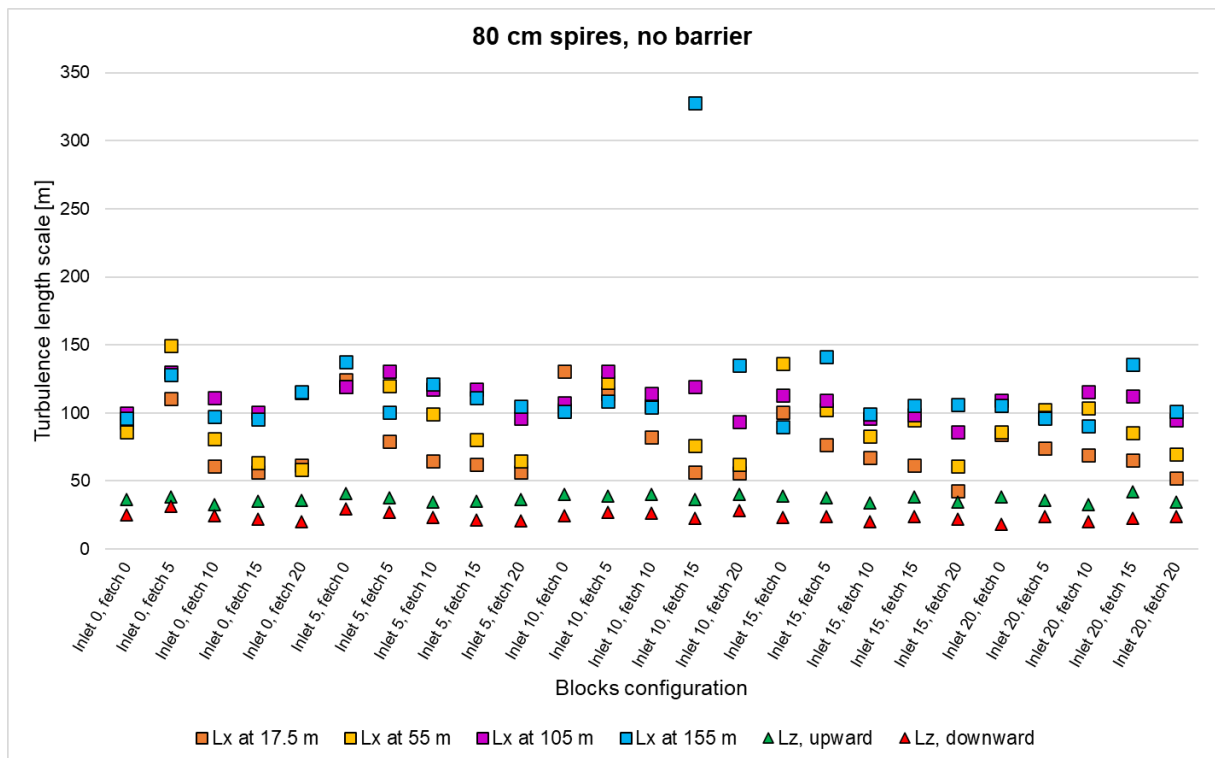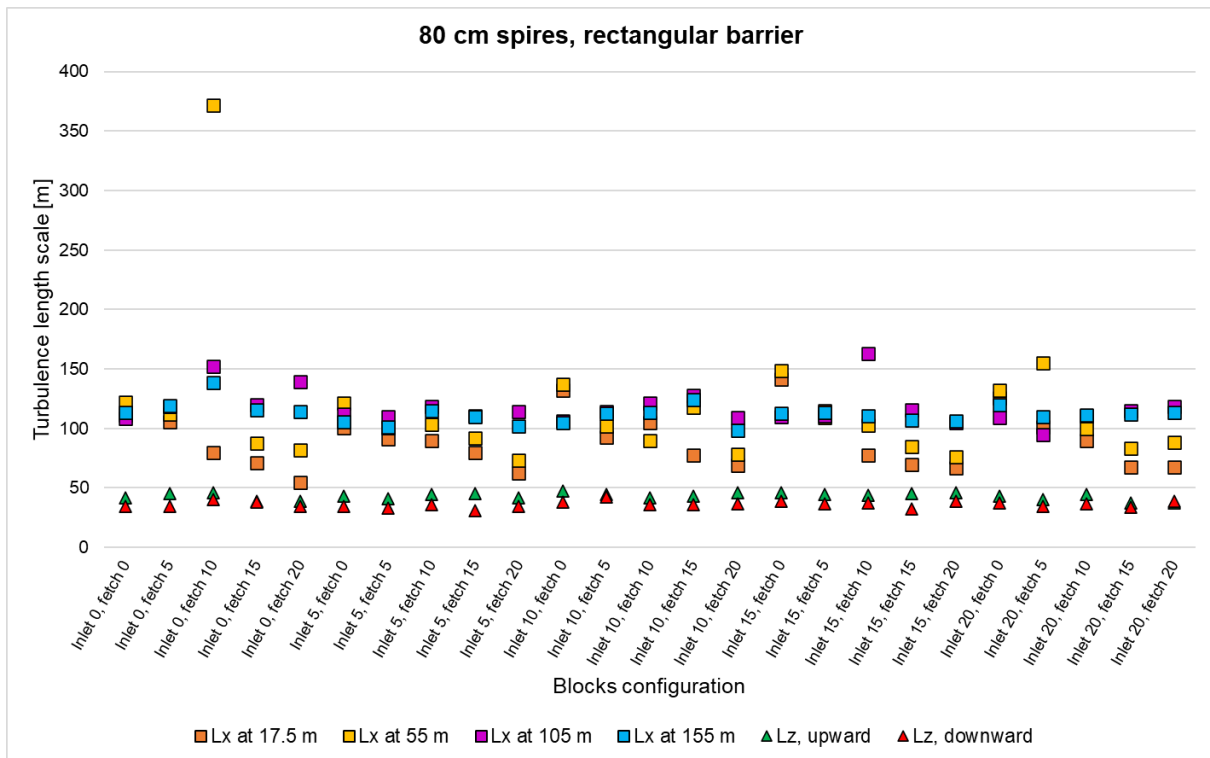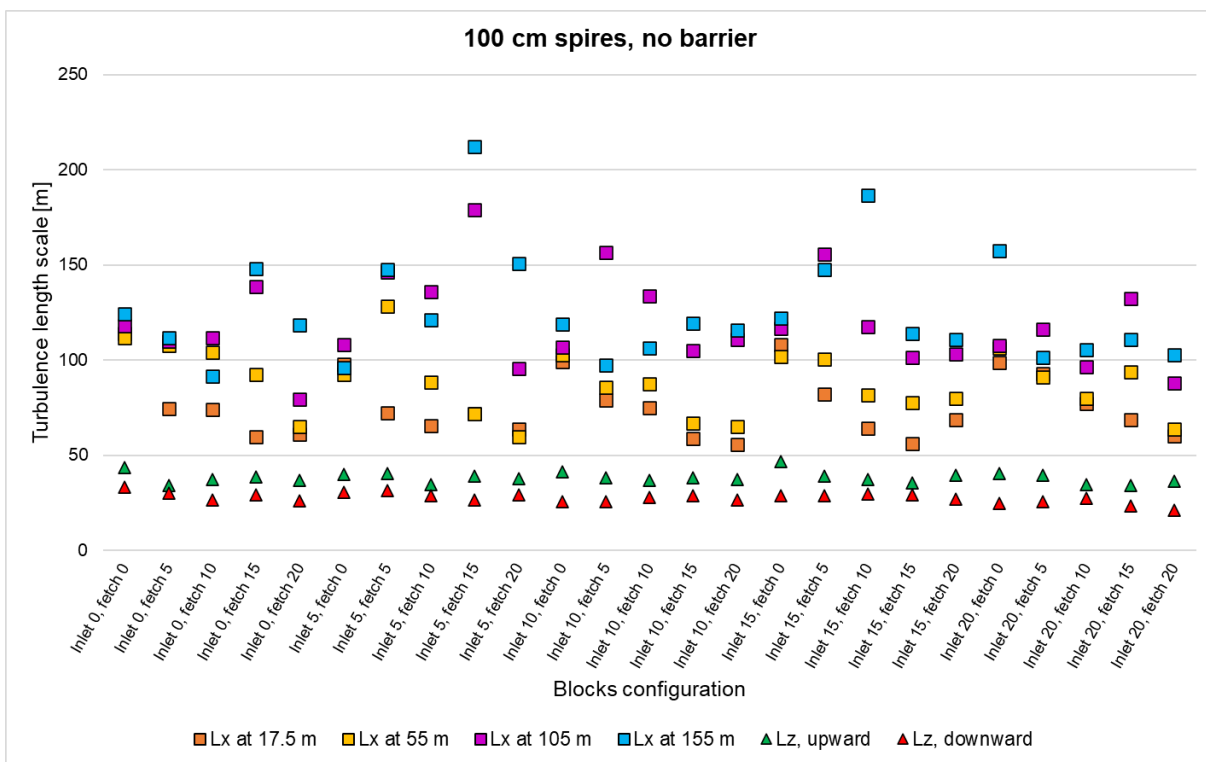

Fig. 7.20. Comparison of turbulence length scales values for different blocks elevations for the arrangements with 80 cm tall spires and no barrier (cases 2-1 to 2-25)
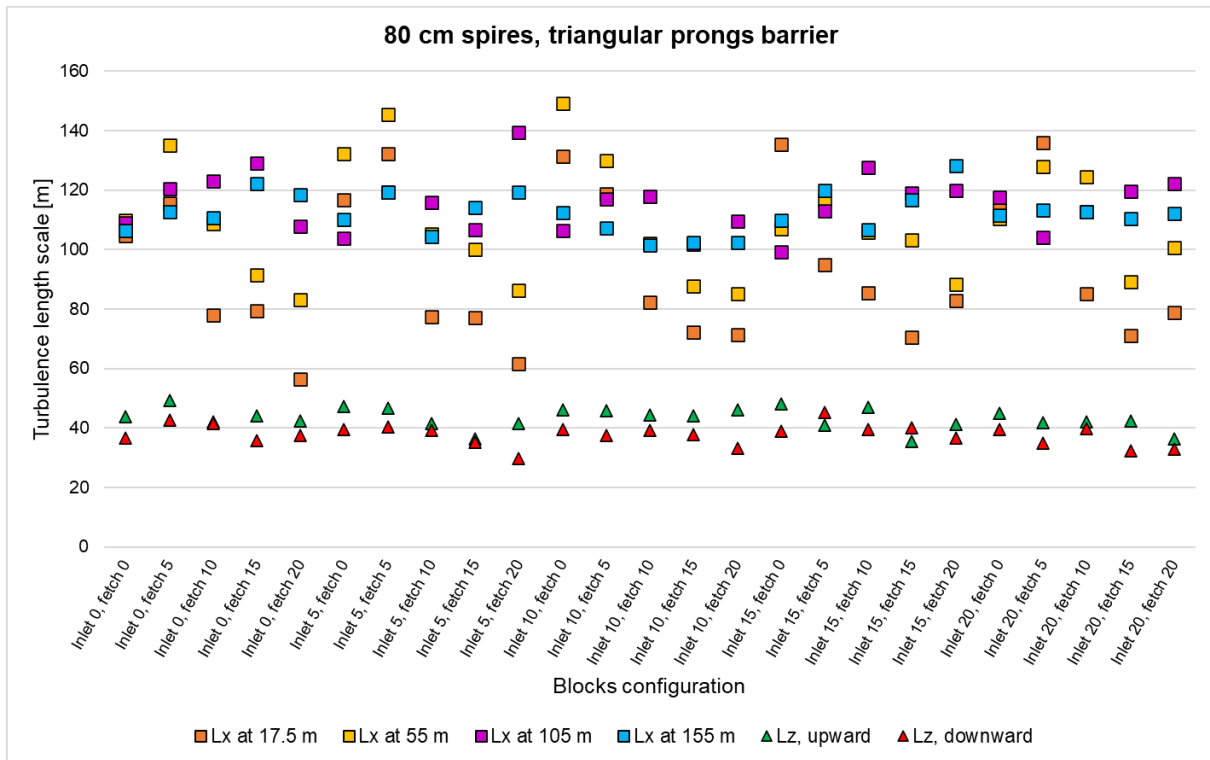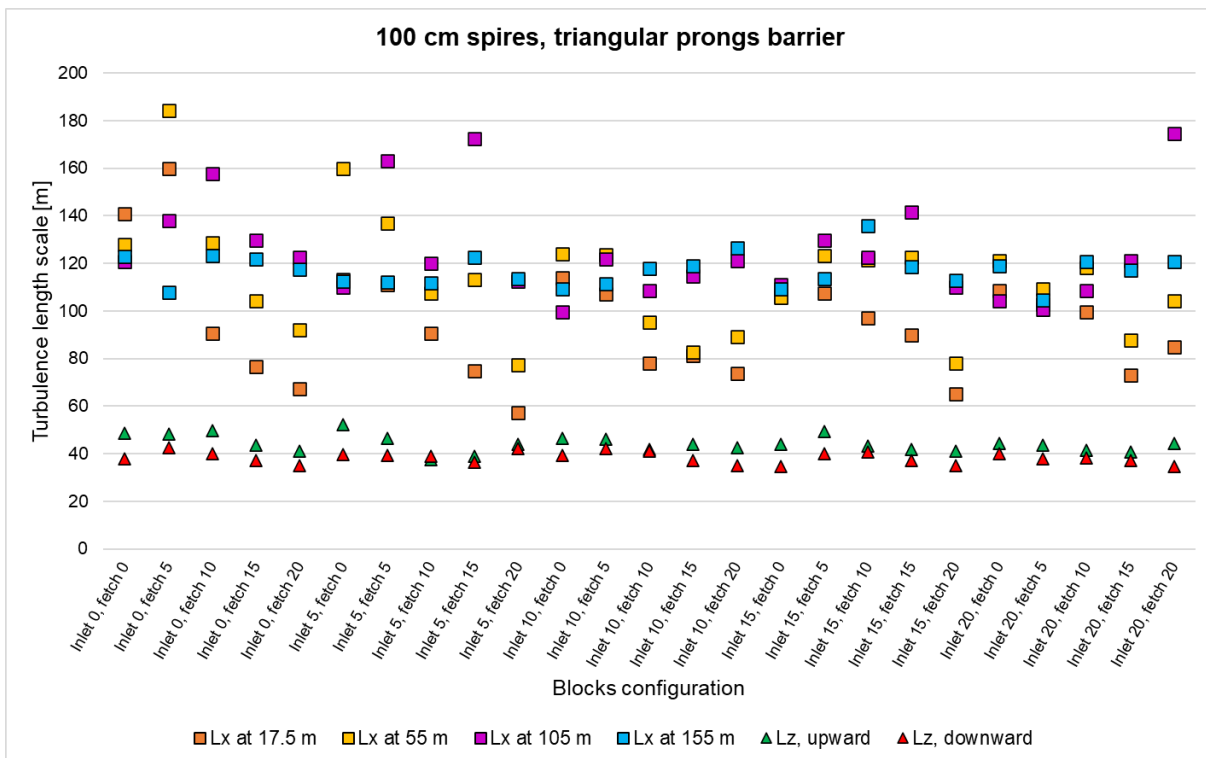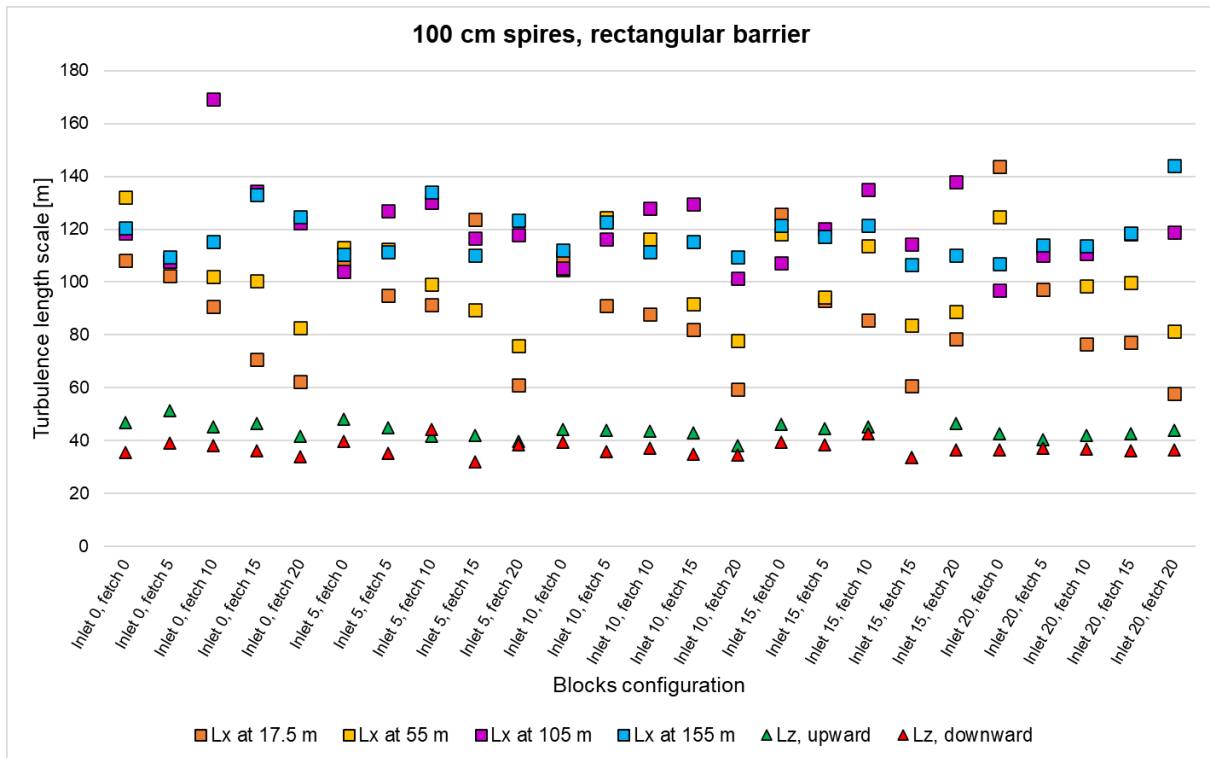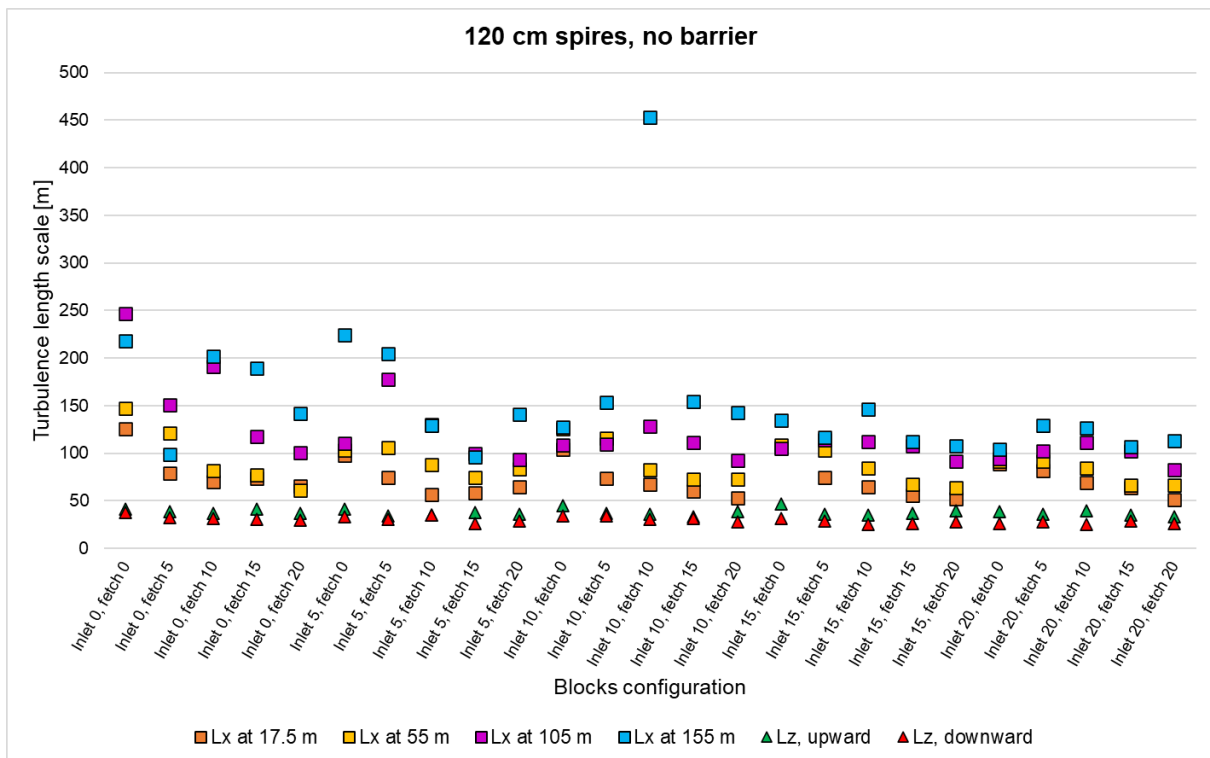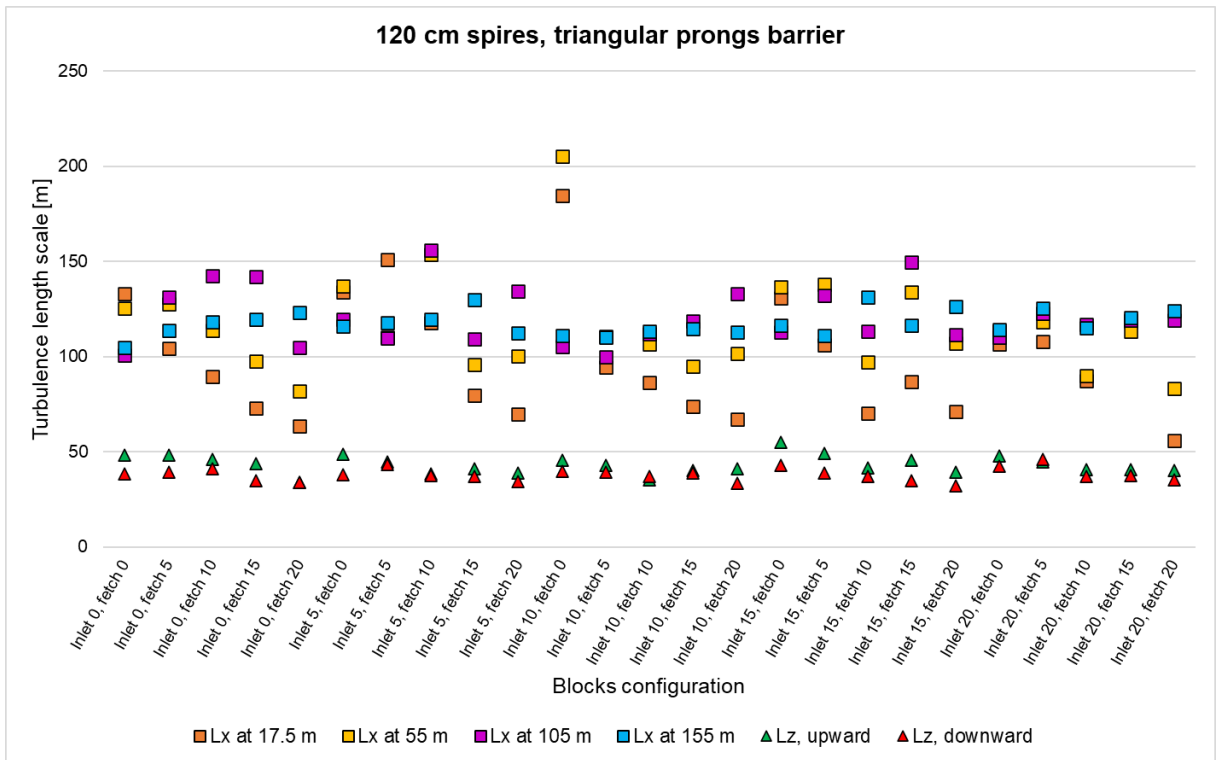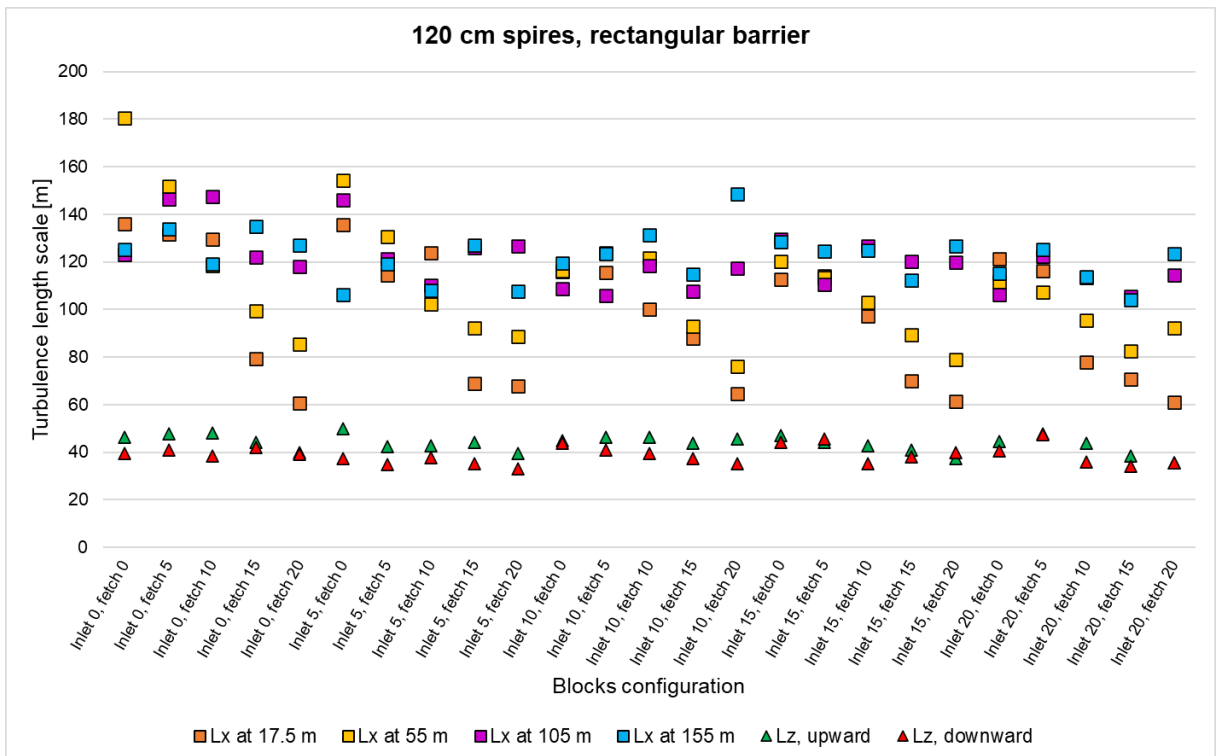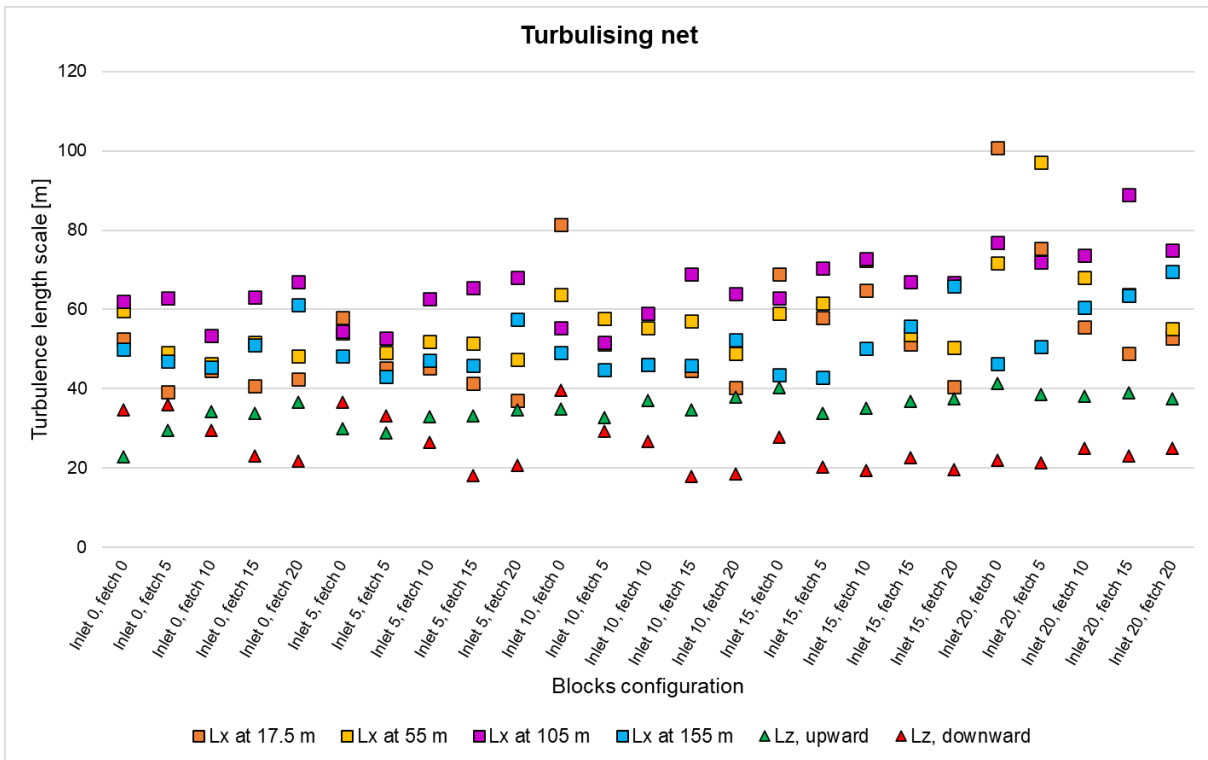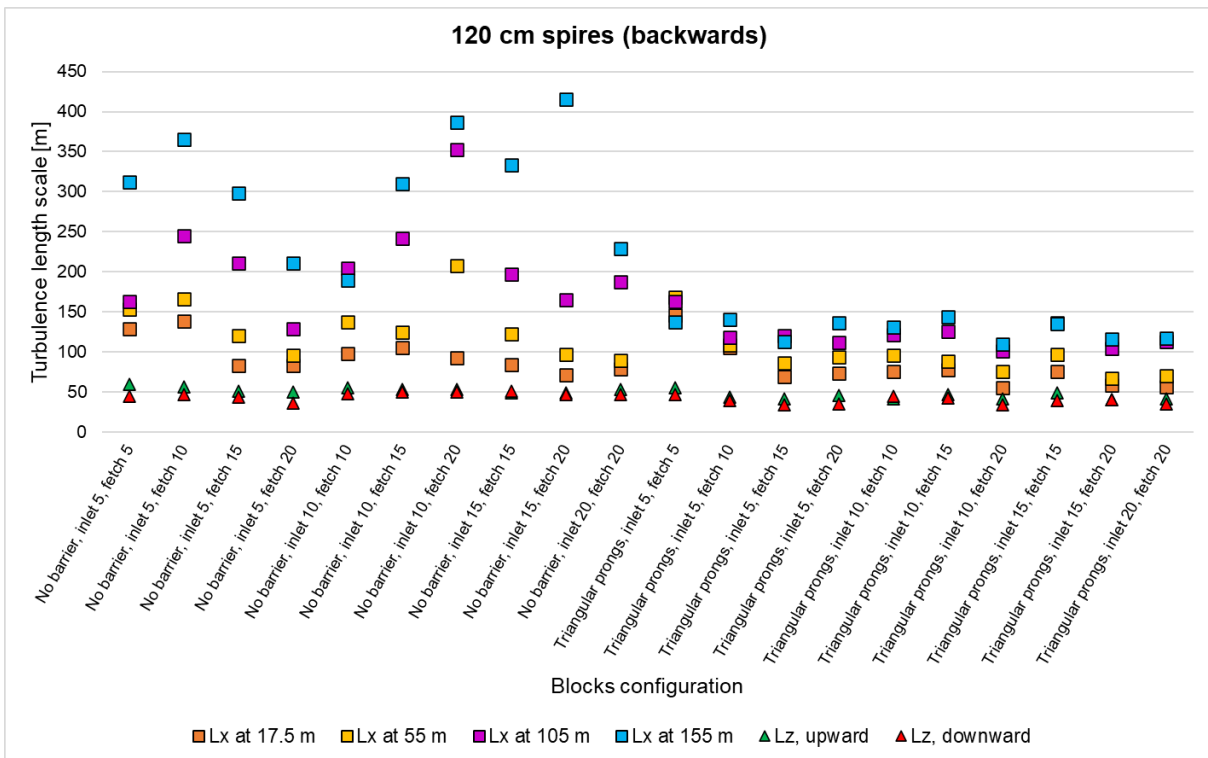
Fig. 7.21. Comparison of turbulence length scales values for different blocks elevations for the arrangements with 80 cm tall spires and triangular prongs barrier (cases 2-26 to 2-50)

Fig. 7.22. Comparison of turbulence length scales values for different blocks elevations for the arrangements with 80 cm tall spires and rectangular barrier (cases 2-51 to 2-75)

Fig. 7.23. Comparison of turbulence length scales values for different blocks elevations for the arrangements with 100 cm tall spires and no barrier (cases 2-101 to 2-125)

Fig. 7.24. Comparison of turbulence length scales values for different blocks elevations for the arrangements with 100 cm tall spires and triangular prongs barrier (cases 2-126 to 2-150)

Fig. 7.25. Comparison of turbulence length scales values for different blocks elevations for the arrangements with 100 cm tall spires and rectangular barrier (cases 2-76 to 2-100)

Fig. 7.26. Comparison of turbulence length scales values for different blocks elevations for the arrangements with 120 cm tall spires and no barrier (cases 3-26 to 3-50)

Fig. 7.27. Comparison of turbulence length scales values for different blocks elevations for the arrangements with 120 cm tall spires and triangular prongs barrier (cases 3-1 to 3-25)

Fig. 7.28. Comparison of turbulence length scales values for different blocks elevations for the arrangements with 120 cm tall spires and rectangular barrier (cases 3-51 to 3-75)

Fig. 7.29. Comparison of turbulence length scales values for different blocks elevations for the arrangements with turbulence net (bars and patches) (cases 3-96 to 3-120)

Fig. 7.30. Comparison of turbulence length scales values for different blocks elevations and barrier types for the arrangements with 120 cm spires mounted backwards (cases 3-76 to 3-95)

As can be seen in the plots presented in Fig. 7.19-Fig. 7.30, the distribution of the values of the longitudinal turbulence length scales is much more chaotic than, for example, the values of the parameters of vertical mean wind speed and turbulence intensity profiles analysed in the previous subsection. The values of the vertical length scales, however, are kept at rather stable levels for different blocks' elevations. Moreover, the following can be observed in these plots:

- The values of the vertical length scale are, in general, larger (at about 40 m) when moving upward than when moving downward (at about 30 m), which corresponds with literature (Duchêne-Marullaz, 1977), comp. Eq. (3.21), both when considering the trend and the approximate values. This is only not true in the few cases where the elevation of the blocks at the fetch length and at the inlet is at a low level (0 or 5 cm) at the same time, for the cases without any spires or barrier (Fig. 7.19 and Fig. 7.29);
- The values of the vertical length scale when moving upward and downward are closer together (both at about 40-50 m) in the cases with 120 cm spires mounted backwards;
- For the cases with the arrangement without any spires, barriers or turbulising net, the cases with 120 cm spires mounted backwards and the cases with spires and no barrier, the longitudinal turbulence length scales increase with height. This pattern corresponds with the literature sources (Duchêne-Marullaz, 1977; ESDU 74031, 1974; ESDU 86035, 2000; Kozmar, 2011a). However, this is not true for the cases with turbulising net or with barriers, where the distribution of the turbulence length scale values along the height of the wind tunnel is more scattered. In these cases, the largest values of the longitudinal turbulence length scales are usually observed at the height of 105 m (in real-life scale);
- The values of the longitudinal turbulence length scales are reaching very large values (of about 350-400 m) in the cases with the 120 cm spires mounted backwards and no barrier. This often results in values of the longitudinal turbulence length scale being outside of the bounds recommended in (ESDU 74031, 1974), but closer to the larger values derived from a different model (taking into account the reference wind speed as well) given in (ESDU 86035, 2000);
- On the other hand, the values of the longitudinal turbulence length scales are at a rather modest level (rarely exceeding 80) in the cases with the turbulising net;
- For the configurations with spires, the clearest trends depending on the elevation of the blocks at the fetch length can be observed for the longitudinal turbulence length scales at the two lowest probes (at the real-life scale heights of 17.5 and 55 m), with the one for the lowest probe at 17.5 m being the most distinguished. The longitudinal turbulence length scales at these measurement points are decreasing with the increase of the blocks' elevation at the fetch length. The trends are particularly strong for the cases with triangular prongs barrier (see Fig. 7.24 and Fig. 7.27).

The comparisons of the turbulence length scales between the cases with different types of barriers for each of the tested heights of the spires are shown in Fig. 7.31-Fig. 7.33 and the comparisons between the cases with different spires heights for each of the tested barrier setups are shown in Fig. 7.34-Fig. 7.36.
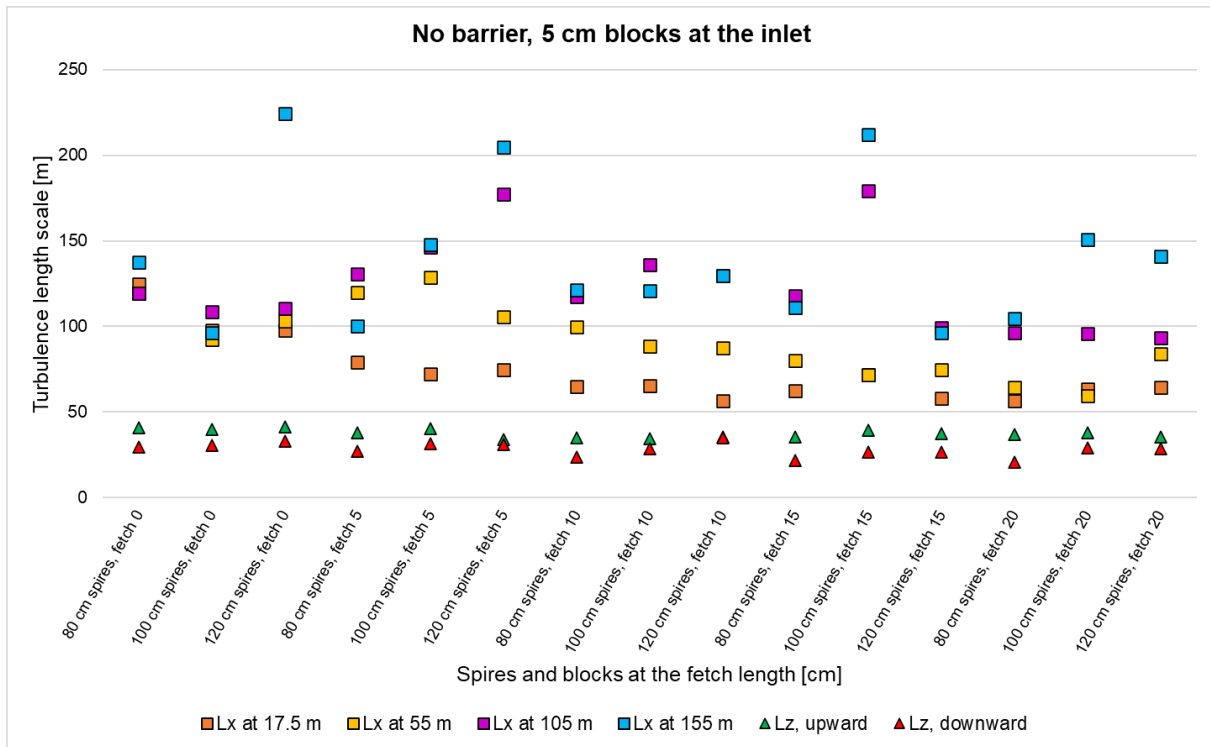
Fig. 7.31. Comparison of turbulence length scales values for different blocks elevations at the fetch length and spires heights for the arrangements with no barrier (cases 2-2, 2-9, 2-12, 2-19, 2-22, 2-102, 2-109, 2-112, 2-119, 2-122, 3-27, 3-34, 3-37, 3-44 and 3-47)
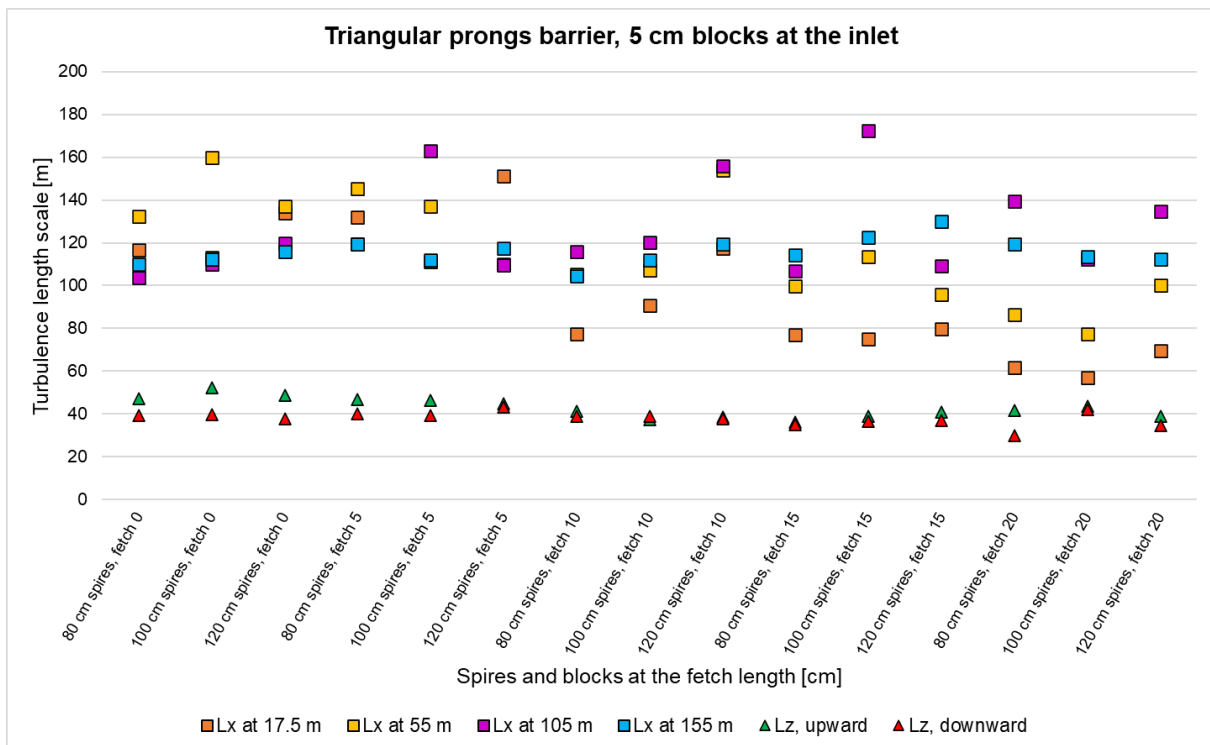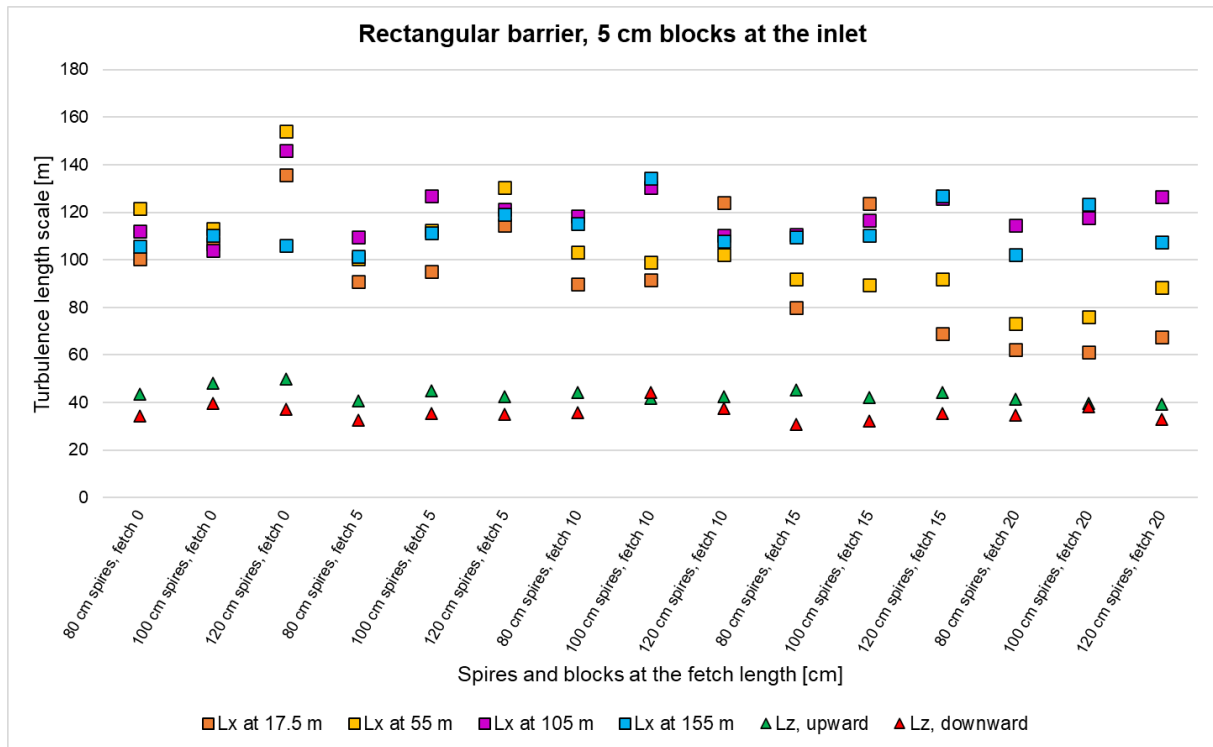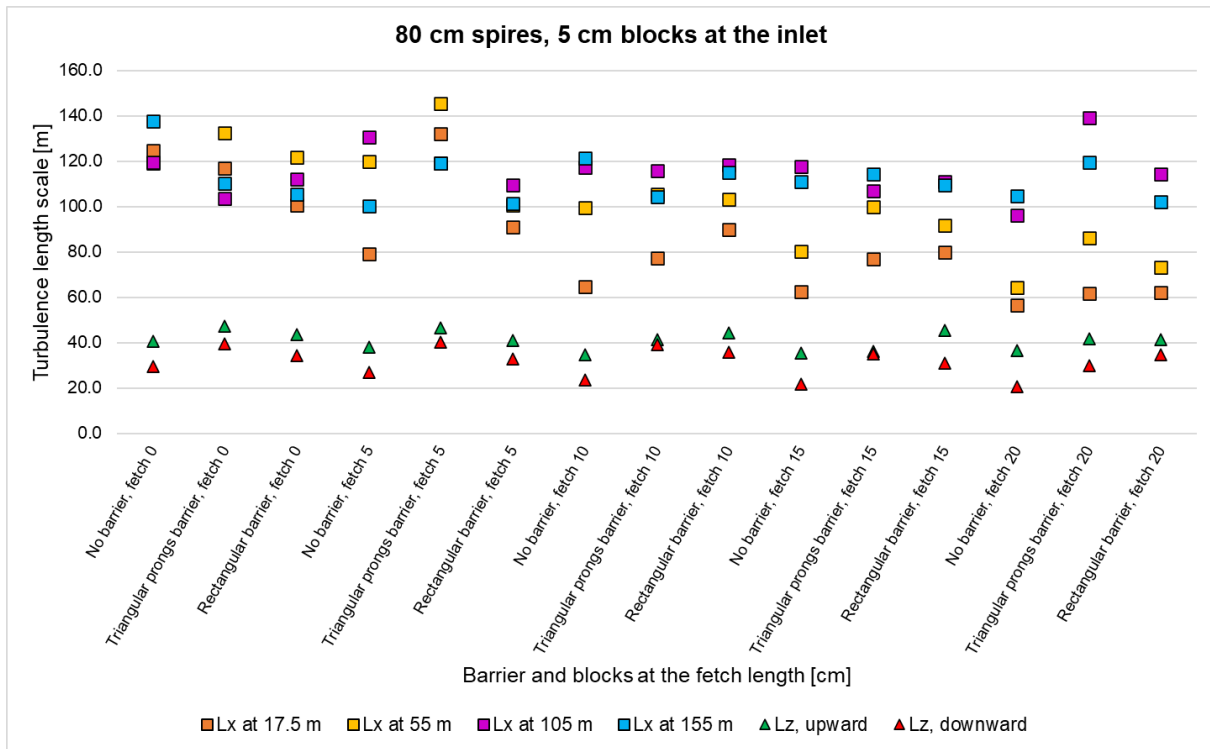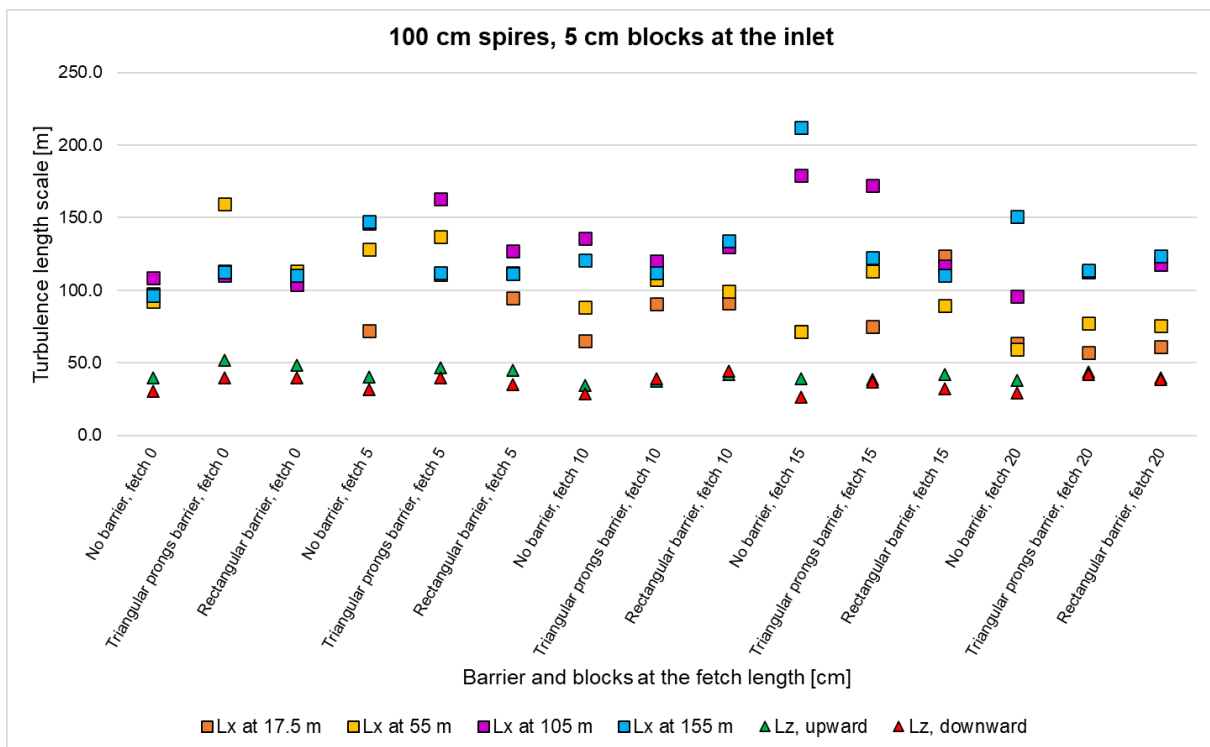

Fig. 7.32. Comparison of turbulence length scales values for different blocks elevations at the fetch length and spires heights for the arrangements with triangular prongs barrier (cases 2-27, 2-34, 2-37, 2-44, 2-47, 2-127, 2-134, 2-137, 2-144, 2-147, 3-2, 3-9, 3-12, 3-19 and 3-22)
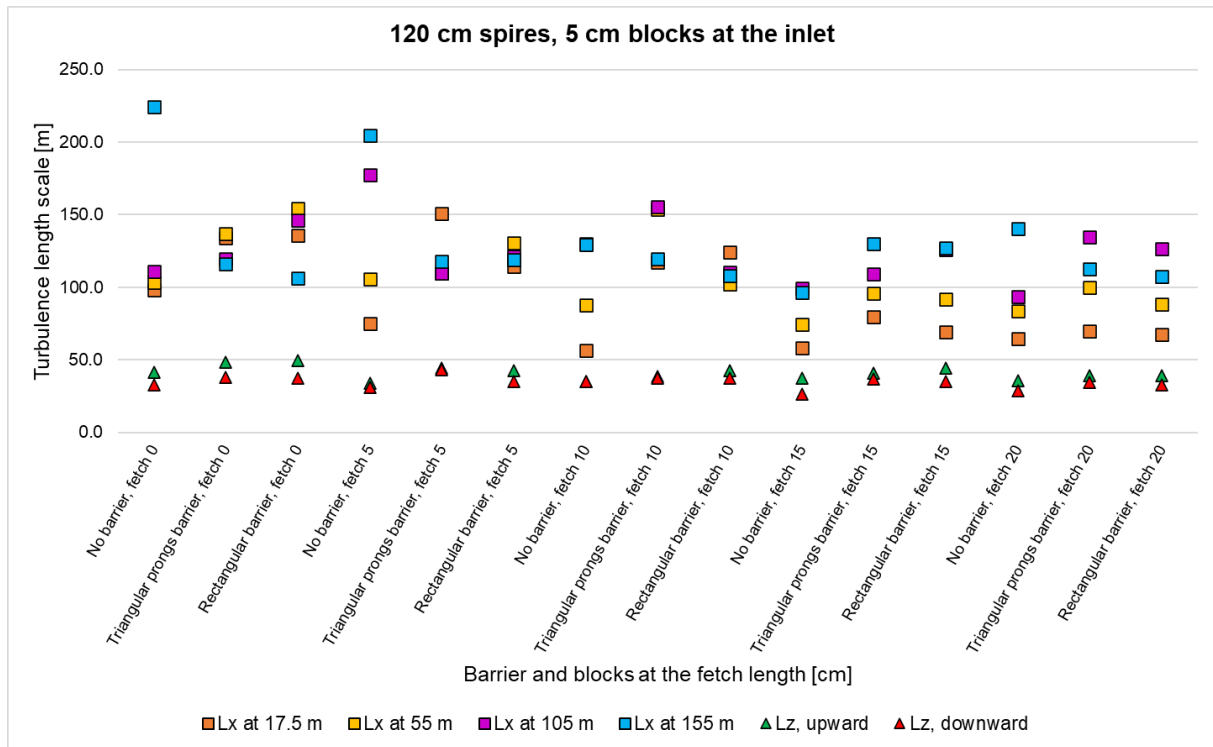
Fig. 7.33. Comparison of turbulence length scales values for different blocks elevations at the fetch length and spires heights for the arrangements with rectangular barrier (cases 2-52, 2-59, 2-62, 2-69, 2-72, 2-77, 2-84, 2-87, 2-94, 2-97, 3-52, 3-59, 3-62, 3-69 and 3-72)

Based on the plots presented in Fig. 7.31-Fig. 7.33, the following conclusions can be drawn:

- There seem to be only superficial differences between the values of the vertical length scales when comparing different heights of spires with the same type of barrier;
- There is no clear pattern of the influence of the height of the spires on the values of the longitudinal turbulence length scales;
- With the higher elevations of the blocks at the fetch length (15 and 20 cm), the increasing trend of the longitudinal turbulence length scales with the increase of height can be noticed;
- In some cases, a sudden change in the vertical profile of the longitudinal turbulence length scales can be observed, from increasing to rather constant (fluctuating around a value) or even decreasing. It is highly possible that this is an effect of the barrier, as this can usually be observed in cases with a barrier (the rectangular one in particular) and occurs at a height that corresponds to the height of the barrier.

Fig. 7.34. Comparison of turbulence length scales values for different blocks elevations at the fetch length and barrier types for the arrangements with 80 cm spires (cases 2-2, 2-9, 2-12, 2-19, 2-22, 2-27, 2-34, 2-37, 2-44, 2-47, 2-52, 2-59, 2-62, 2-69 and 2-72)

Fig. 7.35. Comparison of turbulence length scales values for different blocks elevations at the fetch length and barrier types for the arrangements with 100 cm spires (cases 2-77, 2-84, 2-87, 2-94, 2-97, 2-102, 2-109, 2-112, 2-119, 2-122, 2-127, 2-134, 2-137, 2-144 and 2-147)

Fig. 7.36. Comparison of turbulence length scales values for different blocks elevations at the fetch length and barrier types for the arrangements with 120 cm spires (cases 3-2, 3-9, 3-12, 3-19, 3-22, 3-27, 3-34, 3-37, 3-44, 3-47, 3-52, 3-59, 3-62, 3-69 and 3-72)

Based on the plots presented in Fig. 7.34-Fig. 7.36, the following conclusions can be drawn:

- The values of the vertical turbulence length scales increase with the addition of the barriers. This pattern is very similar for all the analysed heights of the spires;
- The patterns of longitudinal turbulence length scales are rather chaotic with any type of barrier. However, it can be noticed that the differences between these values at different heights are largest in the cases without any barrier. Furthermore, these cases also sometimes result in reaching very high values (above 200 m), in particular for the turbulence length scale at the highest measuring point (corresponding to 155 m in real-life scale).

The following general conclusions can be stated, based on the complete analysis of the influences of roughness elements on the turbulence length scales presented in this subsection:

- Vertical turbulence length scale values when moving upward are, in general, in good agreement with the values from the literature (Duchêne-Marullaz, 1977; Kozmar, 2011c), while when moving downward, this match is best in the cases without any barriers;
- The values of the longitudinal turbulence length scales show mostly chaotic patterns. However, with the higher spires, it seems that these trends are more consistently increasing with the height, in particular with higher elevations of the blocks at the fetch length;
- While the values of the longitudinal turbulence length scales are, in general, in the ranges comparable to the literature (Duchêne-Marullaz, 1977; Kozmar, 2011c),

obtaining a proper vertical profile of this value (or desired variety of this value with height) is more difficult. This was expected, as the value of this parameter is largely influenced by the spires, which generate similar levels of vorticity along their height. While the type of barriers used has a smaller influence on these values, the higher elevation of the blocks at the fetch length may be applied to increase the vertical variety of this parameter;

- According to the empirical relationship between the values of longitudinal turbulence length scale values and vertical turbulence length scale values when moving downward given by (Duchêne-Marullaz, 1977), comp. Eq. (3.22), the ratio of these two values is approximately 5:1.

While possibly an arbitrary condition, this might be a useful tool for further investigation of the test cases. From all the cases, this condition was closely achieved ($L_z^\downarrow/L_x \in (0.17 \div 0.23)$) in the cases where no barriers are present. Furthermore, with the higher spires (100 cm and 120 cm), it was not achieved for any values of $L_x(55$ m$)$. The more detailed results for this analysis are presented in Tab. 7.1-Tab. 7.3 for different heights where L_x is measured. It should be noted that every considered arrangement consists of 25 different cases in total, which are the combinations of the blocks' elevations at the inlet and at the fetch length.

Tab. 7.1. Statistics of the ratios of the analysed cases that fulfil the condition $L_z^\downarrow/L_x(55$ m$) \in (0.17 \div 0.23)$

Spires and barrier arrangement	Mean $L_z^\downarrow/L_x$ ratio	Number of cases where $L_z^\downarrow/L_x \in (0.17 \div 0.23)$	Percentage of cases where $L_z^\downarrow/L_x \in (0.17 \div 0.23)$
No spires, no barriers	0.276	6	24%
80 cm spires, no barrier	0.271	5	20%
80 cm spires, triangular prongs	0.354	0	0%
80 cm spires, rectangular barrier	0.351	1	4%
100 cm spires, no barrier	0.324	0	0%
100 cm spires, triangular prongs	0.351	0	0%
100 cm spires, rectangular barrier	0.372	0	0%
120 cm spires, no barrier	0.347	0	0%
120 cm spires, triangular prongs	0.340	1	4%
120 cm spires, rectangular barrier	0.370	0	0%
Turbulising net	0.456	1	4%
Total	–	**14**	**5.1%**

Tab. 7.2. Statistics of the ratios of the analysed cases that fulfil the condition $L_z\downarrow/L_x(105\text{ m}) \in (0.17 \div 0.23)$

Spires and barrier arrangement	Mean $L_z\downarrow/L_x$ ratio	Number of cases where $L_z\downarrow/L_x \in (\mathbf{0.17} \div \mathbf{0.23})$	Percentage of cases where $L_z\downarrow/L_x \in (\mathbf{0.17} \div \mathbf{0.23})$
No spires, no barriers	0.215	14	56%
80 cm spires, no barrier	0.220	15	60%
80 cm spires, triangular prongs	0.330	1	4%
80 cm spires, rectangular barrier	0.312	0	0%
100 cm spires, no barrier	0.240	8	32%
100 cm spires, triangular prongs	0.314	2	8%
100 cm spires, rectangular barrier	0.314	1	4%
120 cm spires, no barrier	0.263	4	16%
120 cm spires, triangular prongs	0.319	0	0%
120 cm spires, rectangular barrier	0.326	0	0%
Turbulising net	0.405	0	0%
Total	–	**45**	**16.4%**

Tab. 7.3. Statistics of the ratios of the analysed cases that fulfil the condition $L_z\downarrow/L_x(155\text{ m}) \in (0.17 \div 0.23)$

Spires and barrier arrangement	Mean $L_z\downarrow/L_x$ ratio	Number of cases where $L_z\downarrow/L_x \in (\mathbf{0.17} \div \mathbf{0.23})$	Percentage of cases where $L_z\downarrow/L_x \in (\mathbf{0.17} \div \mathbf{0.23})$
No spires, no barriers	0.193	9	36%
80 cm spires, no barrier	0.215	11	44%
80 cm spires, triangular prongs	0.338	0	0%
80 cm spires, rectangular barrier	0.324	0	0%
100 cm spires, no barrier	0.229	8	32%
100 cm spires, triangular prongs	0.330	0	0%
100 cm spires, rectangular barrier	0.317	0	0%
120 cm spires, no barrier	0.214	8	32%
120 cm spires, triangular prongs	0.325	0	0%

Spires and barrier arrangement	Mean $L_z^{\downarrow}/L_x$ ratio	Number of cases where $L_z^{\downarrow}/L_x \in (0.17 \div 0.23)$	Percentage of cases where $L_z^{\downarrow}/L_x \in (0.17 \div 0.23)$
120 cm spires, rectangular barrier	0.321	0	0%
Turbulising net	0.512	0	0%
Total	–	**36**	**13.1%**

It should be noted that, while the experiments carried out for this study always used the same measuring heights, the values obtained at the higher probes might not always be important or relevant to the simulation of the flow in the wind tunnel. This would be true in the cases of lower terrain roughness categories being simulated (0 or I, where the boundary layer thickness is lower) or when the height of the investigated building/object is significantly shorter than the highest point on the measuring probe (e.g. buildings of about 60-100 m).

The turbulence length scales are a dimensional parameter that depends directly on the scale of the model, therefore, it is not always possible to properly recreate them for given tests in the wind tunnel, as there are other factors that impact the selection of the model scale. Moreover, (Kozmar, 2011c) indicated that it might not be possible to reproduce all the phenomena that govern the size of the turbulence length scales in nature, i.e. the dependence of the turbulence length scales on reference wind velocity and the pattern of increase with height. Given the fact that there are, in general, large discrepancies between the values of turbulence length scales provided in different sources (in particular for the suburban and urban terrain categories), it can be stated that a simulation of these parameters is successful when their values are in a range similar to the standards.

7.3. Effects of roughness elements on frequency length scales

The final analysis presented in this chapter concerns the frequency length scales. For the sake of brevity, this analysis was only done for the cases related to the lowest and highest measuring points and for only 3 shortest distances of 12.5, 25 and 37.5 m, which resulted in a total of 6 different values for each test case. These results are described by the distance between the two points Δz and the mean height above the ground level between these two points z. Due to the little influence of the blocks at the inlet on the results, the full comparison was only done for the cases without any spires or barriers (Fig. 7.37), with turbulising net (Fig. 7.38) and with 120 cm spires mounted backwards (Fig. 7.39). For the cases with spires and barriers, an analysis was conducted taking into account a set level of blocks' elevation at the inlet of 5 cm. These analyses considered the influence of different spires heights and blocks' elevations at the fetch length with the same type of barrier (Fig. 7.40-Fig. 7.42) and the influence of different types of barriers and blocks' elevations at the fetch length with the same heights of spires (Fig. 7.43-Fig. 7.45).

For better clarity of the plots, the results related to the lowest measuring point are marked in red, while the points related to the highest measuring point are marked in green. Similarly, the shortest distances between the points $\Delta z = 12.5$ m are indicated with a square, the medium distances between the points $\Delta z = 25$ m are indicated with a diamond and the longest distances between the points $\Delta z = 37.5$ m are indicated with a triangle.
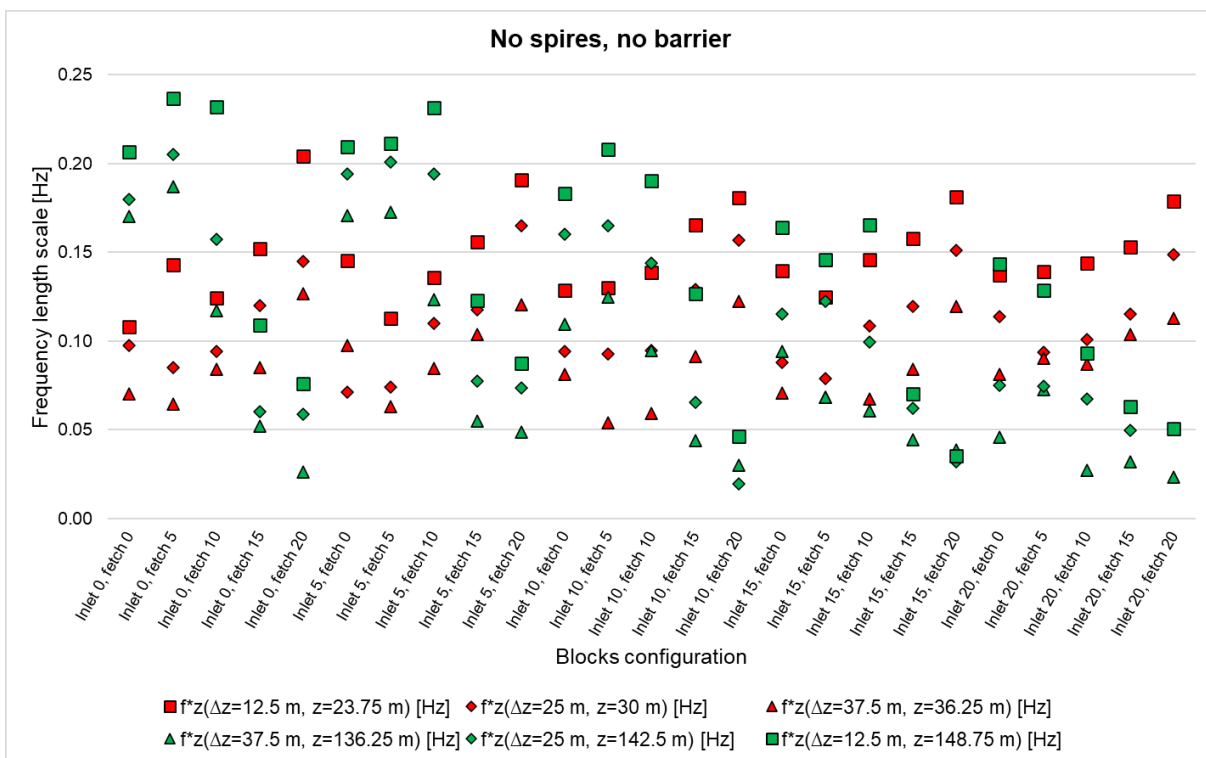
Fig. 7.37. Comparison of frequency length scales values for different blocks elevations for the arrangements without spires or barrier (cases 1-1 to 1-25)
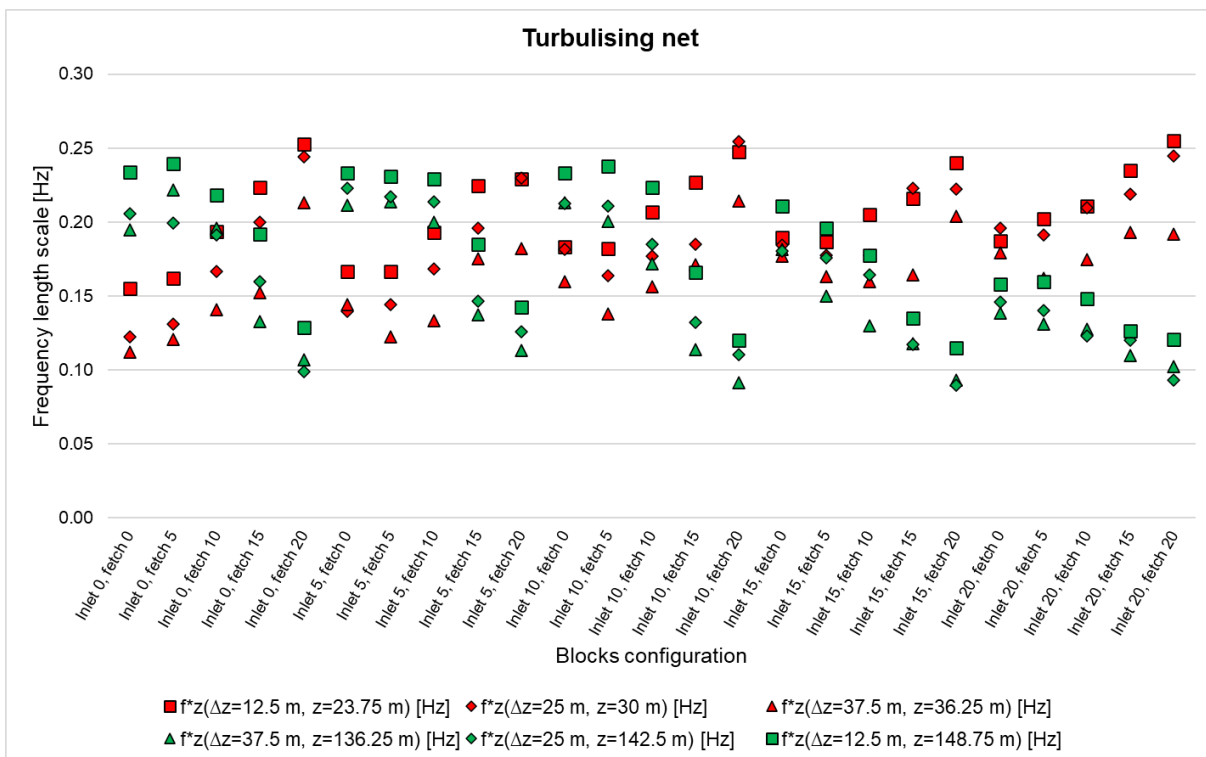

Fig. 7.38. Comparison of frequency length scales values for different blocks elevations for the arrangements with turbulence net (bars and patches) (cases 3-96 to 3-120)
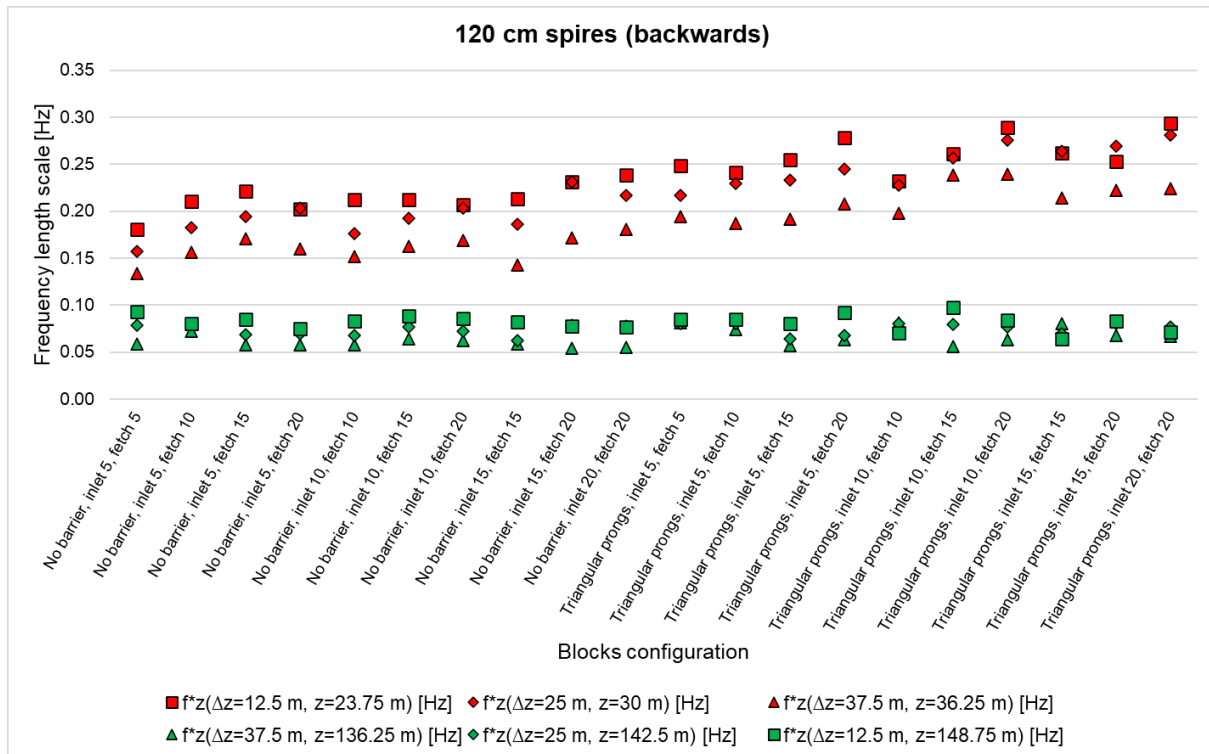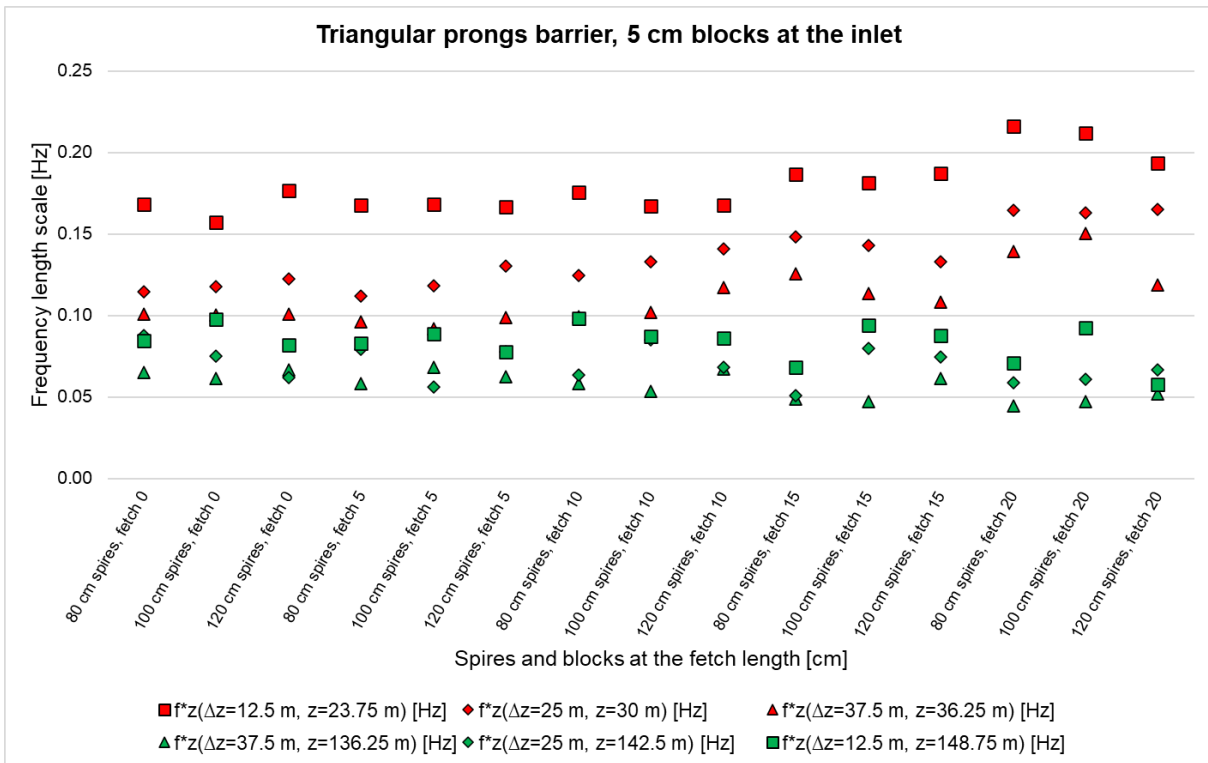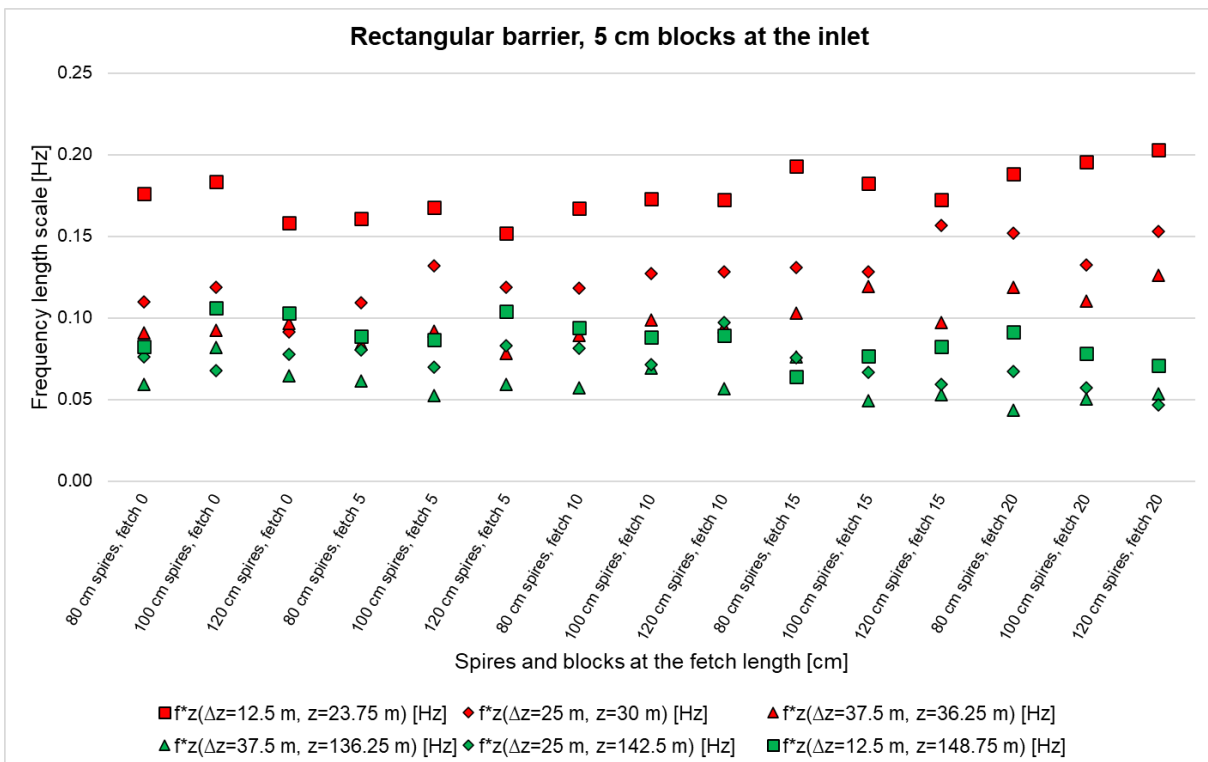
Fig. 7.39. Comparison of frequency length scales values for different blocks elevations and barrier types for the arrangements with 120 cm spires mounted backwards (cases 3-76 to 3-95)

The following observations can be formulated based upon the plots (Fig. 7.37-Fig. 7.39):

- For the cases without barriers, spires or turbulising net (Fig. 7.37) and with a turbulising net (Fig. 7.38), an increasing trend can be observed in the values of the frequency length scales related to the lowest measuring point with the increase of the elevation of the blocks at the fetch length. This trend seems to be more consistent with the higher blocks at the inlet (however, this increase is less steep for the cases with blocks at the inlet elevated at 20 cm);

- On the other hand, the frequency length scale values related to the highest measuring point for the cases shown in these two plots are relatively high for blocks' elevations of 0-10 cm at the fetch length (usually highest for 5 cm), while decreasing for the higher blocks' elevations;

- Comparing the values related to the lowest and highest measuring points, it can be seen that the values related to the highest measuring point are higher than the ones related to the lowest measuring point for configurations with blocks at the inlet and at the fetch length elevated at 0-10 cm, while for the higher blocks elevations, they are higher for the lowest measuring point (Fig. 7.37 and Fig. 7.38);

- The values of frequency length scales in the cases with turbulising net are highest, in the range of about 0.1 to 0.25 Hz (compared to 0.05 to 0.2 Hz for the case without the turbulising net, barrier or spires);

- For the case with 120 cm spires mounted backwards (Fig. 7.39), the values related to the lowest point are much higher (0.15-0.3 Hz) than the ones related to the highest point (0.05-0.1 Hz);

- For these cases, the frequency length scales related to the highest measuring point seem to vary very little with the increasing distance Δ*z*, in particular with higher blocks' elevations. At the lowest point, there is a small increase in the frequency length scale values with the increase of the elevation height of the blocks both at the inlet and at the fetch length.
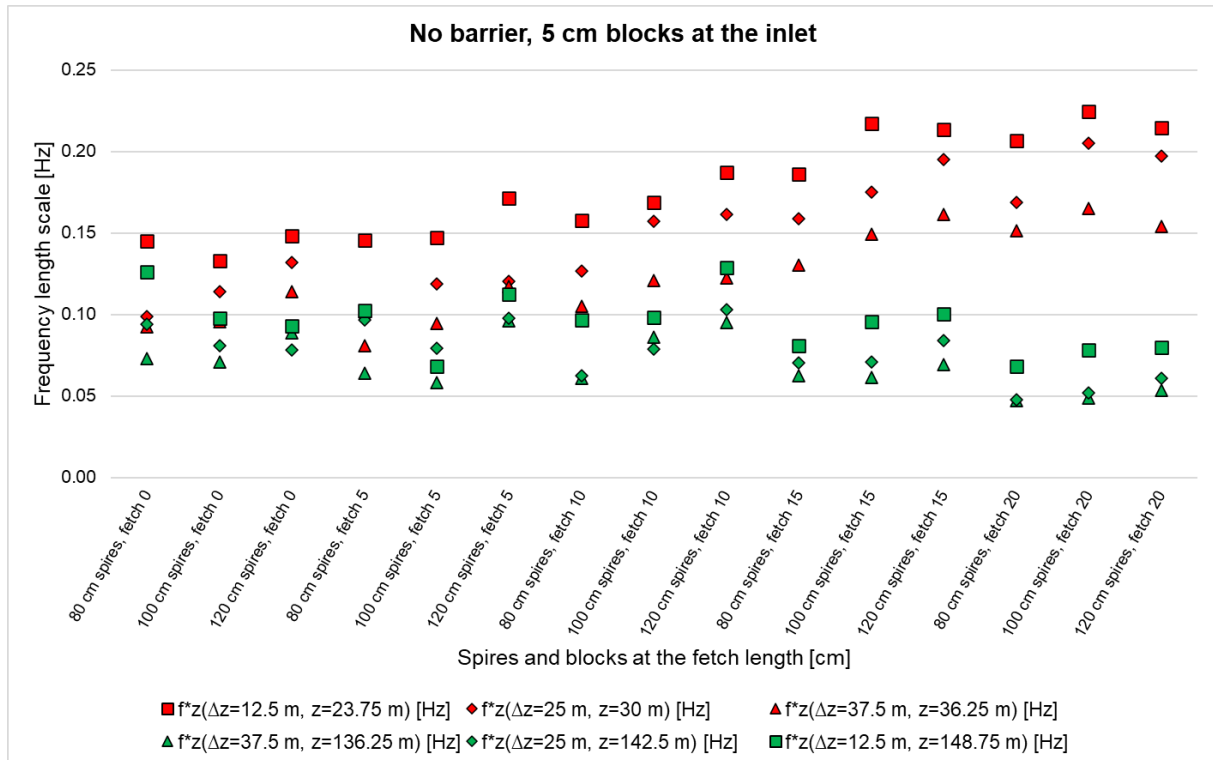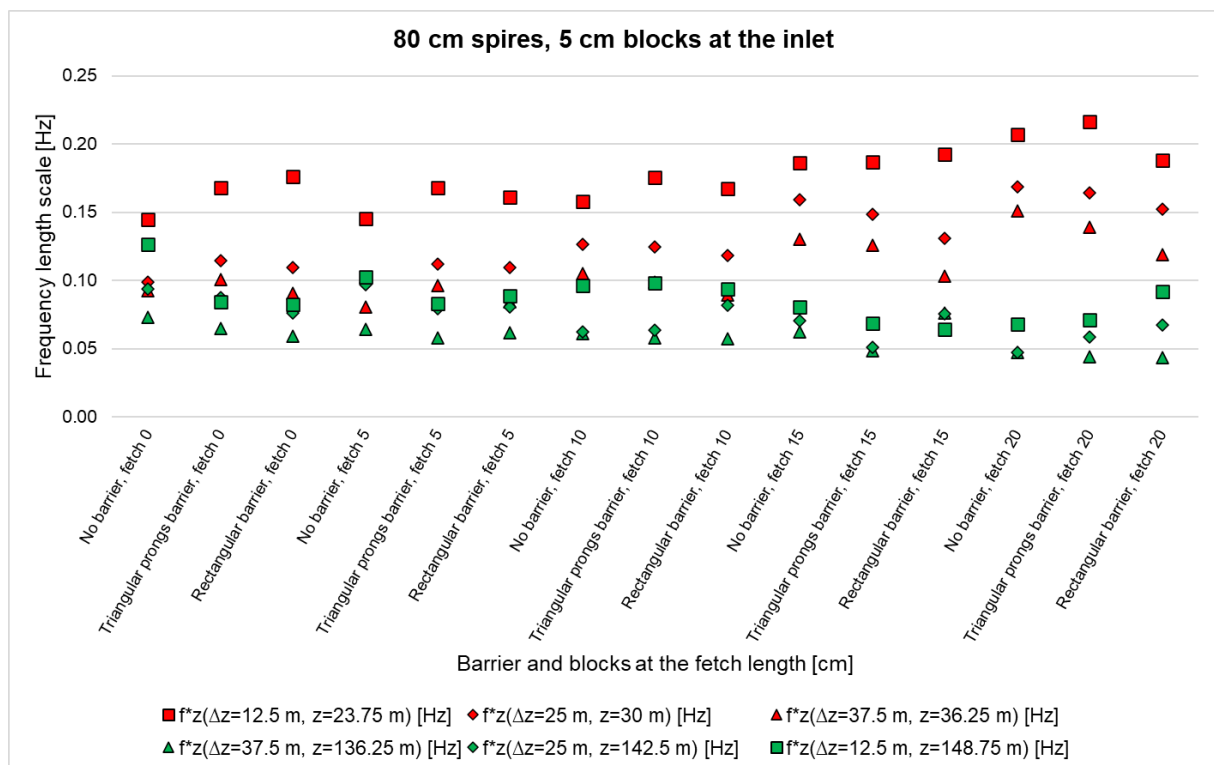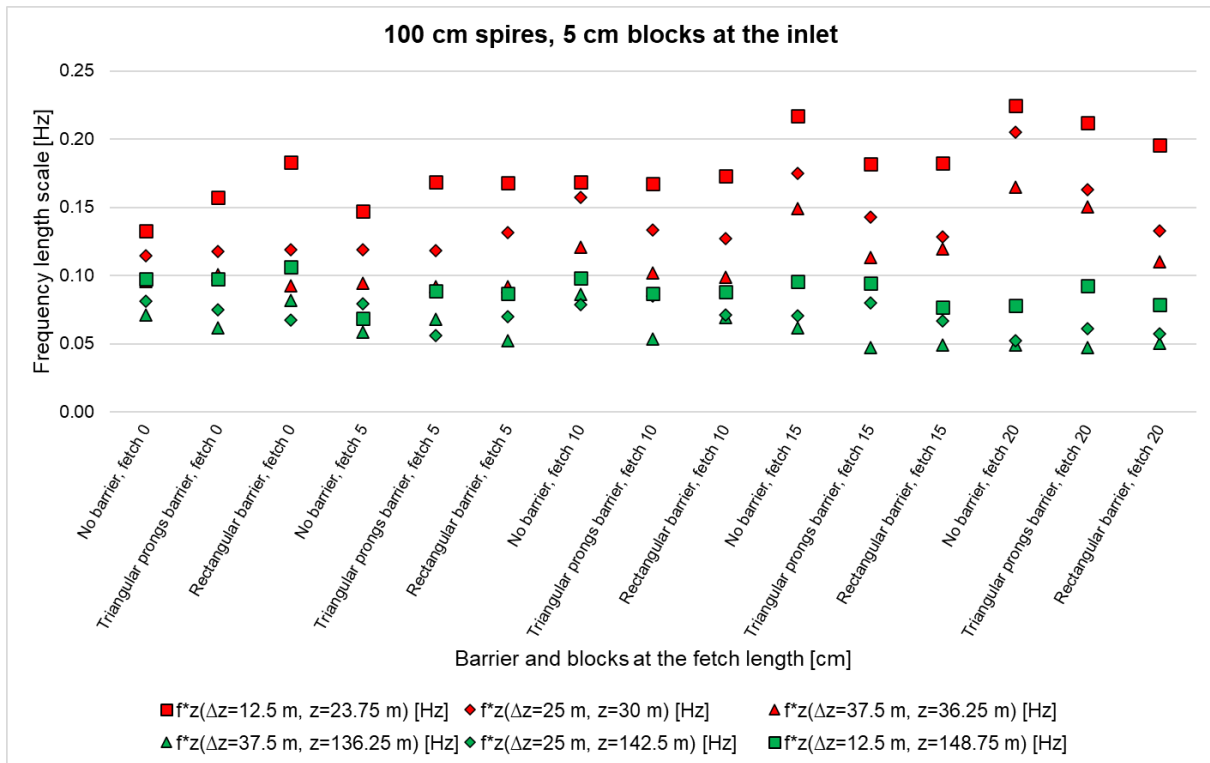

Fig. 7.40. Comparison of frequency length scales values for different blocks elevations at the fetch length and spires heights for the arrangements with no barrier (cases 2-2, 2-9, 2-12, 2-19, 2-22, 2-102, 2-109, 2-112, 2-119, 2-122, 3-27, 3-34, 3-37, 3-44 and 3-47)

Fig. 7.41. Comparison of frequency length scales values for different blocks elevations at the fetch length and spires heights for the arrangements with triangular prongs barrier (cases 2-27, 2-34, 2-37, 2-44, 2-47, 2-127, 2-134, 2-137, 2-144, 2-147, 3-2, 3-9, 3-12, 3-19 and 3-22)
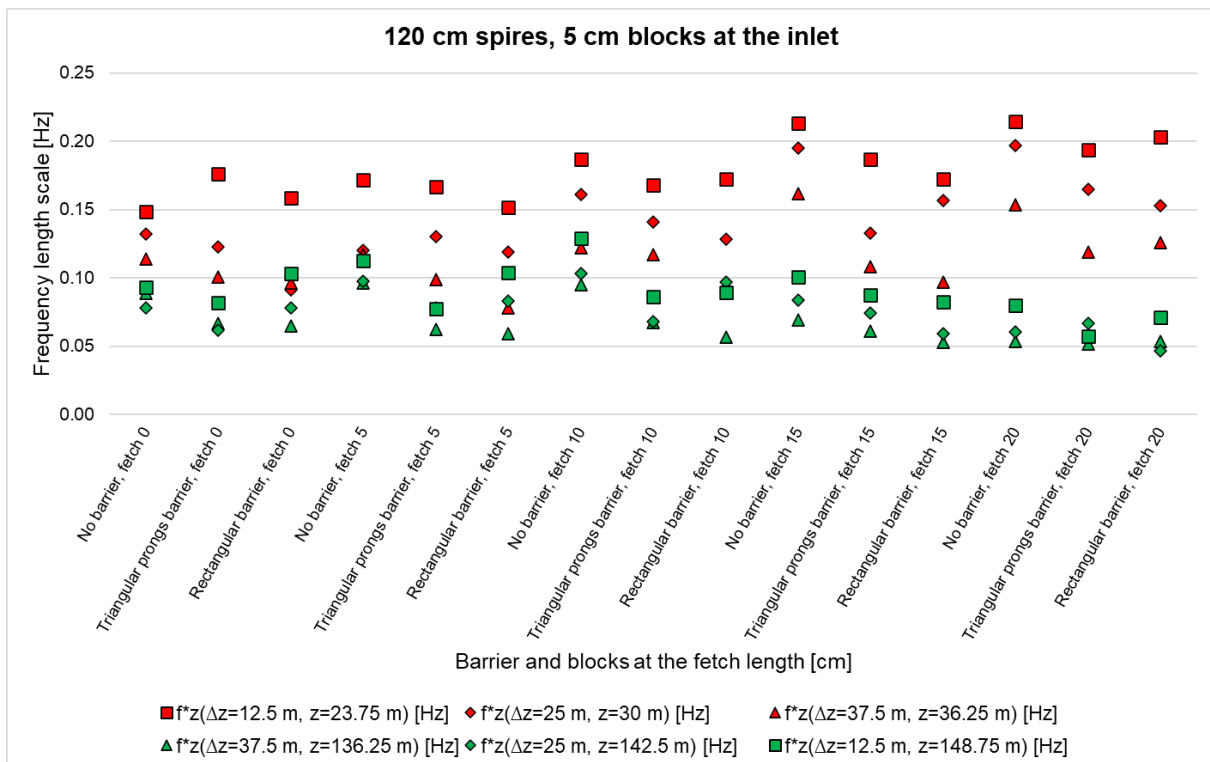

Fig. 7.42. Comparison of frequency length scales values for different blocks elevations at the fetch length and spires heights for the arrangements with rectangular barrier (cases 2-52, 2-59, 2-62, 2-69, 2-72, 2-77, 2-84, 2-87, 2-94, 2-97, 3-52, 3-59, 3-62, 3-69 and 3-72)

Based on the plots presented in Fig. 7.40-Fig. 7.42, the following conclusions can be drawn:

- In the cases without the barriers, the frequency length scales related to the lowest measuring point increase with the height of the spires, however, the increase seems to be also caused by the blocks' elevation at the fetch length, which appears to be a more decisive factor for this increase;
- A similar trend can be observed for the cases with barriers, however, the influence of the blocks' elevation in these cases is much less prominent (in particular in the cases with a rectangular barrier);
- The frequency length scales related to the highest measuring point increase with the height of the spires, but decrease with the higher blocks' elevations at the fetch length, which results in a highly non-linear relationship;
- For the lower blocks' elevations at the fetch length (0-5 cm) and the barriers present, the highest values of the frequency length scales are usually observed for the spires of 100 cm height.

Fig. 7.43. Comparison of frequency length scales values for different blocks elevations at the fetch length and barrier types for the arrangements with 80 cm spires (cases 2-2, 2-9, 2-12, 2-19, 2-22, 2-27, 2-34, 2-37, 2-44, 2-47, 2-52, 2-59, 2-62, 2-69 and 2-72)

Fig. 7.44. Comparison of frequency length scales values for different blocks elevations at the fetch length and barrier types for the arrangements with 100 cm spires (cases 2-77, 2-84, 2-87, 2-94, 2-97, 2-102, 2-109, 2-112, 2-119, 2-122, 2-127, 2-134, 2-137, 2-144 and 2-147)

Fig. 7.45. Comparison of frequency length scales values for different blocks elevations at the fetch length and barrier types for the arrangements with 120 cm spires (cases 3-2, 3-9, 3-12, 3-19, 3-22, 3-27, 3-34, 3-37, 3-44, 3-47, 3-52, 3-59, 3-62, 3-69 and 3-72)

Based on the plots presented in Fig. 7.43-Fig. 7.45, the following conclusions can be drawn:

- There is a very strong influence of the blocks' elevation at the fetch length on the values of the frequency length scales, which impacts the results more than the barrier type used in most cases;
- In the cases with low (0-10 cm) blocks' elevations at the fetch length, higher values of the frequency length scales related to the lowest measuring point can be observed for the cases with either type of barrier than without any barrier. For the cases with higher blocks at the fetch length, the cases without any barrier yield the highest results;
- The cases with a rectangular barrier produce the highest values of frequency length scales in the cases where the blocks are not elevated at the fetch length. For the cases with the low elevation of the blocks at the fetch length (5-10 cm), the highest values can be observed for the cases with a triangular barrier. For the highest blocks' elevations (15-20 cm), the highest values can be observed for the cases without any barrier.

Summing up the plots and their analysis presented above, several other conclusions can be drawn:

- In general, the dependence of the values of the frequency length scale on the distance between the two points Δz is in line with the literature and the expectations – the shorter the distance, the higher the values of the frequency length scale. Only very few cases (with spires mounted backwards and particularly high blocks elevations) seem to slightly diverge from this trend;
- For the cases with spires and barriers, larger values of the frequency length scales were observed in relation to the lowest measuring point, while for the cases without any barrier or spires, with lower blocks' elevations, the larger values are related to the highest measuring point and with higher blocks' elevations – for the lowest measuring point;
- The values of frequency length scales at the three analysed distances Δz (12.5 m, 25 m and 37.5 m) are between 0.05 Hz to 0.25 Hz (0.3 Hz in some cases with 120 cm spires mounted backwards). This would result in period scales of about 4 s to 20 s, which can be applied e.g. for averaging the values of wind action on a building.

The model of equivalent peak wind actions, which takes into account the frequency and period scales of the gusts, suggests that the averaging period for a gust frequency should be based on the size of the building. In the case of vertical scales (which is applicable to e.g. tall buildings), the considered size would be the height of the building. Cook (1985, 1990) recommends the following periods depending on the building heights: $T_{min} = 3$ s for $H < 30$ m, $T_{min} = 5$ s for $H = 30 \div 50$ m, $T_{min} = 10$ s for $H = 50 \div 100$ m and $T_{min} = 15$ s for $H > 100$ m. This results in frequency scales of 0.33 Hz, 0.2 Hz, 0.1 Hz and 0.067 Hz, respectively for these distances. Therefore, it can be stated that the obtained values of vertical frequency length scales for different distances Δz are consistent with the literature pertaining to the real-life scale.

8. Results discussion and analysis for selected cases

In this chapter, five cases are discussed in detail, selected upon being the most suitable representations of each of the five terrain roughness categories referenced in (PN-EN 1991-1-4, 2011) based on the method described in subsection 6.2. For each of these cases, all the relevant plots are presented below and the numerical results are discussed in detail. It should be noted that the results for each of the tested cases can be found in the attached file *Results.xlsx* and all the plots for the test cases that best match the different terrain roughness categories according to (ASCE/SEI 7, 2022; ISO 4354, 2009; PN-EN 1991-1-4, 2011) can be found in the attached file *Plots.pdf*.

The most significant results regarding the vertical mean wind speed profiles, turbulence intensity profiles, longitudinal and vertical turbulence length scales and frequency length scales for the cases that best match the wind flow structure typical for different terrain categories according to (PN-EN 1991-1-4, 2011) are summarised in Tab. 8.1.

Tab. 8.1. Wind flow parameters for the cases selected as best matching different terrain categories according to (PN-EN 1991-1-4, 2011)

Category (case) / Parameter	Category 0 (case 3-98)	Category I (case 3-99)	Category II (case 2-128)	Category III (case 3-10)	Category IV (case 2-82)
α exponent	0.10	0.15	0.17	0.21	0.25
Roughness length z_0 [m]	0.00	0.06	0.11	0.40	0.87
β exponent	-0.51	-0.42	-0.08	-0.18	-0.17
Turbulence parameter z_0^T [m]	4.81	2.98	0.00	0.14	0.11
Turbulence intensity at 30 m $I_{v,30}$	8.8%	10.3%	16.9%	21.5%	25.0%
Relative error Δ_α	0.081	0.140	0.018	0.096	0.049
Relative error Δ_{z_0}	0.041	5.017	1.252	0.349	0.133
Relative error Δ_β	3.644	2.205	0.533	0.039	0.277
Relative error $\Delta_{I_{v,30}}$	0.093	0.067	0.356	0.226	0.150
RMSE of power-law wind profile	0.032	0.014	0.027	0.024	0.029
RMSE of logarithmic wind profile	0.031	0.024	0.032	0.030	0.031

Category (case) / Parameter	Category 0 (case 3-98)	Category I (case 3-99)	Category II (case 2-128)	Category III (case 3-10)	Category IV (case 2-82)
RMSE of power-law turbulence intensity profile with PN-EN 1991-1-4	0.069	0.049	0.028	0.013	0.023
RMSE of logarithmic turbulence intensity profile with PN-EN 1991-1-4	0.053	0.040	0.029	0.013	0.023
RMSE of measured turbulence intensity with ESDU 85020	0.043	0.045	0.025	0.016	0.039
Longitudinal turbulence length scale $L_x(17.5)$ [m]	81.4	69.0	114.1	104.1	93.1
$L_x(30)$ [m]	72.3	63.2	120.8	110.8	96.7
$L_x(42.5)$ [m]	65.8	57.4	126.3	118.1	90.6
$L_x(55)$ [m]	63.8	59.0	124.1	127.6	94.4
$L_x(67.5)$ [m]	64.5	64.5	128.2	178.7	107.5
$L_x(80)$ [m]	59.0	61.2	108.4	192.5	103.9
$L_x(92.5)$ [m]	61.1	68.1	112.6	167.2	114.7
$L_x(105)$ [m]	55.3	62.8	99.8	131.3	120.2
$L_x(117.5)$ [m]	53.9	59.5	101.4	116.8	130.4
$L_x(130)$ [m]	54.8	60.6	110.1	119.7	138.8
$L_x(142.5)$ [m]	50.6	54.3	114.4	118.6	127.7
$L_x(155)$ [m]	49.0	43.4	109.4	113.7	117.3
Vertical turbulence length scale $L_{z\uparrow}$ [m]	34.9	40.4	46.4	48.1	44.5
Vertical turbulence length scale $L_{z\downarrow}$ [m]	39.6	27.9	39.5	39.4	38.5

Category (case) / Parameter	Category 0 (case 3-98)	Category I (case 3-99)	Category II (case 2-128)	Category III (case 3-10)	Category IV (case 2-82)
Frequency length scale $f_z^*(\Delta z = 12.5\ \text{m}, z = 23.75\ \text{m})$	0.183	0.189	0.165	0.173	0.165
Frequency length scale $f_z^*(\Delta z = 25\ \text{m}, z = 30\ \text{m})$	0.181	0.184	0.101	0.125	0.118
Frequency length scale $f_z^*(\Delta z = 37.5\ \text{m}, z = 36.25\ \text{m})$	0.160	0.177	0.089	0.099	0.106
Frequency length scale $f_z^*(\Delta z = 12.5\ \text{m}, z = 148.75\ \text{m})$	0.233	0.211	0.103	0.085	0.093
Frequency length scale $f_z^*(\Delta z = 25\ \text{m}, z = 142.5\ \text{m})$	0.213	0.180	0.088	0.078	0.070
Frequency length scale $f_z^*(\Delta z = 37.5\ \text{m}, z = 136.25\ \text{m})$	0.213	0.182	0.087	0.077	0.059

Further results and discussions in this chapter will be divided into the in-depth analysis of each case that was selected as representative of each of the five terrain roughness categories. In subsections 8.1 to 8.5, detailed plots and their analysis is conducted for each of these cases.

8.1. Terrain roughness category 0 – Case 3-98

Case 3-98, with a setup consisting of the turbulising net and blocks at the inlet elevated at 10 cm height, was selected as the closest match for terrain category 0, which corresponds to coastal areas exposed to the open sea. The vertical mean wind speed profile for this case is shown in Fig. 8.1 and the turbulence intensity profile is shown in Fig. 8.2.
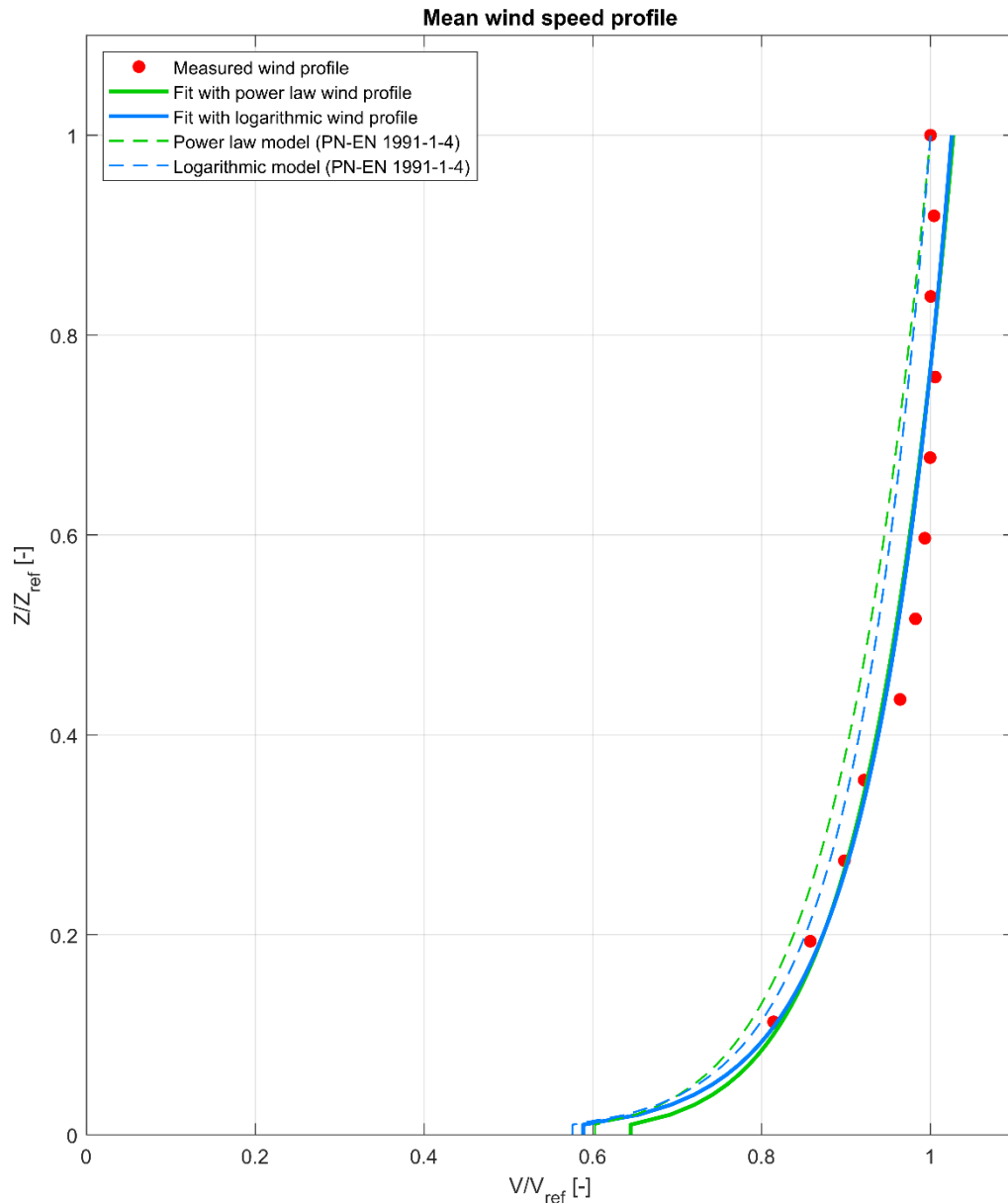
Fig. 8.1. Vertical mean wind speed profile for the Case 3-98

The two main parameters that determine the vertical wind speed profiles are very close to the values suggested by the standard (with roughness length being almost an exact match at z_0 equal to 0.003, while α exponent at 0.10 being very close to the target value of 0.11, with relative errors of 0.041 and 0.081, respectively). These values result in the profiles of very slight curvature and thus little change in the wind speed with height, mostly observed at the lower heights. The obtained wind profiles are very close to the model ones from the standard, with a slight transition to the right. The RMSE values between the model profiles from (PN-EN 1991-1-4, 2011) and the profiles obtained from the measurements are 0.032 for the power-law profile and 0.031 for the logarithmic profile. The wind velocity values from the measurements, marked with red dots, are also closely matched with the obtained fit, with the goodness of fit parameters of R^2 equal to 0.94 and 0.95, and RMSE equal to 0.02 and 0.13 for power-law and logarithmic profiles, respectively. These results are very satisfactory, especially considering that only 4 out of 295 test cases were initially assigned to this terrain category.
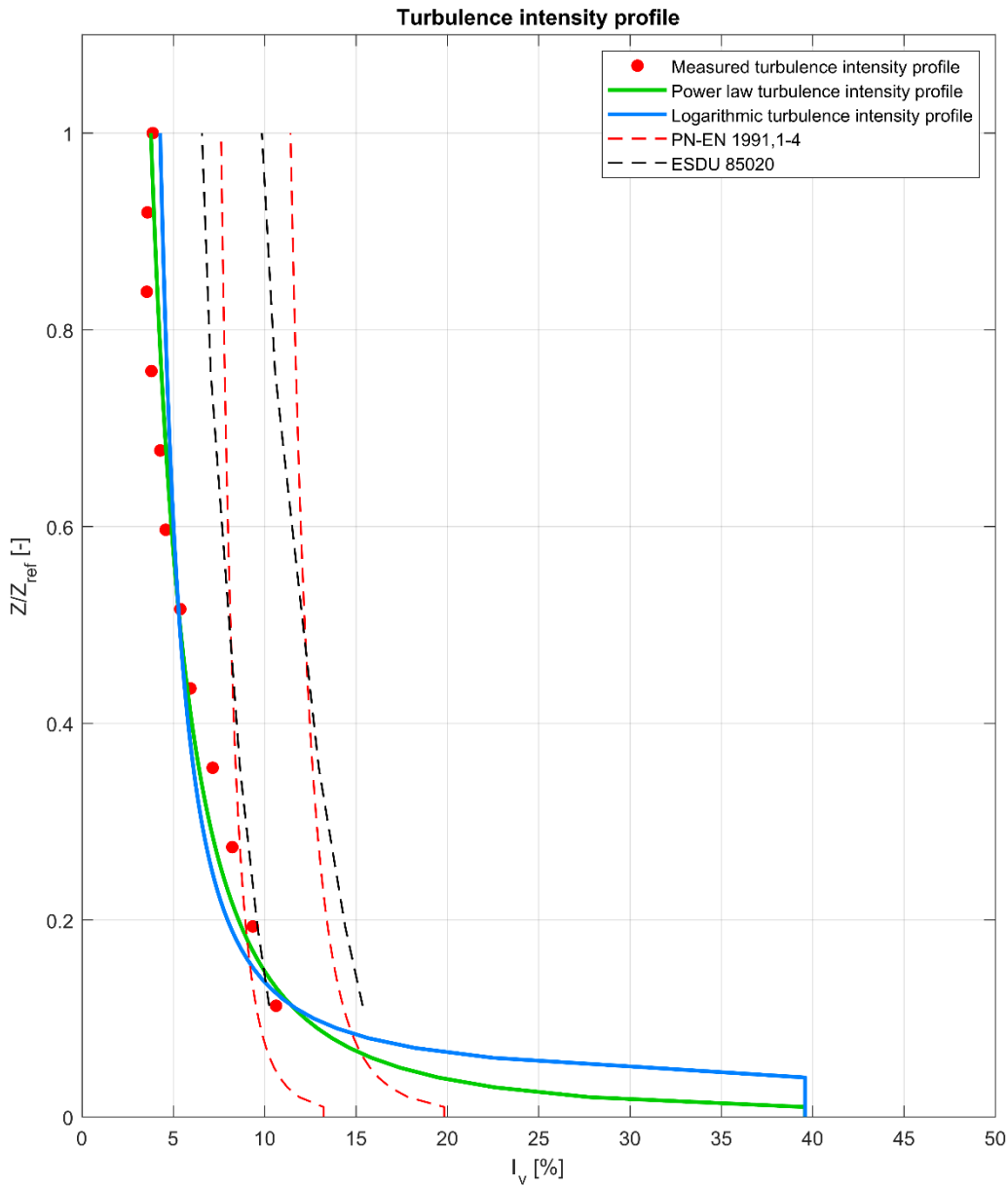
Fig. 8.2. Vertical turbulence intensity profile for the Case 3-98

The turbulence intensity profile is more difficult to obtain for this terrain category. In general, very low values of turbulence intensity are expected for this terrain category, between about 12% closer to the ground to 8% at higher altitudes. The values obtained for this case are smaller, between about 10% to only about 4% at higher altitudes. This only barely fits in the ±20% bounds for the two lowest probes. It should be mentioned that out of the 4 test cases assigned to the terrain category 0, this was still the best match in terms of turbulence intensity, with RMSE values of 0.043 with reference to (ESDU 85020, 2002) and 0.053-0.069 with reference to (PN-EN 1991-1-4, 2011). Moreover, the parameters that define the vertical turbulence profiles, with β exponent at -0.51 and, in particular, z_0^T at 4.81 m, vastly diverge from the target, producing a vertical profile with a steep increase in the lowest parts. The very high (absolute) values of these parameters seem to mostly affect the curvature of the profiles at the lowest parts (below the level of the 1st measuring probe), indicating values which would not be observed from a measurement. This effect seems amplified by a very low value of z_{min} at 1 m for this category, which means that the profiles are plotted below the point

where they would correctly describe the wind flow either in reality or in a wind tunnel. At the higher altitudes of about 0.5 Z_{ref} and above, there are almost constant values of the turbulence intensity. This is because the turbulising network with an even pattern of elements produces a relatively uniform vertical profile of mean wind speed and turbulence intensity along the height of the wind tunnel. In this case, it is modified at the lower heights with 10 cm blocks at the inlet segment, which effectively disturb the flow at and around this lower region of the simulated boundary layer. This is visible in particular at the 6 lowest probes, with turbulence intensities at these heights varying from about 10% to 5%, while for the higher probes, the turbulence intensity levels are at an approximately constant level of 4%. The goodness of fit parameters for the turbulence intensity profiles is satisfactory at R^2 equal to 0.95 and 0.87, and RMSE equal to 0.006 and 0.009 for power-law and logarithmic profiles, respectively.
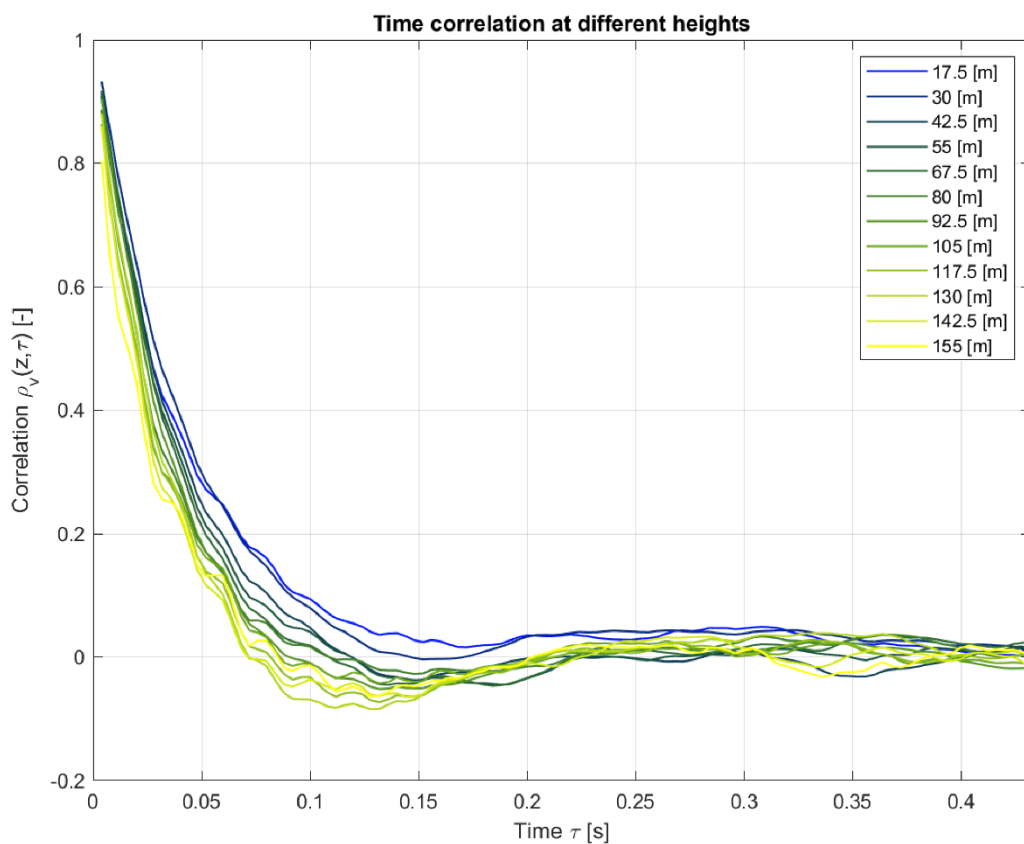
Fig. 8.3. Time correlation at different heights for the Case 3-98
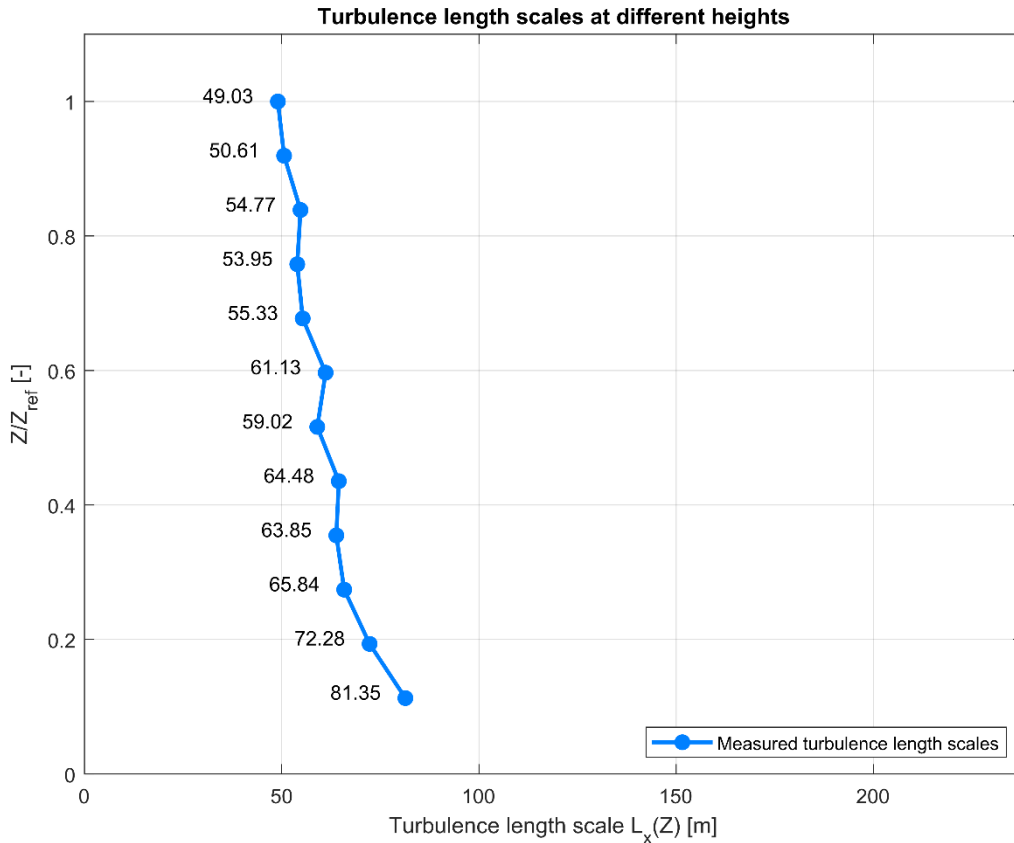
Fig. 8.4. Longitudinal turbulence length scale $L_x(Z)$ at different heights for the Case 3-98

The next analysed characteristics are time autocorrelations (shown in Fig. 8.3) and longitudinal turbulence length scales at different heights (Fig. 8.4), which were calculated based on these autocorrelations. The autocorrelations plots show high fluctuations of the correlation time scales, particularly around the horizontal axis. The correlations reach 0 at a time step (lag) of about $\tau = 0.1$ s for most measuring points, besides the 2 lowest probes. The longitudinal turbulence length scales assume relatively low values between about 50 m and 80 m, much lower than what can be expected for a wind flow over an open terrain exposed to sea. Furthermore, they are decreasing with height (especially at the lower heights), which is uncharacteristic and does not match the field measurement results adopted in the standards. They tend to approximately constant values at about 0.6 Z_{ref}. These small values of longitudinal turbulence length scales can possibly be attributed to the small grid sizes of the turbulising net, which would physically limit the development of larger eddies in the wind tunnel. This may be a strong disadvantage of the turbulising net.

Fig. 8.5 shows vertical spatial correlations at different distances Δz between the two points, when moving upward or downward (in relation to the lowest and to the highest measuring point). As mentioned in the earlier chapters, this is an anisotropic relation, and in this case, it can be mostly observed at shorter distances, where the downward correlation has a much steeper decrease. For larger distances, the upward correlation has a character close to the exponential curve, while the downward correlation is more linear, which is in line with the results of field studies (Duchêne-Marullaz, 1977). The values of vertical turbulence lengths are 34.9 m when moving upward and 39.6 m when moving downward. This is rather

146

uncharacteristic, as most sources report the scale while moving upward to be larger than when moving downward, comp. Eq. (3.21).
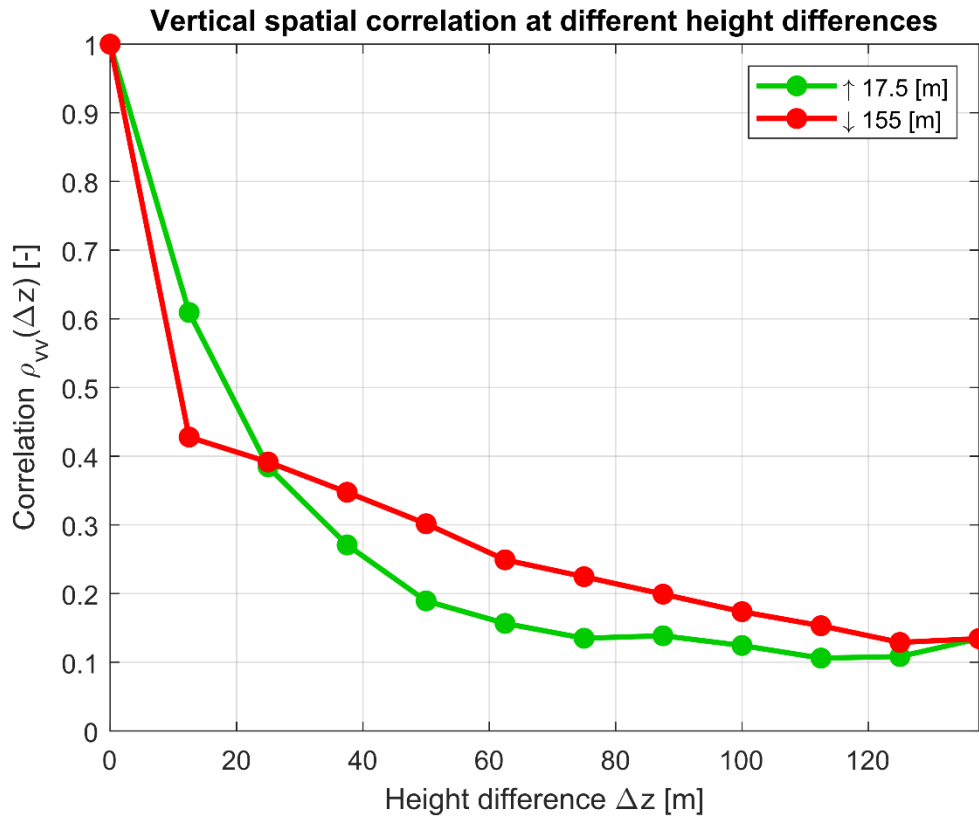
Fig. 8.5. Vertical spatial correlation at different height differences for the Case 3-98

Fig. 8.6 shows power spectral densities at each measurement point, in a log-log presentation which is more convenient for this parameter, as discussed earlier in this work (comp. Fig. 3.2). However, this characteristic is also plotted with a linear-linear presentation in the Attachment 3 to this work (for all of the representative test cases discussed in detail). The results are calculated directly from FFT and using the Welch method, as described in subsection 6.1, and compared against the Davenport, von Kármán and Kaimal model spectra. The calculated spectra show general agreement with the models, especially in the range of about 1 to 10 of the non-dimensional frequency. However, the calculated spectra are slightly higher than the models, especially on lower heights of about 17.5-80 m (Fig. 8.6a-Fig. 8.6f).

The results obtained with both the Welch method and the direct approach from FFT show good agreement in the trend, however, the values obtained directly from FFT are much more scattered. As the same pattern is repeated in all the test cases, it should be stated that the Welch method is clearly a more accurate approach, however, the direct method from FFT can be used as a decent approximation of the power spectral densities. This corresponds with the results obtained by (Moravej, 2019) who compared the two methods.

A region with a decreasing slope of approximately 2/3 inclination (height-to-length ratio) is barely present in the reduced frequency range of about 1 to 10, particularly for the probes located at higher altitudes. However, this region is not very well developed due to the relatively large dispersion of the values of the power spectra. The presence of this region

indicates the Kolmogorov inertial subrange (Kolmogorov, 1941), which is important in the cases of wind loading studies (Kozmar, 2011b).

e) PSD at 67.5 [m] in full scale

f) PSD at 80 [m] in full scale

g) PSD at 92.5 [m] in full scale

h) PSD at 105 [m] in full scale
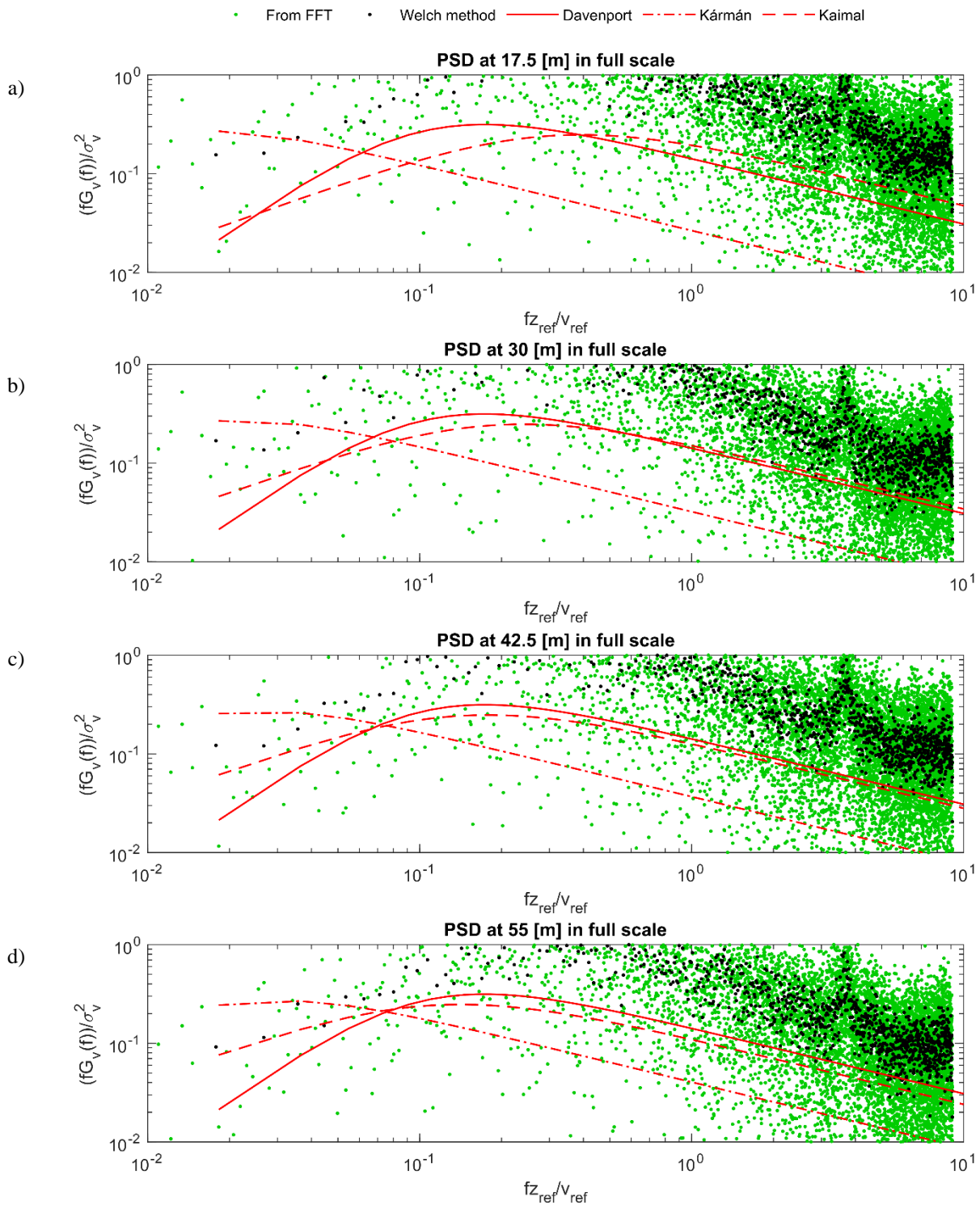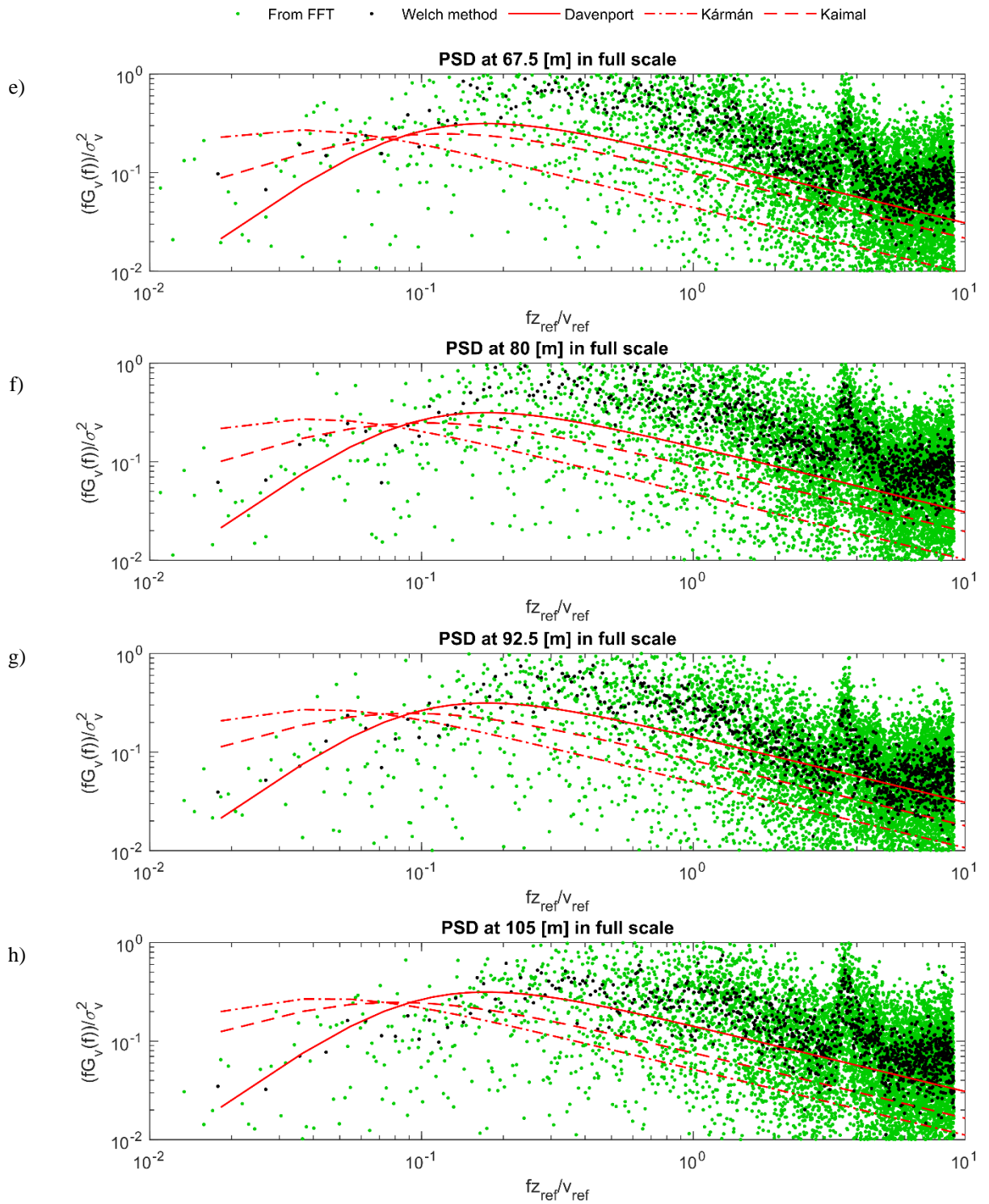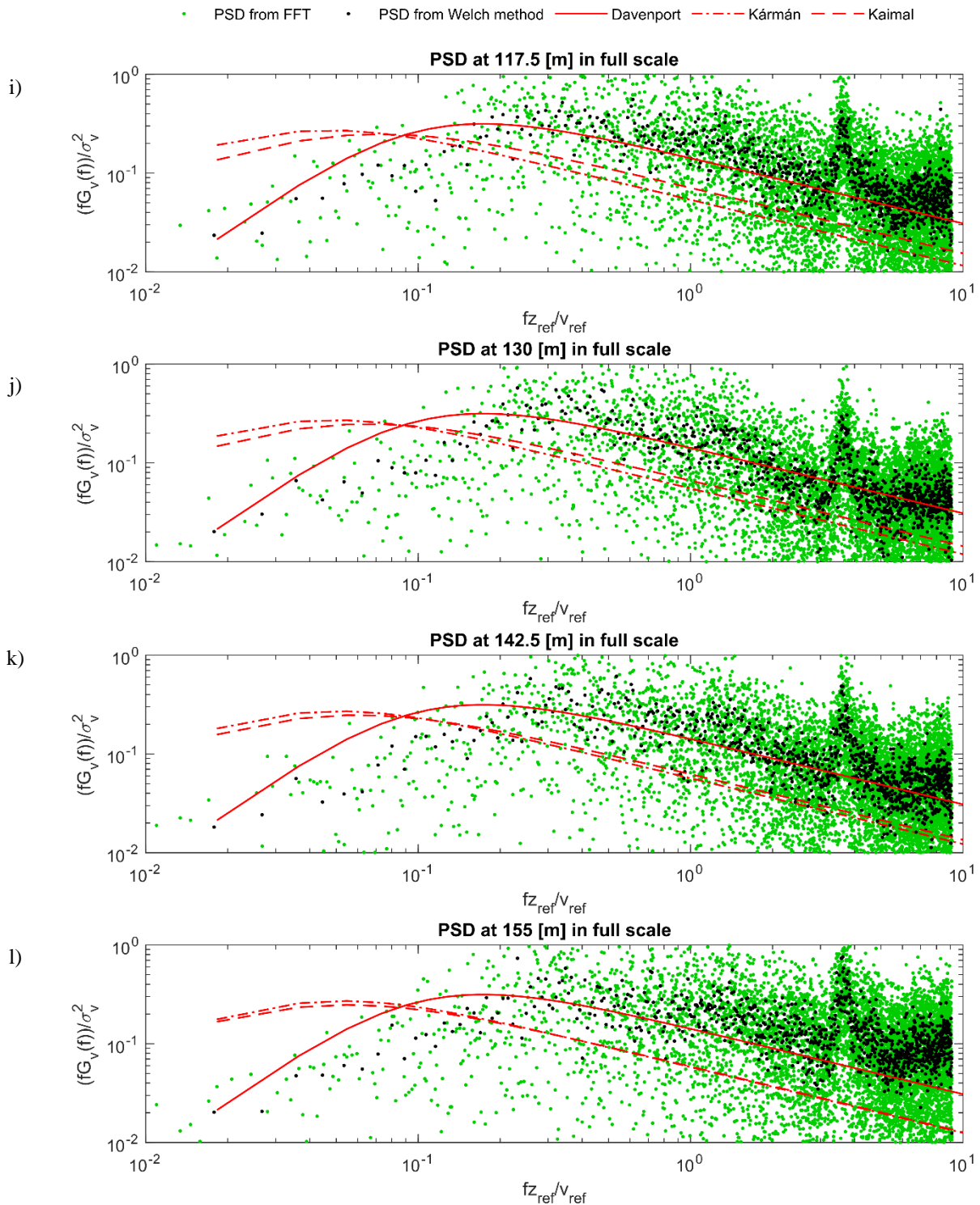
Fig. 8.6. Power density spectra at different heights, calculated with the Welch method and directly from FFT and compared against the reference spectra from Davenport, von Kármán and Kaimal, for the Case 3-98

Slight peaks can be noticed in the spectra for all the measuring heights, particularly notable at the higher altitudes. These peaks occur at the reduced frequency of about 3.6, which corresponds to 0.4 Hz in real-life scale. Similar effects were observed during field measurements (Newberry et al., 1973), where small peaks where found in the spectrum at frequencies of about 0.1-0.25 Hz. According to the authors, these peaks might correspond to

the pulsations of the windward pressure "cushion". As both the referenced field tests and the presented wind tunnel tests are based on pressure measurements, the presence of these peaks in the wind tunnel tests might be caused by a similar phenomenon that also occurs in nature.

Fig. 8.7-Fig. 8.9 show plots of co-coherence. For the sake of brevity, only the plots for distances Δz of 12.5 m, 25 m and 37.5 m are presented in this work. All of the plots for every pair of points (for the discussed representative test cases) can be found in Attachment 3. The calculated functions of co-coherence are also approximated by the Davenport model, Bowen model and modified Bowen model. Furthermore, the plots also show the values of the exponential decay coefficient C_z for the Davenport model and coefficients c_1 and c_2 for the Bowen model.
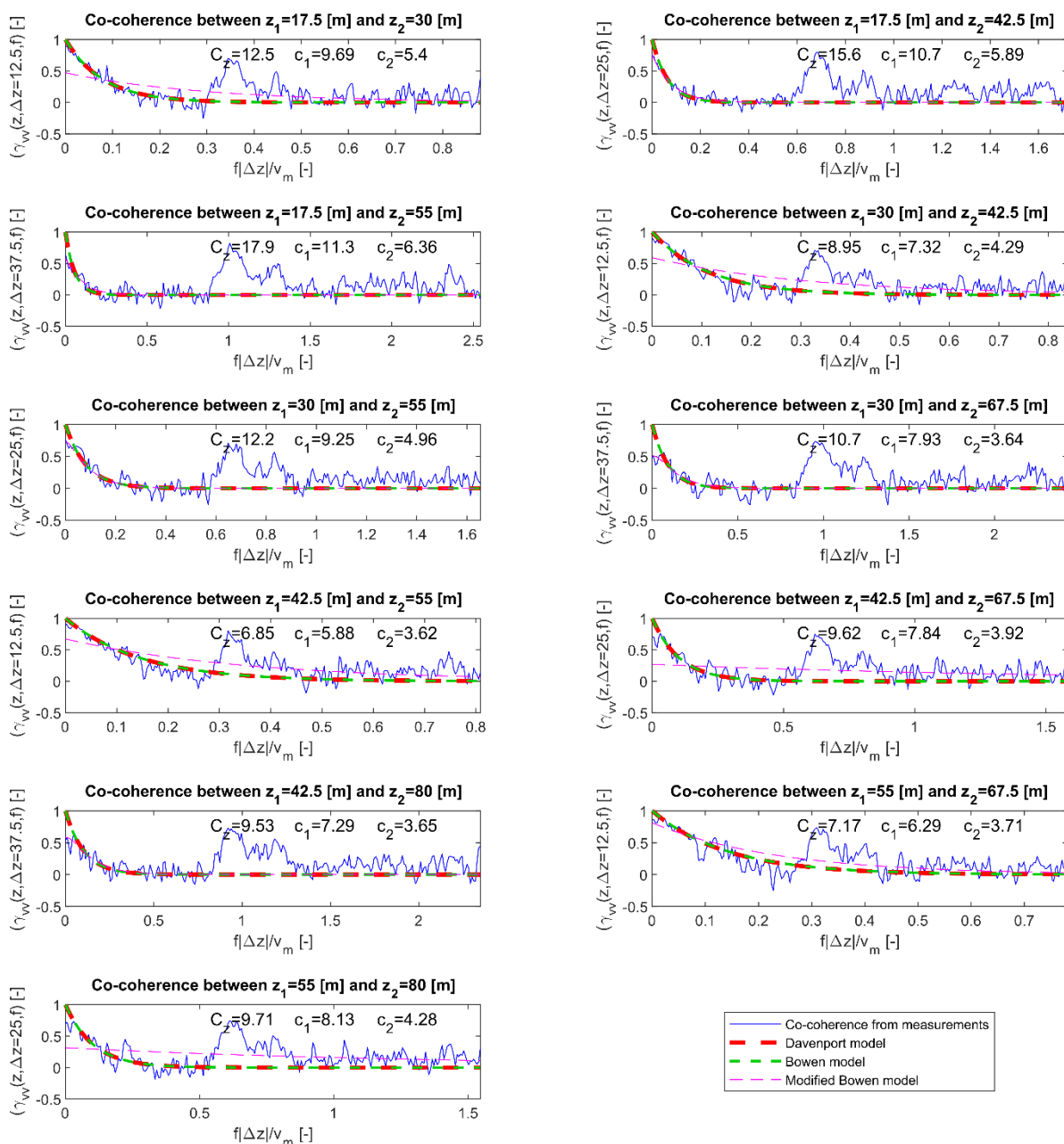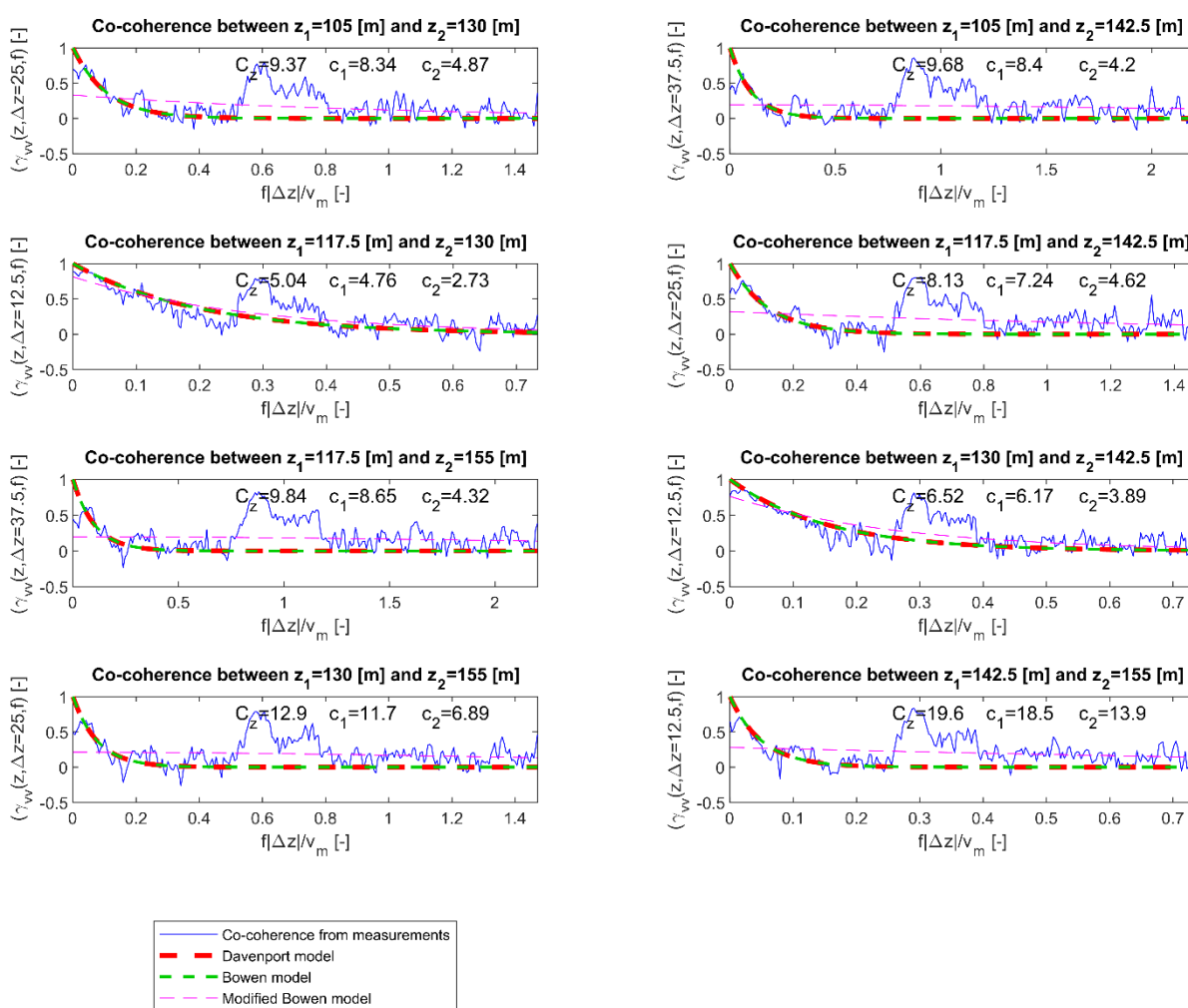

Fig. 8.7. Vertical co-coherence between the points with Δ_z equal to 12.5 m, 25 m and 37.5 m for the Case 3-98, with fit according to the Davenport model, Bowen model and modified Bowen model – plots 1-11
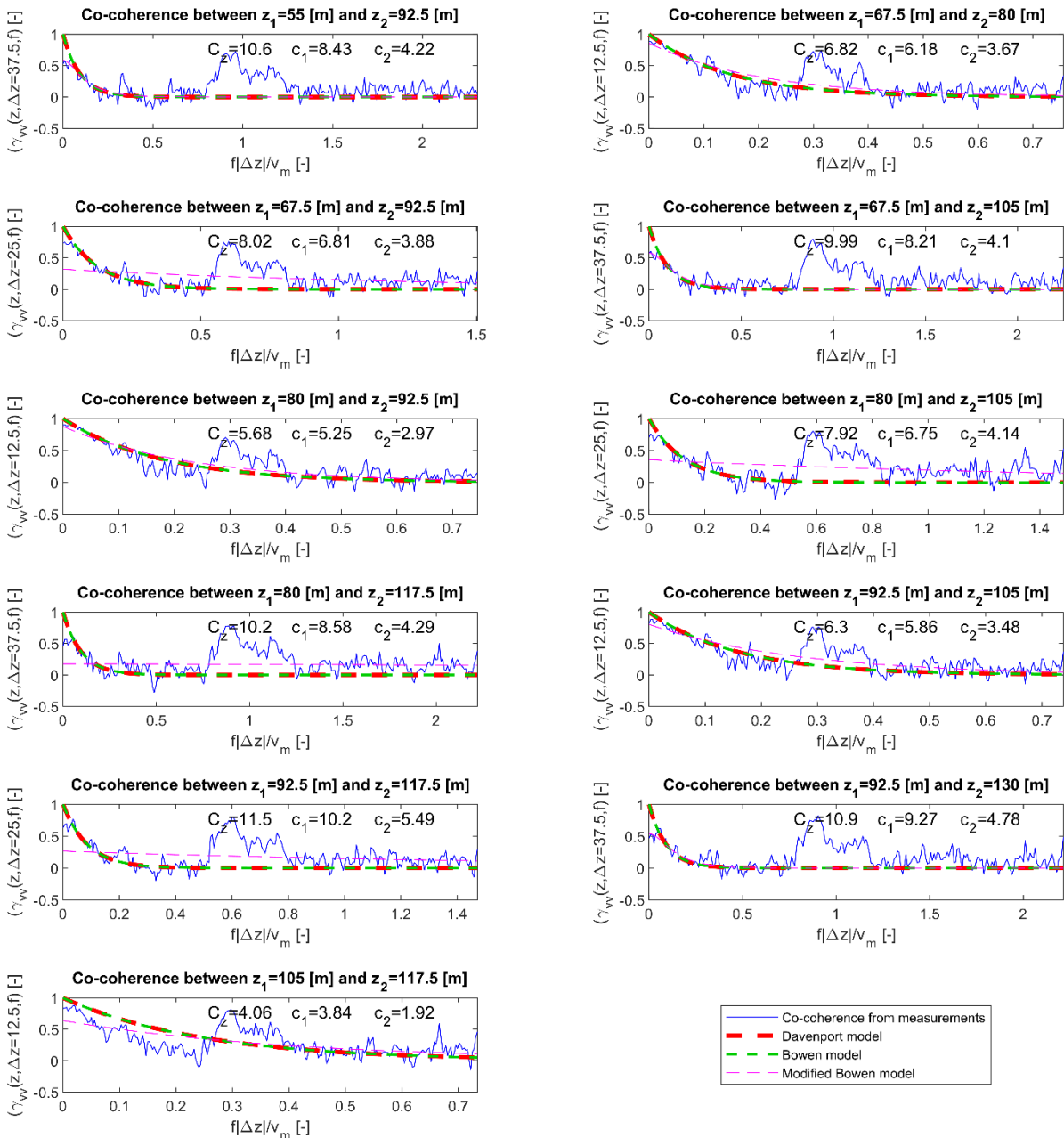
Fig. 8.8. Vertical co-coherence between the points with Δ_z equal to 12.5 m, 25 m and 37.5 m for the Case 3-98, with fit according to the Davenport model, Bowen model and modified Bowen model – plots 12-22

The co-coherence for each of the three analysed distances is well estimated by the fit from the Davenport and Bowen models. Approximation by both of these models produces the same curves for all the analysed cases. According to (Bowen et al., 1983; Cheynet, 2018), the Bowen model can be treated as a generalisation of the Davenport model, taking into account the influence on the exponential decay by the effects of increasing eddies size with altitude and the blockage by the surface at heights below 40 m. However, it seems that these effects are not replicated in this case in the wind tunnel tests.

The exponential decay for the Davenport model was reported to be about 7 (Davenport, 1962) or, if using the relationship from ISO 4354 (2009) given in Eq. (3.44), between 9.1 and 10.8 (depending on the mean height between the two considered points). The exponential decay coefficients of about 7 for the Davenport model are reported mostly for the distances Δz of

12.5 m (6 out of 11 cases), at heights above 40 m. The values of this coefficient tend to be larger at lower altitudes and smaller at higher ones. Values of about 9.1-10.8 were observed for a total of 10 cases, mostly at Δz of 37.5 m.

The exponential decay coefficients for the Bowen model were reported to be 11 and 6, respectively (Bowen et al., 1983). Similar values can be observed only for 4 cases, two of which are close to the ground level (17.5 and 42.5 m; 17.5 and 55 m), and two concerning the higher altitudes (92.5 and 117.7 m; 130 and 155 m).

There is a notable peak occurring at each of the presented charts, at a reduced frequency that corresponds to 0.4 Hz (in real-life scale). This is similar to the peaks observed in the power density spectra (Fig. 8.6) and may confirm the potential presence of the phenomenon reported by (Newberry et al., 1973).

Fig. 8.9. Vertical co-coherence between the points with Δ_z equal to 12.5 m, 25 m and 37.5 m for the Case 3-98, with fit according to the Davenport model, Bowen model and modified Bowen model – plots 23-30

The modified Bowen model, which takes into account the possibility of the co-coherence model not being equal to 1.0 at the reduced frequency of 0, gives a decent approximation of the calculated co-coherence function for the larger distances Δz between the two considered points at the heights closer to the ground level and for smaller distances Δz at the higher

altitudes. In some cases, the fit from this model seems influenced by the peak in the co-coherence function mentioned in the previous paragraph, which results in a worse fit.
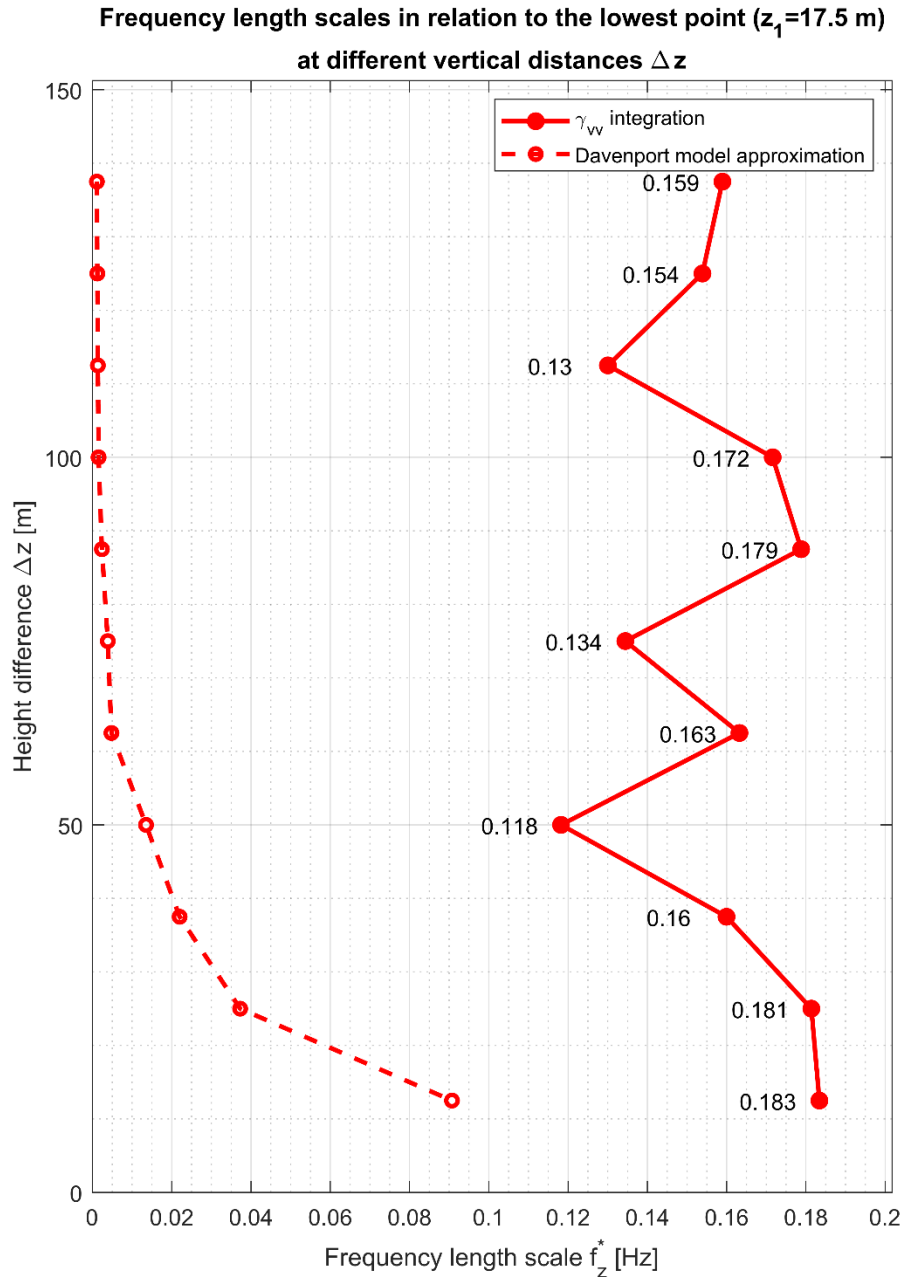
Fig. 8.10. Frequency length scales in relation to the lowest measurement point and different Δ_z values for the Case 3-98

Fig. 8.10 and Fig. 8.11 show the frequency length scales distribution at different vertical distances Δz, taking into account the correlations with the lowest measuring point at 17.5 m (Fig. 8.10) and the correlations with the highest measuring point at 155 m (Fig. 8.11). The results are directly calculated from the co-coherence functions and approximated using the Davenport model exponential decay.

As mentioned in subsection 7.3, for the cases without any spires or barriers, the frequency scales at higher altitudes are larger than at lower heights, which can be seen here. The values of frequency length scales are between 0.12 Hz and 0.18 Hz in relation to the lowest

measuring point and between 0.16 Hz and 0.23 Hz in relation to the highest measuring point. For the lowest point, the values are distributed in a rather chaotic pattern, oscillating around a mean value, while for the highest point, a clear decreasing trend with the increase of distance Δz between the two considered points can be noticed. It should be emphasised that even for the largest distance Δz of 155 m, the frequency length scale is 0.16 Hz, which would result in an averaging period T_z^* of only about 6 s, much smaller than the values of 15 s recommended by (Cook, 1985, 1990) for buildings of height above 100 m.
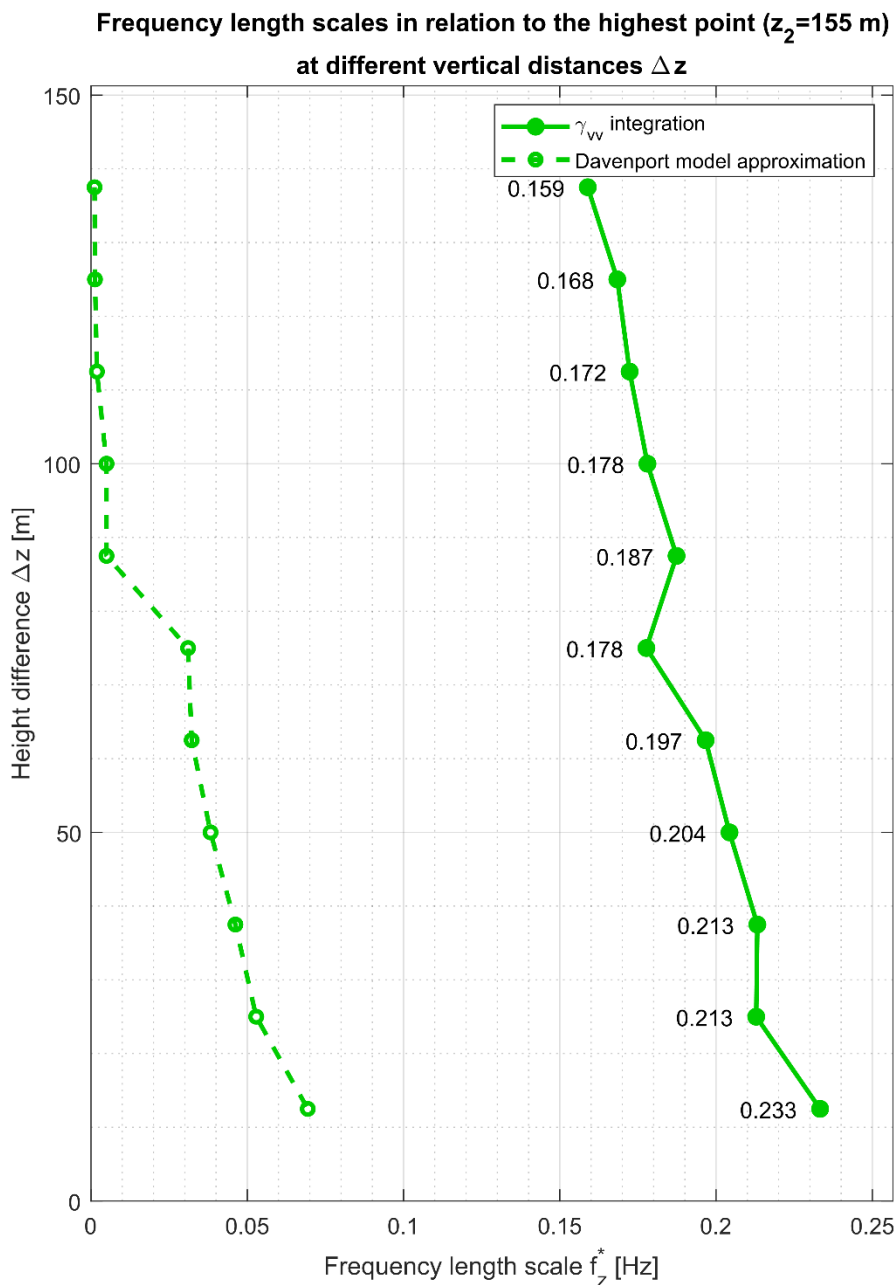
Fig. 8.11. Frequency length scales in relation to the highest measurement point and different Δ_z values for the Case 3-98

The values approximated from the Davenport model are much lower than the ones calculated from the co-coherence function. These values are at about 0.02 Hz-0.09 Hz at the 4-6 smallest distances Δz, then close to 0 for all the larger distances. It should be highlighted that this approximation is therefore not on the safe/conservative side e.g. for the purpose of analysing

wind actions on structures (as they would result in a longer averaging period and thus underestimated gust/peak values, comp. Fig. 3.1).

8.2. Terrain roughness category I – Case 3-99

Case 3-99, with a setup consisting of the turbulising net and blocks at the inlet elevated at 15 cm height, was selected as the closest match for terrain category 1, which corresponds to lakes or areas with negligible vegetation and without obstacles. The vertical mean wind speed profile for this case is shown in Fig. 8.12 and turbulence intensity profile is shown in Fig. 8.13.
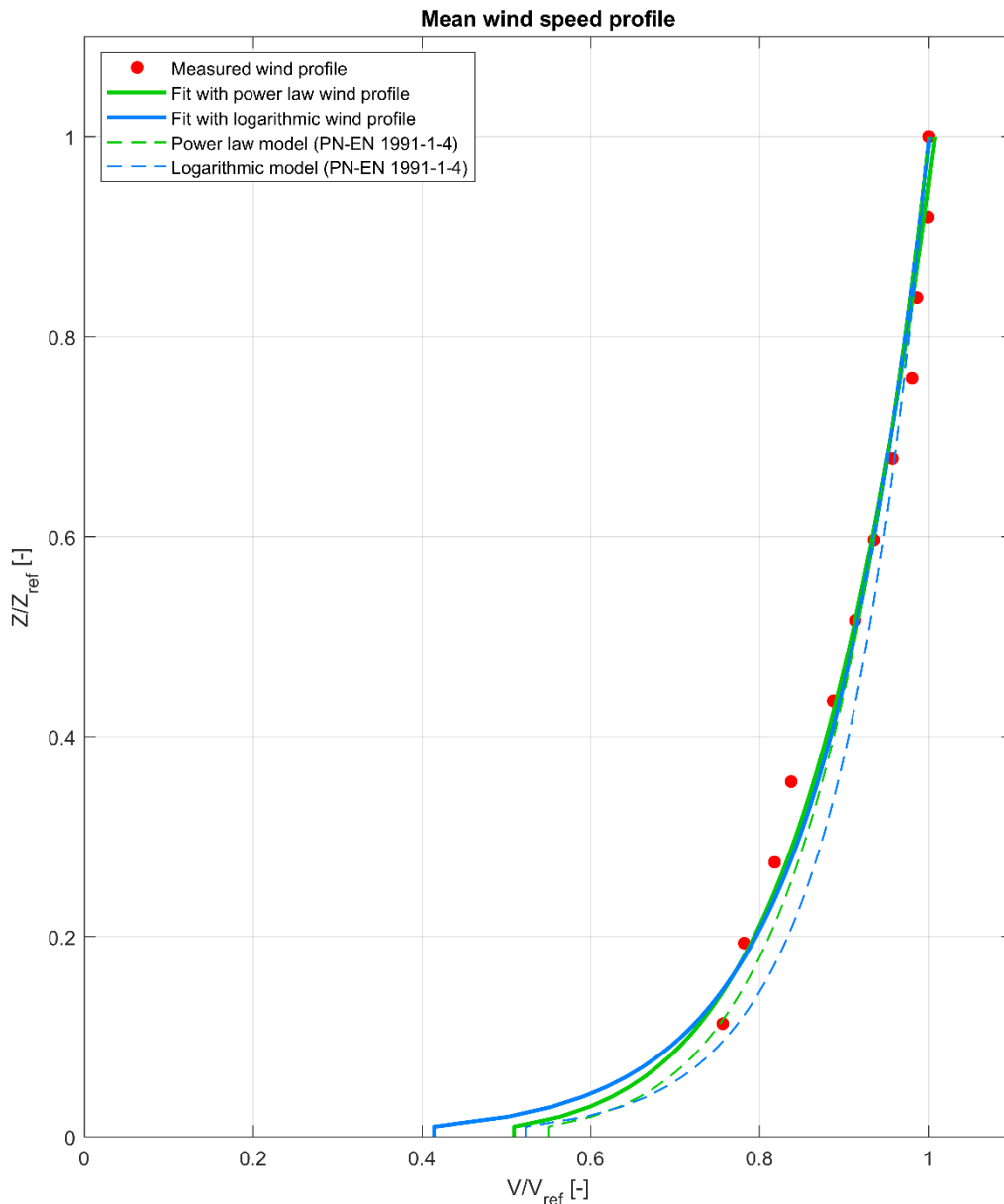
Fig. 8.12. Vertical mean wind speed profile for the Case 3-99

In this case, the assignment to the terrain category I was based only on the α exponent, as the assignment based on the roughness length z_0 would place it in the terrain category II. However, as can be seen in Fig. 8.12, the calculated power law and logarithmic profiles match very well with the model profiles from the standards, with the latter only significantly

diverging at the lower heights (in the region below the lowest measuring probe). This resulted in a relative error of the α exponent at 0.14 and for z_0 at 5.02. Out of the 4 test cases that were assigned to this terrain category, this one still resulted in the best match to the standard, with the RMSE values between the model profiles from (PN-EN 1991-1-4, 2011) and the profiles obtained from the measurements at 0.014 for the power-law profile and 0.024 for the logarithmic profile. This gives an even better fit than e.g. for the case 3-98, where the wind profile parameters matched more closely with the standard. The wind velocity values from the measurements, marked with red dots, are also closely matched with the obtained fit, with the goodness of fit parameters of R^2 equal to 0.98 and 0.96, and RMSE equal to 0.014 and 0.15 for power-law and logarithmic profiles, respectively.
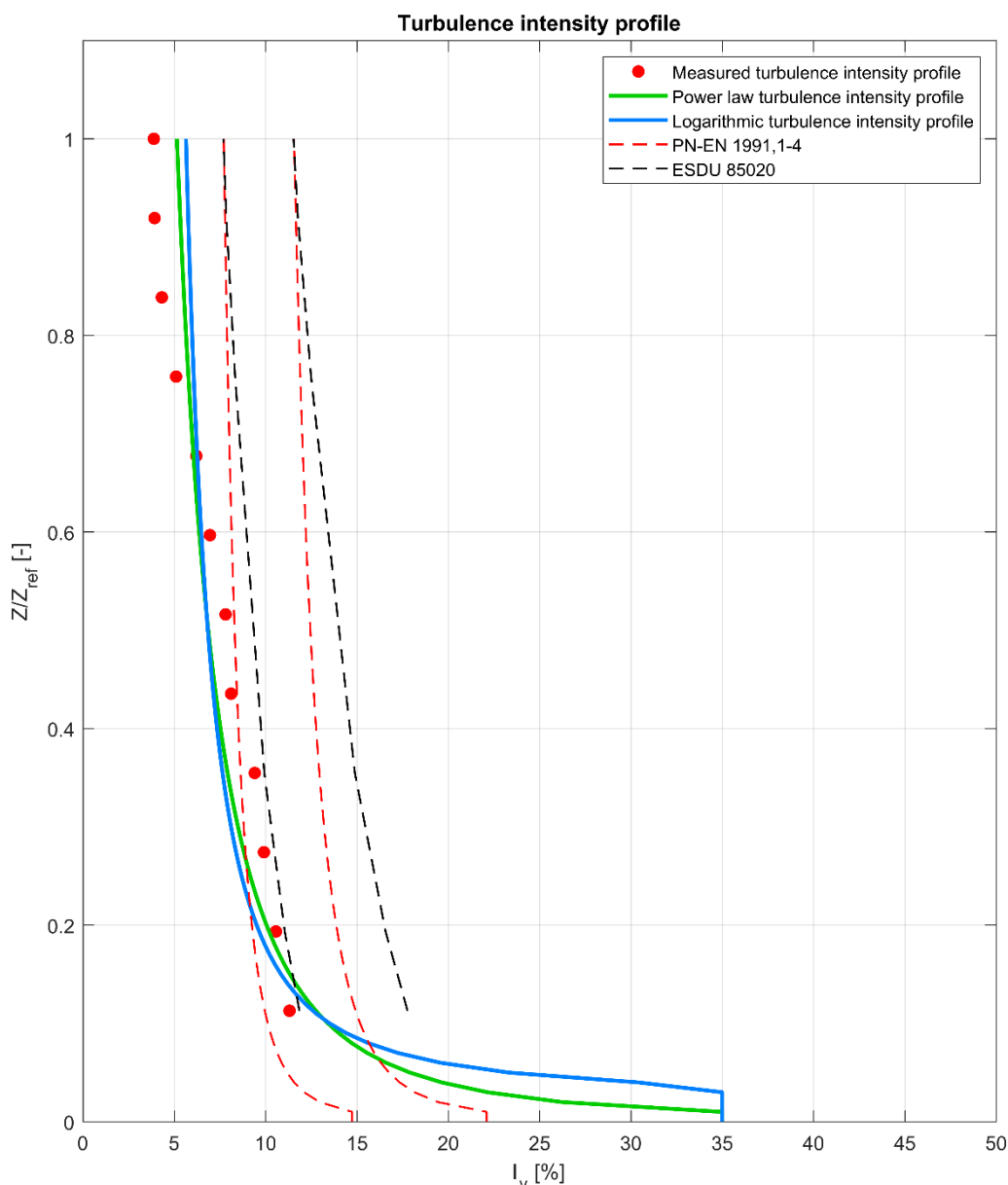
Fig. 8.13. Vertical turbulence intensity profile for the Case 3-99

Similarly as in the test case 3-98, it was difficult to obtain the wind turbulence intensity profile matching the standards. This is due to once again using the turbulising net as the main device of the turbulence generation (the only difference from the case 3-98 is the higher

elevation of the blocks at the inlet). Rather low values of turbulence intensity are expected for this terrain category, between about 15% closer to the ground to 10% at higher altitudes. The values obtained for this case are smaller, between about 11% to only about 4% at higher altitudes. This only barely fits in the ±20% bounds from (PN-EN 1991-1-4, 2011) for the four lowest probes and is still lower than the bounds from (ESDU 85020, 2002). Once again, out of the 4 test cases assigned to the terrain category I, this was still the best match in terms of turbulence intensity, with RMSE values of 0.045 with reference to (ESDU 85020, 2002) and 0.04-0.049 with reference to (PN-EN 1991-1-4, 2011). Moreover, the parameters that define the vertical turbulence profiles, β exponent at -0.42 and, in particular, z_0^T at 2.98 m, vastly diverge from the target, producing a vertical profile with a steep increase in the lowest parts and linear, slight decrease along the heights of about 0.5 Z_{ref}. This is because the turbulising network with an even pattern of elements produces a relatively uniform vertical profile of mean wind speed and of turbulence intensity along the height of the wind tunnel. The height at which the influence of the blocks at the inlet seems to take an effect on the turbulence is at about 0.75 Z_{ref}, as above this height the turbulence intensity values are very close to the test case 3-99, therefore they are only affected by the turbulising net. The goodness of fit parameters for the turbulence intensity profiles are sufficient at R^2 equal to 0.83 and 0.74, and RMSE equal to 0.012 and 0.014 for power-law and logarithmic profiles, respectively.

Fig. 8.14 shows the time autocorrelations plots and Fig. 8.15 shows the longitudinal turbulence length scales at different heights for case 3-99. The autocorrelations plots are smooth with very little fluctuation (only present for the two highest probes) of the correlation time scales. The correlations reach 0 at a lag of about $\tau = 0.07$ s (highest point) and $\tau = 0.15$ s (lowest point). Similarly to case 3-98, the longitudinal turbulence length scales assume relatively low values between about 40 m and 70 m, much lower than what can be expected at an open terrain. Furthermore, they are almost constant along the height and decrease at higher altitudes, which is uncharacteristic and does not match the field measurement results. This confirms that it is impossible to obtain the higher values of the longitudinal turbulence length scales (and their increase with height) with the use of a turbulising net. In fact, very similar, low values of the turbulence length scales are obtained for all the test cases with turbulising net (comp. Fig. 7.29 and see Attachment 2).
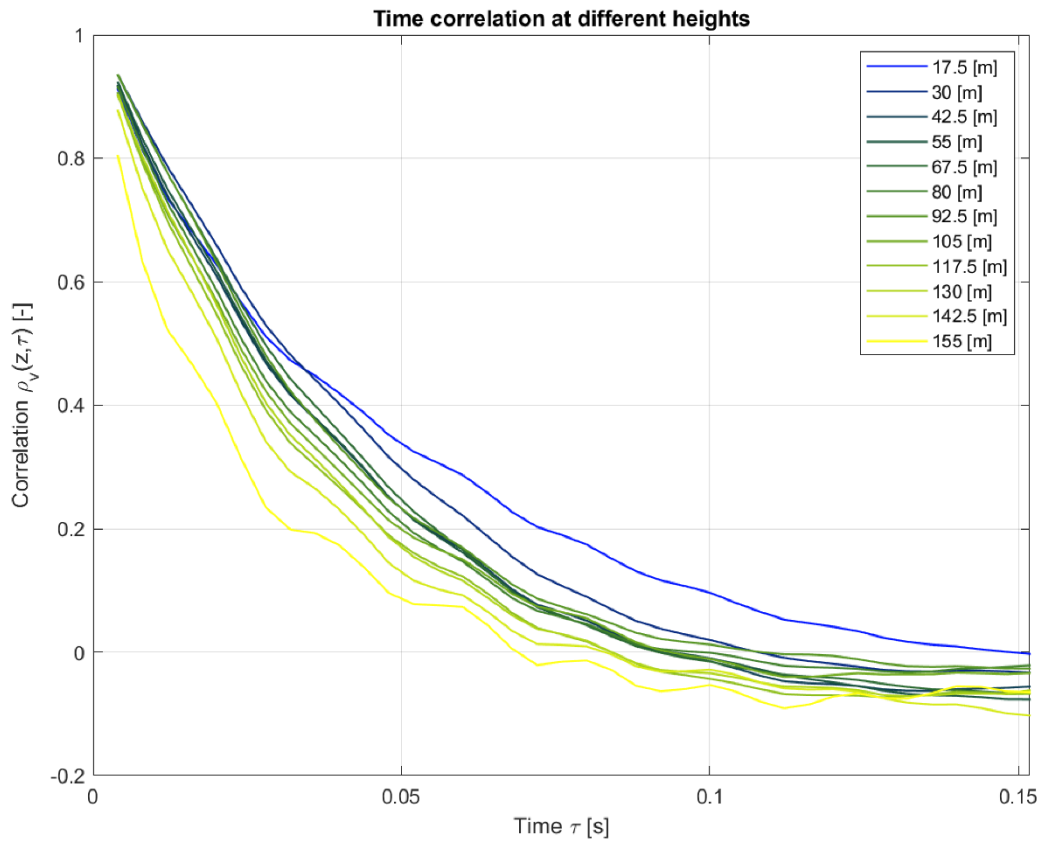
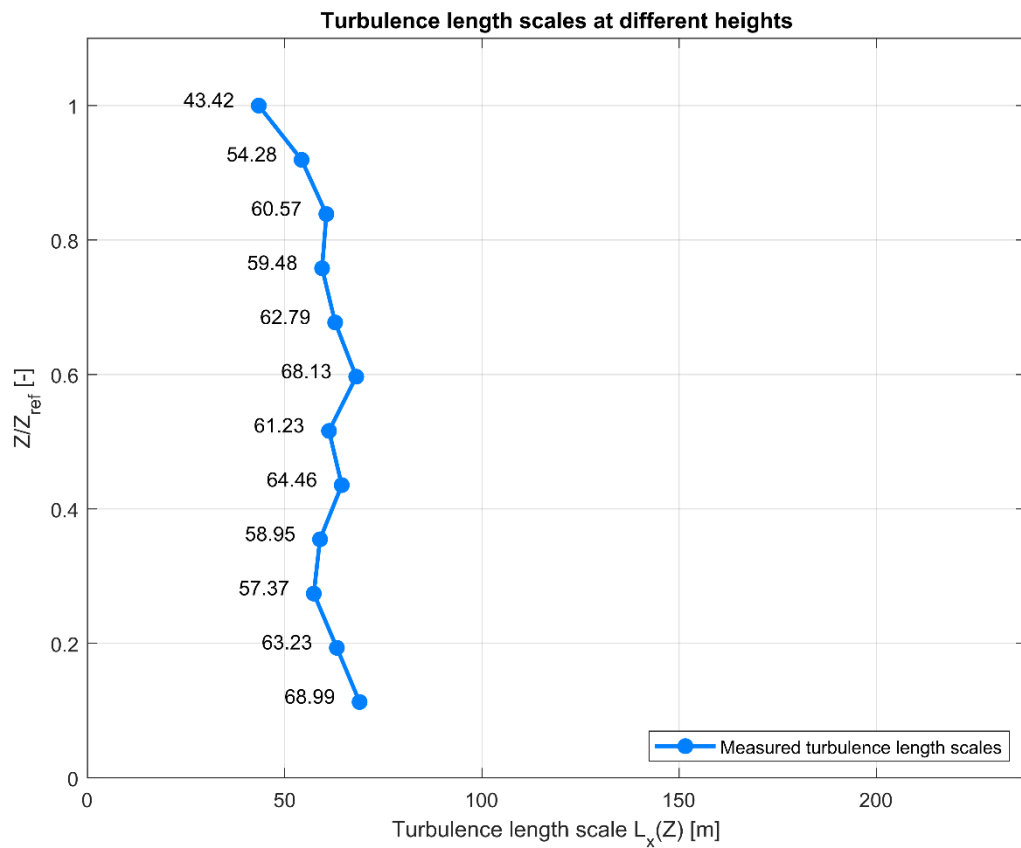Fig. 8.14. Time correlation at different heights for the Case 3-99

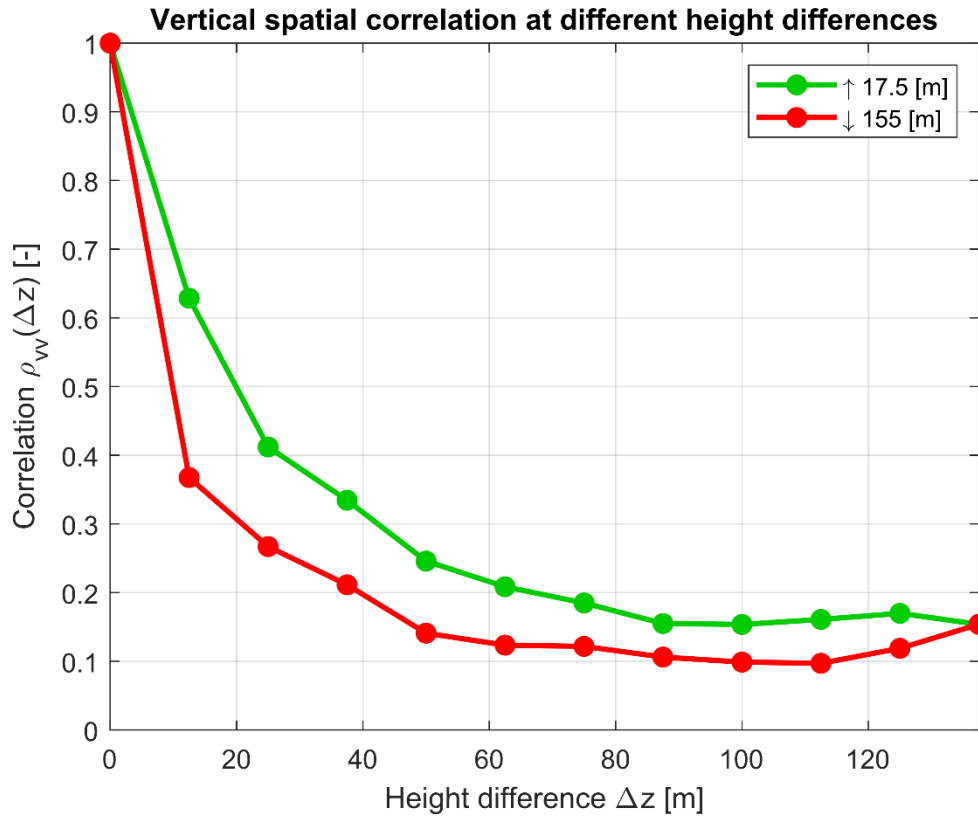Fig. 8.15. Longitudinal turbulence length scale $L_x(Z)$ at different heights for the Case 3-99

Fig. 8.16. Vertical spatial correlation at different height differences for the Case 3-99

Fig. 8.16 shows vertical spatial correlations at different distances Δz between the two points, when moving upward or downward, for the case 3-99. As mentioned, this is an anisotropic relation, and in this case it can be mostly seen at shorter distances, where the downward correlation has a much steeper decrease. For larger distances, both the upward and the downward correlation are close to exponential curves, but separated from each other. The values of vertical turbulence lengths are 40.4 m when moving upward and 27.9 m when moving downward, which is close to the results of field measurements obtained by (Duchêne-Marullaz, 1977) (comp. Tab. 3.2).

Fig. 8.17 shows power spectral densities at each measurement point for case 3-99. The plots of these values are very similar to case 3-98, analysed in the previous subsection, and therefore the detailed analysis can be omitted here for the sake of brevity.

The presence of slight peaks at the reduced frequency corresponding to 0.4 Hz in real-life scale can be clearly distinguished here, similar to test case 3-98. This might further prove the existence of the phenomena recorded in the field measurements (Newberry et al., 1973) in wind tunnel tests.
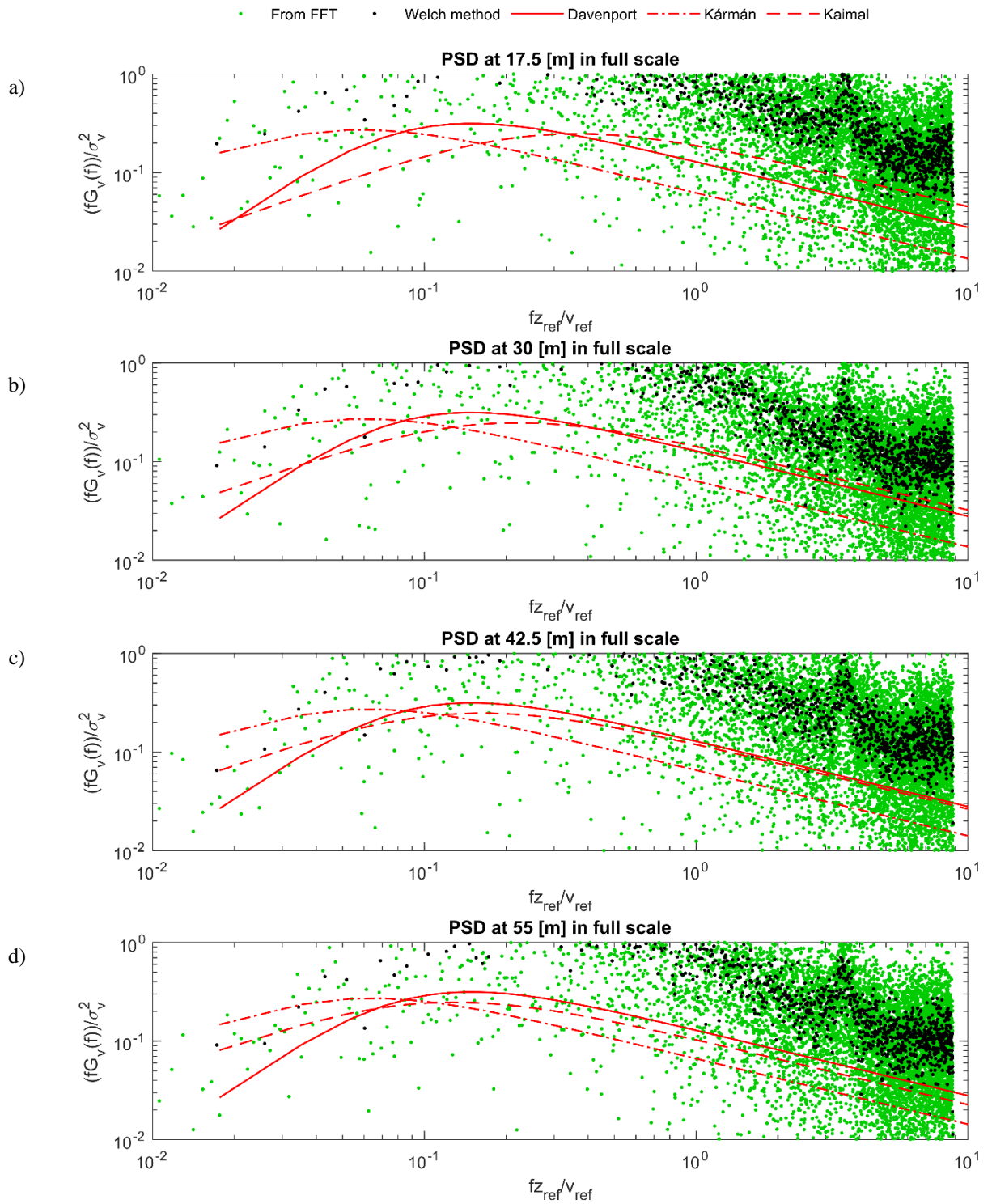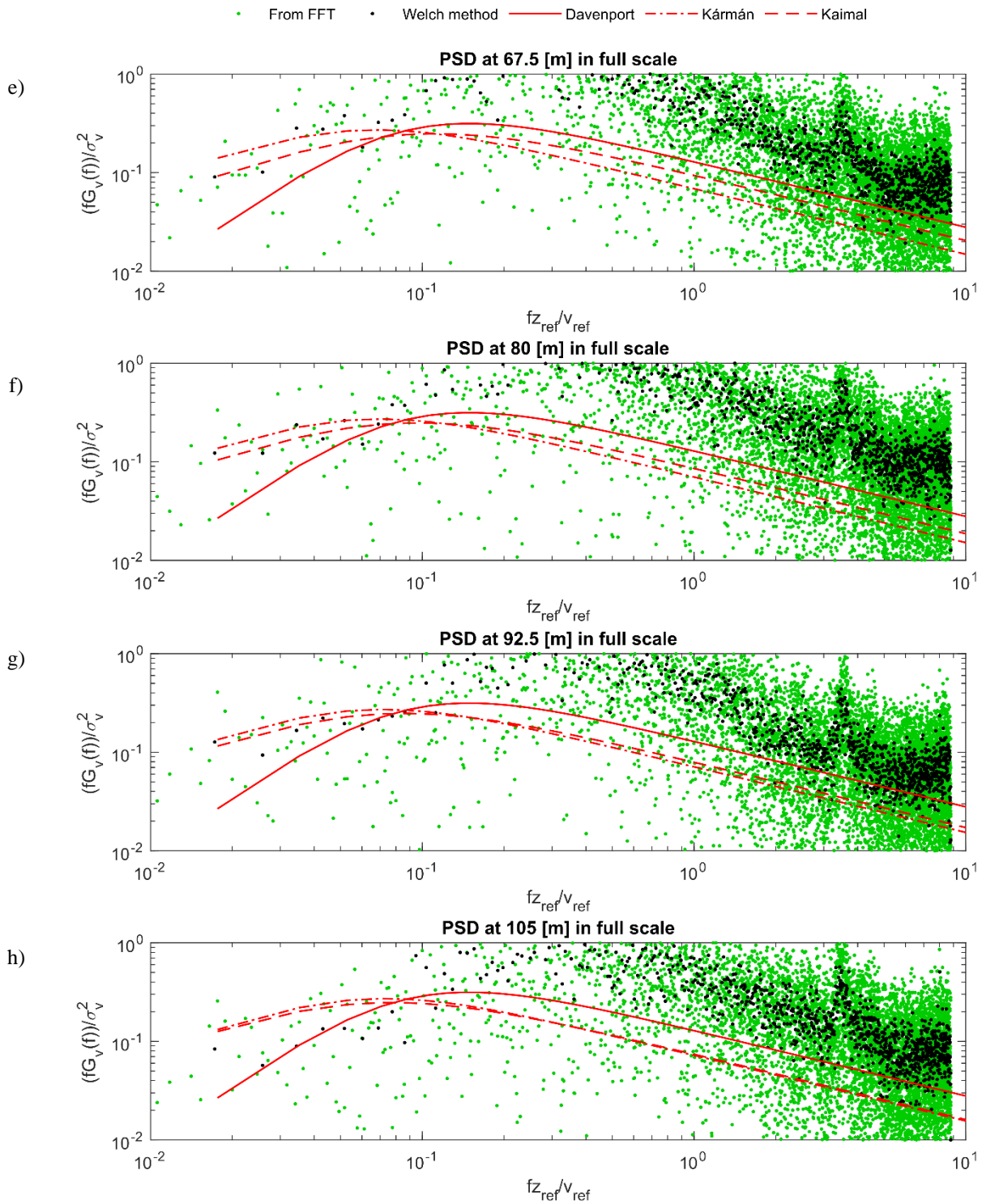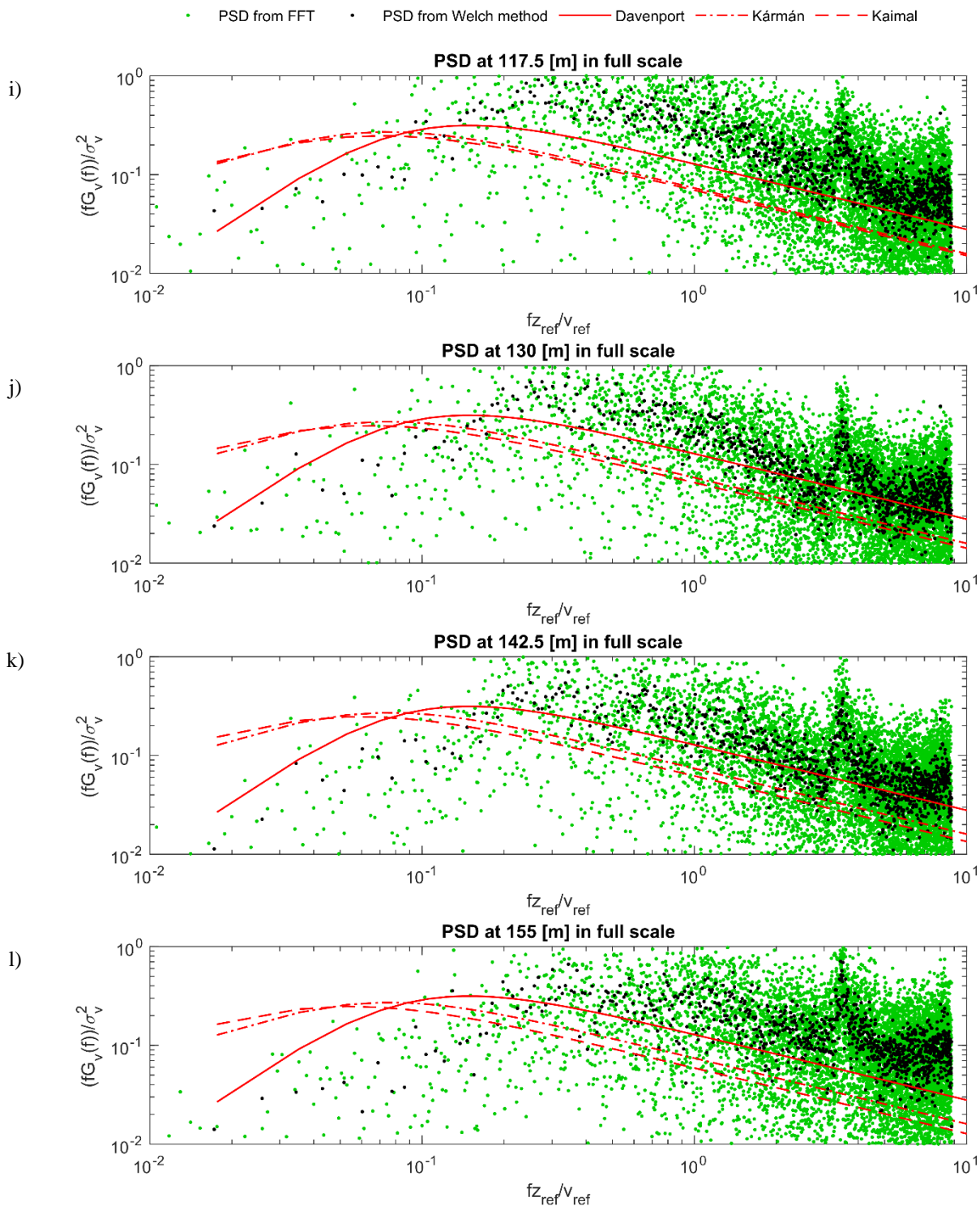
Fig. 8.17. Power density spectra at different heights, calculated with the Welch method and directly from FFT and compared against the reference spectra from Davenport, von Kármán and Kaimal, for the Case 3-99

Fig. 8.18-Fig. 8.20 show selected plots of co-coherence for the case 3-99, for distances Δz of 12.5 m, 25 m and 37.5 m.
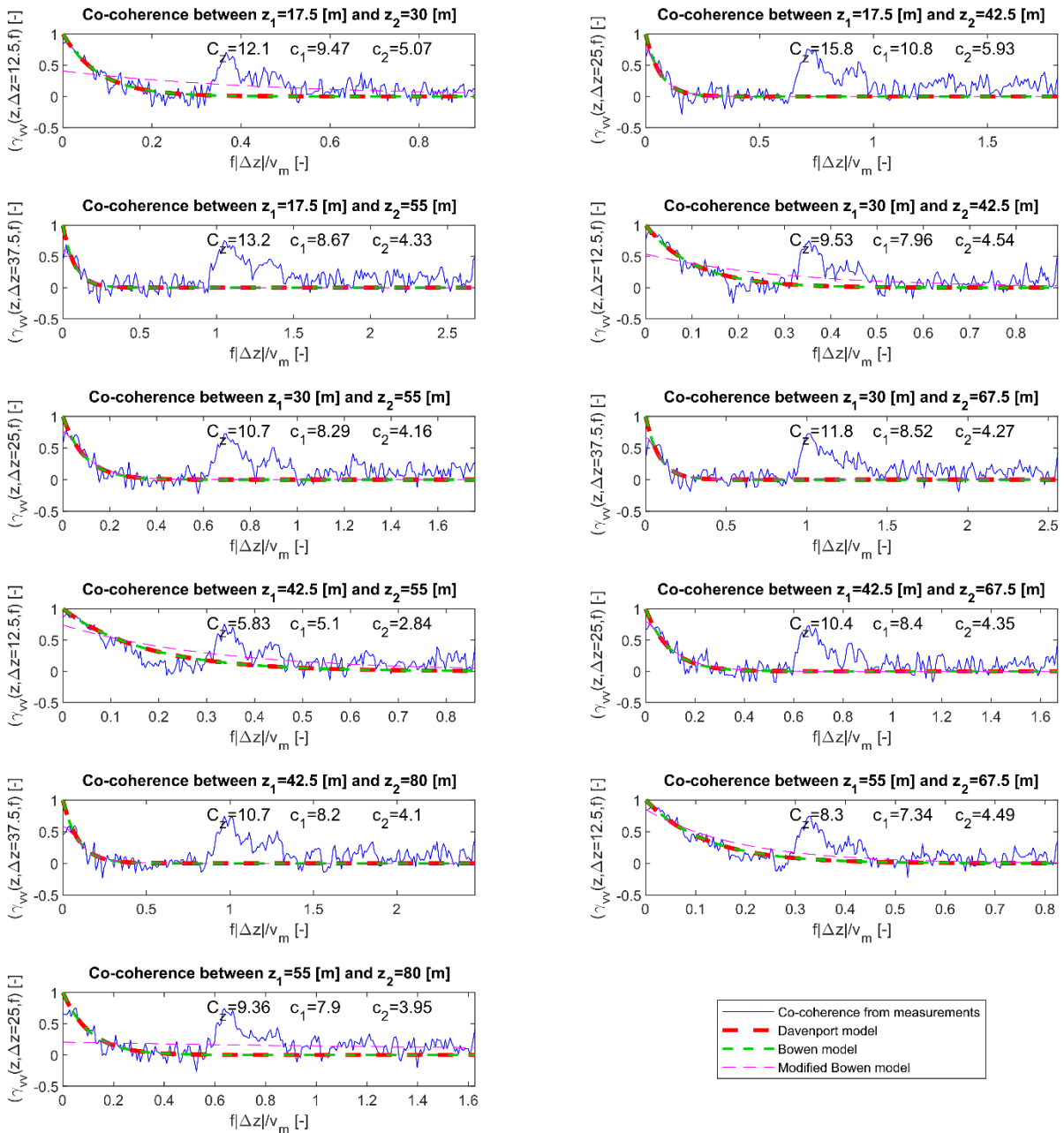
Fig. 8.18. Vertical co-coherence between the points with Δ_z equal to 12.5 m, 25 m and 37.5 m for the Case 3-99, with fit according to the Davenport model, Bowen model and modified Bowen model – plots 1-11

The co-coherence for each of the three analysed distances is well estimated by the fit from the Davenport and Bowen models, with both of these models producing the same curves for all the analysed cases, which is in line with the analysis of Fig. 8.15 suggesting a very small change in the sizes of eddies along the height. This means that the effects observed by (Bowen et al., 1983) are not replicated in the wind tunnel in this case.

Comparing the exponential decay coefficients of the Davenport model with various sources, they are close to the value of 7 for a total of 5 cases, for the distances Δz of either 12.5 m or 25 m. Values of about 9.1-10.8 were observed for a total of 9 cases, mostly for the distances Δz of either 25 m or 37.5 m.

The exponential decay coefficients for the Bowen model that reach similar values to the literature can be observed only for 2 cases (17.5 and 42.5 m; 105 and 142.5 m). Similarly to case 3-98, a peak can be noticed at each of the presented charts, at a reduced frequency that corresponds to 0.4 Hz (in real-life scale).
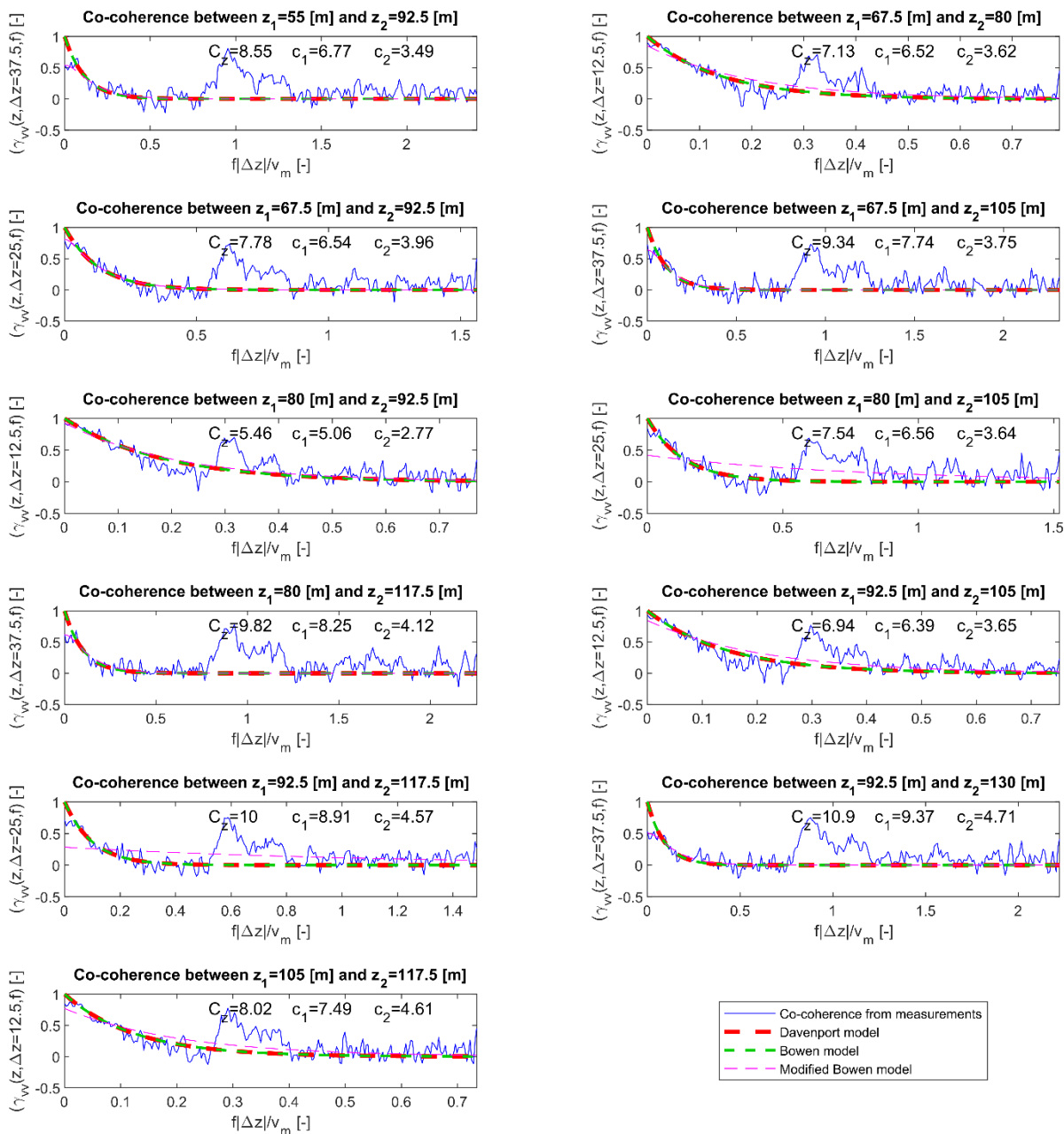

Fig. 8.19. Vertical co-coherence between the points with Δ_z equal to 12.5 m, 25 m and 37.5 m for the Case 3-99, with fit according to the Davenport model, Bowen model and modified Bowen model – plots 12-22

The modified Bowen model gives a decent approximation of the calculated co-coherence function for the larger distances Δz between the two considered points at the heights closer to the ground level and for smaller distances Δz at the higher altitudes. Once again, in some cases the fit from this model seems influenced by the peak in the co-coherence function mentioned in the previous paragraph, which results in a worse fit.

Comparing the values of exponential decay coefficients for different models with the previously analysed case 3-98, it can be seen that these coefficients have very similar values between these two cases (for the same pairs of points in both cases). This seems not to be true only in the results related to the highest probes.
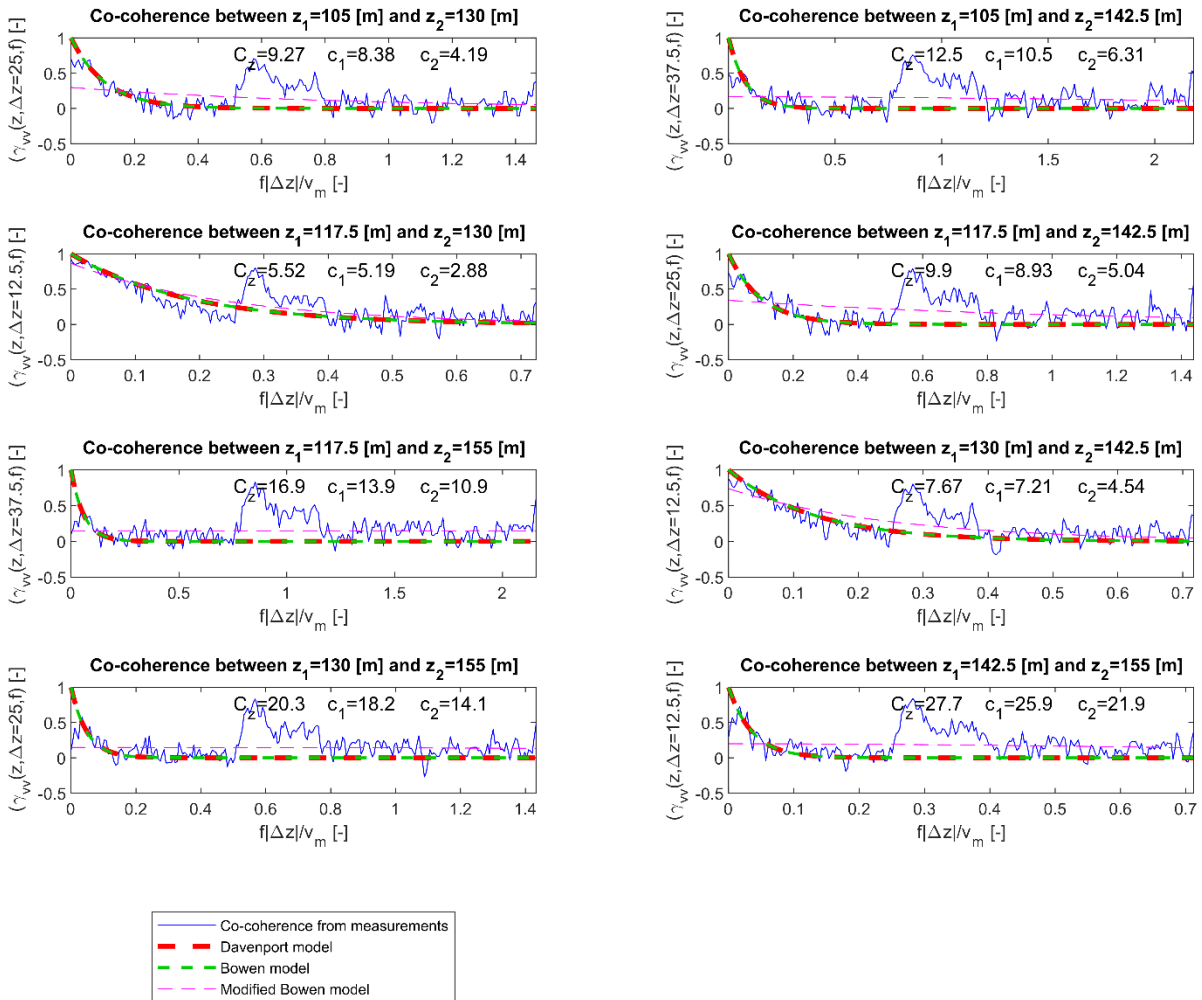

Fig. 8.20. Vertical co-coherence between the points with Δ_z equal to 12.5 m, 25 m and 37.5 m for the Case 3-99, with fit according to the Davenport model, Bowen model and modified Bowen model – plots 23-30

Fig. 8.21 and Fig. 8.22 show the frequency length scales distribution at different vertical distances Δz, taking into account the correlations with the lowest measuring point at 17.5 m (Fig. 8.21) and the correlations with the highest measuring point at 155 m (Fig. 8.22).

The observed phenomenon that the frequency scales at higher altitudes are larger than on lower heights can also be seen here. The values of frequency length scales are between 0.13 Hz and 0.19 Hz in relation to the lowest measuring point and between 0.15 Hz and 0.21 Hz in relation to the highest measuring point. For both points, they are distributed in a rather chaotic pattern and only slightly vary with the increasing distance Δz between the two points. Similar to the case 3-98, even for the largest distance Δz of 155 m, the frequency length scale is 0.16 Hz, which would result in an averaging period T_z^* of only about 6 s, much smaller than the values of 15 s recommended by (Cook, 1985, 1990) for buildings of height above 100 m and therefore potentially producing larger peak gust values.

The values approximated from the Davenport model are much lower than the ones calculated from the co-coherence function. These values are at about 0.01 Hz-0.09 Hz at the 3-6 smallest distances Δz, then close to 0 for all the larger distances.
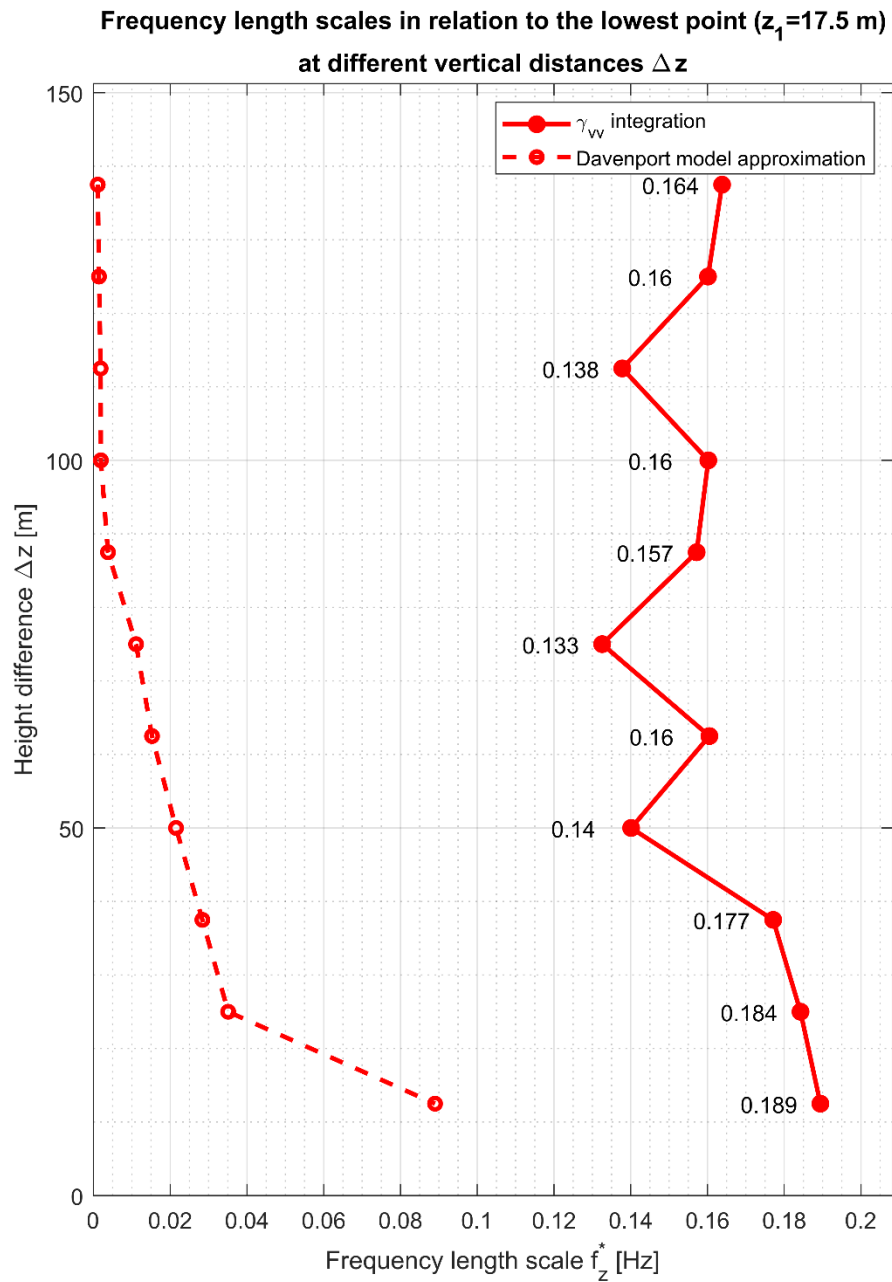
Frequency length scales in relation to the lowest point (z_1=17.5 m)

at different vertical distances $\triangle z$

Fig. 8.21. Frequency length scales in relation to the lowest measurement point and different Δ_z values for the Case 3-99

Frequency length scales in relation to the highest point (z$_2$=155 m)

at different vertical distances △z
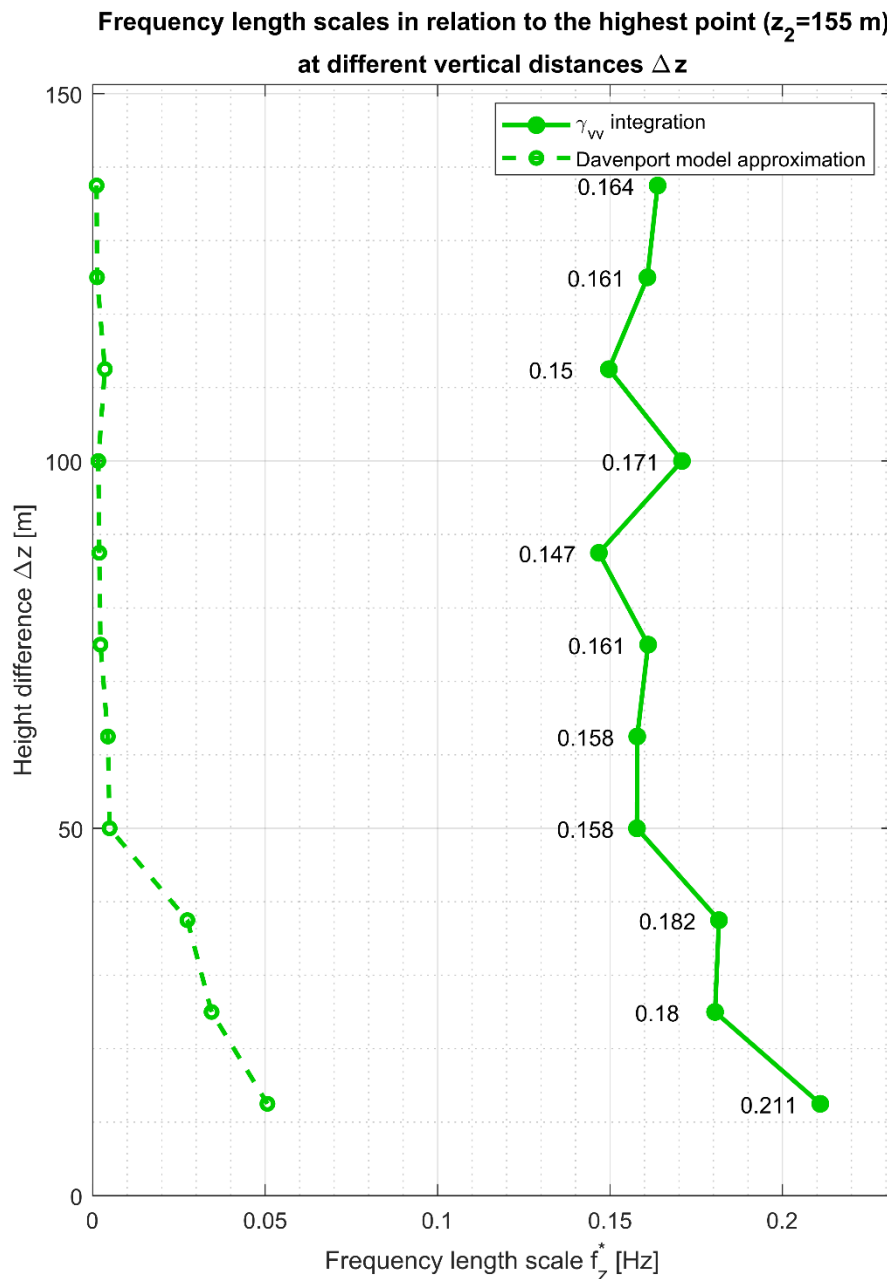
Fig. 8.22. Frequency length scales in relation to the highest measurement point and different Δ_z values for the Case 3-99

8.3. Terrain roughness category II – Case 2-128

Case 2-128, with a setup consisting of the 100 cm spires, triangular prongs barrier and blocks at the inlet elevated at 10 cm height, was selected as the closest match for terrain category II, which corresponds to open terrain with low vegetation. The vertical mean wind speed profile for this case is shown in Fig. 8.23 and turbulence intensity profile is shown in Fig. 8.24.

In this case, the α exponent at 0.17 is very close to the value suggested by the standard (with a relative error of only 0.018), while the roughness length z_0 is considerably higher at 0.11 compared to 0.05 target value (relative error of 1.25). The obtained wind profiles are very close to the model ones from the standard, with a slight transition to the left. The RMSE values between the model profiles from (PN-EN 1991-1-4, 2011) and the profiles obtained

from the measurements are 0.027 for the power-law profile and 0.032 for the logarithmic profile, which can be considered a very good fit.
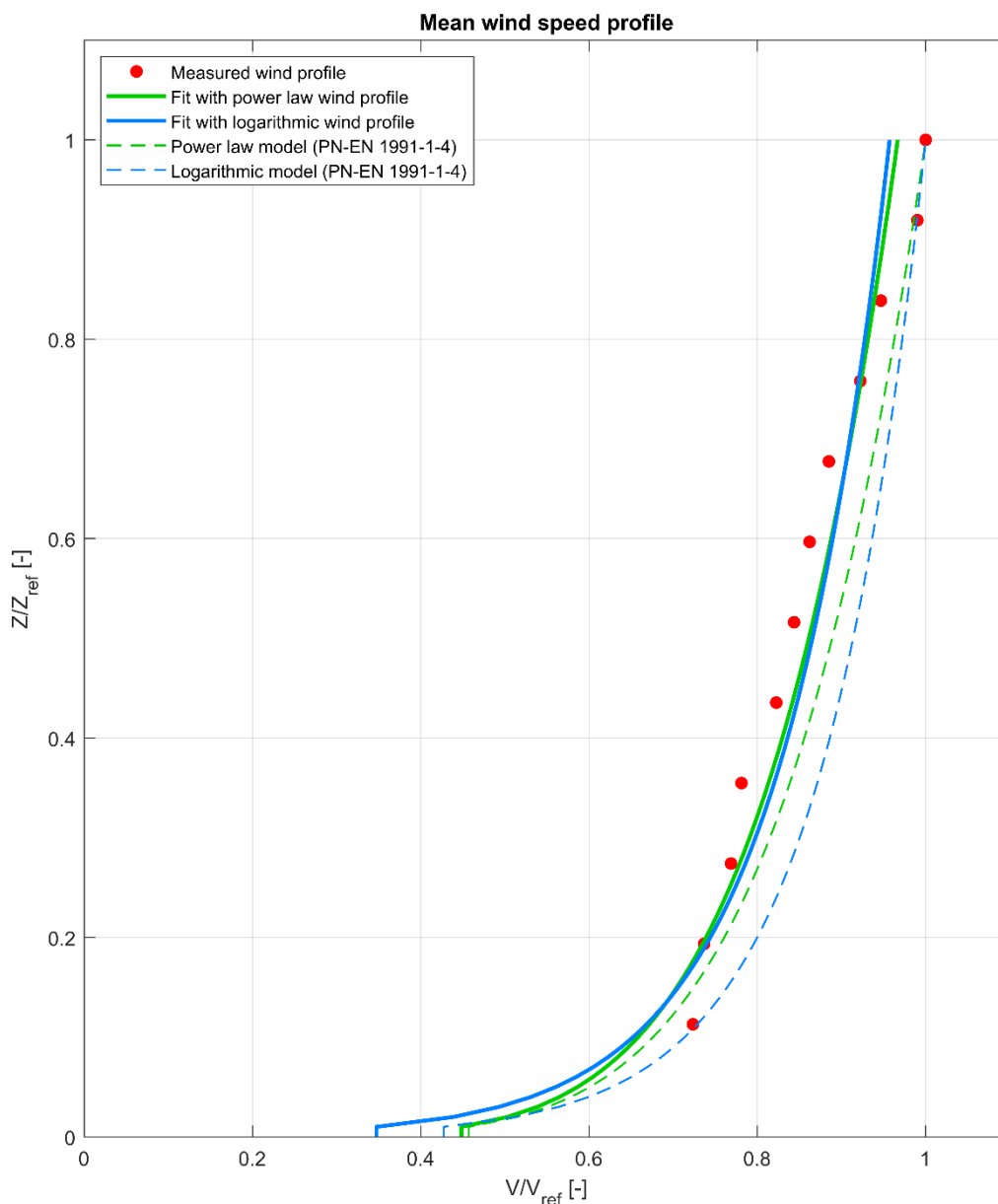

Fig. 8.23. Vertical mean wind speed profile for the Case 2-128

The largest discrepancies (especially in the case of the logarithmic wind profile) can be observed in the region of the wind profile close to the ground, where it is mostly affected by the value of the roughness length z_0. It should be emphasised that the wind profile (and the value of this parameter) was obtained with a setup of only spires, barrier and blocks at the inlet, with no blocks over the fetch length – as can be seen in the analysis presented in subsection 7.1, the elevation of the blocks at the fetch length would further increase the value of this parameter. The wind velocity values from the measurements, marked with red dots, are closely matched with the obtained fit, with goodness of fit parameters of R^2 equal to 0.92 and 0.89, and RMSE equal to 0.03 and 0.38 for power-law and logarithmic profiles, respectively. Based on this analysis, it can be stated that the vertical mean wind speed profile is satisfactorily recreated for the open terrain category in the wind tunnel for this test case.
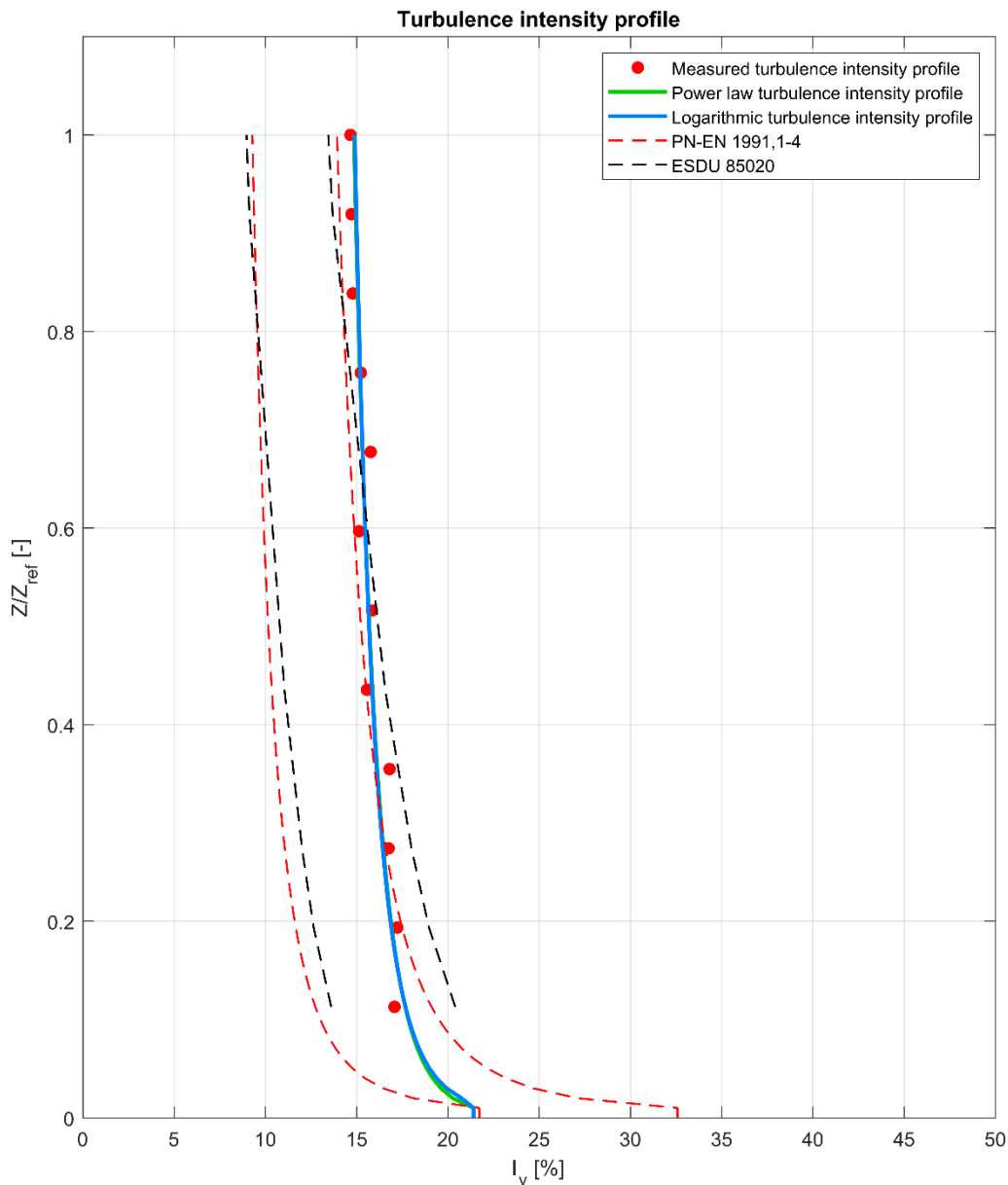
Fig. 8.24. Vertical turbulence intensity profile for the Case 2-128

In this case, the turbulence intensity profile is almost constant along the whole height, with a very little decrease from about 17% near the ground to about 15% at higher altitudes. This might be caused by the lack of blocks at the fetch length. However, the wind turbulence is within the ±20% bounds recommended by (ESDU 85020, 2002) for 7 lowest points (but very close to the upper boundary), being also just past the upper boundary suggested by (PN-EN 1991-1-4, 2011) for most points. The suggested values are in the range of 17% near the ground to 11% around the height of Z_{ref}. However, this was the best match in terms of turbulence intensity fit out of the 23 test cases assigned to the II terrain category, with RMSE values of 0.025 with reference to (ESDU 85020, 2002) and 0.028-0.029 with reference to (PN-EN 1991-1-4, 2011). The higher turbulence obtained for the investigated test cases may result from the higher roughness length value z_0 (it should also be noted that the reference value of z_0 according to (PN-EN 1991-1-4, 2011) is 0.05 while in (ESDU 85020, 2002), the values are taken for a slightly lower z_0 equal to 0.03). The parameters that define the vertical turbulence profiles are very low, with β exponent at -0.08 and z_0^T at 10^{-4} m, which results in

almost constant values of these profiles along the height. The goodness of fit parameters for the turbulence intensity profiles are decent at R^2 equal to 0.84 and 0.83 for power-law and logarithmic profiles, respectively, and RMSE equal to 0.004 for both the power-law and logarithmic profiles.

Fig. 8.25 shows the time autocorrelations plots and Fig. 8.26 shows the longitudinal turbulence length scales at different heights for the case 2-128. The autocorrelations plots are rather smooth, with larger-size fluctuations of the correlation time scales, particularly around the horizontal axis. The correlations reach 0 at a lag of about $\tau = 0.12$ s (highest point) and $\tau = 0.3$ s (lowest point). The longitudinal turbulence length scales are, for the most analysed heights, within the boundaries recommended by (ESDU 74031, 1974). An increase can be clearly noticed at the lower heights up to about 0.4 Z_{ref}, from the values of 114 m to 128 m. Around the height of about 0.5 Z_{ref}, a steep decrease to a value of about 100 m can be seen, then a further increasing trend can be observed at the highest altitudes (besides the highest probe), back to a value of about 114 m. However, this last part of the plot, consisting of probes 8-12, is slightly below the ±30% uncertainty bounds suggested by the standard. In general, the reproduction of the longitudinal turbulence length scales according to the referenced standard for the open flat terrain type can be considered decent, despite the steep decrease in the middle part of the plot.
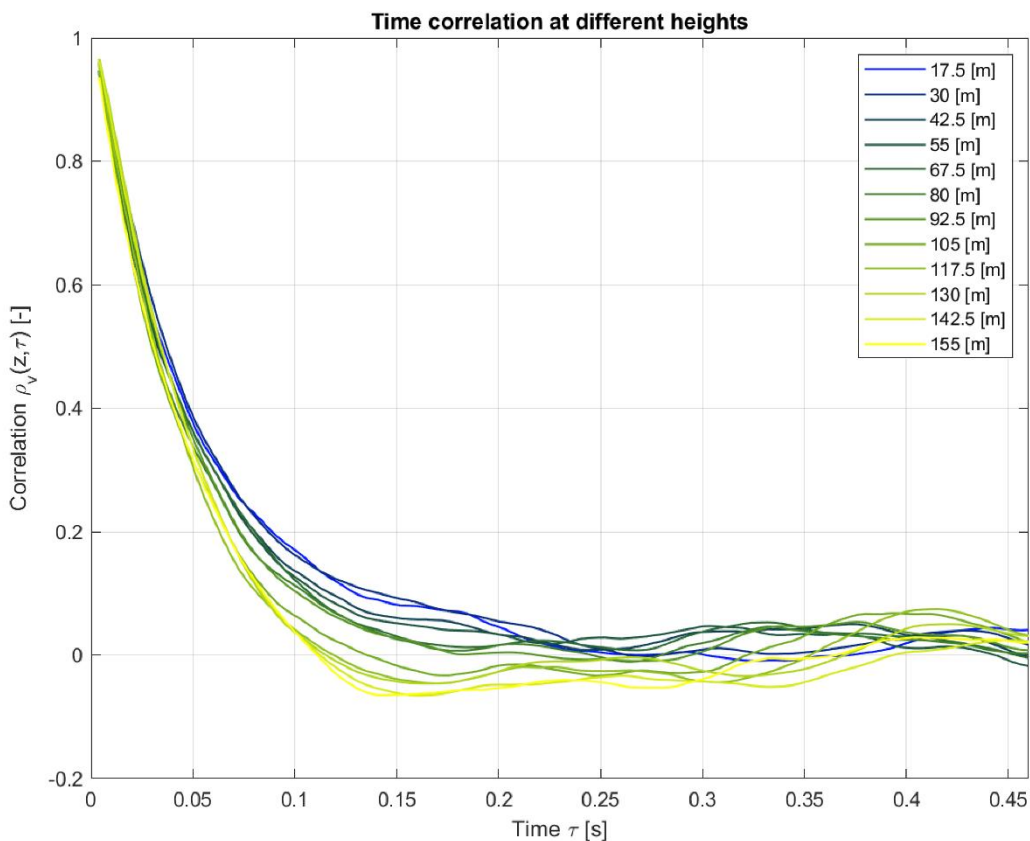

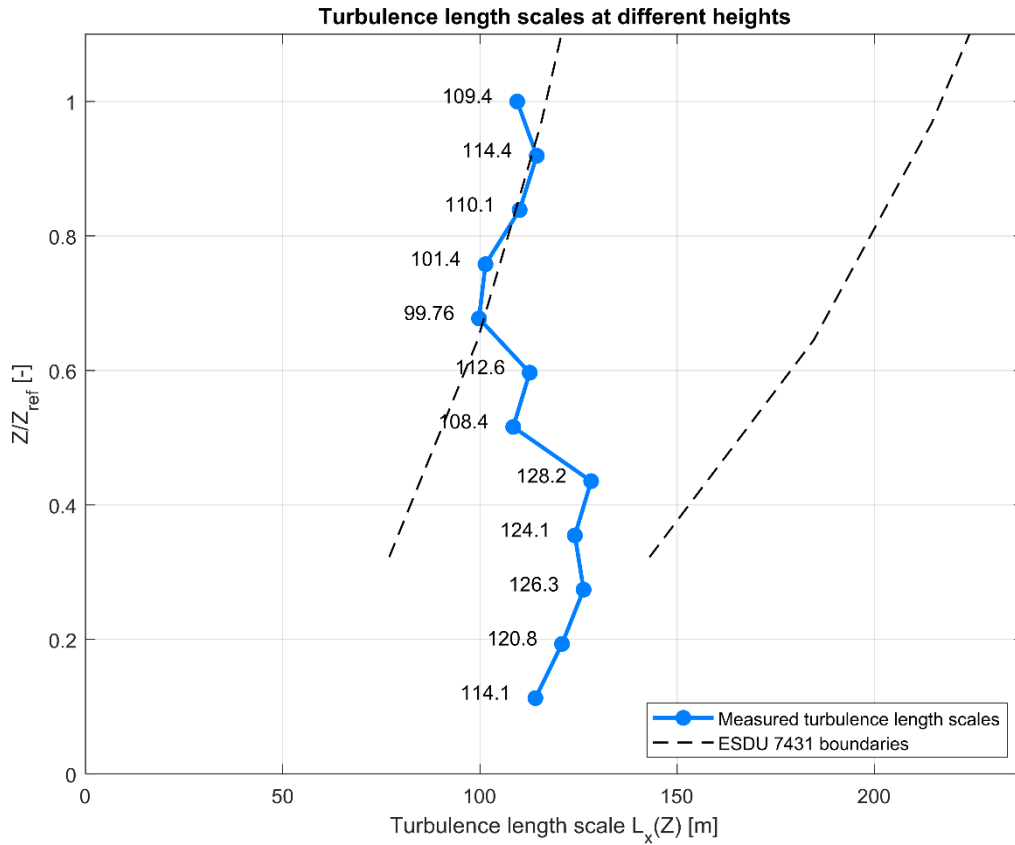Fig. 8.25. Time correlation at different heights for the Case 2-128

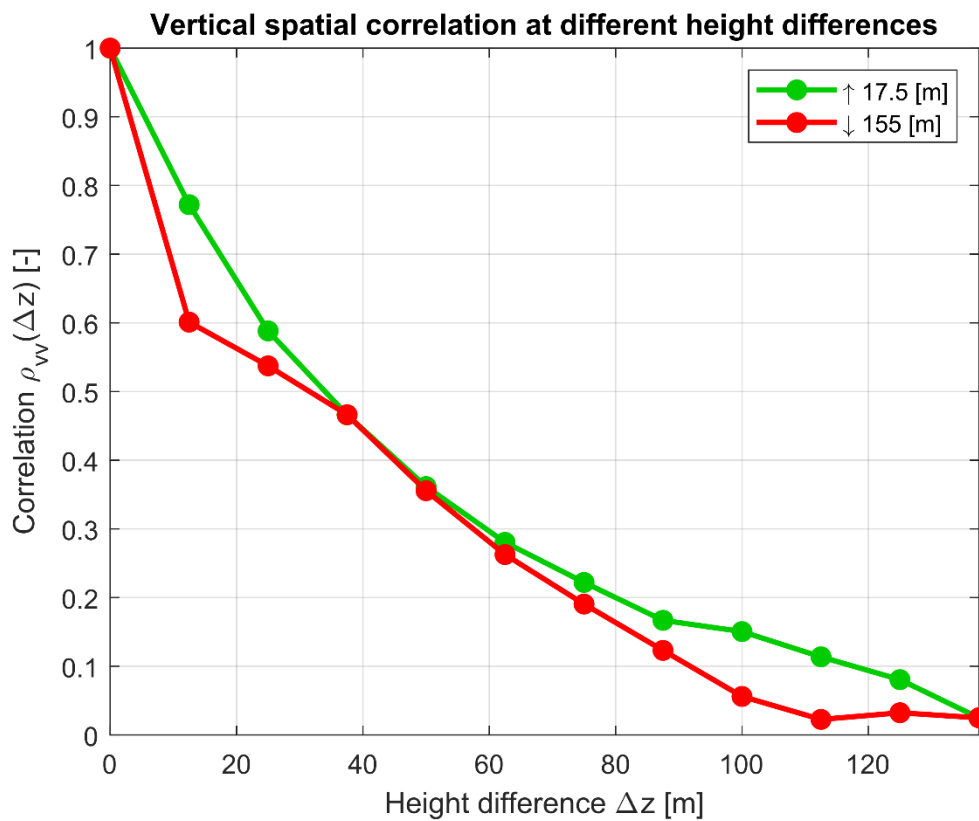Fig. 8.26. Longitudinal turbulence length scale $L_x(Z)$ at different heights for the Case 2-128

Fig. 8.27. Vertical spatial correlation at different height differences for the Case 2-128

Fig. 8.27 shows vertical spatial correlations at different distances Δz between the two points, when moving upward or downward, for the case 2-128. In this case, the curves when moving either upward or downward are very similar, with discrepancies only at the distances Δz of about 0-20 m and 100-120 m. Both of these correlations are almost linear. The values of vertical turbulence length scales are 46.4 m when moving upward and 39.5 m when moving downward. The higher vertical turbulence length scale when moving upward than when moving downward is in good agreement with the literature (Duchêne-Marullaz, 1977).

Fig. 8.28 shows power spectral densities at each measurement point for the case 2-128. The calculated spectra show good agreement with the models, reaching slightly lower values than these models. These seem similar to literature where wind tunnel power spectral densities are considered (Kozmar, 2011b; Yu et al., 2021). Furthermore, this is closer to the slope of 2/3 inclination, suggesting the clear presence of the Kolmogorov inertial subrange (Kolmogorov, 1941).

The results obtained with both the Welch method and the direct approach from FFT show good agreement in the trend, with once again the values obtained directly from FFT being much more scattered. However, in this case, the values obtained from both methods are generally less dispersed than in the cases representative for terrain categories 0 and I. This suggests the turbulising net's presence (or lack of the spires/barrier at the inlet) is a factor that leads to more dispersed power spectral densities in wind tunnel tests.

In this case, the presence of slight peaks at the frequency of about 0.4 Hz in real-life scale can be only observed for the 6 lowest probes (Fig. 8.28a-Fig. 8.28f). Furthermore, these peaks are relatively smaller than for cases 3-98 and 3-99. The lack of these peaks at some of the probes (at higher altitudes) suggests that they are an effect of roughness elements that is naturally occurring in the wind flow and not e.g. a result of the measuring technique or noise in the signal.
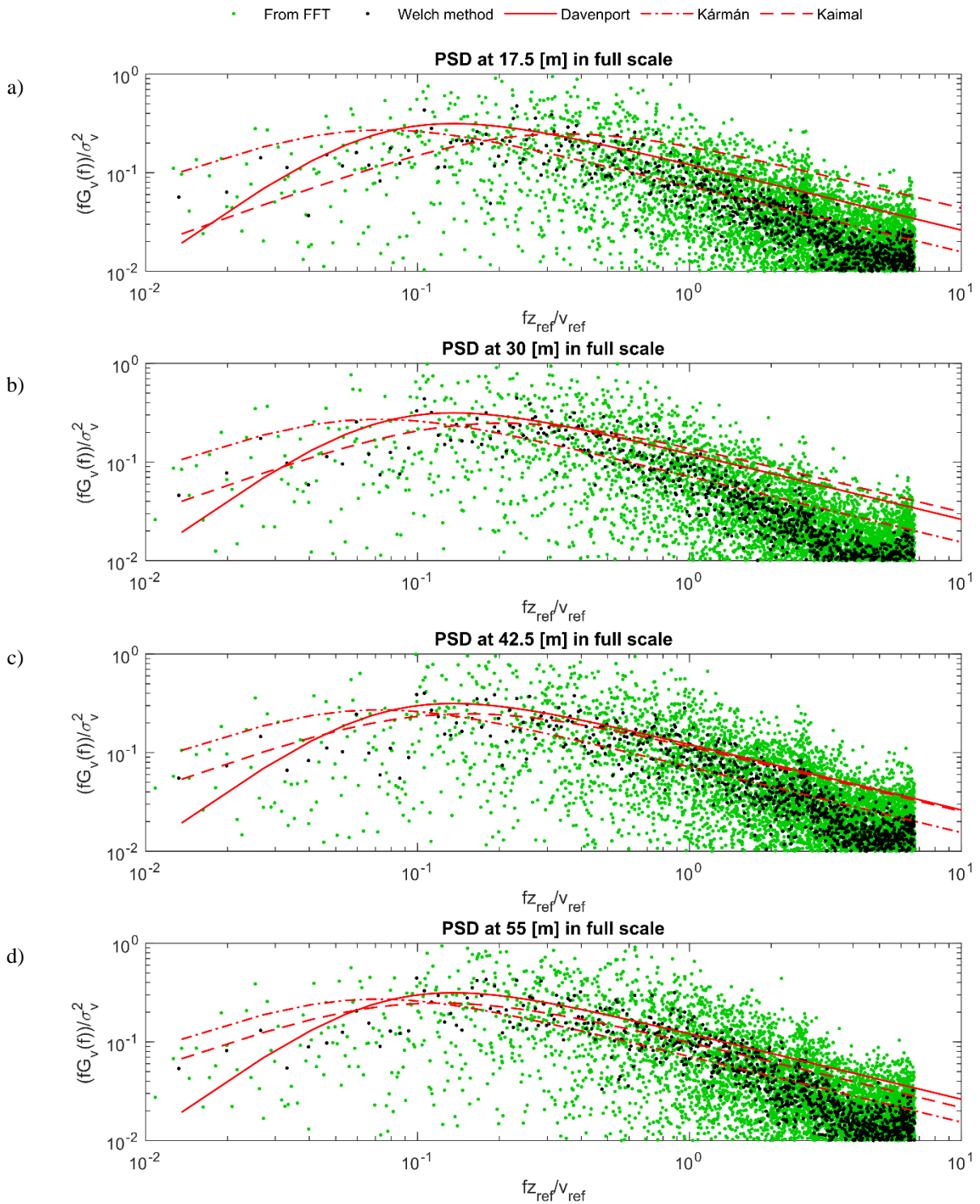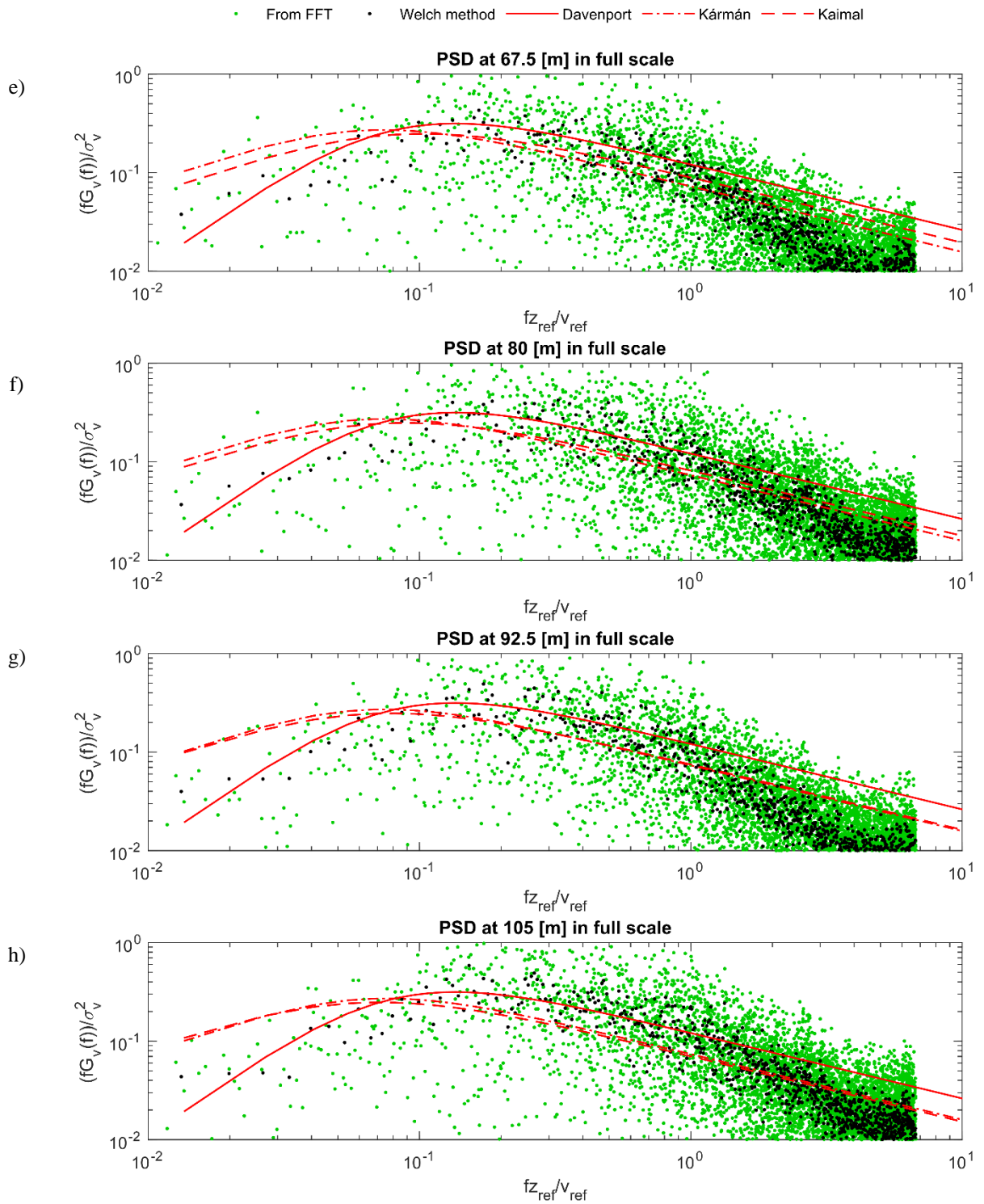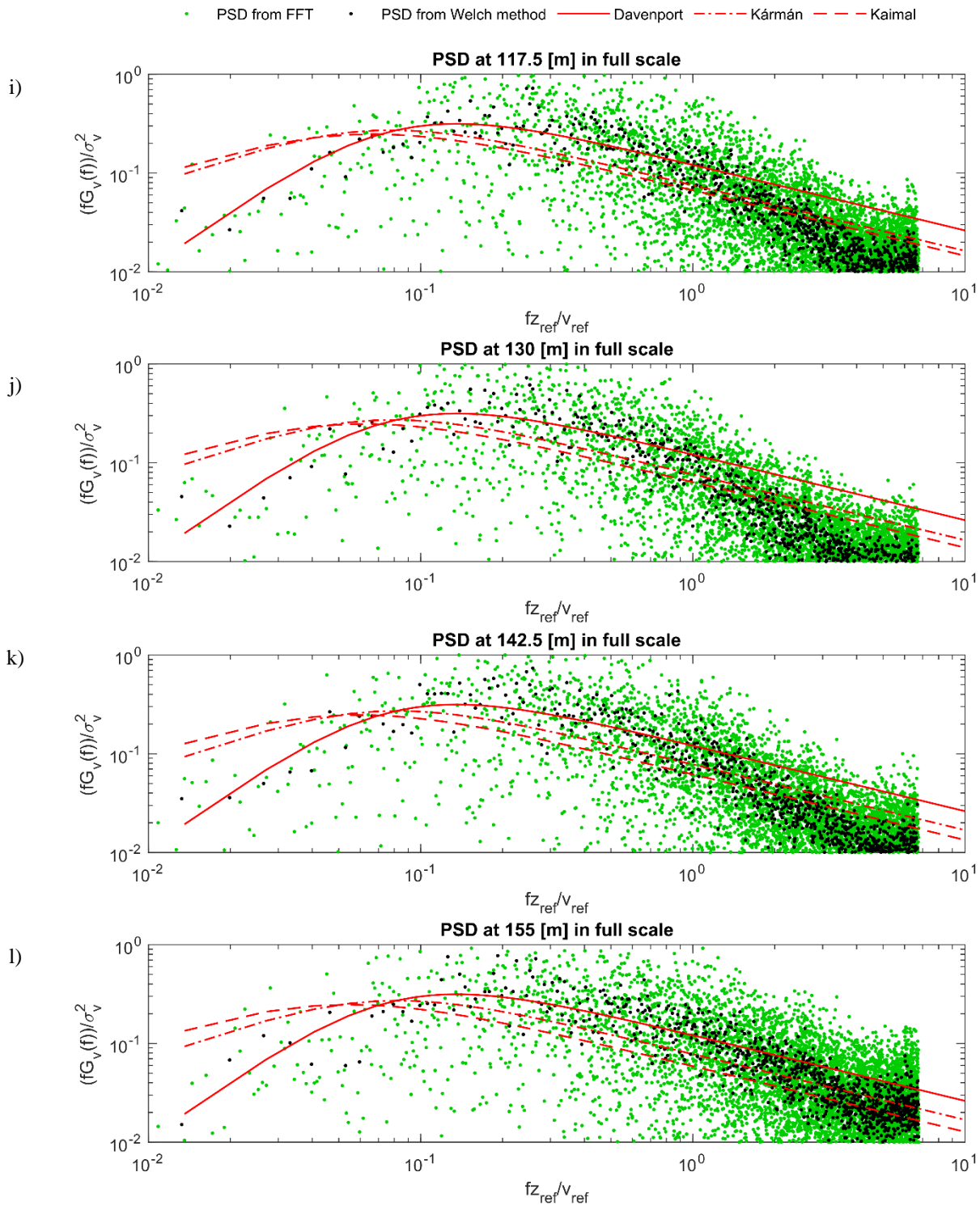
Fig. 8.28. Power density spectra at different heights, calculated with the Welch method and directly from FFT and compared against the reference spectra from Davenport, von Kármán and Kaimal, for the Case 2-128

Fig. 8.29-Fig. 8.31 show selected plots of co-coherence for the case 2-128, for distances Δz of 12.5 m, 25 m and 37.5 m.
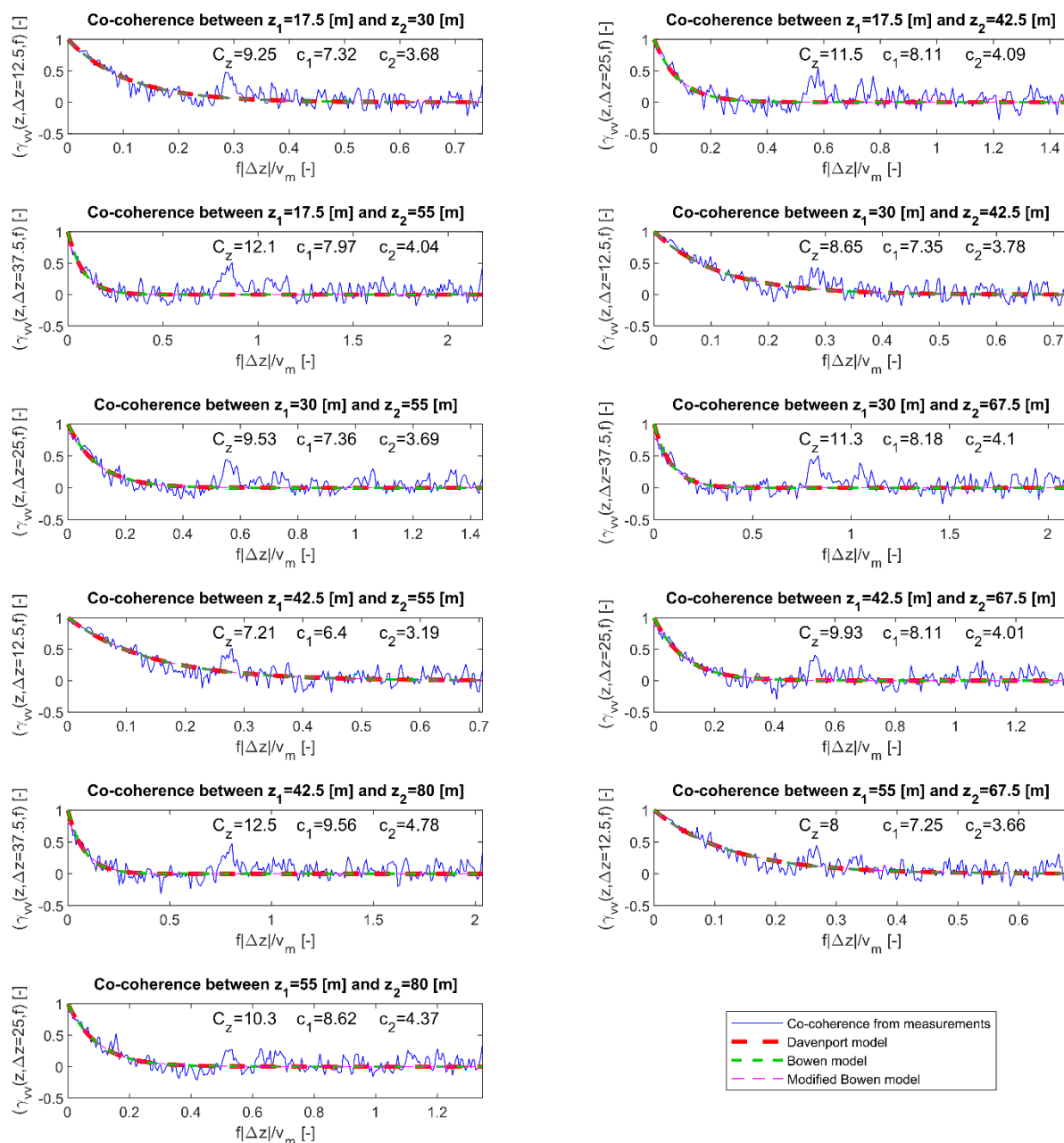
Fig. 8.29. Vertical co-coherence between the points with Δ_z equal to 12.5 m, 25 m and 37.5 m for the Case 2-128, with fit according to the Davenport model, Bowen model and modified Bowen model – plots 1-11

The co-coherence for each of the analysed pairs of points is well estimated by the fit from Davenport and Bowen models, with both of these models producing the same curves for all the analysed cases (same as for the previous two analysed test cases), further suggesting that the effects observed by (Bowen et al., 1983) may not be possible to replicate in the wind tunnel.

Comparing the exponential decay coefficients of the Davenport model with various sources, they are close to the value of 7 for only 4 cases, usually reaching higher values. Values of about 9.1-10.8 were observed for a total of 11 cases. However, it should be noted that for this test case, this coefficient only reaches a much higher value (21.8) for the co-coherence between the two highest points.

The exponential decay coefficients for the Bowen model reach values similar to the literature only for 1 case (117.5 and 155 m), in other cases usually reaching lower values. The slight peaks at a value of about 0.4 Hz in real-life scale are much less prevalent for this test case and only observable for several pairs of points, mostly closer to the ground level. This means that they do not affect the modified Bowen model, which gives a good approximation of the calculated co-coherence function for all the presented test cases and produces the same curves as the Davenport model and the Bowen model.
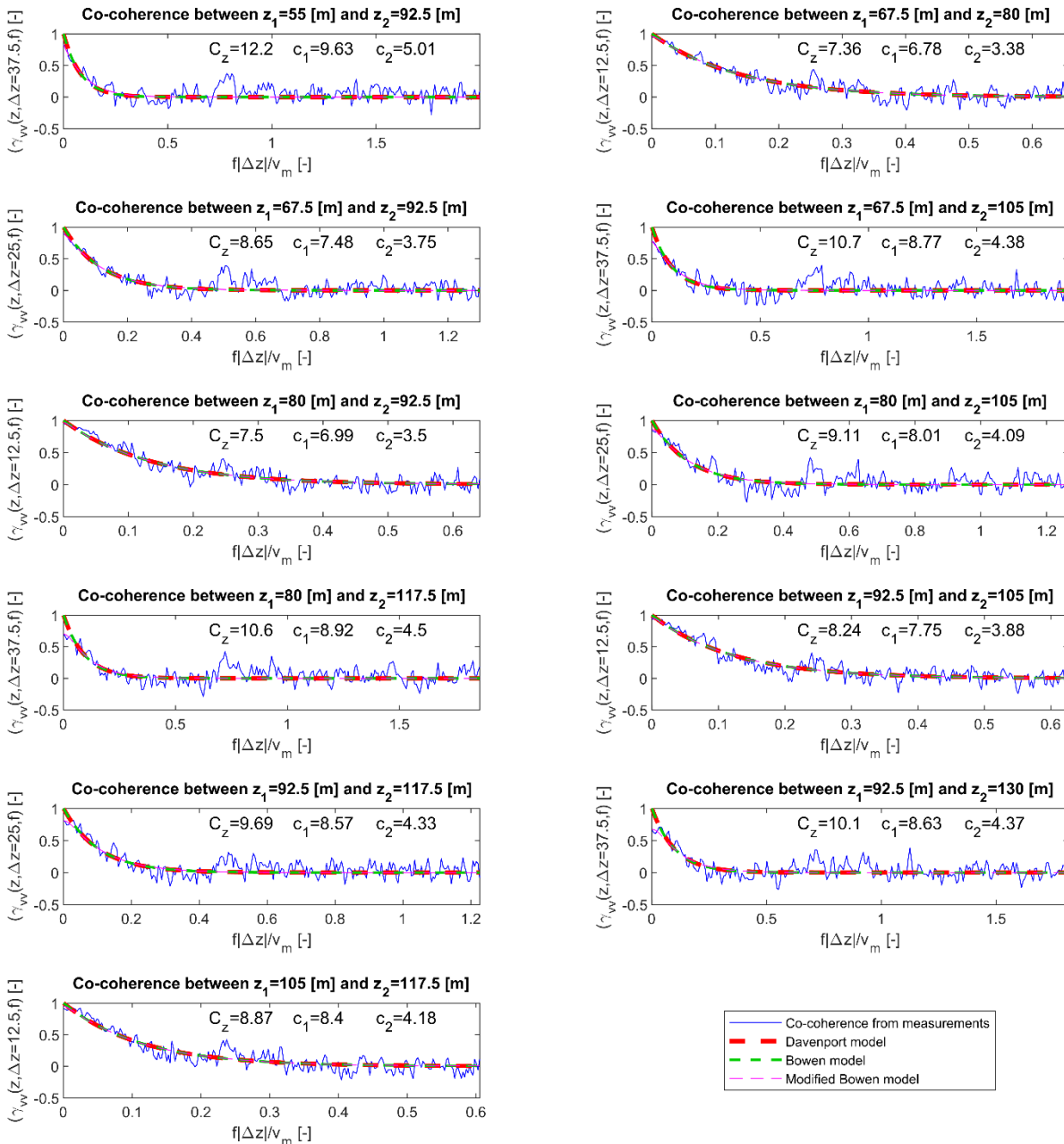

Fig. 8.30. Vertical co-coherence between the points with Δ_z equal to 12.5 m, 25 m and 37.5 m for the Case 2-128, with fit according to the Davenport model, Bowen model and modified Bowen model – plots 12-22

Comparing the values of exponential decay coefficients for different models with the two previously analysed cases (3-98 and 3-99), it can be seen that these coefficients have very similar values between these three cases (when comparing the same pairs of points in both cases). This seems not true only at the lowest and highest measuring points.
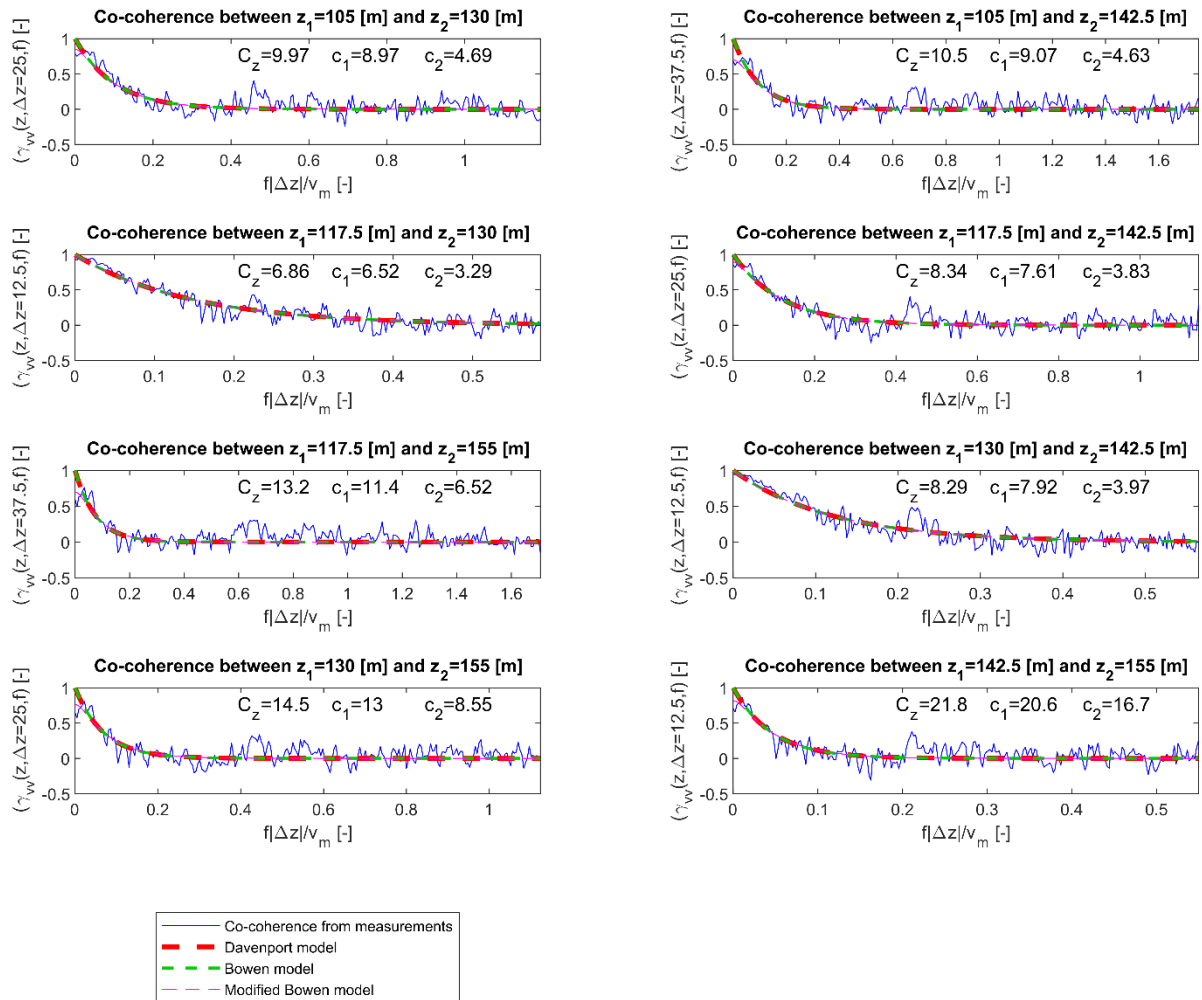
Fig. 8.31. Vertical co-coherence between the points with Δ_z equal to 12.5 m, 25 m and 37.5 m for the Case 2-128, with fit according to the Davenport model, Bowen model and modified Bowen model – plots 23-30

Fig. 8.32 and Fig. 8.33 show the frequency length scales distribution at different vertical distances Δz, taking into account the correlations with the lowest measuring point at 17.5 m (Fig. 8.32) and the correlations with the highest measuring point at 155 m (Fig. 8.33).

In this case, the values reported in relation to the lowest measuring point are higher than the values reported in relation to the highest measuring point, as observed in subsection 7.3 for the cases with spires and barriers. Furthermore, the values of frequency length scales for this test case are lower than for the cases 3-98 and 3-99, between 0.05 Hz and 0.17 Hz for the lowest measuring point and between 0.03 Hz and 0.1 Hz for the highest measuring point. For both points, there is a decreasing trend with the increase of distance Δz between the two considered points. For the relations to the lowest measuring point, the frequency scale at a distance of about 50 m is 0.1 Hz (resulting in an averaging period T_z^* of about 10 s) and at a distance of about 100 m is 0.07 Hz (resulting in an averaging period T_z^* of about 15 s), which corresponds very good to the values recommended by (Cook, 1985, 1990) for buildings of these heights. This suggests that applying the frequency scales as reference values for averaging the wind loads in wind tunnel tests might be a good practice for wind loading studies.

The values estimated based on the Davenport model give a slightly better approximation of the frequency length scales for the 2 shortest distances Δz in the cases related to the lowest measuring point and for the 4 shortest distances Δz in the cases related to the highest measuring point. However, these approximations are still lower than the values directly calculated from the co-coherence and therefore not on the safe side. The values for larger distances Δz are close to 0 in both cases.
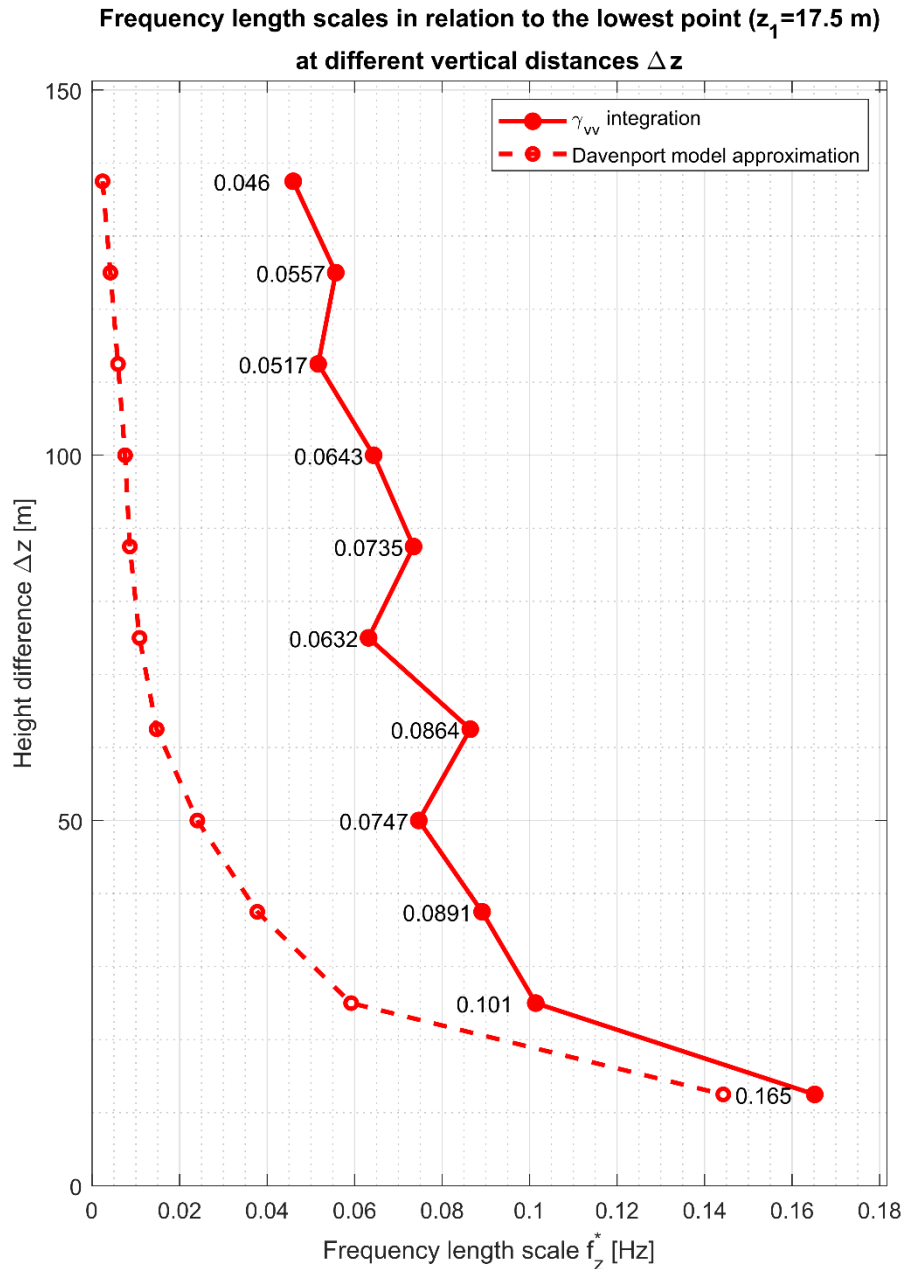

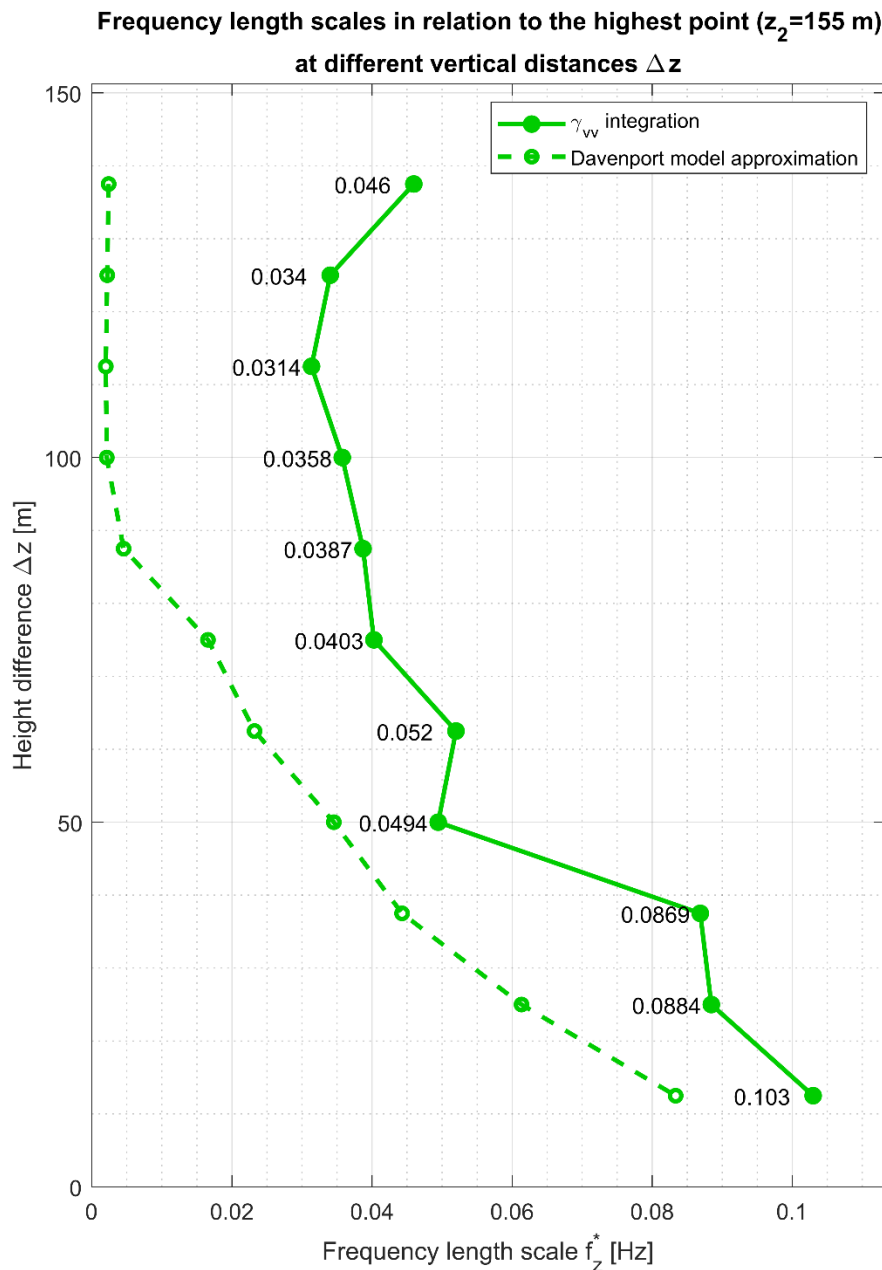Fig. 8.32. Frequency length scales in relation to the lowest measurement point and different Δ_z values for the Case 2-128

Fig. 8.33. Frequency length scales in relation to the highest measurement point and different Δ_z values for the Case 2-128

8.4. Terrain roughness category III – Case 3-10

Case 3-10, with a setup consisting of the 120 cm spires, triangular prongs barrier and blocks at the fetch length elevated at 5 cm height, was selected as the closest match for terrain category III, which corresponds to suburban areas or forests. The vertical mean wind speed profile for this case is shown in Fig. 8.34 and turbulence intensity profile is shown in Fig. 8.35.

In general, it is easier to simulate higher terrain categories (suburban and urban) in the wind tunnel. The two main parameters that determine the vertical wind speed profiles are close to the values suggested by the standard, with the α exponent at 0.21 (relative error of 0.096) and roughness length z_0 equal to 0.4 (relative error of 0.349).
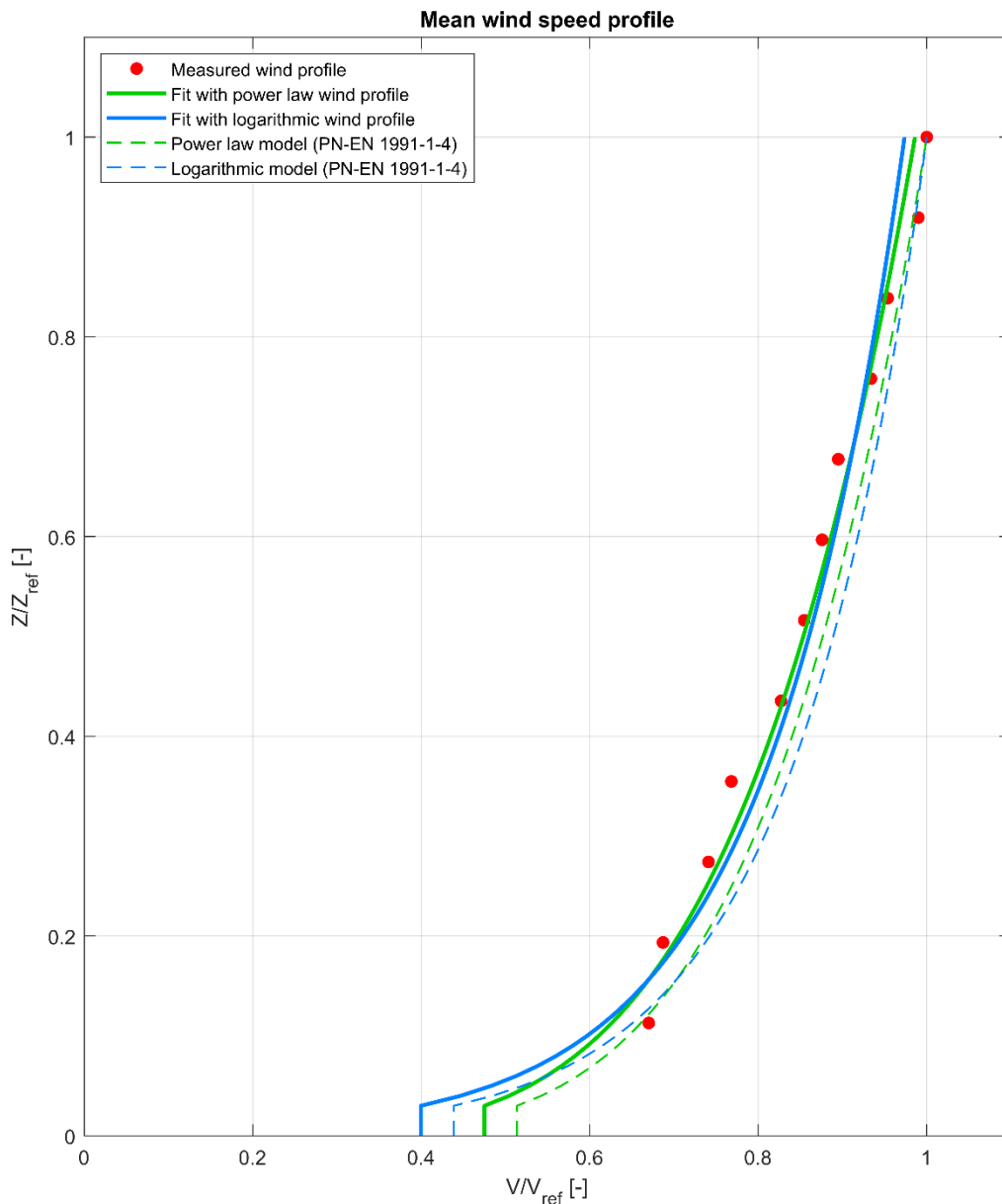
Fig. 8.34. Vertical mean wind speed profile for the Case 3-10

This results in the profiles with moderately high change in wind speed along the height, decreasing to a value of about 0.4-0.5 of v_{ref} at the height of z_{min} and to about 0.6-0.7 of v_{ref} at the height of the lowest measuring point. The obtained wind profiles are very close to the model ones from the standard, with a slight transition to the left along the whole analysed height. The RMSE values between the model profiles from (PN-EN 1991-1-4, 2011) and the profiles obtained from the measurements are 0.024 for the power-law profile and 0.03 for the logarithmic profile. The wind velocity values from the measurements, marked with red dots, are also closely matched with the obtained fit, with goodness of fit parameters of R^2 equal to 0.97 and 0.95, and RMSE equal to 0.02 and 0.3 for power-law and logarithmic profiles, respectively. This results in a very good recreation of the wind profile for the suburban terrain in the wind tunnel.
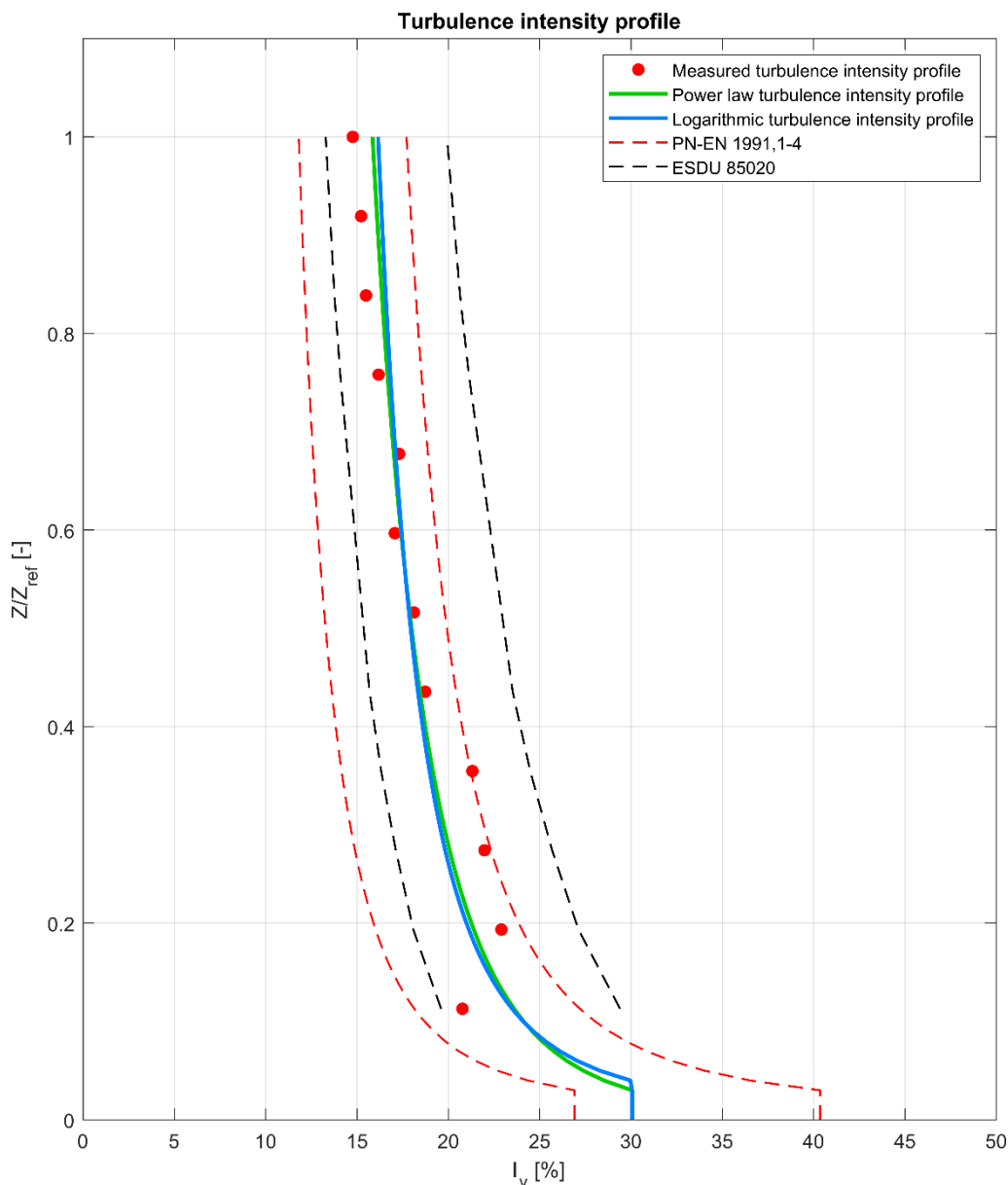
Fig. 8.35. Vertical turbulence intensity profile for the Case 3-10

In this case, the simulation of the turbulence intensity profile for the suburban terrain is excellent, fitting very well within the ±20% suggested by either of the standards, with the power-law and logarithmic profiles being very close to the suggested values. This results in the RMSE values of 0.016 with reference to (ESDU 85020, 2002) and 0.013 with reference to (PN-EN 1991-1-4, 2011). The turbulence intensity values are between 23% closer to the ground to about 15% at higher altitudes, with the recommended values from (ESDU 85020, 2002) between about 24% and 17%. The proper simulation of the turbulence intensity in this case may be largely attributed to the presence of the blocks elevated at 5 cm over the fetch length, which generates additional roughness along the whole length of the test section. The parameters that define the vertical turbulence profiles are also closely matched with the target values, with β exponent at -0.18 (relative error of 0.039) and z_0^T at 0.14 m (relative error of 0.521), resulting in the desired change of the turbulence along the height. The goodness of fit parameters for the turbulence intensity profiles are sufficient at R^2 equal to 0.75 and 0.7, and RMSE equal to 0.015 and 0.016 for power-law and logarithmic profiles, respectively.
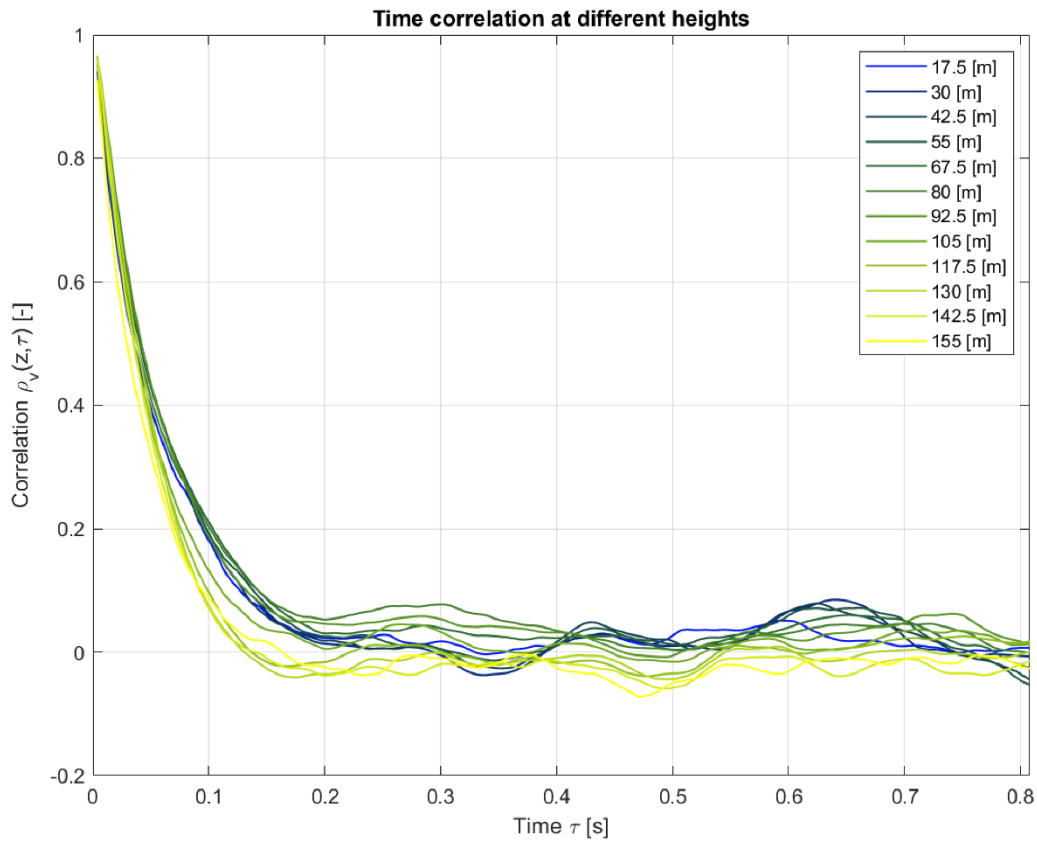
Fig. 8.36. Time correlation at different heights for the Case 3-10
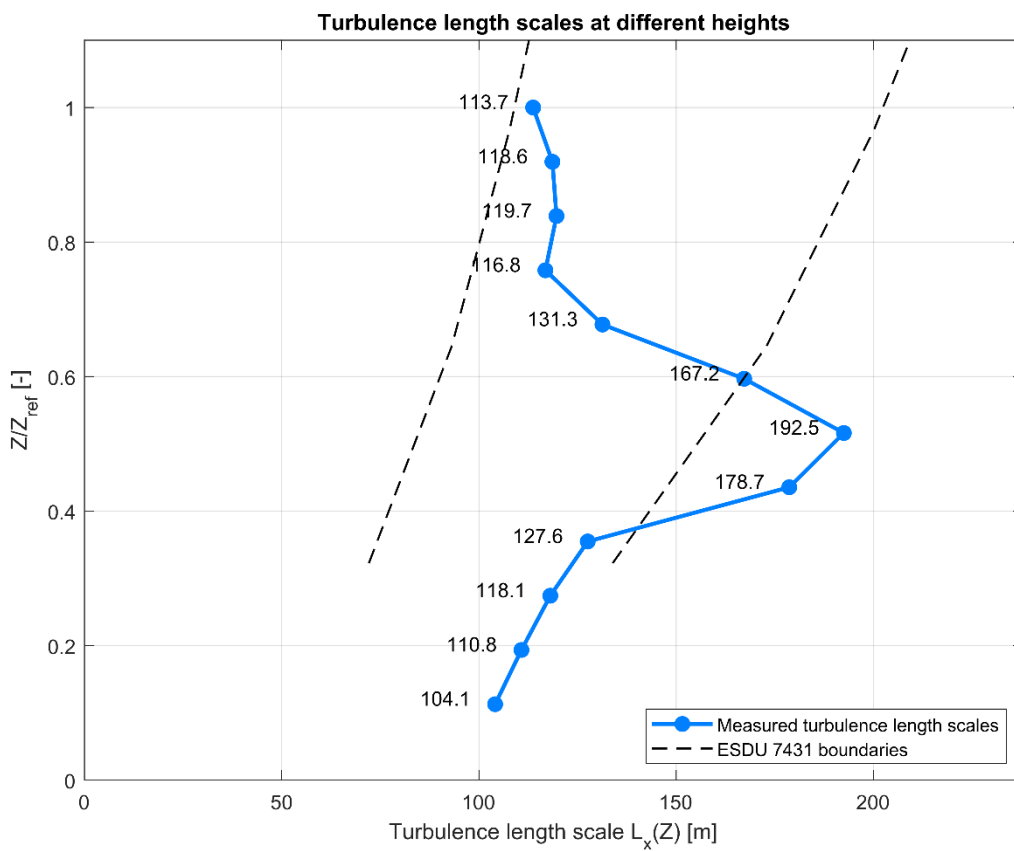

Fig. 8.37. Longitudinal turbulence length scale $L_x(Z)$ at different heights for the Case 3-10

Fig. 8.36 shows the time autocorrelations plots and Fig. 8.37 shows the longitudinal turbulence length scales at different heights for the case 3-10. The autocorrelations plots are characterised by moderate fluctuations of the correlation time scales, particularly around the horizontal axis. The correlations reach 0 at a lag of about $\tau = 0.15$ s (highest point) and $\tau = 0.4$ s (lowest point). The longitudinal turbulence length scales are, for the most analysed heights, within the boundaries recommended by (ESDU 74031, 1974), besides the steep increase at around $0.5\ Z_{ref}$ (reaching the longitudinal turbulence length scales of about 179 m and 193 m) that is larger than the assumed ±30% uncertainty bounds. Similar to the plot shown for the open flat terrain (Fig. 8.26), an almost linear increase can be clearly noticed at the lower heights to about $0.4\ Z_{ref}$, from 104 m to 128 m. Besides the higher values at the middle heights, the turbulence length scale values are approximately constant at about 118 m for the 4 highest measurement points. Similar phenomena have been noticed by (Kozmar, 2011c; Lim et al., 2007), with the former indicating that achieving the increase of this value at higher altitudes might be impossible in wind tunnel tests. This has been attributed to an inability of the larger-scale eddies to develop inside the wind tunnels due to confined space, which is in contrast to nature. With this in mind, the reproduction of the turbulence length scales for the suburban terrain type can be considered sufficient in this case.
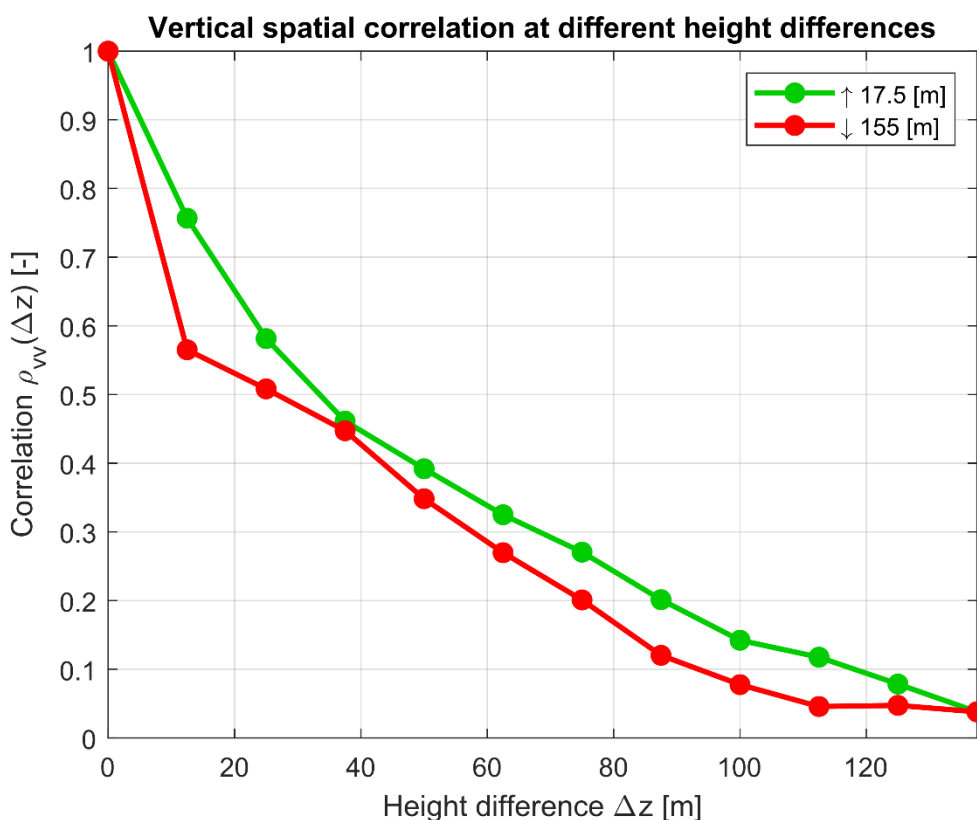
Fig. 8.38. Vertical spatial correlation at different height differences for the Case 3-10

Fig. 8.38 shows vertical spatial correlations at different distances Δz between the two points, when moving upward or downward, for the case 3-10. The differences resulting from the anisotropic character of this relation can be mostly seen at the shorter distances, where the downward correlation has a much steeper decrease. For larger distances, the upward correlation has a character close to an exponential curve, while the downward correlation is more linear up to a distance Δz of about 100 m, which is in line with the results of field

studies (Duchêne-Marullaz, 1977). The values of vertical turbulence lengths are 48.1 m when moving upward and 39.4 m when moving downward. The higher vertical turbulence length scale when moving upward than when moving downward is in good agreement with literature (Duchêne-Marullaz, 1977).

Fig. 8.39 shows power spectral densities at each measurement point for the case 3-10. The calculated spectra show good agreement with the models, reaching slightly lower values than these models for the higher reduced frequencies. This also results in the slope of 2/3 inclination, suggesting the clear presence of Kolmogorov inertial subrange (Kolmogorov, 1941).

The comparison between the Welch method and direct calculation from FFT draws similar conclusions as in the case of the open flat terrain. The results are also, similarly to case 2-128, less scattered than for cases 3-98 and 3-99. This suggests that the type of turbulence-generating method (i.e. turbulising net against the barriers and spires) influences this dispersion.

In this case, the presence of slight peaks at the frequency of about 0.4 Hz in real-life scale can be only observed for the lower probes (Fig. 8.39a-Fig. 8.39d and Fig. 8.39f) and the peaks are smaller than for cases 3-98 and 3-99. This pattern is similar to case 2-128 (Fig. 8.28).
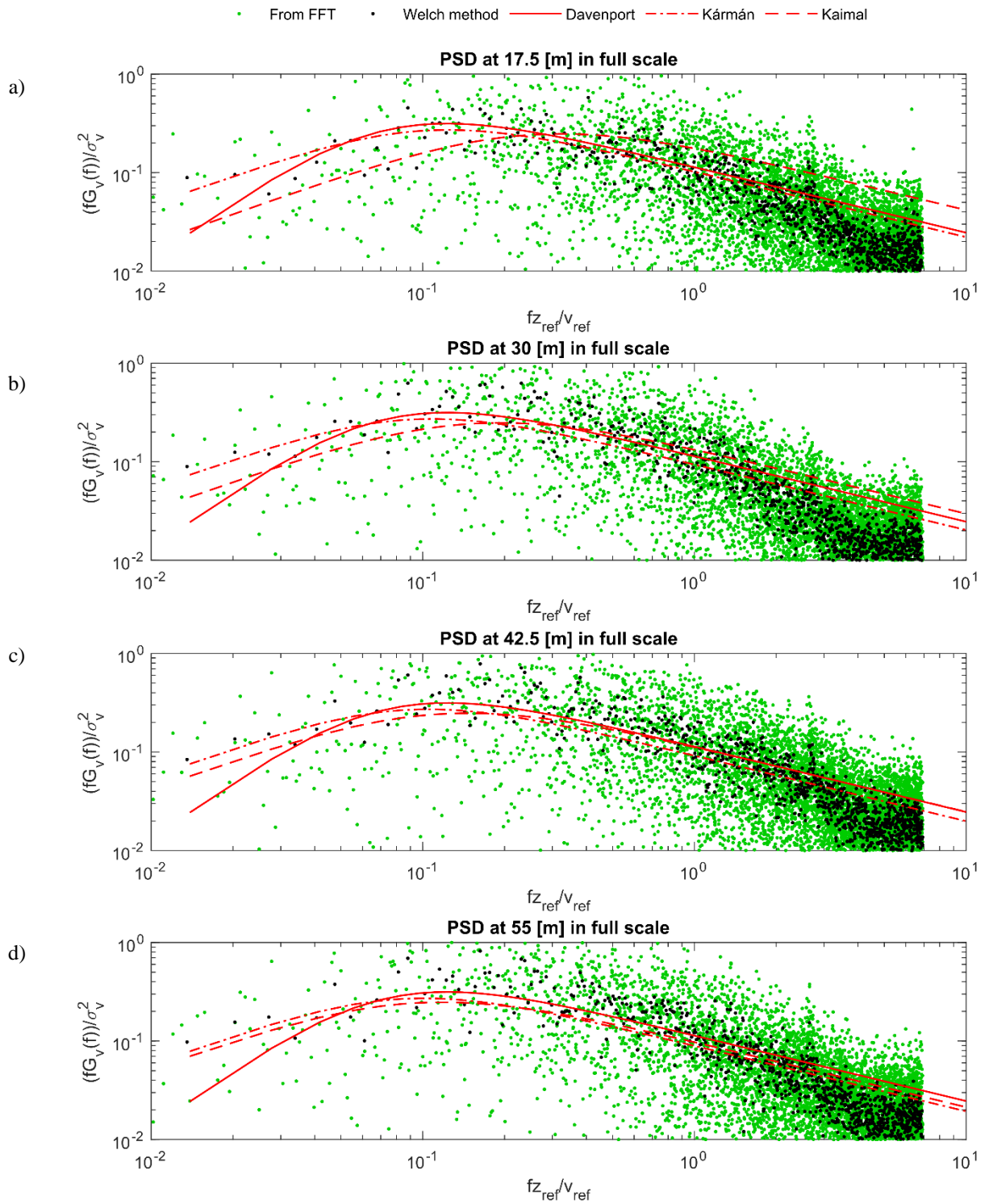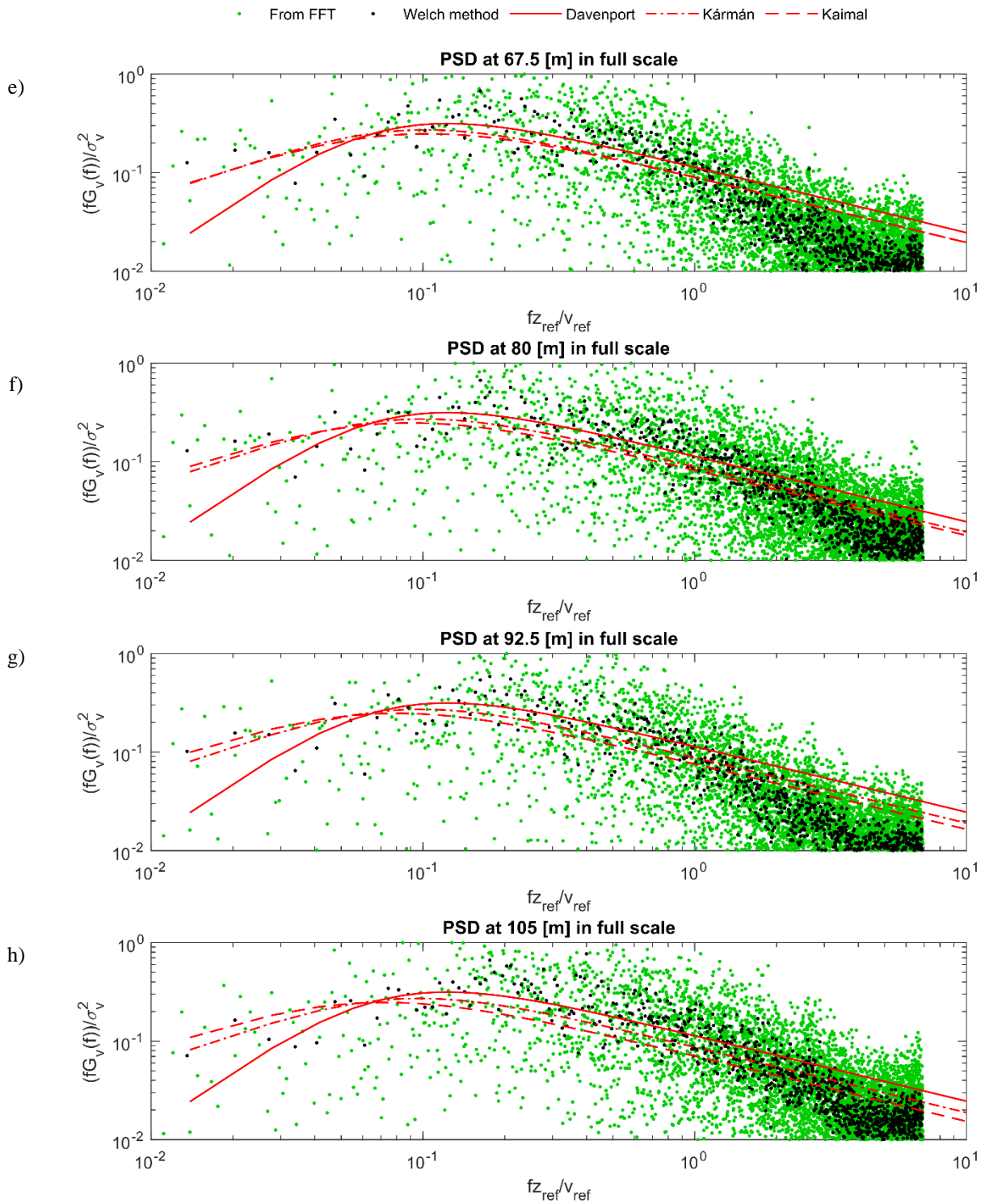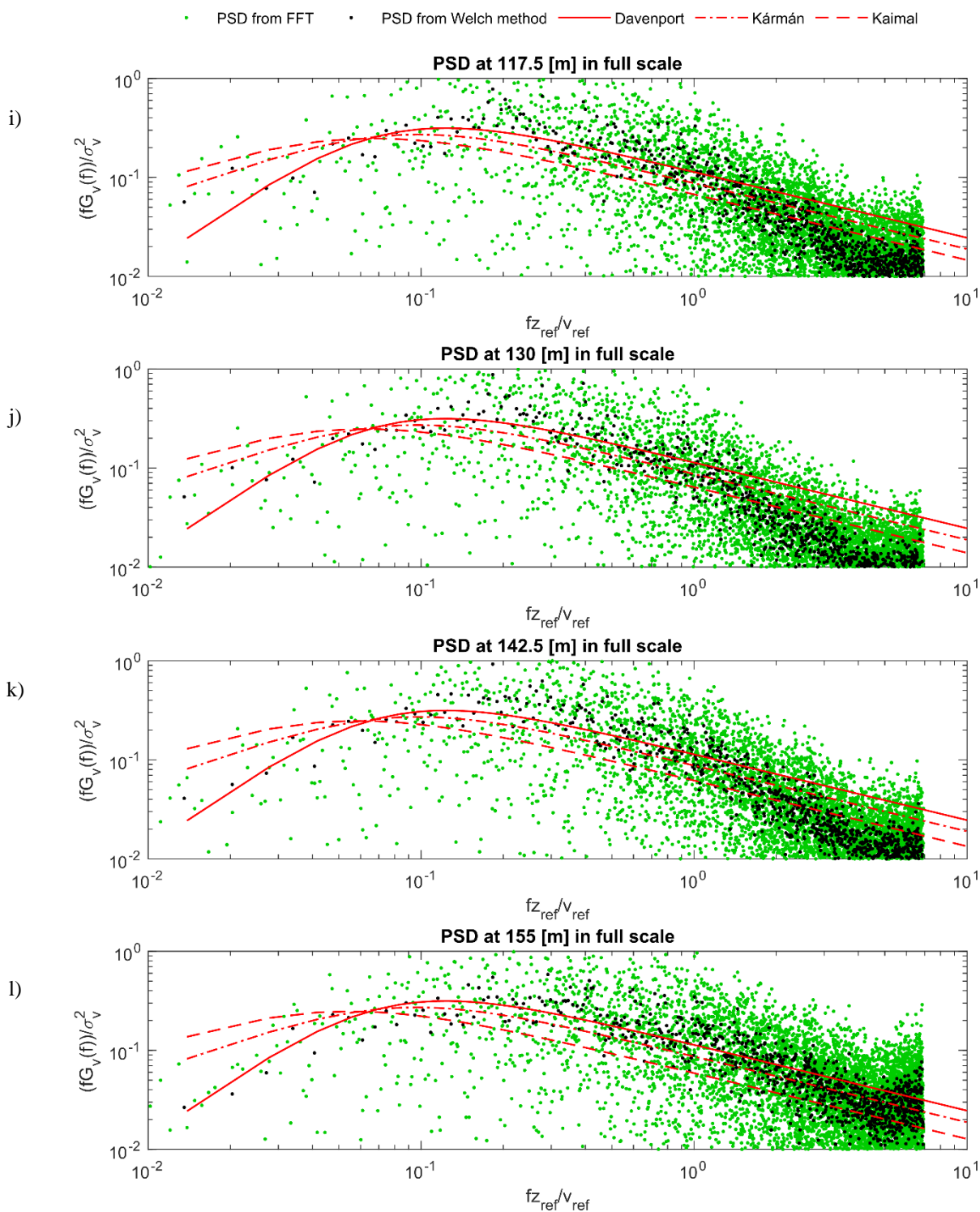
Fig. 8.39. Power density spectra at different heights, calculated with the Welch method and directly from FFT and compared against the reference spectra from Davenport, von Kármán and Kaimal, for the Case 3-10

Fig. 8.40-Fig. 8.42 show selected plots of co-coherence for the case 3-10, for distances Δz of 12.5 m, 25 m and 37.5 m.

Fig. 8.40. Vertical co-coherence between the points with Δ_z equal to 12.5 m, 25 m and 37.5 m for the Case 3-10, with fit according to the Davenport model, Bowen model and modified Bowen model – plots 1-11

The co-coherence for each of the analysed pairs of points is well estimated by the fit from Davenport and Bowen models, with both of these models producing the same curves for all the analysed cases (same as for the previously analysed test cases), further suggesting that the effects observed by (Bowen et al., 1983) may not be possible to replicate in the wind tunnel.

Comparing the exponential decay coefficients of the Davenport model with various sources, they are close to the value of 7 for 5 cases, always at a distance Δz of 12.5 m. Values of about 9.1-10.8 were observed for a total of 11 cases. Once again, in this test case, the exponential decay coefficient for the Davenport model only reaches a much higher value (29.9) for the co-coherence between the two highest points.

The exponential decay coefficients for the Bowen model reach values similar to the literature only for 1 case, which is the same pair of points as for the case 2-128 (117.5 and 155 m), in other cases being usually at lower values. The slight peaks at a value of about 0.4 Hz in real-life scale are much less prevalent for this test case and only observable for several pairs of points, mostly closer to the ground level. This means that they do not affect the modified Bowen model, which gives a good approximation of the calculated co-coherence function for all the presented test cases and produces the same curves as the Davenport model and the Bowen model.
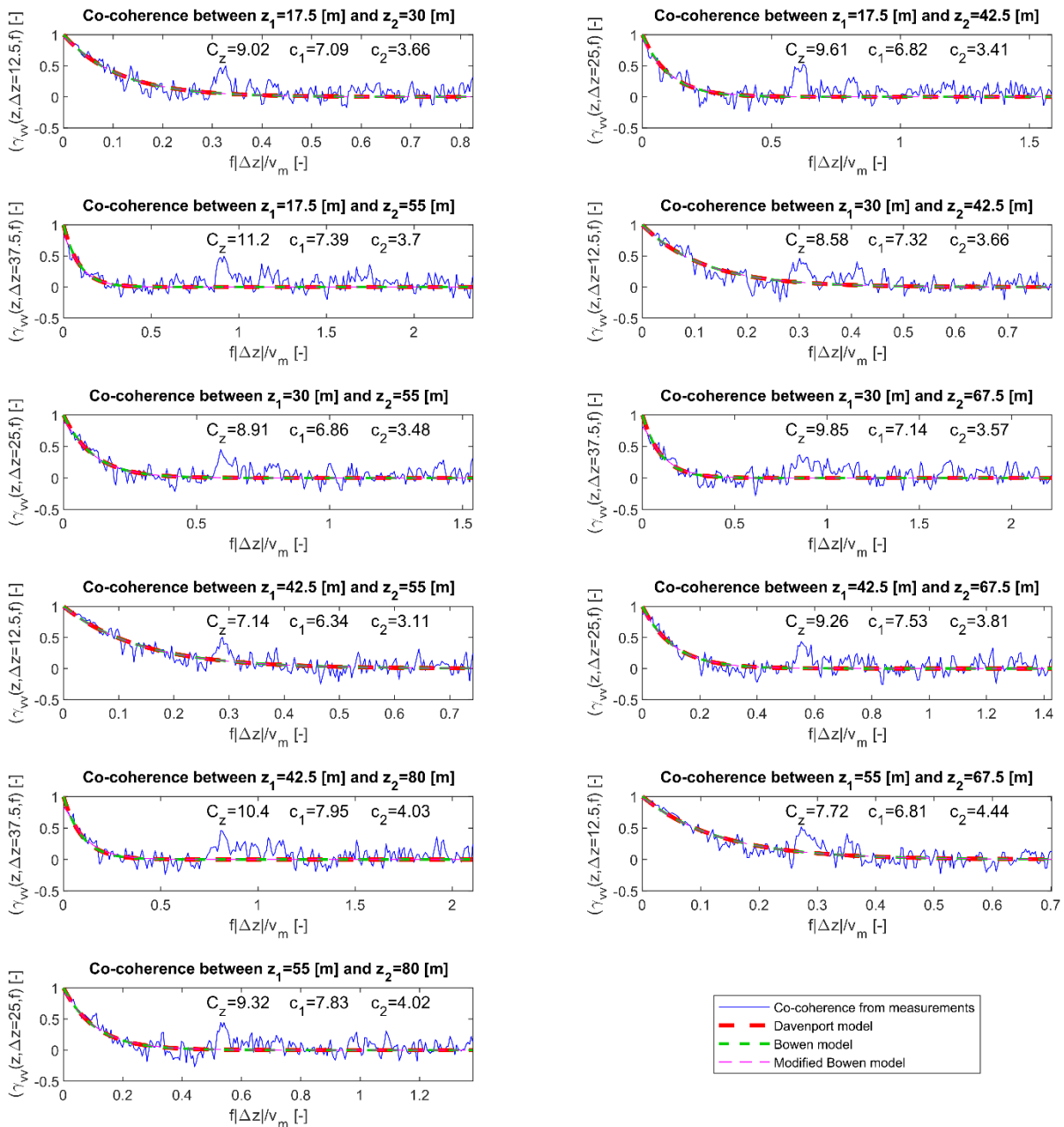

Fig. 8.41. Vertical co-coherence between the points with Δ_z equal to 12.5 m, 25 m and 37.5 m for the Case 3-10, with fit according to the Davenport model, Bowen model and modified Bowen model – plots 12-22

Comparing the values of exponential decay coefficients for different models with the three previously analysed cases (3-98, 3-99 and 2-128), it can be seen that these coefficients have very similar values between all these cases (for the corresponding pairs of points). This seems

not to be true only at the lowest and highest probes. It seems that the presence of the turbulising net mostly causes differences in the values of these coefficients at the near-ground level.
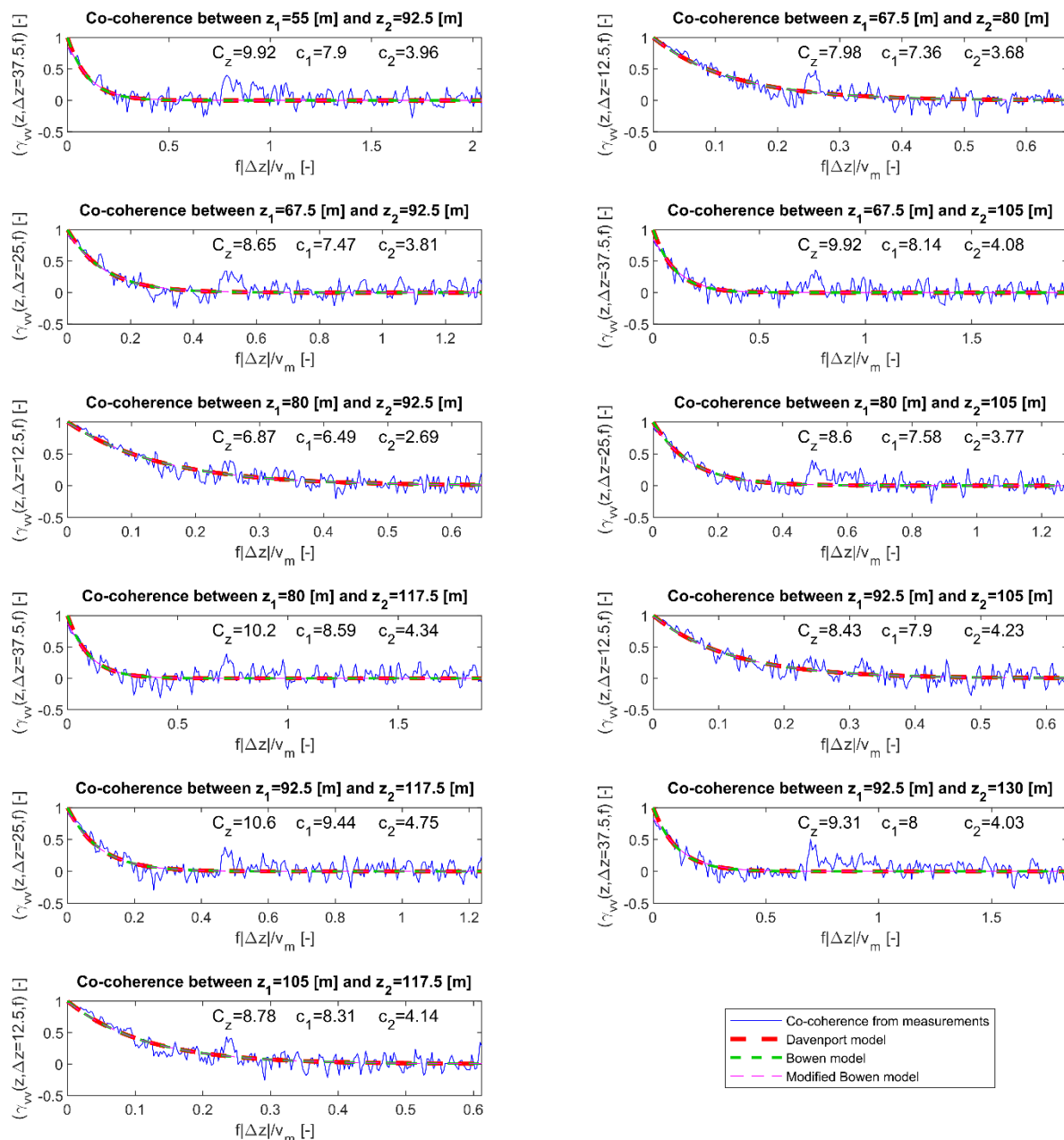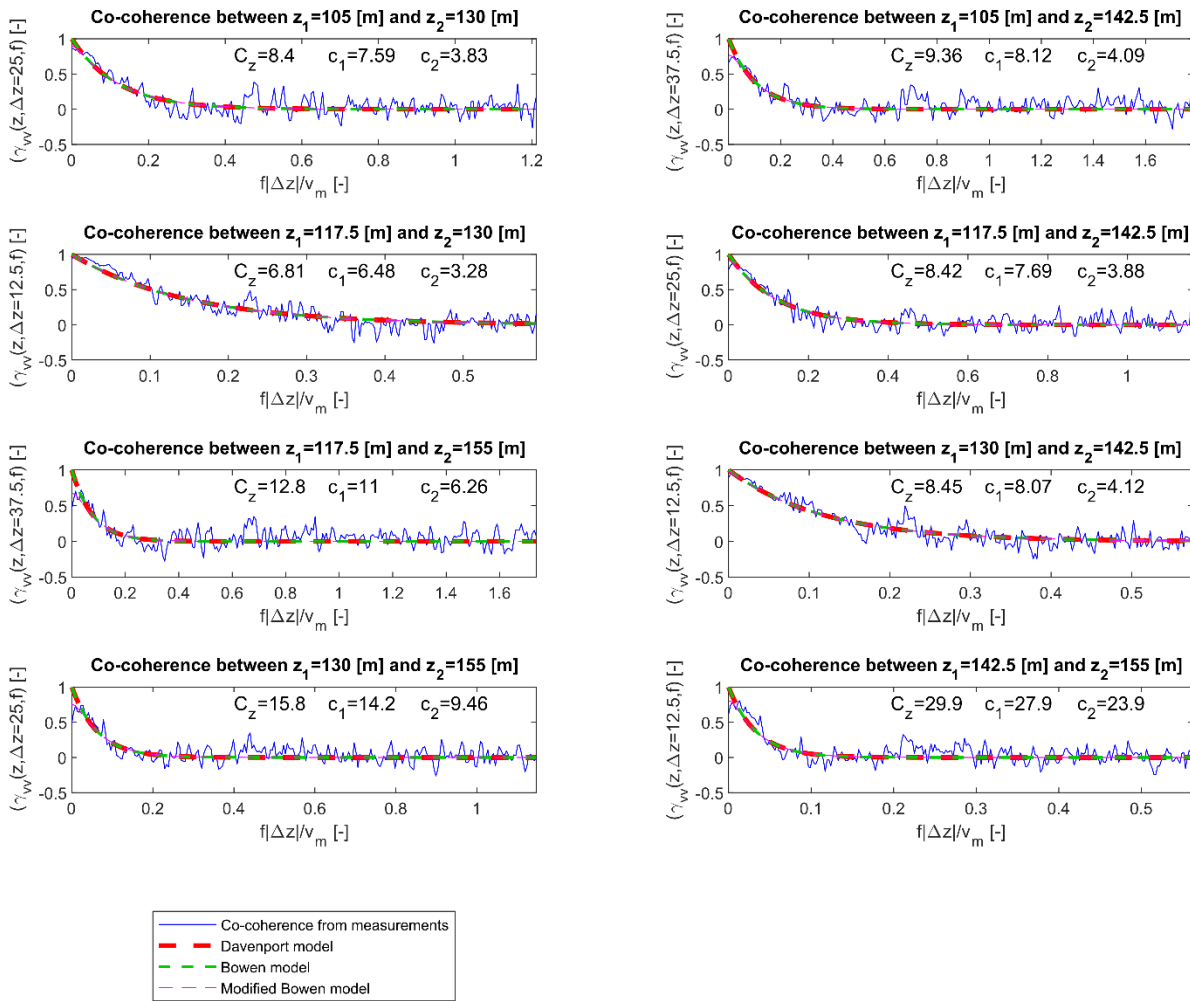

Fig. 8.42. Vertical co-coherence between the points with Δ_z equal to 12.5 m, 25 m and 37.5 m for the Case 3-10, with fit according to the Davenport model, Bowen model and modified Bowen model – plots 23-30

Fig. 8.43 and Fig. 8.44 show the frequency length scales distribution at different vertical distances Δz, taking into account the correlations with the lowest measuring point at 17.5 m (Fig. 8.43) and the correlations with the highest measuring point at 155 m (Fig. 8.44).

In this case, similar to case 2-128, the values reported in relation to the lowest measuring point are higher than the values reported in relation to the highest measuring point, as observed in subsection 7.3 for the cases with spires and barriers. The frequency length scales are, in general, slightly lower than for the test case representing the open flat terrain, ranging from 0.04 Hz to 0.17 Hz for the lowest measuring point and from 0.04 Hz to 0.08 Hz for the highest measuring point. For the relations with both points, there is a decreasing trend with the increase of distance Δz between the two considered points, however, with a much more random pattern in the case of the highest point. Considering a comparison to the values recommended for design, the relations to the lowest measuring point result in the frequency scale at a distance of about 50 m of 0.08 Hz (resulting in an averaging period T_z^* of about 12.5 s) and at a distance of about 100 m is 0.06 Hz (resulting in an averaging period T_z^* of

about 16.7 s). These values of the period scales are slightly larger than the values recommended by (Cook, 1985, 1990) for buildings of these heights. This suggests that the larger roughness may result in longer averaging periods and thus slightly reduce the gust values. This is a reasonable conclusion considering that the turbulence for a terrain with larger roughness usually consists of eddies with larger energy but of smaller sizes.

Frequency length scales in relation to the lowest point (z_1=17.5 m)

at different vertical distances Δz
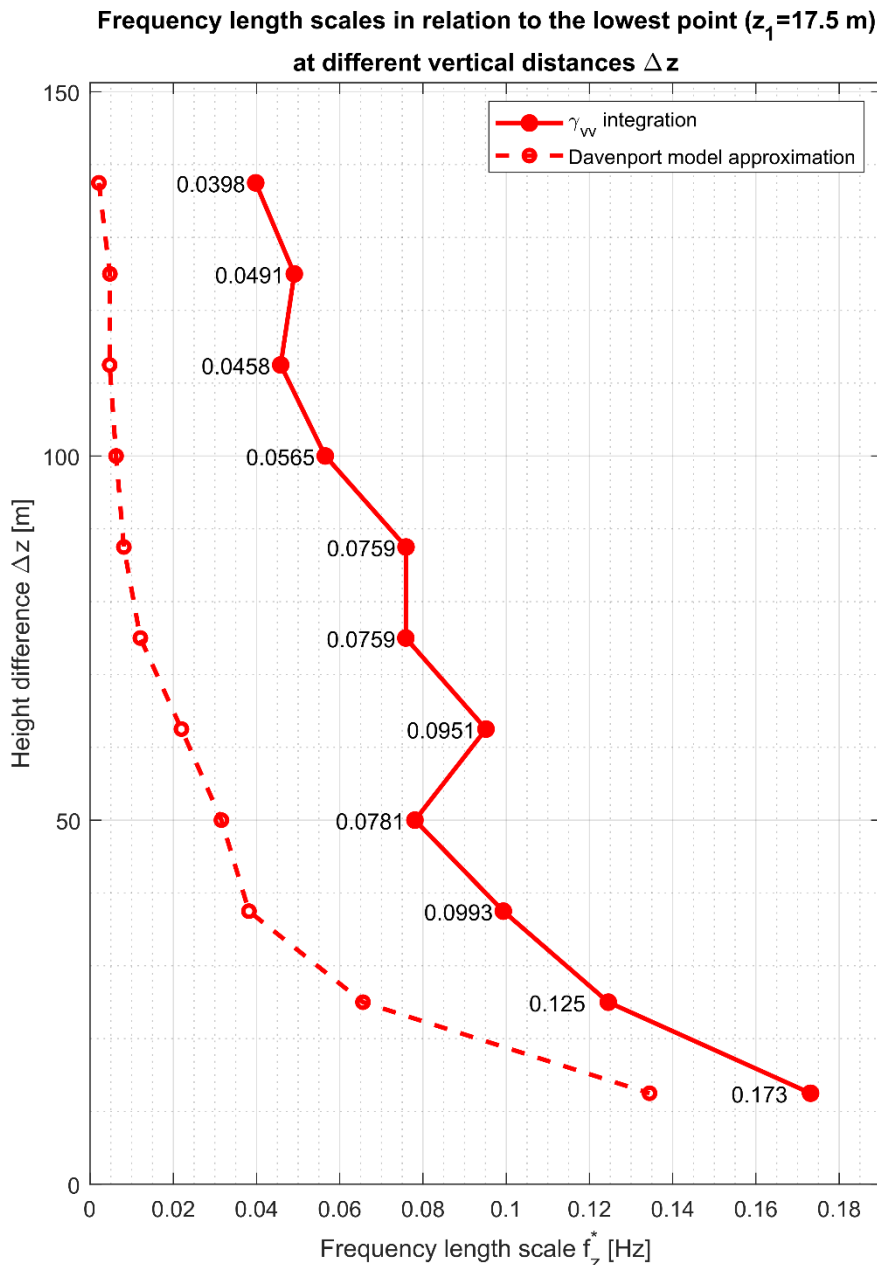
Fig. 8.43. Frequency length scales in relation to the lowest measurement point and different Δ_z values for the Case 3-10

The values estimated based on the Davenport model give a moderately sufficient approximation of the frequency length scales for the 4 shortest distances Δz in both analysed cases at a similar level as for case 2-128, with values for larger distances Δz decreasing almost to 0. However, these approximations are still lower than the values directly calculated from the co-coherence and therefore not on the safe side. A clear pattern of an exponential decrease with height, in particular for the lowest measuring point, can be observed for these

values, which might be considered a smoothening of the much more chaotic pattern derived from the direct calculations based on the co-coherence function.
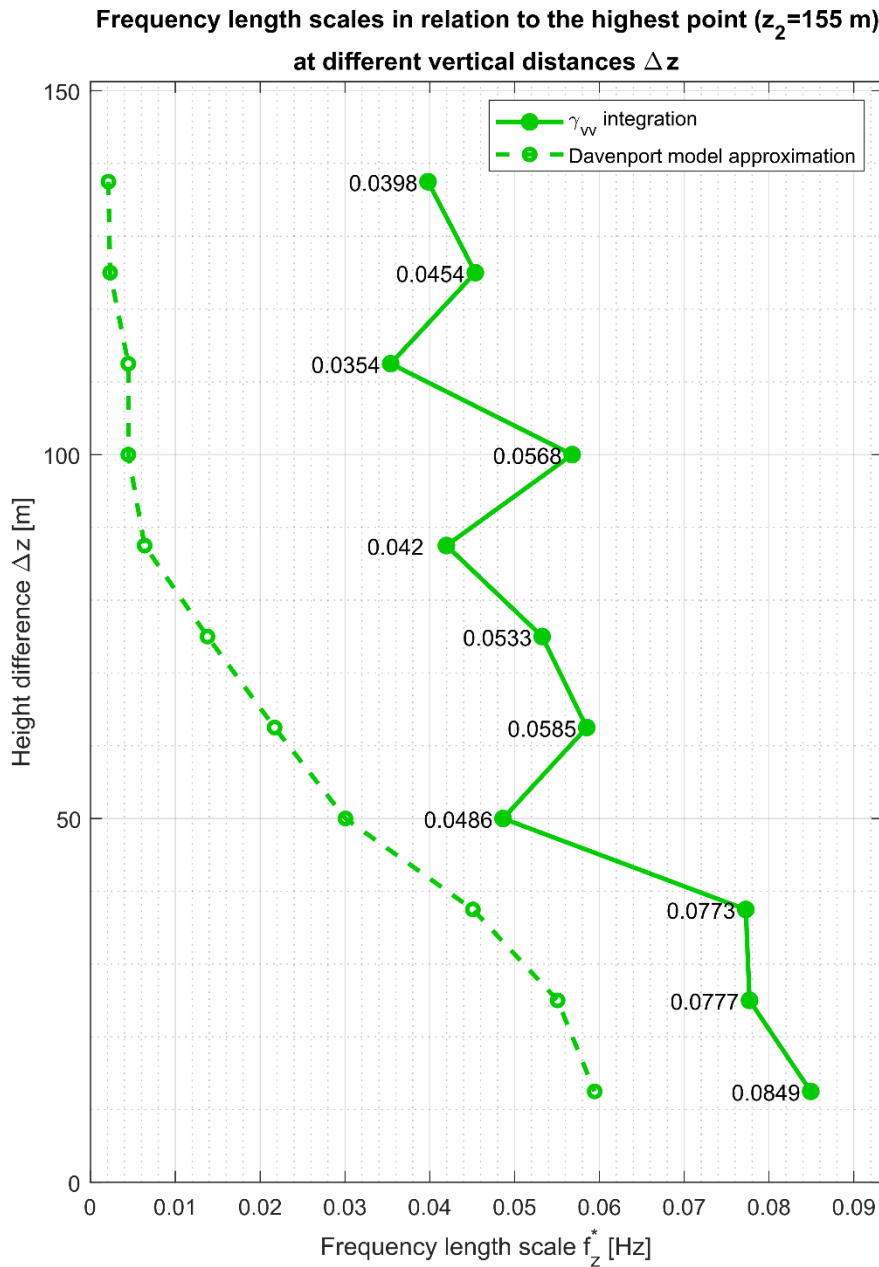
Fig. 8.44. Frequency length scales in relation to the highest measurement point and different Δ_z values for the Case 3-10

8.5.   Terrain roughness category IV – Case 2-82

Case 2-82, with a setup consisting of the 100 cm spires, rectangular barrier, blocks at the inlet elevated at 15 cm height and at the fetch length elevated at 5 cm height, was selected as the closest match for terrain category IV, which corresponds to urban areas. The vertical mean wind speed profile for this case is shown in Fig. 8.45 and turbulence intensity profile is shown in Fig. 8.46.

The vast majority of the investigated test cases were assigned to the urban terrain category, as it is the easiest one to replicate in the wind tunnel and also, due to the design of the assigning

algorithm, it included all the test cases with higher values of vertical mean wind speed profile parameters. For the selected case, the α exponent at 0.25 is very close to the target value of 0.24 (relative error of 0.049) and the roughness length z_0 at 0.87 is slightly lower than the target value of 1.0 (relative error of 0.133). However, it should be noticed that, in general, different codes recommend values of the roughness length for urban terrain category between 0.7-1.0.
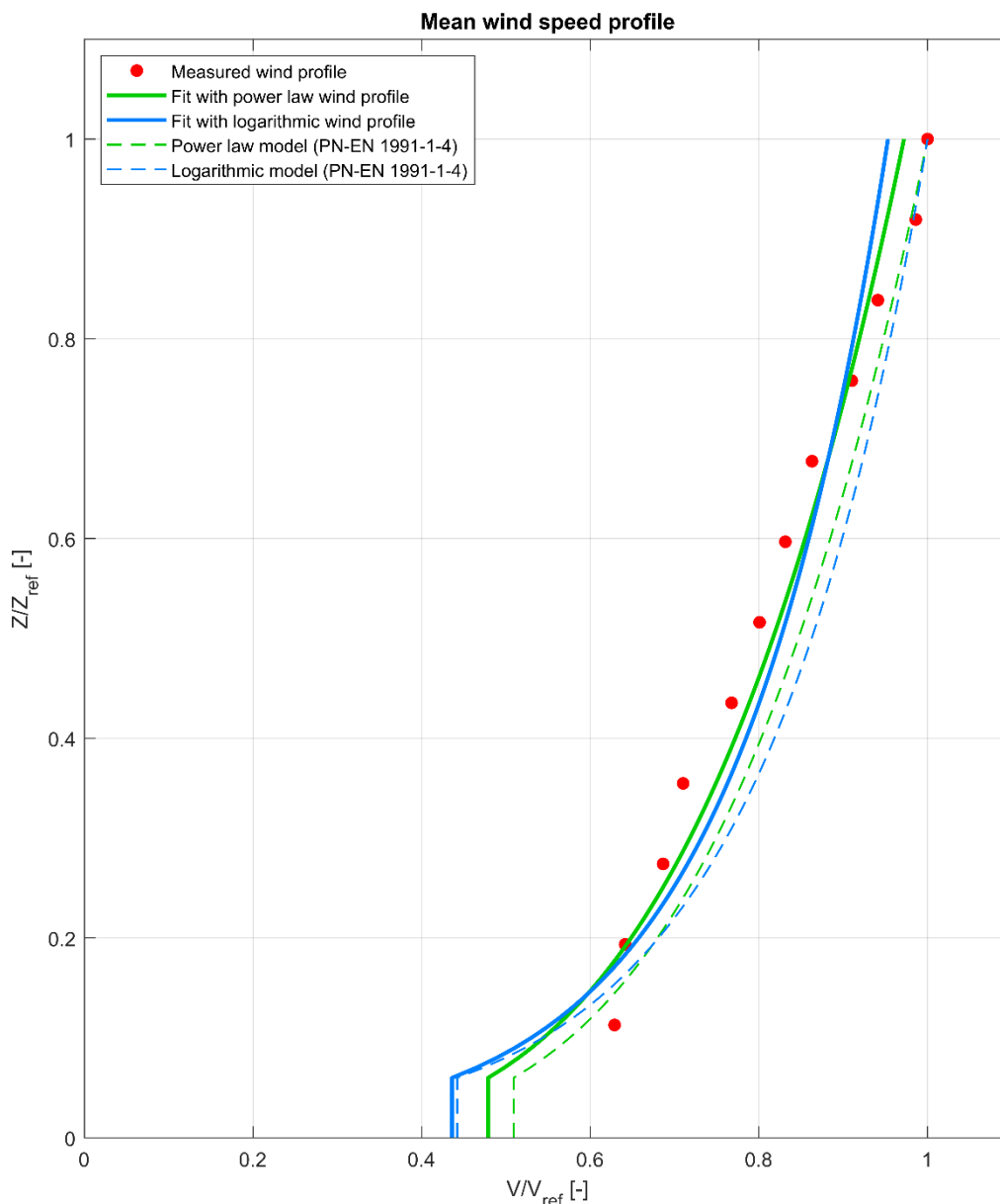
Fig. 8.45. Vertical mean wind speed profile for the Case 2-82

The obtained values of these two parameters result in the profiles that closely match the model ones from the standard, with a slight transition to the left. It should be noted that even in the lowest region (below the lowest measuring probe), the match is quite good, especially for the logarithmic wind profile. The RMSE values between the model profiles from (PN-EN 1991-1-4, 2011) and the profiles obtained from the measurements are 0.029 for the power-law profile and 0.031 for the logarithmic profile. The wind velocity values from the measurements, marked with red dots, are also closely matched with the obtained fit, with

goodness of fit parameters of R^2 equal to 0.95 and 0.94, and RMSE equal to 0.032 and 0.477 for power-law and logarithmic profiles, respectively. Out of the 242 test cases assigned to this category, about 30 different cases could also be taken as the representative ones (with preference scores of about 0.98), with several others (e.g. cases 3-8, 3-9, 3-59) providing a better fit for the vertical mean wind speed profile than the chosen one. However, the presented test case 2-82 was selected as a compromise resulting in the best recreation of both the mean wind speed profile and the turbulence intensity profile at the same time.
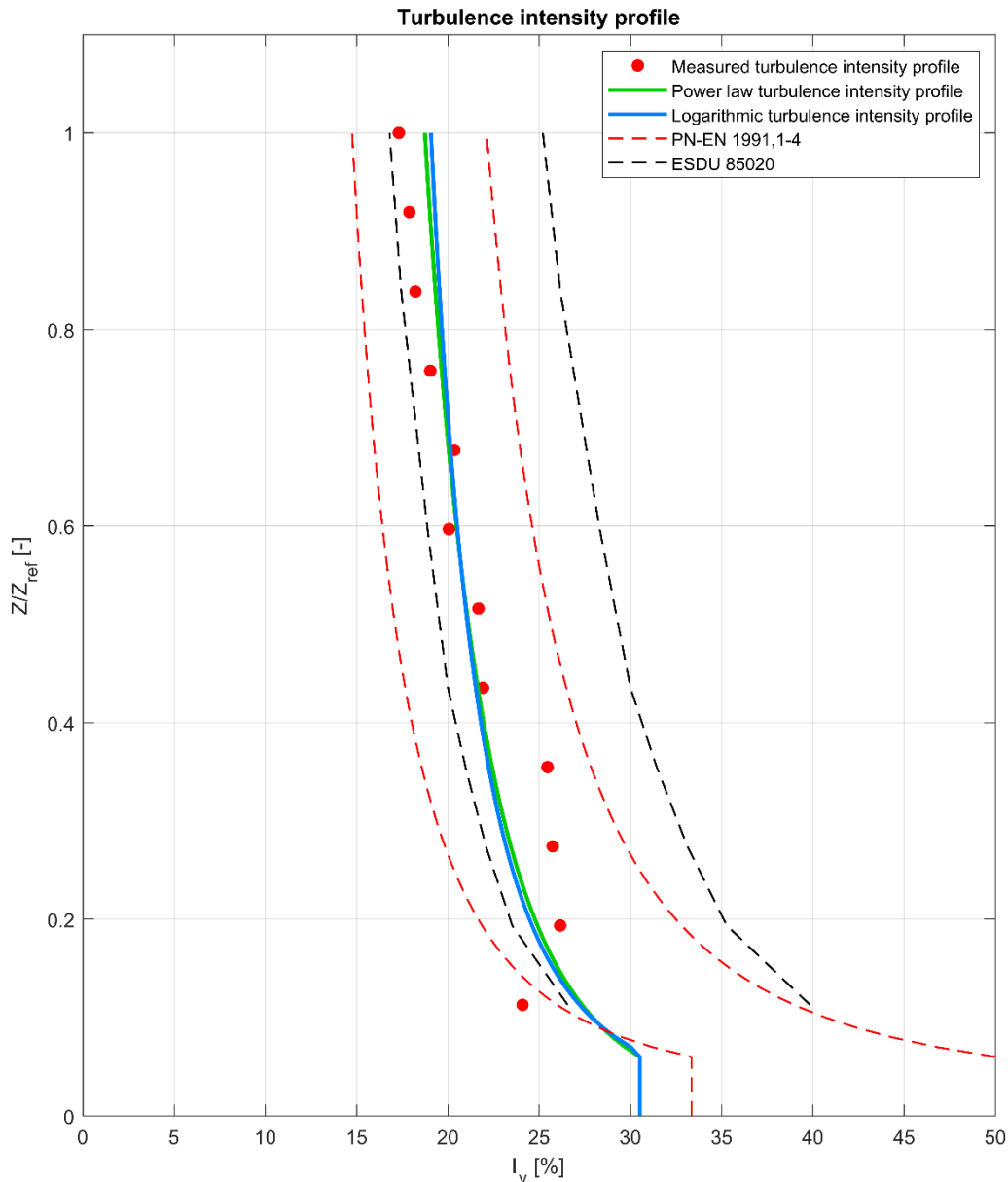
Fig. 8.46. Vertical turbulence intensity profile for the Case 2-82

The turbulence intensity values along the height are characterised by a very good fit within the ±20%, with the exception of the lowest measuring point that has a slightly lower value outside of the lower bound, which results in the profiles not fitting within these bounds at the near ground level. The RMSE values of turbulence intensity are 0.039 with reference to (ESDU 85020, 2002) and 0.023 with reference to (PN-EN 1991-1-4, 2011). Similarly as in case 3-10 representing the suburban terrain, the good agreement obtained here may also be

attributed to the presence of the blocks elevated at 5 cm over the fetch length. The expected values of turbulence intensity for urban terrain (roughness length $z_0 = 1.0$ m) are between about 33% closer to the ground to 21% around the height of Z_{ref}. This was matched sufficiently with the values in the range of about 26% and 17%. The parameters that define the vertical turbulence profiles are lower than the desired target values, with β exponent at -0.17 (relative error of 0.277) and z_0^T at 0.11 m (relative error of 0.894), which results in slightly too low values at the near-ground region. The goodness of fit parameters for the turbulence intensity profiles are sufficient at R^2 equal to 0.71 and 0.67, and RMSE equal to 0.018 and 0.019 for power-law and logarithmic profiles, respectively. The relatively low values of R^2 can be attributed to probes 2, 3 and 4, where – possibly due to the presence of the barrier – the turbulence intensity values slightly diverge to the right of the best-fit profiles.

Fig. 8.47 shows the time autocorrelations plots and Fig. 8.48 shows the longitudinal turbulence length scales at different heights for the case 2-82. The autocorrelations plots are smooth. The correlations reach 0 at a lag of about $\tau = 0.15$ s (highest point) and $\tau = 0.2$ s (lowest point). The longitudinal turbulence length scales are well within the ±30% uncertainty bounds recommended by (ESDU 74031, 1974). Furthermore, a general increasing trend can be observed along almost the whole analysed height, up to about 130 m. This results in a very satisfactory recreation of the longitudinal length scales for urban terrain type in the wind tunnel for the presented test case.
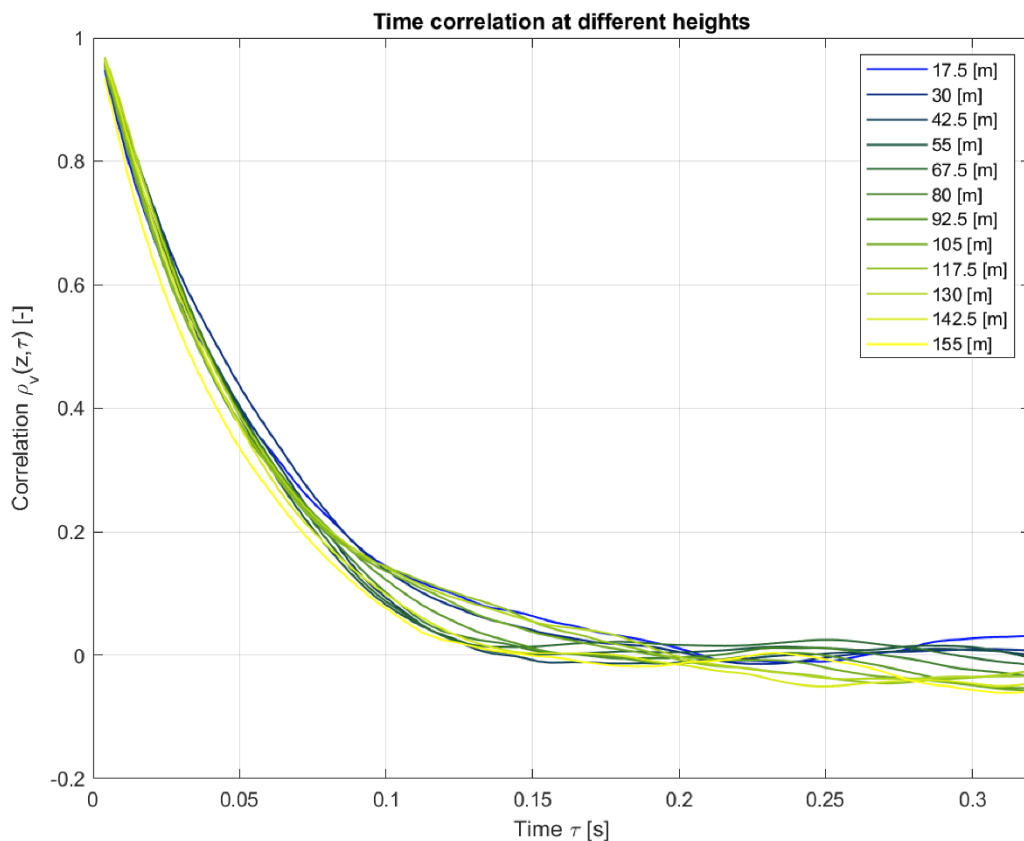

Fig. 8.47. Time correlation at different heights for the Case 2-82
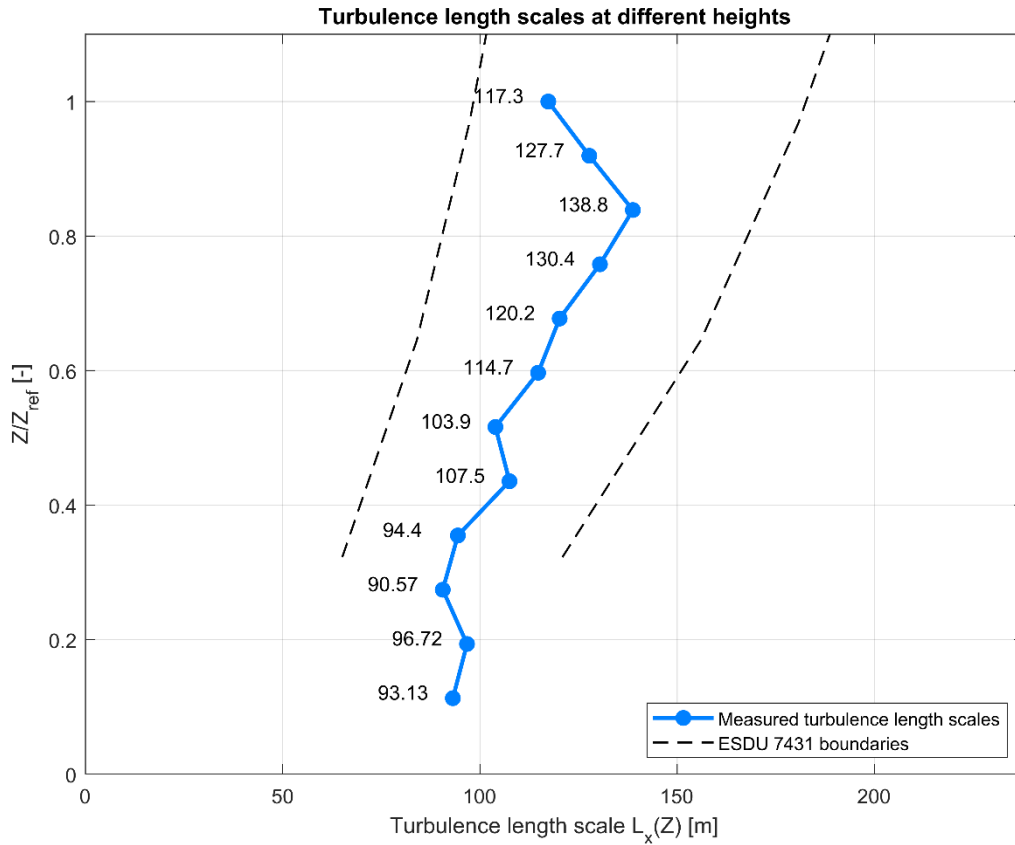
Fig. 8.48. Longitudinal turbulence length scale $L_x(Z)$ at different heights for the Case 2-82
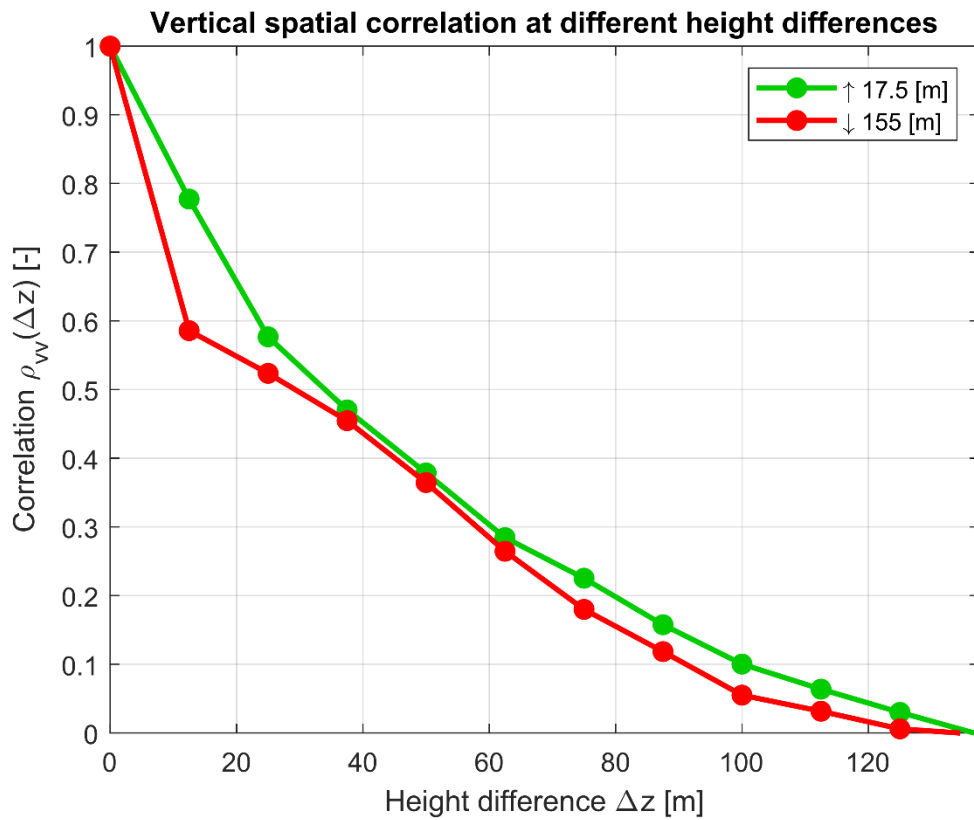

Fig. 8.49. Vertical spatial correlation at different height differences for the Case 2-82

Fig. 8.49 shows vertical spatial correlations at different distances Δz between the two points, when moving upward or downward, for the case 2-82. In this case, the curves when moving either upward or downward are very similar, with notable discrepancies only for the shortest distances Δz of about 20 m. Both of these correlations are close to an exponential curve. The values of vertical turbulence lengths are 44.5 m when moving upward and 38.5 m when moving downward. The higher vertical turbulence length scale when moving upward than when moving downward is in good agreement with literature (Duchêne-Marullaz, 1977). After analysing the vertical length scales for each of the selected representative cases, it can be observed that they are very similar for terrain categories II, III and IV. Furthermore, analysing the results presented in subsection 7.2, the only elements of the experimental setup that significantly influence the values of vertical length scales are the presence of a barrier or lack thereof and, especially, the turbulising net.

Fig. 8.50 shows power spectral densities at each measurement point for the case 2-82. The calculated spectra show good agreement with the models, usually reaching slightly lower values than these models. The Kolmogorov inertial subrange (Kolmogorov, 1941) is clearly present here, with the decreasing slope of 2/3 inclination clearly visible for all the measuring heights.

The dispersion of the results around the trend for both applied methods is very similar to cases 2-128 and 3-10. The presence of slight peaks at the frequency of about 0.4 Hz in real-life scale can be only observed for the 3 lowest probes (Fig. 8.50a-Fig. 8.50c) and once again, the peaks are relatively small. The lack of these peaks at some of the probes (at higher altitudes) further confirms that they are an effect naturally occurring in the wind flow that may be caused by the roughness elements present in the setup.

Analysing the power spectral densities for different terrain types leads to a conclusion that it is mostly the type of turbulence-generating elements that affect these characteristics and not necessarily the exact height of spires, type or barriers or elevation of the blocks in the wind tunnel. Furthermore, obtaining spectra that are in good agreement with the theoretical models in wind tunnel seems relatively easy. However, it should be noted that their proper recreation is strongly dependent on adopting the correct model scales (especially the frequency scale k_f) and choosing a sufficiently high sampling frequency according to these scales.
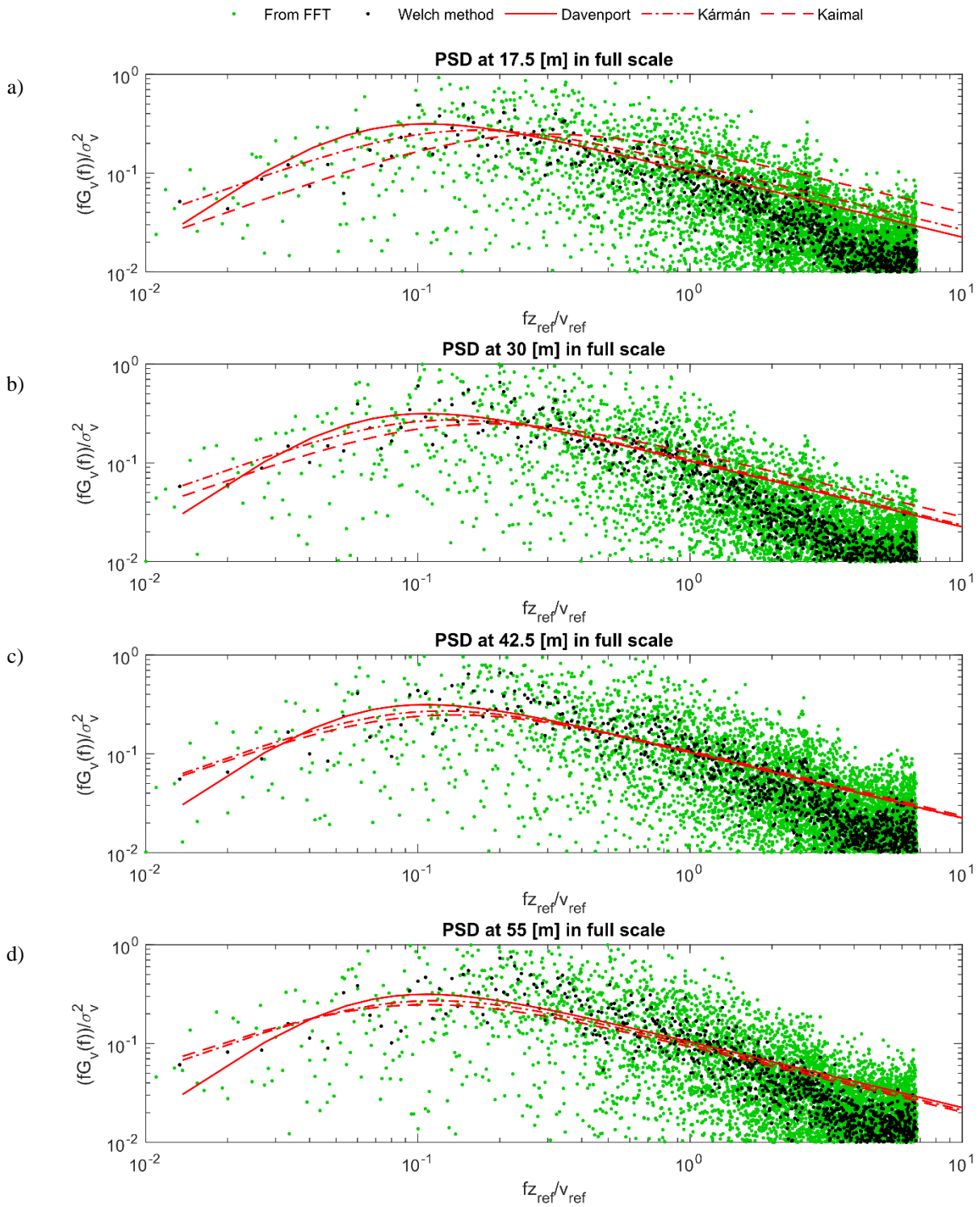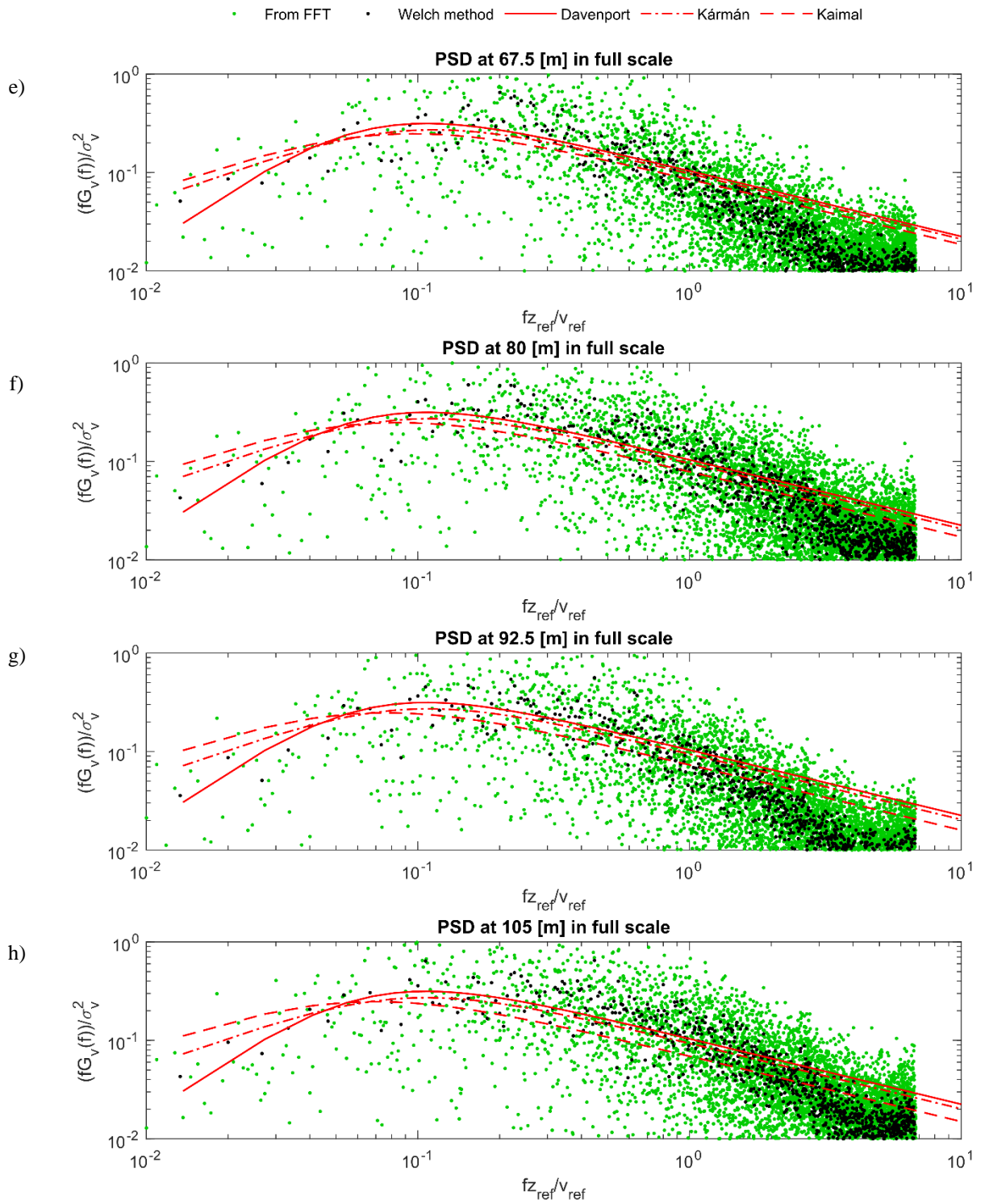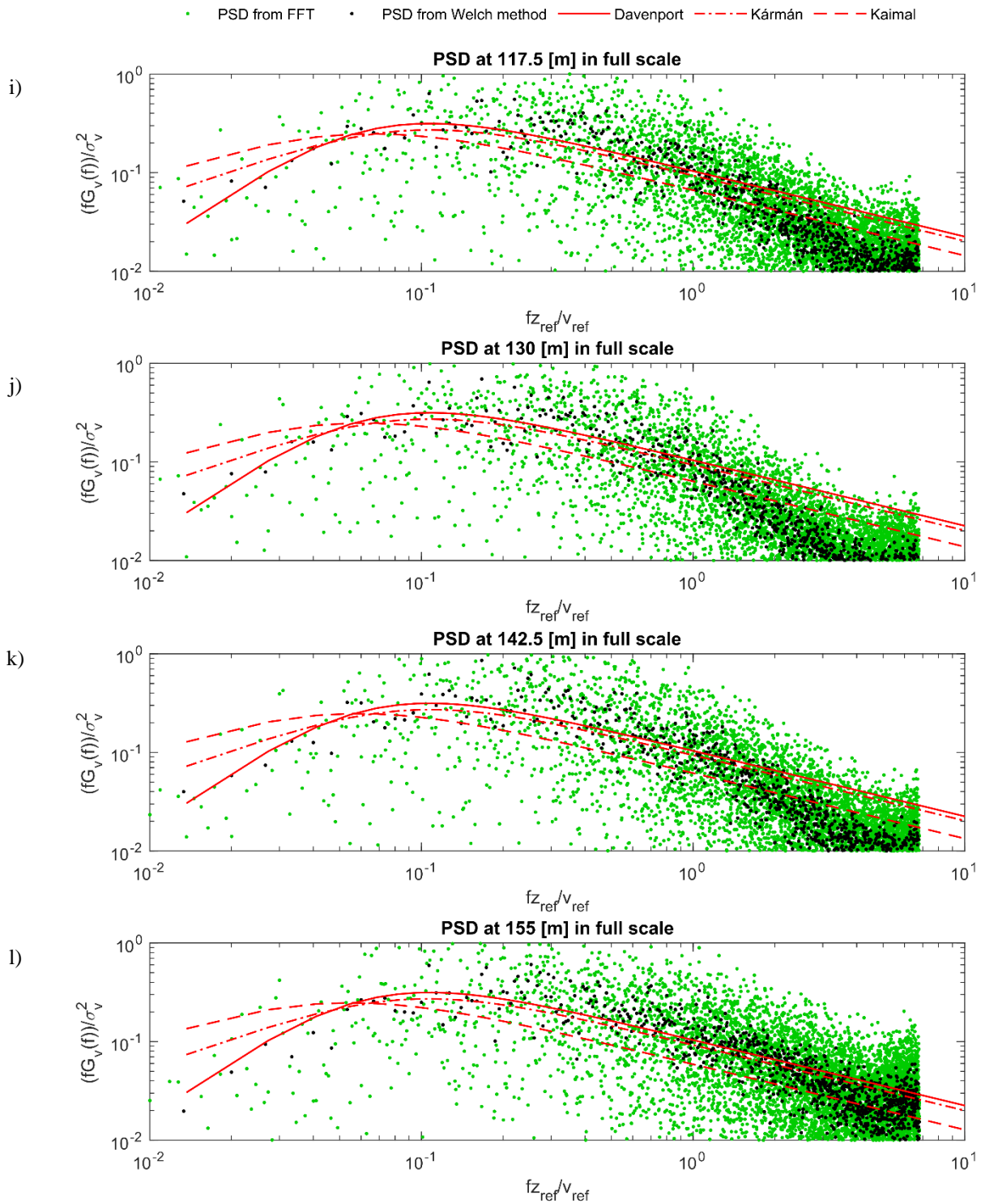
Fig. 8.50. Power density spectra at different heights, calculated with the Welch method and directly from FFT and compared against the reference spectra from Davenport, von Kármán and Kaimal, for the Case 2-82

Fig. 8.51-Fig. 8.53 show selected plots of co-coherence for the case 2-82, for distances Δz of 12.5 m, 25 m and 37.5 m.

Fig. 8.51. Vertical co-coherence between the points with Δ_z equal to 12.5 m, 25 m and 37.5 m for the Case 2-82, with fit according to the Davenport model, Bowen model and modified Bowen model – plots 1-11
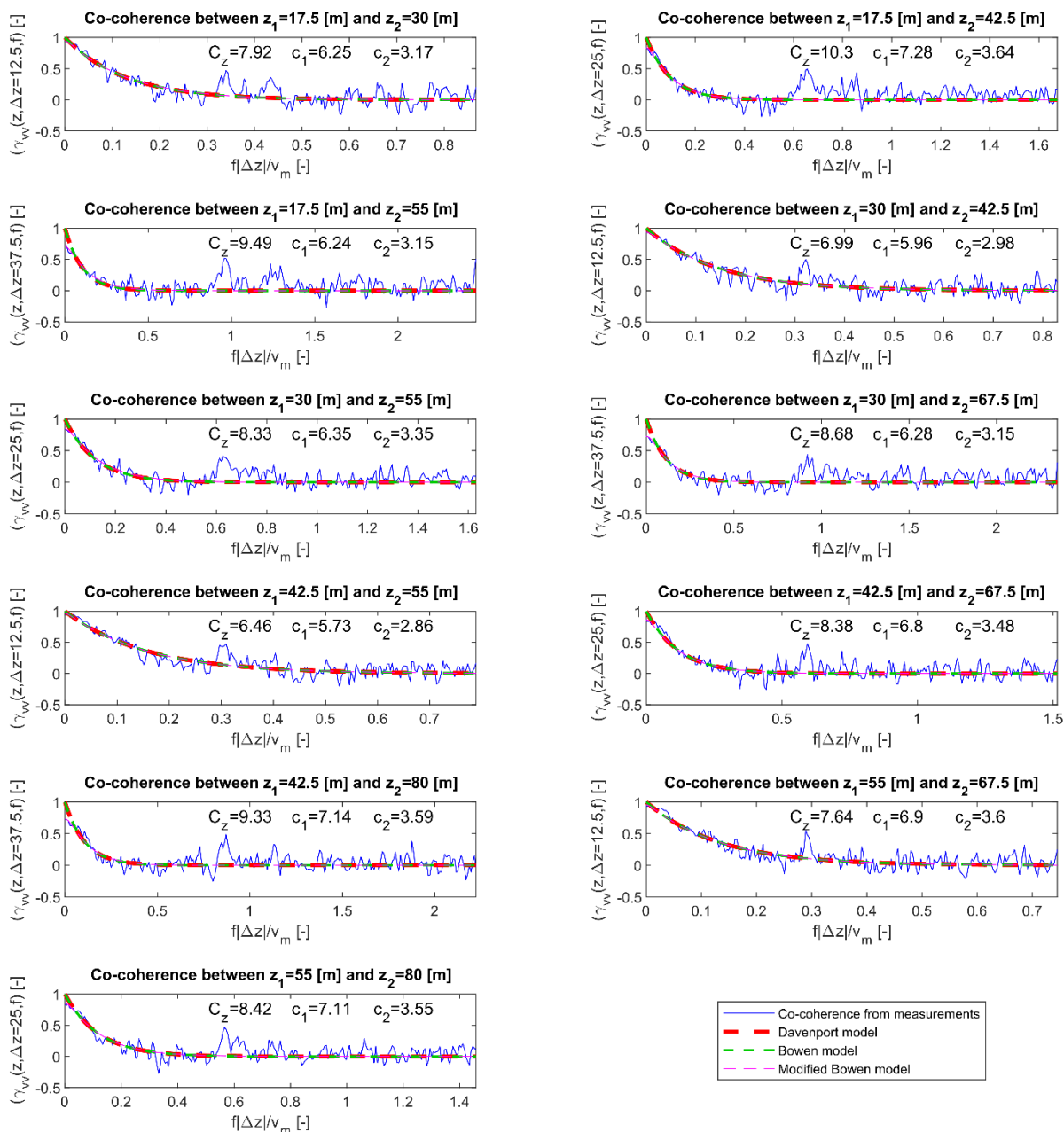
The co-coherence for each of the analysed pair of points is well estimated by the fit from each of the three applied models, with every one of these models producing the same curves for all the analysed cases (same as for the two previously analysed test cases), further suggesting that the effects observed by (Bowen et al., 1983) may not be possible to replicate in the wind tunnel.

Comparing the exponential decay coefficients of the Davenport model with various sources, they are close to the value of 7 for 8 cases, usually at a distance Δz of 12.5 m. Values of about 9.1-10.8 were observed for a total of 8 cases. Once again, in this test case, the exponential decay coefficient for the Davenport model reaches a much higher value (26.4) only for the co-coherence between the two highest points.

The exponential decay coefficients for the Bowen model reach values similar to the literature only for 1 case (117.5 and 155 m), the same as for cases 2-128 and 3-10. For other pairs of points, they are usually at lower values. The slight peaks at a value of about 0.4 Hz in real-life scale are much less prevalent for this test case and only observable for several pairs of points, mostly closer to the ground level and do not affect the fit obtained for the modified Bowen model.

Fig. 8.52. Vertical co-coherence between the points with Δ_z equal to 12.5 m, 25 m and 37.5 m for the Case 2-82, with fit according to the Davenport model, Bowen model and modified Bowen model – plots 12-22

Comparing the values of exponential decay coefficients for different models between all the analysed test cases, it can be seen that these coefficients have very similar values (for the corresponding pairs of points) for all of these test cases, besides the lowest and highest pairs of probes. This further suggests that the presence of the turbulising net mostly causes differences in the values of these coefficients at the near-ground level, while the different

turbulising elements have a much smaller effect on these coefficients than the heights above the ground and distances between the two points Δz.
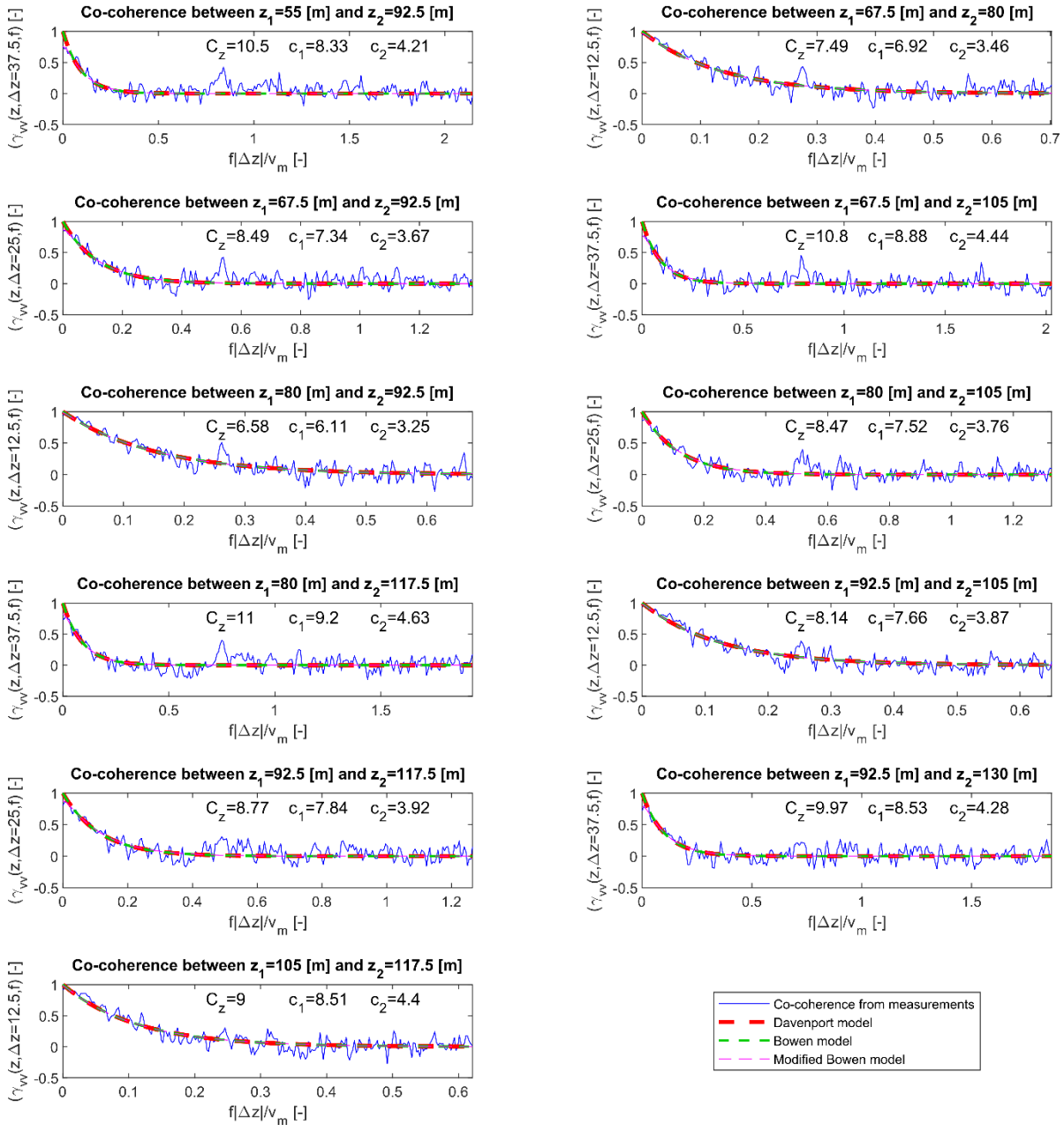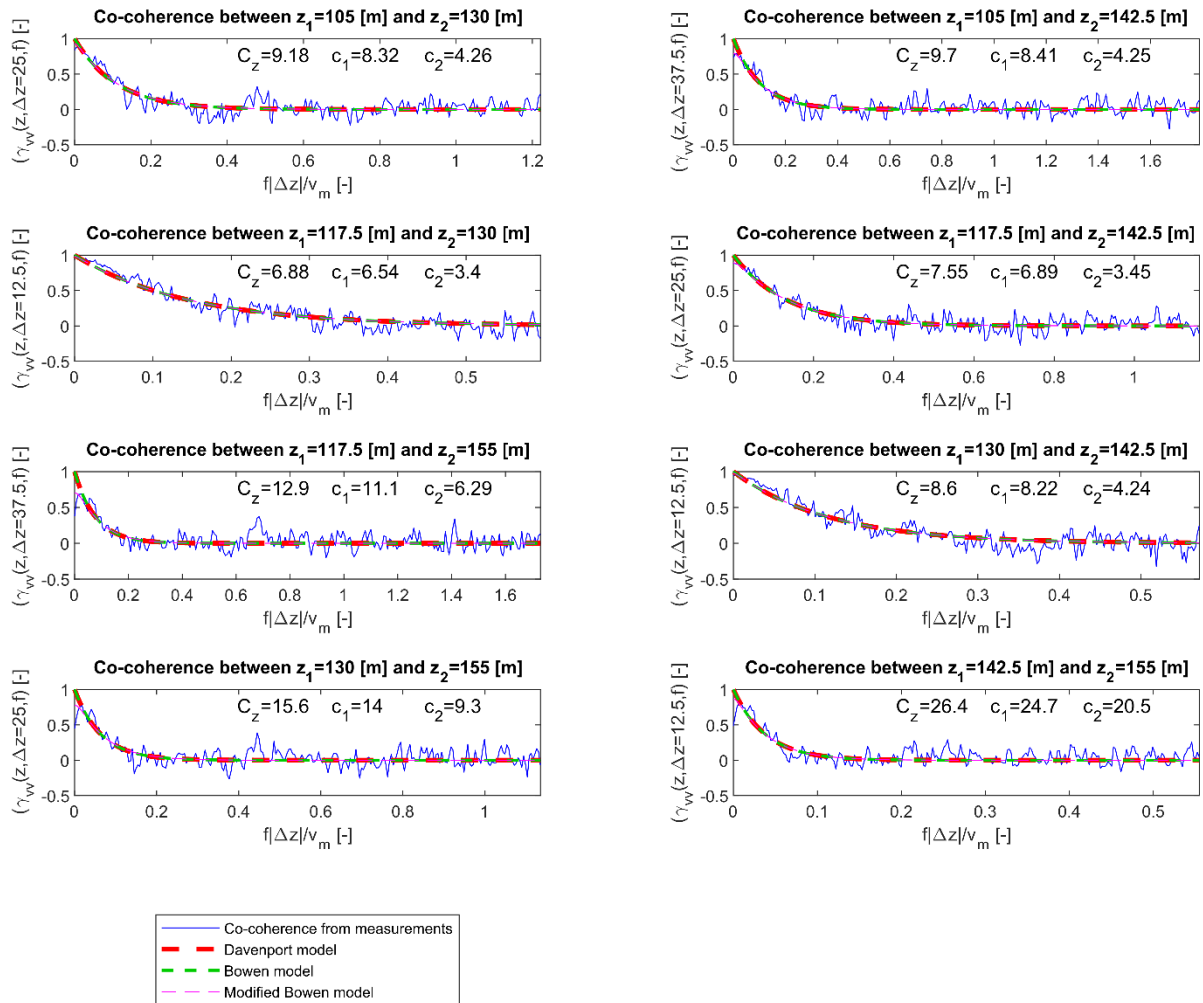

Fig. 8.53. Vertical co-coherence between the points with Δ_z equal to 12.5 m, 25 m and 37.5 m for the Case 2-82, with fit according to the Davenport model, Bowen model and modified Bowen model – plots 23-30

Fig. 8.54 and Fig. 8.55 show the frequency length scales distribution at different vertical distances Δz, taking into account the correlations with the lowest measuring point at 17.5 m (Fig. 8.54) and the correlations with the highest measuring point at 155 m (Fig. 8.55).

In this case, similar to case 2-128, the values reported in relation to the lowest measuring point are higher than the values reported in relation to the highest measuring point, as observed in subsection 7.3 for the cases with spires and barriers. The frequency length scales are, in general, slightly lower than for the test cases with smaller roughness, particularly at the higher distances Δz, ranging between 0.04 Hz and 0.17 Hz for the lowest measuring point and between 0.03 Hz and 0.09 Hz for the highest measuring point. For the relations to both of these points, there is a decreasing trend with the increase of distance Δz between the two considered points. Considering a comparison with the values recommended for design, the relations to the lowest measuring point result in the frequency scale at a distance of about 50 m of 0.08 Hz (resulting in an averaging period T_z^* of about 12.5 s) and at a distance of about 100 m is 0.04 Hz (resulting in an averaging period T_z^* of about 25 s). These values of the period scales are larger than the values recommended by (Cook, 1985, 1990) for buildings

of these heights. This further confirms that the larger roughness results in longer averaging periods and thus reduces the gust values, particularly when considering the larger distances.
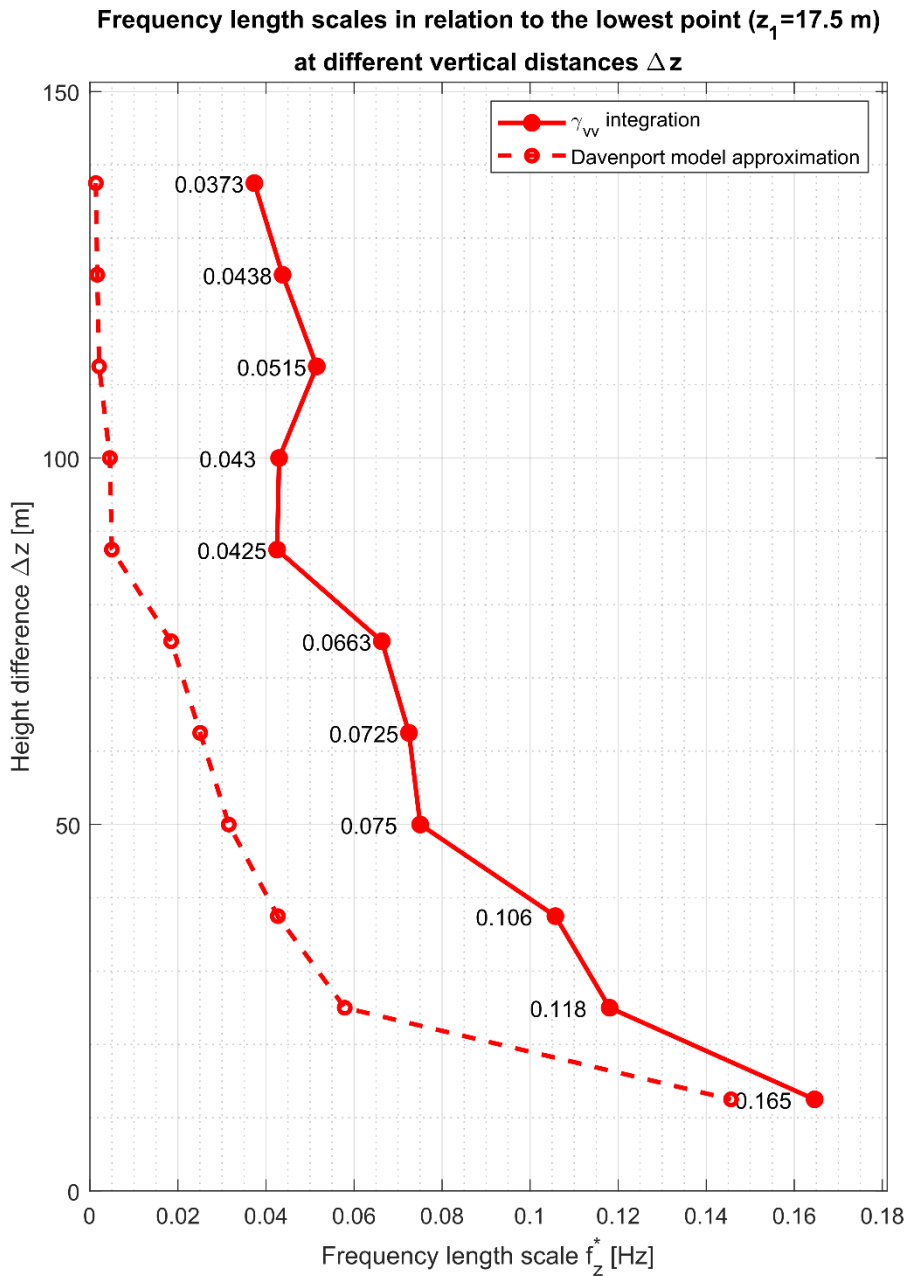
Fig. 8.54. Frequency length scales in relation to the lowest measurement point and different Δ_z values for the Case 2-82

The values estimated based on the Davenport model give a better approximation of the frequency length scales than any of the other 4 test cases analysed before. In particular, this approximation seems decent for the 4 shortest distances Δz in relation to the highest measuring point and for the shortest distance Δz in relation to the lowest measuring point, with values for larger distances Δz decreasing to values close to 0. However, these approximations are still lower than the values directly calculated from the co-coherence and therefore not on the safe side. Similarly to case 3-10, a clear pattern of an exponential decrease with height, in particular for the lowest measuring point, can be observed for these

values, which might be considered a smoothening of the much more chaotic pattern derived from the direct calculations based on the co-coherence function.

Based on the analysis of the frequency length scales and co-coherence functions, the models based on exponential functions (e.g. Davenport model) seem only valid for the smaller distances Δz of about 12.5-37.5 m between the two points, the height above the ground notwithstanding. In the case of such distances, the exponential decay coefficient for the Davenport model is kept at relatively low values between about 6 and 11, which is in general agreement with the values from field measurements (Newberry et al., 1973). However, these models do not provide a correct approximation of the co-coherence function for larger distances Δz, at least in the case of wind tunnel model studies.
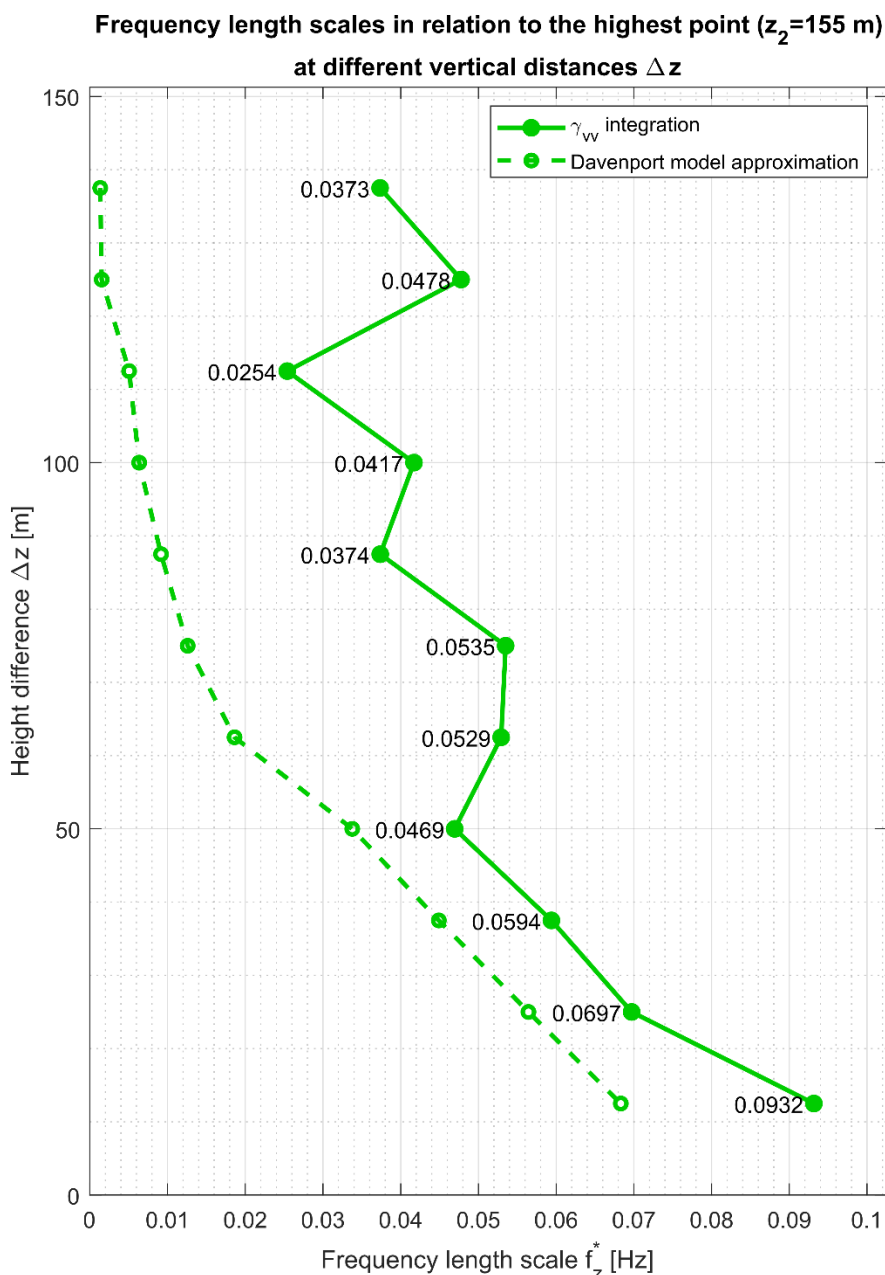

Fig. 8.55. Frequency length scales in relation to the highest measurement point and different Δ_z values for the Case 2-82

9. Conclusions and final remarks

The most significant conclusions of this work are collected in this chapter, together with a concise summary of the more detailed and partial conclusions that were drawn during the analyses in previous chapters. This is divided into three subsections, each one dedicated to different problems undertaken in this work. In subsection 9.1, the conclusions regarding the terrain roughness identification and the proposed extended terrain roughness classification are listed. Subsection 9.2 is focused on the wind tunnel simulations of different types of atmospheric boundary layer depending on the terrain roughness. Subsection 9.3 includes general guidelines, based on the extensive number of analysed test cases, related to selective manipulation of wind flow characteristics through the changes in the configuration of the roughness elements in the wind tunnel. Planned further studies on the subjects investigated in this work are presented in subsection 9.4.

9.1. Conclusions regarding the proposed terrain roughness classification

Thorough research and comparisons were done in chapter 3 on the subject of terrain roughness classifications according to different standards. These comparisons took into account various wind flow characteristics. The conducted literature review led to suggesting an authorial terrain roughness classification that would reflect more roughness parameters, which was done in chapter 4. The main aim of this classification is more precise terrain roughness identification for the purpose of wind tunnel tests. The most significant findings of this part of the work are the following:

1. The comparison of vertical mean wind speed profiles according to different standards shows that it is reasonable to distinguish more different terrain roughness categories related to urban areas, similar to e.g. (ISO 4354, 2009).

2. The roughness analysis of models of real-life areas showed that there can be significant differences in roughness parameters (mean roughness height k_r and standard deviation of the roughness elements σ_r) for areas that would seemingly fit into the same terrain category. This is particularly observable for suburban and urban terrains.

3. Providing a clear definition of the applied measure of terrain roughness for a given terrain category rather than a descriptive one leads to an unequivocal identification of the terrain roughness category for a given area, which is pivotal for wind tunnel tests. Adding another parameter for the terrain roughness description leads to a more complete and precise identification.

4. The proposed terrain roughness classification addresses the most important discrepancies and issues with proper terrain roughness assignment for a real-life area related directly to its roughness characteristics. This was done in a relatively direct and simple way that would be feasible for practical application.

5. It can be expected that the major differences between the extended terrain roughness categories in the introduced classification (i.e. between suburban categories III and IV, and between urban categories V, VI and VII) would be observed in the parameters related to the turbulence rather than directly influencing the mean wind velocity profiles.

6. Introducing greater diversification of suburban and urban terrain roughness categories, this classification is in line with the results of wind tunnel tests. These tests prove that it is easy to obtain various combinations of different wind flow characteristics that are comparable with different aspects of suburban and urban terrain categories according to different standards.

The above conclusions demonstrate that **the first thesis** of the work positioned in chapter 2, which states:

Additional parameters used to describe the terrain roughness can lead to better identification and classification of a real-life area for the purpose of wind tunnel tests.

can be considered proven. The introduction of additional roughness parameters and the proposed terrain roughness classification that followed allowed for a clear distinction between the analysed models of real-life areas. These models evidently exhibit different patterns of urbanisation, nevertheless they would be assigned into a single terrain roughness category in accordance with the most commonly referenced existing standards.

The more detailed conclusions regarding this part of the work are listed below:

- The wind flow description according to the categories provided in the most commonly referenced standards is practically limited to the vertical mean wind speed profile and a simplified description of the turbulence intensity. This may be practical for standard engineering practice, but not sufficient for proper wind tunnel simulation;
- For the wind flow simulation in the wind tunnel, the roughness of the blocks at the fetch length does not scale directly to the roughness in real-life terrain. Therefore, additional turbulence-generating elements are required to artificially achieve wind flow characteristics similar to nature;
- For the three analysed standards (ASCE/SEI 7, 2022; ISO 4354, 2009; PN-EN 1991-1-4, 2011), the vertical wind profiles are very similar for a given terrain category. However, there are differences in the types of categories according to each of these standards;
- Limiting the applicability of the wind profile description to a certain lowest height above the ground level, which depends on the terrain roughness category is a reasonable suggestion, as providing an exact and reliable description of mean wind speed in the region immediately above the ground is impossible;
- There are very significant differences in the turbulence length scales recommended by different standards (ESDU 74031, 1974; ESDU 86035, 2000; PN-EN 1991-1-4, 2011). These differences are not only in the values but also in the proposed models of their vertical change or types of parameters that affect them (e.g. different gradient heights z_g between different terrain roughness categories or taking into account the reference mean wind speed).

9.2. Conclusions of the wind tunnel tests

A total of 295 test cases were investigated in the wind tunnel tests. The cases were varied through different setups of turbulence-generating elements: blocks at the inlet and at the fetch length, spires, barriers and a turbulising net. The measuring setup consisted of 12 Pitot tubes in a vertical arrangement connected to pressure scanners and the adopted model geometrical scale was 1:250. The results were processed to obtain the wind flow characteristics: vertical mean wind speed and turbulence intensity profiles, longitudinal and vertical turbulence length scales, power density spectra, vertical co-coherence and frequency length scales. This provided a complete (vertical) description of the wind flow for the purpose of wind tunnel tests. Based upon these results, an analysis of the influence of different turbulence-generating elements on various wind flow parameters was conducted. Cases that best represent the terrain roughness categories according to different standards were selected and a thorough analysis was done for the cases matching the terrain categories according to (PN-EN 1991-1-4, 2011). The main conclusions regarding the wind tunnel simulations of different types of atmospheric boundary layer are presented below.

1. The three terrain categories which correspond to open flat terrain, suburban terrain and urban terrain can be simulated in the wind tunnel with very satisfactory precision. All of the analysed wind flow characteristics reached values that are in good agreement with the standards. It should be noted that these are the three terrain categories that are most often required for wind tunnel simulations for civil engineering.

2. The terrain categories which correspond to terrain exposed to open sea and terrain near lakes with negligible vegetation can be simulated in the wind tunnel with sufficient accuracy. However, not all of the wind flow characteristics can be simulated with good agreement with the standards.

3. The vertical mean wind speed profile parameters – the α exponent and the roughness length z_0 – should be close to the target parameters from the standards for a given category and are, in general, a good condition for the initial assignment of terrain category. Nevertheless, the RMSE between the target profiles from standards and the profiles obtained in the wind tunnel provide a better measure of vertical mean wind speed profile simulation accuracy.

4. The turbulence intensity vertical profiles are idealised models. In the case of turbulence intensity profiles obtained in a wind tunnel, the parameters determining the shape of the power-law or logarithmic curve are less important as a measure of the turbulence intensity simulation than either the RMSE between the target and simulated profiles or, more broadly, fitting within the approximately ±20% uncertainty bounds.

5. A relation can be observed between the simulated vertical profiles of mean wind speed and turbulence intensity. In general, having an almost exact match of the vertical wind profiles comes at a cost of having too low a turbulence intensity profile, while an accurate simulation of turbulence intensity results in a slight transition of the mean wind speed profile to the left from the model profiles. Therefore, a compromise between these two characteristics has to be found. A Multiple Attribute Decision Making method can be very practical for the evaluation of these parameters and finding the most suitable solution.

6. A decent agreement is met between the longitudinal turbulence length scales in wind tunnel tests and the referenced standard for terrain categories II, III and IV. For terrain categories 0 and I, the values obtained in the wind tunnel are much lower than the values from the standards. This is most likely an effect of the turbulising net physically restricting the maximal size of the eddies generated in the wind flow.

7. While the values of longitudinal turbulence length scales obtained in the model tests for terrain categories II, III and IV are, in general, within the ±30% uncertainty bounds suggested by (ESDU 74031, 1974), it is difficult to recreate the increasing trend of these values with height. This might be caused by the confined working section of the wind tunnel, as opposed to an open flow in nature. Usually, a noticeable increase in these values can be observed at lower heights, with the values at higher altitudes being approximately constant. The increase in this value along the whole analysed height was only recreated, to some degree, in the case of the terrain category IV.

8. Anisotropy of the vertical turbulence length scales (when moving upward or downward) that has been recorded in field measurements is also clearly observable in wind tunnel tests. Furthermore, this also leads to a similar anisotropy of the frequency length scales.

9. The power density spectra are in good agreement with the three models (Davenport, Kármán and Kaimal), especially in the frequency range of about 0.2-1 Hz that is related to high-rise and slender tower-like structures.

10. The theoretical models for the co-coherence function provide a good approximation for smaller vertical distances Δz of about 10-40 m, however, they are incorrect for larger distances between the two considered points. Furthermore, the frequency length scales calculated based on the Davenport model underestimate the frequency length scales, which would result in an underestimation of the peak wind pressure values.

11. The frequency length scales are reproduced in the wind tunnel tests with excellent agreement with literature sources for the terrain categories II, III and IV. This means that they can be practical for a more refined model of wind actions on buildings (e.g. interpolation for different sizes of analysed elements).

12. The TOPSIS method applied for the selection of the cases that best match the standards proved to be very useful for this purpose and facilitated a robust evaluation and selection.

The above conclusions demonstrate that **the second thesis** of the work positioned in chapter 2, which states:

It is possible to evaluate the effect of different roughness elements, such as elevated blocks, spires or barriers, on different wind flow characteristics. This approach can lead to more accurate boundary layer simulation in wind tunnel tests.

can be considered proven. The investigation and subsequent analysis of a large number of different configurations of roughness elements led to a selection of representative cases that result in an excellent or very good recreation of real-life wind flow characteristics in wind tunnel tests. Furthermore, the obtained data was used to elaborate guidelines (in subsection

9.3) on more accurate simulations of these characteristics based on how they are influenced by different turbulence-generating elements.

A summary of the more detailed findings of the analysis is the following:

- Wind tunnel setups with a turbulising net are better for simulations of the lower terrain categories (0 and I), while setups with spires and barriers are more suitable for the simulation of higher terrain categories (II, III and IV);
- Setups with a turbulising net result, in general, in more chaotic patterns of certain wind flow characteristics (autocorrelation time scales, frequency length scales along the height distribution) than the setups with spires and barriers;
- Based on the analysis of the goodness of fit parameters for the power-law and logarithmic wind profiles, it can be stated that both of these models are very suitable for the description of the values measured in the wind tunnel. However, the goodness of fit parameters for the turbulence intensity are usually lower, yet still provide a satisfactory fit;
- Presence of barriers may lead to local larger discrepancies in the measured values of mean wind speed and turbulence intensity in the region close to the ground. However, this does not always result in a detrimental effect on the vertical profiles fitted to these values;
- The anisotropy of the frequency length scales is different depending on the wind tunnel setup. When spires and barriers are present, the frequency length scales assume larger values in relation to the lowest measuring point. In the cases without any barrier or spires and with low elevations of the blocks, larger values of the frequency length scales are related to the highest measuring point;
- Small peaks are appearing in some of the obtained power density spectra at a frequency of about 0.4 Hz in a real-life scale, however, this is a phenomenon that has also been observed in field tests. The Kolmogorov inertial subrange can be clearly identified for the higher frequency ranges in the analysed test cases, in particular for the terrain categories II, III and IV;
- Experimental setups with a turbulising net result in more dispersed results of the power density spectra than the setups utilising spires and barriers. Moreover, the Welch method results in much less dispersed values of power density spectra around the trend than the direct calculation from FFT.

9.3.   Proposed guideline for wind tunnel simulations of boundary layers

This subsection is intended as a sort of best practice guideline, strongly based on the detailed analysis (particularly conducted in chapters 7 and 8), that would be practical for more effective wind tunnel simulations of different types of atmospheric boundary layer. Although based on the tests performed in a single wind tunnel, the instructions are formulated in a more general way, so that they could be applied (at least to a limited degree) in most similar boundary layer wind tunnels.

While intended for a simulation of the wind flow in nature, the air stream in a wind tunnel is confined by the dimensions of the working section, therefore it may act differently. This and the limited upwind fetch length are the main reasons why the roughness elements cannot be

directly transitioned/scaled from nature and instead, additional turbulence-generating elements and techniques are required for the simulation, whether the tests concern model or 1:1 scale. This is a fundamental principle of wind tunnel testing. Below are detailed steps and techniques that can be applied to achieve the desired wind flow structure in a wind tunnel.

1. Selection of the scales of the model tests, starting with the geometrical scale, should always be the first step of the wind tunnel setup preparation. Besides the restrictions regarding this selection mentioned in chapter 5, related to the blockage ratio and a compromise of recreating sufficient details in the model and sufficiently large surroundings around it, some tests may require taking into account additional conditions for scaling. The analysis of the investigated test cases showed that the longitudinal turbulence length scales are physically restricted by the size of the wind tunnel cross-section and, in particular cases, by the grid size of a turbulising net. This has to be addressed in the tests where these characteristics may have a particularly strong impact on the results (e.g. wind turbine tests).

2. As a general rule it can be stated that the turbulising nets are more appropriate for simulation of the lower terrain categories (corresponding to terrains exposed to open sea, lakes or with negligible vegetation), while the higher terrain categories (corresponding to open flat terrain, suburban terrain and urban terrain) are better simulated with setups of barriers and spires.

3. The distinction between the blocks at the inlet and at the fetch length is reasonable for experimental purposes. The blocks at the inlet have a smaller influence on the wind flow characteristics, however, they are important for roughness generation in the cases of lower terrain categories, where the blocks along the fetch length would result in too large roughness. On the other hand, the blocks along the fetch length are necessary for the higher terrain roughness categories (suburban and urban terrains). Furthermore, it seems that elevating the blocks at the fetch length above 5-10 cm does not result in satisfactory simulations. On the other hand, blocks at the inlet may be raised higher, as they act similarly to a barrier.

4. Based on the extensive analysis conducted in chapter 7, it can be stated that the influence of different turbulence-generating elements and combinations thereof on various wind flow characteristics – in particular, the ones related to vertical mean wind speed and turbulence intensity profiles – is largely non-linear. Therefore, in most cases, there should exist a way to modify the values of one parameter with little impact on the other ones. This can be useful for the precise calibration of the wind tunnel setup.

5. Both the α exponent and the roughness length z_0 show an increasing trend with the increase in the elevation of the blocks along the fetch length. However, in the case of the α exponent, this trend seems to be more linear, while for z_0, the trend is closer to an exponential curve. Furthermore, it seems that the impact of the blocks at the fetch length on the values of these parameters is larger in the setups with lower spires.

6. The β exponent shows a highly non-linear trend with different values of the elevation of the blocks at the fetch length. Furthermore, this value is largely influenced by the presence of a barrier, reaching very high (absolute) values in cases without any barrier. It can be stated that a barrier is necessary to properly recreate the value of this

parameter. The turbulence intensity level at the height of 30 m shows a similar trend to the α exponent and the values of these two characteristics are usually closest together in the cases with the low elevation of the blocks at the fetch length of about 0-5 cm. Furthermore, the presence of a barrier in the setup largely influences this value (increasing with the barrier present and reaching the highest values in the cases with a rectangular barrier).

7. The longitudinal turbulence length scale trends which are similar to nature (increase with height along the whole boundary layer thickness) are difficult to recreate in wind tunnel tests. In general, an increase can be easily identified in the near-ground region, then its value reaches an almost constant level. According to the tests results, this increase along the whole length of the wind tunnel is better recreated when using the high spires mounted backwards (with the full face of the pyramid turned in the upwind direction) and a barrier. However, it should be noted that the setups with the spires mounted backwards seem to deteriorate the accuracy of recreation of the other wind flow characteristics.

8. The influence of the height of the spires on longitudinal and vertical turbulence length scales is very little (when comparing the same setups of barriers and blocks), therefore it can be said that the spires can be easily reconfigured when calibrating for the other wind flow characteristics without much effect on the turbulence length scales.

9. The ratios of vertical turbulence length scales (when moving downward) to the longitudinal turbulence length scales similar to the literature (of about 0.2) seem easiest to obtain in the setups without any barriers and either without any spires or with the lowest tested spires (comp. Tab. 7.1-Tab. 7.3).

10. There seems to be little impact of the exact type of roughness elements used (e.g. height of the spires, type of barrier, the elevation of the blocks) on the wind flow characteristics in the frequency domain: power density spectra and coherence. The effect of wind tunnel setup on these parameters seems to mostly stem from the general type of elements used (different results between the cases with turbulising net compared to the cases with spires and barrier).

11. The setups using spires and barrier result in more reliable (with a better agreement to the literature) values of frequency length scales compared to the setups with a turbulising net.

12. There is a strong influence of the elevation of the blocks at the fetch length on the obtained values of the frequency length scales, which impacts the results more than the barrier type used in most cases.

13. The provided *MATLAB* subroutine for wind tunnel test processing to obtain main wind flow characteristics may be used as a flexible and robust tool for wind tunnel calibration. With the way the code is prepared, it should be easy to modify and implement for different wind tunnels, different requirements considering the desired wind flow parameters and/or different types of experimental setup (e.g. a different number of measurement points).

As a final note to these guidelines, it should be kept in mind that it is not always possible to correctly simulate all of the wind flow characteristics at the same time – however, it is also

not always necessary for a given wind tunnel study to simulate all of these characteristics. Therefore, a compromise is usually necessary, based on an identification of which characteristics of the wind flow are mandatory to be properly simulated for the target wind tunnel tests and which ones are of secondary importance and may be simulated with less accuracy.

9.4.   Potential future studies on the subject

This thesis constitutes a solid basis for further research work on a variety of topics, which are within different fields of wind engineering: field measurements, experimental wind tunnel tests and theoretical studies. Possible applications of the findings of this study and the planned development of the ideas conceived within this work are presented below.

The terrain roughness classification proposed in this work was based on literature analysis and detailed identification of models of parts of real-life suburban and urban areas. However, this classification has to be validated through field measurements, which would allow for the proper determination of various wind flow characteristics associated with different proposed categories. Recently, such measurements are more available even in urban areas with remote sensing techniques, such as LIDAR (Light Detection and Ranging) measurements (Ricciardelli et al., 2019; Sepe et al., 2018, 2022). Moreover, the timing to further pursue this idea is good, due to the planned major changes in the European standards concerning wind action on buildings (Hansen et al., 2018). This change is mostly aimed at the unification of the methodology and guidelines between different countries in lieu of the current trend of national annexes impacting most of the standard procedures.

Furthermore, the identification of model roughness parameters could be done on a larger scale. This can be done by utilising the data in e.g. cloud format that is used to produce detailed height maps over large areas based on e.g. multispectral imagery and laser altimeter data (Haala & Brenner, 1999) or LIDAR measurements (Zhao et al., 2019). Furthermore, recent techniques of automation of the model creation for computational fluid dynamics (CFD) simulations, like open-source City4CFD software (Pađen et al., 2022a, 2022b) could be used to simplify the model for the calculation of roughness parameters, which would be necessary on large and complex terrains for computational feasibility. This approach would also allow taking into account the effect of fetch length on the classification, as using a larger domain would lead to a better understanding of the extent of areas with given roughness parameters. This is especially important in the cases of the proper distinction between the three proposed urban terrain categories.

As for the further application of the proposed testing techniques for wind tunnel tests (along with the guidelines formulated in subsection 9.3), the flexibility of the prepared *MATLAB* subroutine allows for its application to more complex experimental setups by adding new segments to the code, e.g. including testing the lateral uniformity of the flow (Kłaput, 2020) and introducing the calculation of lateral turbulence length scales. This subroutine is planned for regular use as a tool for model tests preparation in the wind tunnel of the Wind Engineering Laboratory of the Cracow University of Technology. Moreover, it is planned to apply it as one of the main devices for the initial identification of the flow characteristics in the wind tunnels of the Laboratory of Environmental Aerodynamics of the Cracow University of Technology (Pistol et al., 2022), which is currently in the final stages of development. Such

initial tests will be one of the crucial parts in the launch of this new laboratory (which will house two large wind tunnels with a total of four working sections dedicated to different types of investigations), as they will support the proper calibration of the equipment, such as guide vanes, beehive frames and different types of roughness elements to obtain the desired wind flow structure.

The findings of this dissertation could also be further elaborated in theoretical studies focusing on wind action on tall buildings, to develop more refined models firmly based on scientific evidence. These models could use the measured and calculated values of frequency length scales for a given building to determine the averaging period, similar to the models proposed by (Cook, 1985, 1990; Newberry et al., 1973), but also incorporate the spatial averaging methods (Pistol et al., 2020) and combine the two approaches.

10. Literature

10.1. Books, journal publications and conference proceedings

Abramson, J., & Rogers, E. O. (1983). High-speed characteristics of circulation control airfoils. *AIAA Paper*. https://doi.org/10.2514/6.1983-265

Armitt, J., & Counihan, J. (1968). The simulation of the atmospheric boundary layer in a wind tunnel. *Atmospheric Environment*, 2(1), 49–71. https://doi.org/10.1016/0004-6981(68)90019-X

Aufderheide, T., Bode, C., Friedrichs, J., & Kožulović, D. (2014). The Generation of Higher Levels of Turbulence in a Low-Speed Cascade Wind Tunnel by Pressurized Tubes. 11*th World Congress on Computational Mechanics (WCCM XI)*.

Bienkiewicz, B., Cermak, J. E., Peterka, J. A., & Scanlan, R. H. (1983). Active modeling of large-scale turbulence. *Journal of Wind Engineering and Industrial Aerodynamics*, 13(1–3), 465–475. https://doi.org/10.1016/0167-6105(83)90165-4

Bowen, A. J., Flay, R. G. J., & Panofsky, H. A. (1983). Vertical coherence and phase delay between wind components in strong winds below 20 m. *Boundary-Layer Meteorology*, 26(4), 313–324. https://doi.org/10.1007/BF00119530/METRICS

Buckingham, E. (1915). The Principle of Similitude. *Nature*, 96(2406), 396–397. https://doi.org/10.1038/096396D0

Calautit, J. K., Chaudhry, H. N., Hughes, B. R., & Sim, L. F. (2014). A validated design methodology for a closed-loop subsonic wind tunnel. *Journal of Wind Engineering and Industrial Aerodynamics*, 125, 180–194. https://doi.org/10.1016/J.JWEIA.2013.12.010

Cermak, J. E. (2003). Wind-tunnel development and trends in applications to civil engineering. *Journal of Wind Engineering and Industrial Aerodynamics*, 91(3), 355–370. https://doi.org/10.1016/S0167-6105(02)00396-3

Chakraborty, S. (2022). TOPSIS and Modified TOPSIS: A comparative analysis. *Decision Analytics Journal*, 2, 100021. https://doi.org/10.1016/J.DAJOUR.2021.100021

Cheynet, E. (2018). Influence of the Measurement Height on the Vertical Coherence of Natural Wind. *Conference of the Italian Association for Wind Engineering*, 27, 207–221. https://doi.org/10.1007/978-3-030-12815-9_17

Choi, C.-K., & Kwon, D.-K. (1998). Wind tunnel blockage effects on aerodynamic behavior of bluff body. *Wind and Structures*, 1(4). https://doi.org/10.12989/was.1998.1.4.351

Cook, N. J. (1985). *The Designer's Guide to Wind Loading of Building Structures. Part I. Background, Damage, Survey, Wind Data and Structural Classification*. Building Research Establishment Report, Butterworths.

Cook, N. J. (1990). *The Designer's Guide to Wind Loading of Building Structures. Part II. Static Structures*. Building Research Establishment Report, Butterworths.

Davenport, A. G. (1960). Rationale for Determining Design Wind Velocities. *Journal of the Structural Division*, 86.

Davenport, A. G. (1961). The spectrum of horizontal gustiness near the ground in high winds. *Quarterly Journal of the Royal Meteorological Society*, 87(372), 194–211. https://doi.org/10.1002/qj.49708737208

Davenport, A. G. (1962). The response of slender, line-like structures to a gusty wind.

Proceedings of the Institution of Civil Engineers 23.3, 389–408.

Davenport, A. G. (1967). Gust Loading Factors. *Journal of the Structural Division*, 93(3), 11–34. https://doi.org/10.1061/JSDEAG.0001692

Davenport, A. G. (1984). The Response of Chimneys to Wind. *Proceedings of the 5th International Chimney Congress*, 77–85.

Duchêne-Marullaz, P. (1977). Full-scale Measurements of Atmospheric Turbulence in a Suburban Area. *International Conference on Wind Effects on Buildings and Structures*, 23–33.

Durst, C. S. (1960). Wind Speed Over Short Period of Time. *Meteorological Magazine*, 89.

Flaga, A. (2008). *Wind engineering. Fundamentals and applications*. Arkady [in Polish].

Flaga, A. (2022). *Horizontal flows above a flat contact surface with different turbulence (technical report)* [in Polish].

Flaga, A., Błazik-Borowa, E., & Podgórski, J. (2004). *Aerodynamics of slender buildings and bar-cable structures*. Wydawnictwo Politechniki Lubelskiej [in Polish].

Flaga, A., Pistol, A., Krajewski, P., & Flaga, Ł. (2020). Aerodynamic and aeroelastic wind tunnel model tests of overhead power lines in triangular configuration under different icing conditions. *Cold Regions Science and Technology*, 170(February 2020), 102919. https://doi.org/10.1016/j.coldregions.2019.102919

Flaga, Ł., Pistol, A., Kłaput, R., & Flaga, A. (2022). Wind load analysis for tall building in different development scenarios. *8th European-African Conference on Wind Engineering (8EACWE)*, 499–502.

Fossati, F., Muggiasca, S., Viola, I. M., & Zasso, A. (2006). Wind Tunnel Techniques for Investigation and Optimization of Sailing Yachts Aerodynamics. *2nd High Performance Yacht Design Conference*, 105–113.

Franco, I., Gutiérrez, A., & Cataldo, J. (2022). Row of jets in cross-flow as wind barrier. *Journal of Wind Engineering and Industrial Aerodynamics*, 223, 104937. https://doi.org/10.1016/J.JWEIA.2022.104937

Glanville, M. J., & Kwok, K. C. S. (1997). Further investigation of the blockage-tolerant wind tunnel technique. *Journal of Wind Engineering and Industrial Aerodynamics*, 69–71, 987–995. https://doi.org/10.1016/S0167-6105(97)00222-5

Haala, N., & Brenner, C. (1999). Extraction of buildings and trees in urban environments. *ISPRS Journal of Photogrammetry and Remote Sensing*, 54(2–3), 130–137. https://doi.org/10.1016/S0924-2716(99)00010-6

Hansen, S. O., Höffer, R., Rees, J., Ricciardelli, F., & Spehl, P. (2018). Towards the second generation Eurocodes: evolution of EN 1991-1-4 Wind actions. *XV Conference of the Italian Association for Wind Engineering – IN-VENTO* 2018.

Harris, R. I. (1970). The Nature of the Wind. *CIRIA Seminar on Modern Design of the Wind-Sensitive Structures*.

Hui, M. C. H., Larsen, A., & Xiang, H. F. (2009). Wind turbulence characteristics study at the Stonecutters Bridge site: Part I-Mean wind and turbulence intensities. *Journal of Wind Engineering and Industrial Aerodynamics*, 97(1), 22–36. https://doi.org/10.1016/j.jweia.2008.11.002

Iwano, M., & Einstein, H. H. (1993). Stochastic Analysis of Surface Roughness, Aperture

And Flow In a Single Fracture. *ISRM International Symposium - EUROCK* 93. /ISRMEUROCK/proceedings-abstract/EUROCK93/All-EUROCK93/44831

Kaimal, J. C., Wyngaard, J. C., Izumi, Y., & Coté, O. R. (1972). Spectral characteristics of surface-layer turbulence. *Quarterly Journal of the Royal Meteorological Society*, 98(417), 563–589. https://doi.org/10.1002/qj.49709841707

Karman, T. de, & Howarth, L. (1938). On the Statistical Theory of Isotropic Turbulence. *Proceedings of the Royal Society of London. Series A – Mathematical and Physical Sciences*, 164(917), 192–215. https://doi.org/10.1098/RSPA.1938.0013

Kim, S., Alinejad, N., Jung, S., & Fernández-Cabán, P. L. (2022). Comparison of the effective roughness length between field measurements and wind tunnel testing. 8*th European-African Conference on Wind Engineering (8EACWE)*, 7–10.

Kłaput, R. (2020). *Impact of the gaps width in the side walls of the wind tunnel on the results of model tests*. Cracow University of Technology [in Polish].

Kłaput, R., Flaga, A., Pistol, A., Kocoń, A., Rizzo, F., & Flaga, Ł. (2022). Wind pressure distribution on hyperbolic-paraboloid shaped roof of an art gallery. 8*th European-African Conference on Wind Engineering (8EACWE)*, 419–422.

Kłaput, R., Kiesiewicz, B., & Flaga, A. (2021). Measurement error assessment in mean wind pressure measurements at different terrain roughess using pressure scanners. In Wind Effects on Buildings and People [in Polish].

Kolmogorov, A. N. (1941). The local structure of turbulence in incompressible viscous fluid for very large Reynolds numbers. *Proceedings of Academy of Sciences of the USSR*, 30, 299–303.

Kozmar, H. (2008). Influence of spacing between buildings on wind characteristics above rural and suburban areas. *Wind and Structures, An International Journal*, 11(5), 413–426. https://doi.org/10.12989/was.2008.11.5.413

Kozmar, H. (2011a). An alternative approach to experimental simulation of wind characteristics in urban environments. *Procedia Environmental Sciences*, 4, 43–50. https://doi.org/10.1016/j.proenv.2011.03.006

Kozmar, H. (2011b). Characteristics of natural wind simulations in the TUM boundary layer wind tunnel. *Theoretical and Applied Climatology*, 106(1–2), 95–104. https://doi.org/10.1007/s00704-011-0417-9

Kozmar, H. (2011c). Wind-tunnel simulations of the suburban ABL and comparison with international standards. *Wind and Structures, An International Journal*, 14(1), 15–34. https://doi.org/10.12989/was.2011.14.1.015

Kozmar, H., & Laschka, B. (2019). Wind-tunnel modeling of wind loads on structures using truncated vortex generators. *Journal of Fluids and Structures*, 87, 334–353. https://doi.org/10.1016/J.JFLUIDSTRUCTS.2019.03.007

Kuznetsov, S., Ribičić, M., Pospíšil, S., Plut, M., Trush, A., & Kozmar, H. (2017). Flow and turbulence control in a boundary layer wind tunnel using passive hardware devices. *Experimental Techniques*, 41(6), 643–661. https://doi.org/10.1007/S40799-017-0196-Z/FIGURES/36

Lanaro, F. (2000). A random field model for surface roughness and aperture of rock fractures. *International Journal of Rock Mechanics and Mining Sciences*, 37(8), 1195–1210. https://doi.org/10.1016/S1365-1609(00)00052-6

Lawson, T. V. (1980). *Wind Effects on Buildings*. Applied Science Publishers LTD.

Lettau, H. (1969). Note on aerodynamic roughness element description. *Journal of Applied Meteorology*, 8, 828–832.

Lim, H. C., Castro, I. P., & Hoxey, R. P. (2007). Bluff bodies in deep turbulent boundary layers: Reynolds-number issues. *Journal of Fluid Mechanics*, 571, 97–118. https://doi.org/10.1017/S0022112006003223

Mackey, S., Chuen, E. C. C., & Lam, R. (1970). Gust Factors. *Proceedings of the Seminar: Wind Loads on Structures*.

Mackey, S., & Pius, K. (1977). Spatial Configuration of Gusts. *International Conference on Wind Effects on Buildings and Structures*.

Müller, F. P., & Nieser, H. (1975). Measurements of wind-induced vibrations on a concrete chimney. *Journal of Wind Engineering and Industrial Aerodynamics*, 1, 239–248. https://doi.org/10.1016/0167-6105(75)90019-7

Newberry, C. W., Eaton, K. J., & Mayne, J. R. (1973). Wind Loading on Tall Buildings - Further Results from Royex House. *Industrial Aerodynamics Abstracts*, 4(4).

Nutt, J. G. (1963). The Wind Pressures on Buildings and Towers. *Civil Engineering and Public Works Review*, 58, 330–332.

Pađen, I., García-Sánchez, C., & Ledoux, H. (2022a). City4CFD: an open-source framework for automatic reconstruction of simulation-ready 3D city models. *XVII Conference of the Italian Association for Wind Engineering – IN-VENTO* 2022, 142–144.

Pađen, I., García-Sánchez, C., & Ledoux, H. (2022b). Towards automatic reconstruction of 3D city models tailored for urban flow simulations. *Frontiers in Built Environment*, 8, 141. https://doi.org/10.3389/FBUIL.2022.899332/BIBTEX

Perret, L., Basley, J., Mathis, R., & Piquet, T. (2019). The Atmospheric Boundary Layer Over Urban-Like Terrain: Influence of the Plan Density on Roughness Sublayer Dynamics. *Boundary-Layer Meteorology*, 170(2), 205–234. https://doi.org/10.1007/S10546-018-0396-9/FIGURES/14

Pistol, A., Flaga, Ł., Kłaput, R., Polak, M., Kocoń, A., Rizzo, F., & Flaga, A. (2022). The new Laboratory of Environmental Aerodynamics of Cracow University of Technology. *XVII Conference of the Italian Association for Wind Engineering – IN-VENTO* 2022, 133–134.

Pistol, A., Flaga, Ł., Kłaput, R., Rizzo, F., & Flaga, A. (2022). Wind-induced vibrational comfort assessment for complex-shaped tall building. 8*th European-African Conference on Wind Engineering (8EACWE)*, 271–274.

Pistol, A., Kiesiewicz, B., & Flaga, A. (2020). Spatial averaging approach for determining wind pressures and forces on high-rise building. *Advances in Fluid Mechanics XIII*, 151–162.

Ricciardelli, F., Pirozzi, S., Mandara, A., & Avossa, A. M. (2019). Accuracy of mean wind climate predicted from historical data through wind LIDAR measurements. *Engineering Structures*, 201, 109771. https://doi.org/10.1016/J.ENGSTRUCT.2019.109771

Rizzo, F., Pistol, A., Flaga, Ł., Kłaput, R., Polak, M., & Flaga, A. (2022). Wind-induced displacements on hyperbolic paraboloid cable net. 8*th European-African Conference on Wind Engineering (8EACWE)*, 259–263.

Sanz-Andres, A., & Cuerva, A. (2006). Pedestrian wind comfort: Feasibility study of criteria homogenisation. *Journal of Wind Engineering and Industrial Aerodynamics*. https://doi.org/10.1016/j.jweia.2006.06.004

Scruton, C., & Rogers, E. O. (1971). Steady and unsteady wind loading of buildings and structures. *Philosophical Transactions of the Royal Society of London. Series A, Mathematical and Physical Sciences*, 269(1199), 353–379. https://doi.org/10.1098/RSTA.1971.0038

Sepe, V., Avossa, A. M., Rizzo, F., & Ricciardelli, F. (2022). Can Wind Lidars be used to calibrate mean wind profiles? *XVII Conference of the Italian Association for Wind Engineering – IN-VENTO* 2022, 159–160.

Sepe, V., Rizzo, F., Ricciardelli, F., & Avossa, A. M. (2018). Characterization of mean wind profiles and surface roughness assessment from wind LIDAR measurements. *XV Conference of the Italian Association for Wind Engineering – IN-VENTO* 2018.

Sfintesco, D., & Wyatt, T. A. (1977). A Proposed European Code of Practice: Current Work of the ECCS Towards Specification of the Effect of Wind on Structures. *International Conference on Wind Effects on Buildings and Structures*, 643–655.

Shiotani, M., & Iwatani, Y. (1971). Correlations of the Wind Velocities in Relation to the Gust Loadings. *International Conference on Wind Effects on Buildings and Structures*, 57–67.

Siktar, J. M. (2019). Recasting the Proof of Parseval's Identity. *Classical Analysis and ODEs*, 3, 1–10.

Simiu, E. (1974). Wind Spectra and Dynamic Alongwind Response. *Journal of the Structural Division*, 100(9), 1897–1910. https://doi.org/10.1061/JSDEAG.0003880

Simiu, E., & Miyata, T. (2006). *Design of Buildings and Bridges for Wind*. John Wiley & Sons, Inc.

Simiu, E., & Scanlan, R. H. (1986). *Wind Effects on Structures. An Introduction to Wind Engineering*. John Wiley&Sons.

Simiu, E., & Scanlan, R. H. (1996). *Wind effects on structures: fundamentals and applications to design*. John Wiley.

Solari, G. (1987). Turbulence Modeling for Gust Loading. *Journal of Structural Engineering*, 113(7), 1550–1569. https://doi.org/10.1061/(ASCE)0733-9445(1987)113:7(1550)

Takeda, K., & Kato, M. (1992). Wind tunnel blockage effects on drag coefficient and wind-induced vibration. *Journal of Wind Engineering and Industrial Aerodynamics*, 42(1–3), 897–908. https://doi.org/10.1016/0167-6105(92)90096-S

Tamura, Y., Iwatani, Y., Hibi, K., Suda, K., Nakamura, O., Maruyama, T., & Ishibashi, R. (2007). Profiles of mean wind speeds and vertical turbulence intensities measured at seashore and two inland sites using Doppler sodars. *Journal of Wind Engineering and Industrial Aerodynamics*, 95(6), 411–427. https://doi.org/10.1016/J.JWEIA.2006.08.005

Teunissen, H. W. (1980). Structure of mean winds and turbulence in the planetary boundary layer over rural terrain. *Boundary-Layer Meteorology*, 19(2), 187–221. https://doi.org/10.1007/BF00117220

Vita, G., Hemida, H., Andrianne, T., & Baniotopoulos, C. C. (2018). Generating atmospheric turbulence using passive grids in an expansion test section of a wind tunnel. *Journal of Wind Engineering and Industrial Aerodynamics*, 178, 91–104.

https://doi.org/10.1016/J.JWEIA.2018.02.007

Wieringa, J. (1992). Updating the Davenport roughness classification. *Journal of Wind Engineering and Industrial Aerodynamics*, 41(1–3), 357–368. https://doi.org/10.1016/0167-6105(92)90434-C

Wittmann, F. H., & Schneider, F. X. (1974). Wind and Vibrations Measurements at the Munich Television Tower. *Proceedings of the Symposium on Full Scale Measurements of Wind Effects on Tall Buildings and Other Structures*.

Yu, J., Li, M., Stathopoulos, T., Zhou, Q., & Yu, X. (2021). Urban exposure upstream fetch and its influence on the formulation of wind load provisions. *Building and Environment*, 203. https://doi.org/10.1016/j.buildenv.2021.108072

Zhao, R., Pang, M., Liu, C., & Zhang, Y. (2019). Robust Normal Estimation for 3D LiDAR Point Clouds in Urban Environments. *Sensors* 2019*, Vol. 19*, *Page* 1248, 19(5), 1248. https://doi.org/10.3390/S19051248

Żurański, J. A. (1978). *Wind Loads on Buildings and Structures*. Arkady [in Polish].

10.2. Codes and standards

ASCE/SEI 7. (2022). *Minimum Design Loads and Associated Criteria for Buildings and Other Structures*. American Society of Civil Engineers – Structural Engineering Institute.

BS NA EN 1991-1-4. (2010). *UK National Annex to Eurocode 1. Actions on structures. General actions. Wind actions*. BSi British Standards.

ESDU 74031. (1974). *Characteristics of atmospheric turbulence near the ground, Part II: Single point data for strong winds (neutral atmosphere)*. Engineering Sciences Data Unit.

ESDU 80025. (2019). *Mean forces, pressures and flow field velocities for circular cylindrical structures: single cylinder with two-dimensional flow*. Engineering Sciences Data Unit.

ESDU 82026. (2003). *Strong winds in the atmospheric boundary layer. Part* 1*: hourly-mean wind speeds*. Engineering Sciences Data Unit.

ESDU 84015. (2012). *Cylinder groups: mean forces on pairs of long circular cylinders*. Engineering Sciences Data Unit.

ESDU 85020. (2002). *Characteristics of atmospheric turbulence near the ground. Part II: single point data for strong winds (neutral atmosphere)*. Engineering Sciences Data Unit.

ESDU 86035. (2000). *Integral length scales of turbulence over flat terrain with roughness changes*. Engineering Sciences Data Unit.

ISO 2533. (1975). *Standard Atmosphere*. International Organization for Standardization.

ISO 4354. (2009). *Wind actions on structures*. International Organization for Standardization.

PN-77/B-02011. (1977). *Polish Code. Loads in static calculations. Wind load*. Polish Committee for Normalisation and Measures [in Polish].

PN-EN 1991-1-4. (2011). *Actions on Structures. Part 1-4. General Actions. Wind Actions* (Vol. 2, Issue 2005). European Committee for Standardization [in Polish].

RWDI. (2019). *Wind Microclimate Guidelines for Developments in the City of London*.

10.3. Websites and manuals

Lish, T. (2016). *What is Total Error Band & How do You Calculate It?* Setra. https://www.setra.com/blog/what-is-total-error-band-and-how-do-you-calculate-it [date accessed: 2022-05-16].

MATLAB Help Center. (2022a). *Coefficient of Determination (R-Squared)*. Available online: https://www.mathworks.com/help/stats/coefficient-of-determination-r-squared.html [date accessed: 2022-05-20].

MATLAB Help Center. (2022b). *Curve Fitter*. Available online: https://www.mathworks.com/help/curvefit/curvefitter-app.html [date accessed: 2022-05-20].

MATLAB Help Center. (2022c). *Using Filter Designer*. Available online: https://www.mathworks.com/help/dsp/ug/using-filter-designer.html [date accessed: 2022-05-20].

MATLAB Help Center. (2022d). *Welch's power spectral density estimate*. Available online: https://uk.mathworks.com/help/signal/ref/pwelch.html [date accessed: 2022-05-20].

Moravej, M. (2019). *Power Spectral Density using PWELCH vs PSD created by FFT*. MATLAB Central File Exchange. Available online: https://uk.mathworks.com/matlabcentral/fileexchange/70302-power-spectral-density-using-pwelch-vs-psd-created-by-fft [date accessed: 2022-05-20].

SimScale. (2022a). *Advanced Modelling PWC*. Available online: https://www.simscale.com/docs/analysis-types/pedestrian-wind-comfort-analysis/advanced-modelling/ [date accessed: 2022-09-10].

SimScale. (2022b). *Compressible Fluid Flow Analysis*. Available online: https://www.simscale.com/docs/analysis-types/compressible-fluid-flow-analysis/ [date accessed: 2022-09-10].

TE Connectivity. (2017). *DTC INITIUM Pressure Scanning Data Acquisition System*.

TE Connectivity. (2021). *Miniature Electronic Pressure Scanners ESP-16HD/32HD/64HD*.

11. List of attachments

1) **Windflow.m** – authorial *MATLAB* subroutine applied to check the validity of the data, convert the measurement data into velocity time series, calculate the mean wind speed and turbulence intensity profiles, fit the most appropriate power-law and logarithmic curves to vertical profiles, assign the tested case to a category that is best matched, calculate and plot autocorrelation at each point, vertical spatial correlation, longitudinal and vertical turbulence length scales, power density spectra, coherence functions and frequency length scales then save the results in an *Excel* spreadsheet and the figures in a PDF document. Note: some of the functions (saving the figures to a PDF document) require a relatively new version of *MATLAB* (2021b or newer).

2) **Results.xlsx** – *Excel* spreadsheet with all the test cases and all the results obtained from the *MATLAB* subroutine (both the main results regarding the values of the flow parameters and the supplementary data regarding relative errors etc.) listed together.

3) **Plots.pdf** – PDF document containing all the results (in the form of *MATLAB* plots as in chapter 8 of this work) for the test cases that best match the wind flow characteristics provided by different standards (EN, ISO and ASCE).